UNIVERSITY OF SZCZECIN

INSTITUTE OF MARINE AND ENVIRONMENTAL SCIENCES

POLAND

Optimization of diatom culture conditions for the growth of 3D structured biosilica applied in wastewater treatment and nanoparticle synthesis.

By

Aleksandra Golubeva, M.Sc.

Doctoral dissertation

Supervisor:

Prof. Dr hab. Andrzej Witkowski

Institute of Marine and Environmental Sciences

University of Szczecin

Co-supervisor:

Dr. Przemysław Dąbek

Institute of Marine and Environmental Sciences

University of Szczecin

SZCZECIN 2023

OŚWIADCZENIE

Aleksandra Golubeva

Instytut Nauk o Morzu i Środowisku

Uniwersytet Szczeciński

Oświadczam, że moja praca pt.: **"Optimization of diatom culture conditions for the growth of 3D structured biosilica applied in wastewater treatment and nanoparticle synthesis."**

a) została napisana przeze mnie samodzielnie,

b) nie narusza praw autorskich w rozumieniu ustawy z dnia 14 lutego 1994 roku o prawie autorskim i prawach pokrewnych (Dz.U. 2019 r. poz. 1231) oraz dóbr osobistych chronionych prawem,

c) nie zawiera danych i informacji, które uzyskałem / uzyskałam w sposób niedozwolony,

d) nie była podstawą nadania tytułu naukowego lub zawodowego ani mnie ani innej osobie.

Ponadto oświadczam, że treść pracy przedstawionej przeze mnie do obrony, zawarta na przekazanym nośniku elektronicznym jest identyczna z jej wersją drukowaną.

Szczecin, dn.

podpis

OŚWIADCZENIE

Wyrażam zgodę na udostępnienie mojej pracy pt.: **"Optimization of diatom culture conditions for the growth of 3D structured biosilica applied in wastewater treatment and nanoparticle synthesis."**

Szczecin, dn.

<div align="right">

podpis

Aleksandra Golubeva

</div>

OŚWIADCZENIE

Akceptuję ostateczną wersję pracy pt.: "**Optimization of diatom culture conditions for the growth of 3D structured biosilica applied in wastewater treatment and nanoparticle synthesis.**"

Szczecin, dn.

<div style="text-align: right">

podpis

Prof. Dr hab. Andrzej Witkowski

</div>

OŚWIADCZENIE

Akceptuję ostateczną wersję pracy pt.: "**Optimization of diatom culture conditions for the growth of 3D structured biosilica applied in wastewater treatment and nanoparticle synthesis.**"

Szczecin, dn.

<div align="right">podpis
Dr. Przemysław Dąbek</div>

PUBLICATIONS

1) **Golubeva, A.,** Roychoudhury, P., Dąbek, P., Pałczyńska, J., P., Pryshchepa, O., Piszczek, P., Pomastowski, P., Gloc, M., Dobrucka, R., Feliczak-Guzik, A., Nowak, I., Kurzydłowski, K.J., Buszewski, B., & Witkowski, A. (2023a). A novel effective bio-originated methylene blue adsorbent: the porous biosilica from three marine diatom strains of *Nanofrustulum* spp. (Bacillariophyta). *Scientific Reports*, *13*, 9168. https://doi.org/10.1038/s41598-023-36408-6

Contribution – 65% (percent): I conceptualized the study, performed the experiments, interpreted the data, performed statistical analysis and mathematical modeling, prepared figures and tables, drafted the original manuscript, revised it following co-authors' suggestions, led the revision process after the peer review, and submitted the final version.

Detailed description:

The present study investigated the potential application of the porous nanostructured siliceous frustules from the diatom strains of *Nanofrustulum* spp. in wastewater treatment as an eco-friendly adsorbent with high removal efficiency for basic dye.

I established a continuous cultivation of the SZCZCH193 *N. wachnickianum*, SZCZM1342 *N. shiloi*, and SZCZP1809 *N.* cf. *shiloi* strains in a $100 - 500$ mL Erlenmeyer flasks and thoroughly investigated their growth kinetics. I analyzed the raw data and generated growth curves for biomass dry weight. From these curves, I calculated the maximum growth rate for each strain and compared the results with previously published data on *Nanofrustulum* spp. strains. After determining key kinetic parameters such as the maximum growth rate, the highest biomass yield, and the day of the highest biomass production, I designed a series of experiments to investigate the impact of various cultivation parameters, including initial nutrient concentrations (nitrate, phosphate, silicate), temperature, illumination intensity, and salinity, on biomass yield. I analyzed the raw data and performed a one-way ANOVA test to assess the significance of differences in biomass accumulation. I actively participated in the mass scale cultivation in a system of $2 - 5$ L bottles, and in a 70 L photobioreactor (PBR), biomass harvesting, and the cleaning process to obtain the pure biosilica.

I investigated the cleaned biosilica's morphology using SEM, analyzed its elemental composition with the EDS, helped identify functional groups on the biosilica surface through the ATR-FTIR, conducted UV-vis spectroscopy, calculated the band gap of the samples and the point zero charge using the salt addition method. I provided the biosilica samples for studying their porous nature through the low-temperature N_2 adsorption/desorption, measuring the zeta potential, study the crystalline structure by the XRD, and examining the thermal stability as suggested by reviewers during the peer review process. I obtained, analyzed, and interpreted the raw data obtained from these experiments.

Furthermore, I designed and conducted a batch adsorption study, time, pH, and initial dye concentration dependence of methylene blue removal by the diatom frustules from different strains. I analyzed and interpreted the raw data, performed kinetic and isotherm modeling to investigate possible adsorption mechanisms, and calculated each model parameter. I compared our findings with existing literature.

In addition, I took on the responsibility of writing the manuscript draft, creating all figures and tables, and incorporating revisions based on suggestions from co-authors and the peer review process.

2) **Golubeva, A.,** Roychoudhury, P., Dąbek, P., Pryshchepa, O., Pomastowski, P., Pałczyńska, J., Piszczek, P., Gloc, M., Dobrucka, R., Feliczak-Guzik, A., Nowak, I., Buszewski, B., & Witkowski, A. (2023b). Removal of the Basic and Diazo Dyes from Aqueous Solution by the Frustules of *Halamphora* cf. *salinicola* (Bacillariophyta). *Marine Drugs*, *21*, 312. https://doi.org/10.3390/md21050312

Impact Factor: 6.085

Lista czasopism MEiN: 100

Contribution – 70% (percent): I conceptualized the study, performed the experiments, interpreted the data, performed statistical analysis and mathematical modeling, prepared figures and tables, drafted the original manuscript, revised it following co-authors' suggestions, led the revision process after the peer review, and submitted the final version.

Detailed description:

This research introduces a novel eco-friendly adsorbent for basic and diazo dyes in wastewaters — the porous biosilica derived from the marine diatom *H*. cf. *salinicola*, which not only

demonstrated a high potential for wastewater treatment, but also offers opportunities for biorefinery.

I continuously cultivated the strain in a 70 L photobioreactor (PBR), investigated its growth kinetics, analyzed the raw data, prepared growth curves for biomass dry weight and the number of cells, calculated the maximum growth rate for each curve, and compared the results with previously published data for *Halamphora* spp. strains. Additionally, I monitored the nitrate, phosphate, and silicate uptake by the strain. After determination of the main kinetic parameters, such as the maximum growth rate, the maximum biomass yield, and the day of maximum biomass production, I prepared the set of experiments to investigate the influence of cultivation parameters, such as initial concentrations of nitrate, phosphate, and silicate, temperature, illumination intensity, and salinity, on biomass yield. I analyzed the raw data and performed one-way ANOVA test to determine the significance difference in biomass accumulation. After biomass cultivation and harvesting, I took part in the cleaning process to obtain the pure biosilica.

I took part in the investigation of the morphology of the cleaned biosilica by SEM, the elemental composition by EDS, the functional groups on the biosilica surface using ATR–FTIR and performed the UV-vis spectroscopy. I provided the biosilica for the investigation of its porous nature through low temperature N_2 adsorption/desorption, for the zeta potential measurements, for the XRD investigation, and for the thermal stability study, suggested by the reviewers during the peer review process. I obtained, analyzed, and interpreted the raw data from the experiments mentioned above.

I designed and performed the batch adsorption study to determine the dependance of dye removal by the diatom frustules, time and initial dye concentration. I analyzed and interpreted the raw data, performed the kinetic and isotherm modeling in order to investigate possible mechanisms of adsorption, and calculated parameters of these models. I compared our results with the current literature.

I wrote the manuscript draft, prepared all figures and tables, and revised it after co-authors' suggestions and peer review.

3) Roychoudhury, P., **Golubeva, A.,** Dąbek, P., Pryshchepa, O., Sagandykova, G., Pomastowski, P., Gloc, M., Dobrucka, R., Kurzydłowski, K., Buszewski, B. & Witkowski, A. (2022b). Study on Biogenic Spindle-Shaped Iron-Oxide Nanoparticles by *Pseudostaurosira trainorii* in Field of Laser Desorption/Ionization Applications. *International Journal of Molecular Sciences*, *23*, 11713. https://doi.org/10.3390/ijms231911713

Impact Factor: 6.208

Lista czasopism MEiN: 140

Contribution – 20% (percent): I cultivated a *P. trainorii* strain and provided live biomass and the clean frustules for the research, took part in investigations of the morphology, elemental and functional analysis of the IONPs decorated frustules and control frustules, and preliminary LDI–MS investigation of IONPs, performed the zeta potential measurements of IONPs, and helped to obtain, analyze, and illustrate the data.

Detailed description:

This study proposes a rapid and eco-friendly method for synthesizing IONPs using the diatom strain *P. trainorii*, which demonstrated efficient production of intra and extracellular IONPs within 3 days, exhibiting potential in catalytic photodegradation of phenols from water and as a matrix for laser desorption/ionization low molecular weight analytes at nano- and picomolar levels.

I cultivated the strain in 100 – 500 mL Erlenmeyer flasks for preliminary estimation of its potential to synthesize the nanoparticles, performed the large-scale cultivation of the strain using a system of 2 – 5 L bottles and a 70 L photobioreactor (PBR) and provided biomass for further biosynthesis of extra- and intracellular IONPs.

I participated in the process of purification of the synthesized IONPs by ultrafiltration, UV-vis spectroscopic examination of extracellular IONPs, FTIR measurements of the control and IONPs loaded frustules of *P. trainorii*, preliminary LDI-MS analysis, as well as in preparation of the extra- and intracellular IONPs samples for the XRD analysis, TEM, and EDAX. I performed the zeta potential measurements for extracellular IONPs, SEM, EDS, and Elemental mapping for the IONPs loaded frustules. I obtained and helped to analyze, illustrate, and interpret the data. I reviewed and edited the manuscript and participated in revision after the peer review process.

ACKNOWLEDGMENTS

FUNDING

University of Szczecin

Institute of Marine and Environmental Sciences

Aleksandra Golubeva, M.Sc.

Tytuł rozprawy doktorskiej:

Optimization of diatom culture conditions for the growth of 3D structured biosilica applied in wastewater treatment and nanoparticle synthesis

Supervisor: Prof. dr hab. **Andrzej Witkowski**

Co-supervisor: dr **Przemysław Dąbek**

STRESZCZENIE ROZPRAWY DOKTORSKIEJ

W ostatnich latach okrzemki przyciągają uwagę naukowców ze względu na ich zdolność do akumulacji trójglicerydów (TAG), wielonienasyconych kwasów tłuszczowych (PUFA), fukoksantyny i chryzolaminy oraz poprzez trójwymiarowe perforowane pancerzyki krzemionkowe, które mogą mieć różne zastosowania przemysłowe i farmaceutyczne. Obecność pancerzyka umożliwia okrzemkom skuteczną obronę komórki przed toksycznymi związkami występującymi w środowisku morskim. W rezultacie okrzemki stały się jedną z najlepiej przebadanych grup mikroglonów pod względem oceny toksykologicznej wody. Zanieczyszczenie wody pochodzące z procesów przemysłowych jest poważnym problemem, ponieważ związki chemiczne stosowane w przemyśle mogą mieć negatywny wpływ na ekosystemy, organizmy wodne i zdrowie ludzi. Niniejsza praca koncentruje się na wykorzystaniu porowatej biokrzemionki pochodzącej z okrzemek morskich *Nanofrustulum wachnickianum* (szczep SZCZCH193), *N. shiloi* (SZCZM1342), *N.* cf. *shiloi* (SZCZP1809), *Halamphora* cf. *salinicola* (SZCZM1454) i *Pseudostaurosira trainorii* (BA170), do usuwania z zanieczyszczonych wód barwników i fenoli.

Niniejsze badania dotyczą wzrostu wybranych szczepów okrzemek w różnych warunkach hodowli oraz opracowania protokołu hodowli, który zapewni najwyższy uzysk ich biomasy. Porowaty charakter biokrzemionki scharakteryzowano przy pomocy badań makroporów i izoterm adsorpcji/desorpcji azotu w niskiej temperaturze dla rozkładu mezo- i mikroporów w

mikroskopie elektronowym (SEM). Przetestowano zdolność okrzemek do redukcji Fe^{3+}, opracowując tym samym nową metodę 'zielonej' biosyntezy nanocząstek żelaza. Aby lepiej poznać strukturę biokrzemionki, przeprowadzono również ocenę struktury molekularnej i krystalicznej, ładunku powierzchniowego, stabilności termicznej i czystości. Porównano zdolność adsorpcyjną badanej biokrzemionki okrzemkowej barwników kationowych i anionowych z węglem aktywnym, który jest szeroko stosowanym komercyjnie adsorbentem, co sugeruje jego potencjał jako przyjaznego dla środowiska adsorbentu do oczyszczania ścieków. Efektywność adsorpcji biokrzemionki okrzemkowej była wyższa dla barwników kationowych ze względu na tworzenie silnego wiązania elektrostatycznego, natomiast barwnik anionowy był odpychany przez ładunek ujemny na powierzchni pancerzyków. Aktywność fotokatalityczna biokrzemionki okrzemkowej została znacznie zwiększona poprzez wzbogacenie jej powierzchni nanocząsteczkami tlenku żelaza. Dlatego też, niemodyfikowana biokrzemionka może być stosowana jako nowy, przyjazny dla środowiska adsorbent barwników kationowych i anionowych pochodzenia biologicznego, podczas gdy 'zielona' modyfikacja pancerzyków stwarza potencjał do fotokatalitycznej degradacji związków fenolowych. Poprzez wzbogacanie biokrzemionki okrzemkowej różnymi metalami w kontrolowany sposób, istnieje możliwość uzyskania innowacyjnych biomateriałów o nowych i nieznanych dotąd właściwościach.

Słowa kluczowe: *Nanofrustulum*, *Halamphora*, *Pseudostaurosira*, adsorpcja, fotodegradacja, błękit metylenowy, czerwień kongo, fiolet krystaliczny, zieleń malachitowa, nitrofenol, nanocząstki żelaza, biosynteza, tempo wzrostu

ABSTRACT

In recent years diatoms have gained the attention of scientists for their ability to accumulate triglyceride (TAG), polyunsaturated fatty acids (PUFA), fucoxanthin, chrysolaminarin, and their three-dimensional perforated siliceous shells called frustulse, which have various industrial and pharmaceutical applications. The presence of the frustule allows diatoms to successfully defend their cell from toxic compounds in the marine environment. As a result, diatoms have become the most studied group of microalgae in terms of water toxicological assessment. Water pollution from industrial processes is a major concern, as synthetic compounds could have negative effects on the ecosystems, aquatic organisms, and human health. This study focuses on investigating the potential of the porous diatom biosilica extracted from the marine diatoms *Nanofrustulum wachnickianum* (strain SZCZCH193), *N. shiloi* (SZCZM1342), *N.* cf. *shiloi* (SZCZP1809), *Halamphora* cf. *salinicola* (SZCZM1454), and *Pseudostaurosira trainorii* (BA170) for their dye and phenol removal potential.

The research investigates the growth of different diatom strains under various culturing conditions and develops a culturing protocol that will allow to yield the highest biomass. The porous nature of the biosilica was evaluated through SEM studies of the macropore and the low temperature nitrogen adsorption/desorption isotherm for the meso- and micropore distribution. Diatom Fe^{3+} reduction capacity has been examined, establishing a novel method for green biosynthesis of iron oxide nanoparticles. The assessment of the molecular and crystalline structure, surface charge, the thermal stability, and purity has been performed to further understand the nature of the biosilica. The adsorption capacity of the cationic and anionic dyes of the studied diatom biosilica was comparable to that of activated carbon, a widely used commercial adsorbent, suggesting its potential as an environmentally friendly adsorbent for wastewater treatment. The adsorption efficiency of the diatom biosilica was higher for the cationic dyes due to the formation of a strong electrostatic bond, while the anionic dye was repulsed by the negative charge on the surface of the frustule. The photocatalytic activity of the diatom biosilica was significantly enhanced through the decoration of the surface with iron oxide nanoparticles. Therefore, the non-modified diatom biosilica could be used as a novel eco-friendly bio-originated adsorbent of cationic and anionic dyes, while controlled green modification of the frustule presents a potential for photocatalytic degradation of phenolic compounds. Through modification of the diatom biosilica with various metals in a controlled manner, it was possible to obtain innovative biomaterial with new properties.

LIST OF CONTENT

ANNEX I.

Golubeva, A., Roychoudhury, P., Dąbek, Pałczyńska, J., P., Pryshchepa, O., Piszczek, P., Pomastowski, P., Gloc, M., Dobrucka, R., Feliczak-Guzik, A., Nowak, I., Kurzydłowski, K.J., Buszewski, B., & Witkowski, A. (2023a) A novel effective bio-originated methylene blue adsorbent: the porous biosilica from three marine diatom strains of *Nanofrustulum* spp. (Bacillariophyta). *Scientific Reports*, *13*, 9168.

ANNEX II

Golubeva, A., Roychoudhury, P., Dąbek, P., Pryshchepa, O., Pomastowski, P., Pałczyńska, J., Piszczek, P., Gloc, M., Dobrucka, R., Feliczak-Guzik, A., Nowak, I., Buszewski, B. & Witkowski, A. (2023b) Removal of the Basic and Diazo Dyes from Aqueous Solution by the Frustules of *Halamphora* cf. *salinicola* (Bacillariophyta). *Marine Drugs*, *21*, 312.

ANNEX III

Roychoudhury, P., **Golubeva, A.,** Dąbek, P., Pryshchepa, O., Sagandykova, G., Pomastowski, P., Gloc, M., Dobrucka, R., Kurzydłowski, K., Buszewski, B. & Witkowski, A. (2022) Study on Biogenic Spindle-Shaped Iron-Oxide Nanoparticles by *Pseudostaurosira trainorii* in Field of Laser Desorption/Ionization Applications. *International Journal of Molecular Sciences*, *23*, 11713.

INTRODUCTION

Diatoms (derived from Greek *dia* "through" and *temnein* "to cut") is a large group of microorganisms belonging to the Stramenopiles clade also known as Heterokonts. These microorganisms are unicellular and could occur either as a single cell or as a colony. Their chimeric genome, with genes originating from bacteria, red and green algae, is a result of a series of endosymbiotic events (Petersen et al., 2006; Stiller et al., 2014; Sibbald & Archibald, 2020) and proved to be the reason for their unique adaptable metabolism (Dorrell et al., 2017), which allows them to thrive in a wide range of environments, from freshwater and marine to extreme thermal geysers, springs and polar glaciers (Bowler et al., 2010). Diatoms are photoautotrophic organisms responsible for almost 40% of the oceanic and 20% of the global primary production (Falkowski et al., 2005). Nevertheless, they could exhibit mixotrophic or even heterotrophic behavior, discovered for the first time 70 years ago (Lewin, 1953). Another unique feature is their urea cycle, similar to one found in metazoans and absent in red and green algae. The urea cycle promotes rapid recovery from extended nitrogen deficiency, which mostly affects arginine and ornithine cycles (Allen et al., 2011). These metabolites are known to be precursors for the long-chain polyamine compounds, associated with the silica shell formation in the diatom cell (Kröger & Poulsen, 2008). The biomineralization process in diatoms is a complex biological phenomenon, which includes accumulation of silicic acid $Si(OH)_4$ from the environment and biosynthesis of the uniquely sculptured and perforated three-dimensional cell wall in the form of biogenic opal ($SiO_2 \ nH_2O$), known as a frustule. Some attribute the evolutionary triumph of diatoms to the presence of the silica cell wall, because the biomineralization likely requires less energy than synthesis of organic material (Raven, 1983) and the frustule may protect the organism from grazers and mechanical force (Smetacek, 1999). Further studies recognized two additional functions of the silica wall, i.e. a proton buffering role and assistance in light harvesting for photosynthesis. Milligan and Morel (2002) demonstrated that biosilica of the centric diatom *Thalassiosira weissflogii* (Grunow) Fryxell & Hasle serves as an efficient pH buffer, facilitating the enzymatic conversion of bicarbonate to CO_2, crucial for diatoms to acquire inorganic carbon. Fuhrmann et al. (2004) studied the optical structure of the frustules of *Coscinodiscus granii* Gough and concluded that the biosilica has the properties of a photonic crystal, which can couple light into the waveguide and assist in photosynthesis.

Diatoms have gained attention in applied sciences due their capacity to produce diverse bioactive compounds and fine chemicals with great industrial potential. For instance, fucoxanthin exhibits antioxidant, anti-inflammatory, anticancer, and hepatoprotective effects, making it suitable for use in pharmaceuticals and cosmetics (Peng et al., 2011). Unsaturated fatty acids have been utilized as dietary supplements (Roche, 1999; Li, H. Y. et al., 2014), and triacylglycerols (TAG) serve as a carbon source for the conversion into various biofuels (Hildebrand et al., 2012). Additionally, diatoms hold biotechnological potential for biorefinery processes, offering a cost-effective way to produce a number of compounds using diatom biomass (Branco-Vieira et al., 2020).

1.1. *Structure of the diatom frustule*

The shape of the cells as well as the intricate patterns of nano-scale to micro-scale pores, ridges, and tubular structures are genetically species-specific (Figure 1).
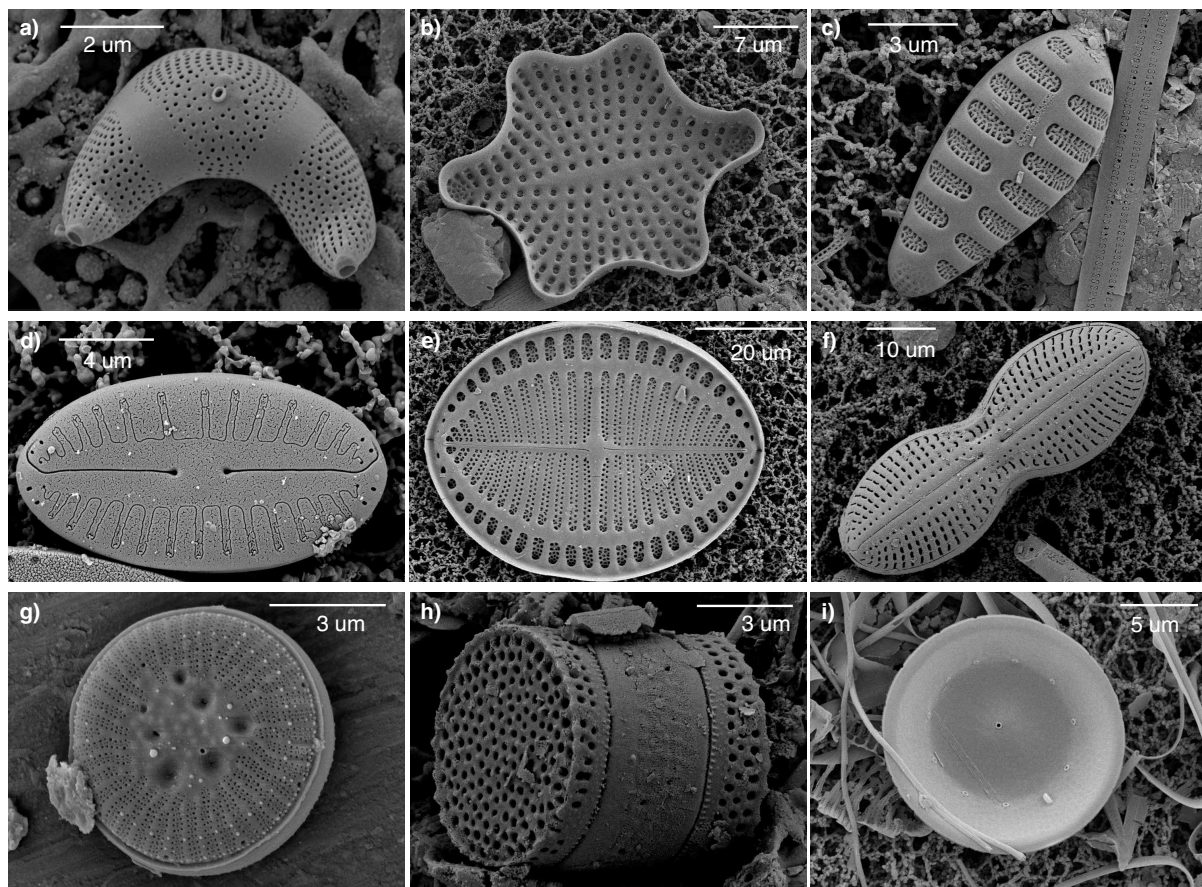
Figure 1. Diversity of the diatom frustules **(a)** *Ceratanaulus creticus* (Drebes & Schulz) Gorecka, Witkowski, Dabek & Ashworth, **(b)** *Perissonoe* sp. Andrews & Stoelzel – internal view, **(c)** *Opephora* sp. Petit, **(d)** *Fallacia* sp. Stickle & Mann, **(e)** *Cocconeis* sp Ehrenberg –

raphe valve, **(f)** *Diploneis* sp. Ehrenberg ex Cleve, **(g)** *Cyclotella* sp. (Kützing) Brébisson, **(h)** *Endictya* sp. Ehrenberg, **(i)** *Thalassiosira nordenskioeldii* – internal view.

Nevertheless, the frustules have a common structural layout resembling a Petri dish (Figure 2): a bigger part called epitheca and a smaller one, the hypotheca. The sides of the theca are called girdle bands, attached to the valves (epivalve and hypovalve, respectively) and provide the overlap between the two thecae. Diatoms are divided into two groups based on their symmetry, i.e. pennate with bilateral symmetry and centric with radial symmetry. Pennate diatoms may possess one or two slits called a raphe with a central nodule, which is the site of the first silica deposition during the valve formation.
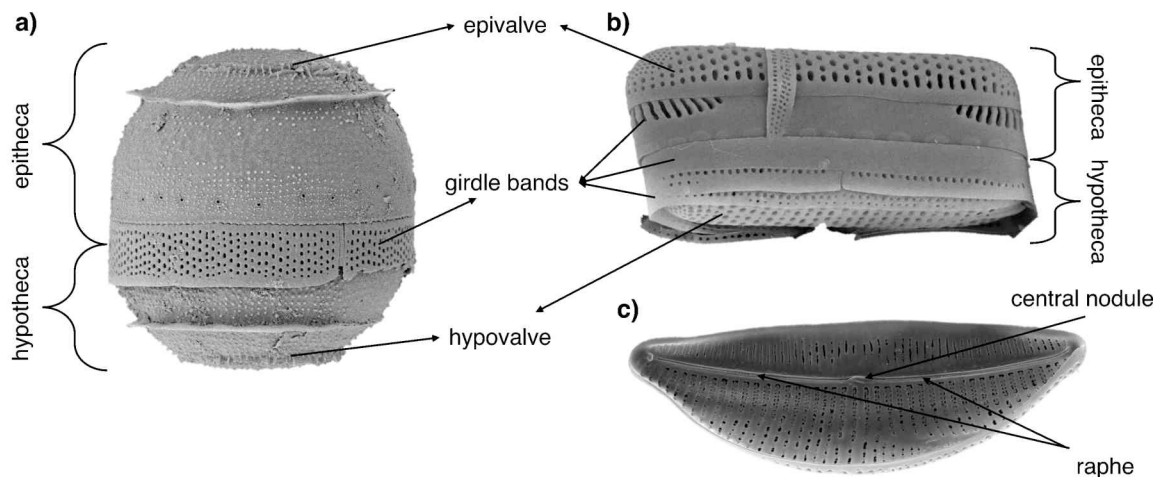
Figure 2. Schematic structure of the diatom frustule, i.e., centric **(a)** *Melosira* sp. Agardh and pennate **(b)** *Grammatophora* sp. Ehrenberg and (c) *Halamphora* sp. (Cleve) Mereschkowsky.

There are two types of micro- and nanoscale perforations on the frustule's surface (Figure 3). The first type is the simple pore (Figure 3a) which is a hole in a homogeneous silica wall, while the second type, the loculus, consist of a hexagonal chamber inside the wall and is separated from other loculi by the vertical spacers with small pores (lateral pores) for communication between them. Usually at one end of the loculus there is a pore membrane (sieve membrane), which could be located on the inside (an outward opening loculus, Figure 3b) as well as on the outside (an inward opening loculus, Figure 3c). A single row of pores or loculi is called a stria. Some diatoms have the same porous architecture on the valves and the girdle bands, but most of the others possess different ornamentation on the valve face and the girdle bands, and sometimes the girdle bands have no sculpturing at all. Additionally, some species of diatoms could possess porous extensions of the valve, called processes. The labiate process (Figure 3d)

is a tube with a simple, round external opening, and an internal slit, while the strutted process (Figure 3e) contain openings at both ends which are surrounded by 2–5 porous chambers for additional support. The main function of these extensions is to maintain contact between contiguous cells and assist with colony formation.
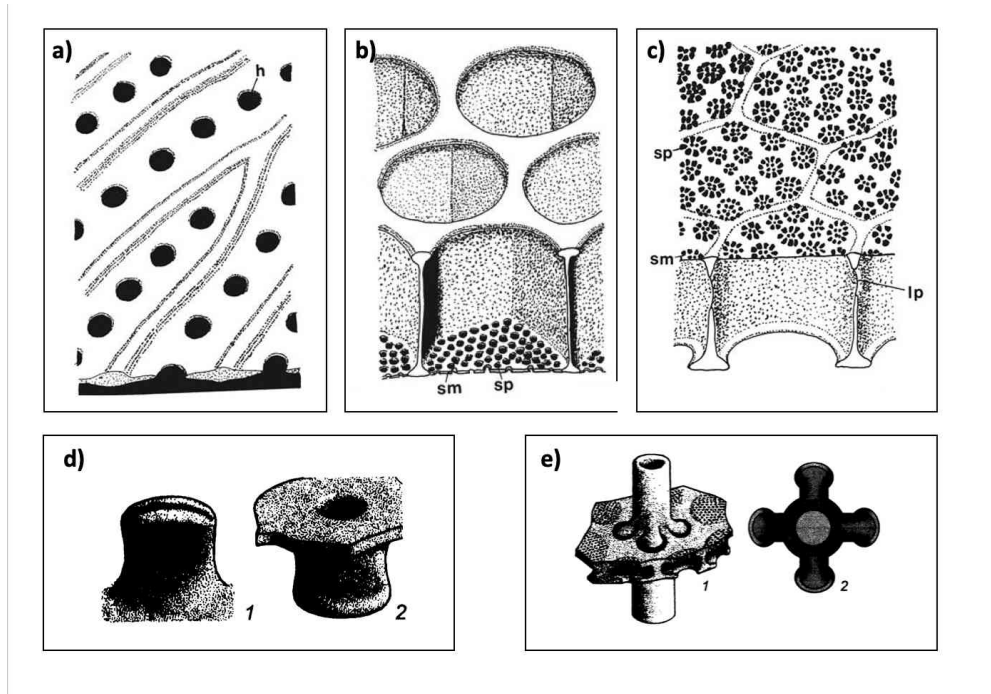
Figure 3. The morphology of the biosilica perforations in diatoms: **(a)** simple pore, **(b)** loculus opening outward, **(c)** loculus opening inward, (h – hole, lp – lateral pore, sm – sieve membrane, sp – sieve pore; from Lee, 2008), **(d)** labiate process (1 – lateral view, 2 – valve view) and **(e)** strutted process (1 – lateral view, 2 – valve view) (from Round et al., 1990) Copyright © 2008 R.E. Lee; ©1990 Marine Biological Association of the United Kingdom.

1.2. *Diatom frustules morphogenesis*

The stiffened architecture of the frustule imposes a limitation on the growth of the cell. The silica cell wall could be synthesized exclusively during the cell division process. There is a specialized membrane-bound compartment located within the diatom cytoplasm called the silicon deposition vesicle (SDV) (Drum & Pankratz, 1964), an organelle known to occur in diatoms, sponges, radiolarians, and synurophytes. The development of the SDV involves intracellular transport of the cell wall-associated proteins (Figure 4a). Proteins, which are not directly involved in the biosilica formation become associated with the silica surface in the extracellular space (frustulins and pleuralins) and assume to be secreted through the standard secretory pathway using secretory vesicles (SV). On the other hand, proteins and long-chain polyamines (LCPAs) involved in silica formation (e.g., silaffins, silacidins, cungulins) are

hypothesized to follow a separated pathway – these proteins are packaged into the SDV transport vesicles (STV), which are targeted for fusion with the SDV (Brunner et al., 2009). *In vitro* studies showed that these biomolecules promote rapid silica precipitation (Kröger et al., 2002), and it is believed that their main functions in diatom morphogenesis are (i) to accelerate silica precipitation and (ii) to provide the template for synthesis of characteristic micro- and nanoperforations on the frustule surface (Gröger et al., 2008a).
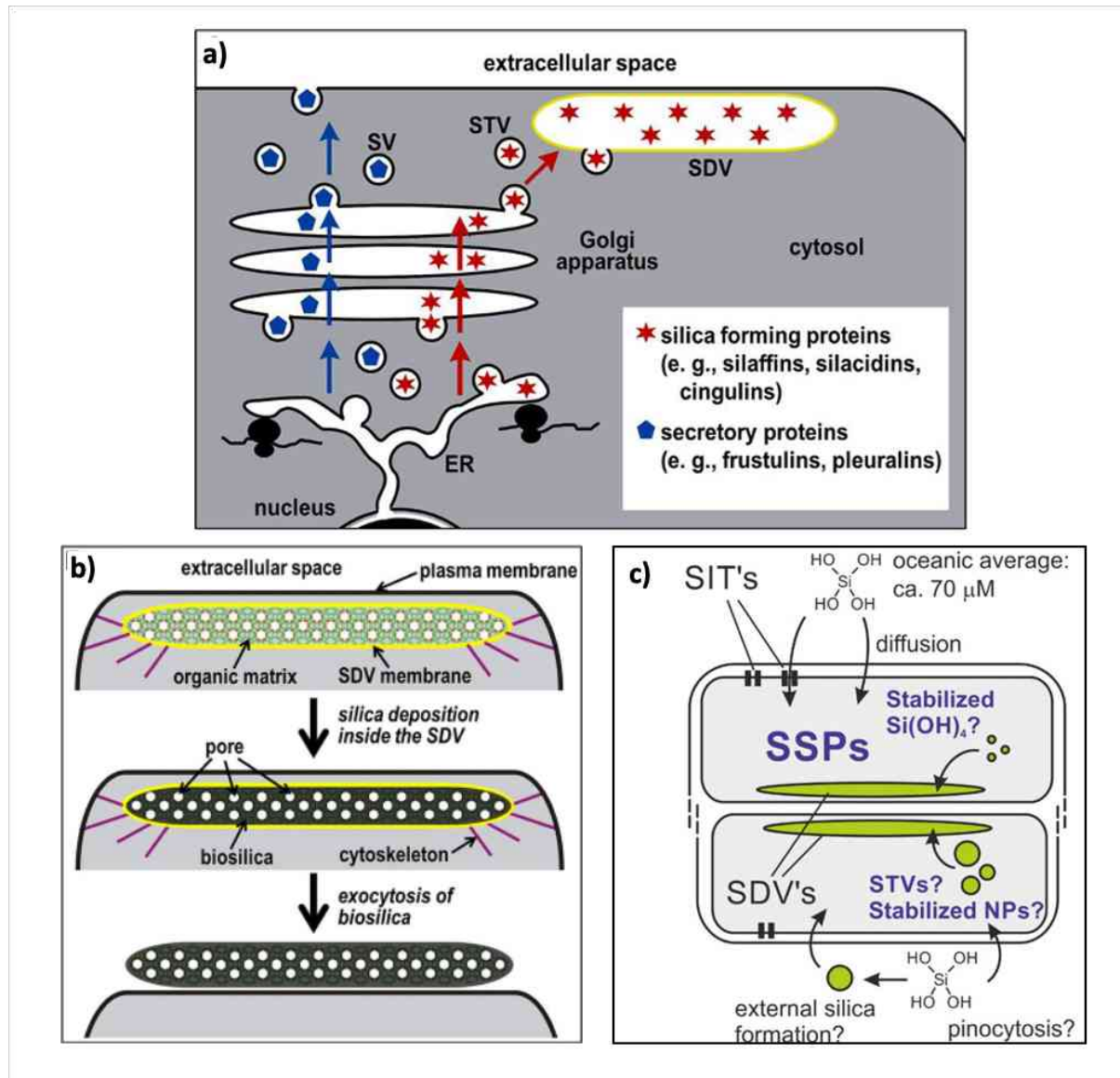
Figure 4. Proposed mechanism of **(a)** the intracellular transport of cell wall-associated proteins during **(b)** the biosilica formation inside the silicon deposition vesicle (SDV – the silicon deposition vesicle, STV – the SDV's transport vesicles, SV – secretory vesicles, ER – endoplasmic reticulum; from Poulsen et al., 2013) and **(c)** the silica uptake following intracellular transport (SITs – the specific silicic acid transporter protein, SSPs – the internal

silicon storage pools, STVs – the silicon transport vesicles, NPs – silicon nanoparticles; from Kolbe & Brunner, 2022) Copyright © 2013 Elsevier Ltd., © 2022 Springer Nature.

The process of valve formation in diatoms involves the deposition of the silica inside the SDV (Figure 4b). It is believed that elements of the cytoskeleton help to maintain the proximity of the SDV membrane to the plasma membrane. The SDV lumen organic matrix is encapsulated within the membrane and composed of forementioned biomolecules. It serves as the micro- and nanopatterned template for silica morphogenesis. After formation and morphogenesis of the frustules in the respective SDV, siliceous elements are delivered to the cell surface through exocytosis and become part of the diatom cell wall (Kröger & Poulsen, 2008).

To synthesize the silica shell in the SDV, diatoms need to uptake enough silicon from the environment (Figure 4c). As mentioned previously, diatom cells take up silicon in the form of silicic acid $Si(OH)_4$ through the specific silicic acid transporter proteins (SITs) and/or through direct pinocytosis across the plasma membrane (Hildebrand, 2000). The accumulated and highly concentrated silica is believed to be deposited in the internal soluble silica ponds (SSPs) (Martin-Jézéquel et al., 2000; Kumar et al., 2020). There are suggestions that diatoms may possess some kind of ligands which form the stable complexes with silica in the SSPs, thereby restricting their ability to precipitate (Sumper, 2004). The mechanism of intracellular transport of silica, which leads to the biosilica formation in the SDV, is still poorly understood. There is a hypothesis suggesting that the silicon transport vesicles (STVs) deliver the silica and silicon nanoparticles (NPs) to the SDVs and merge with developing SDVs (Schmid & Schulz, 1979; Gröger et al., 2008b; Grachev et al., 2017).

1.3. Modification of the diatom frustules

In the past decade there has been a significant increase in research interest regarding the use of the diatom biosilica for various applications, from water remediation to drug delivery, due to their unique and variable perforated architecture, thermal and mechanical stability, inertness, biocompatibility, and nontoxicity. The utilization of diatoms in nanobiotechnology offers several advantages, particularly in terms of cost-effectiveness, no requirement to use hazardous reagents, and the ability to create complex structures. However, while silicon is the primary material used in the diatom frustules, it may not always be suitable for certain applications. To address this limitation, researchers have developed alternative methods to incorporate metals into the diatom frustule (Roychoudhury et al., 2022a).

1.3.1. Metabolic insertion of the diatom biosilica with metal ions

One technique is based on metabolic incorporation of metal ions inside the silica frustule during diatom cultivation. The diffusion of metal ions through specific silicic acid transporters and direct pinocytosis lead to incorporation of metal ions into silica frustule biosynthesis inside the cell. Candidate metals for metabolic insertion are titanium as $Ti(OH)_4$ and germanium as $Ge(OH)_4$, due to their ability to form a soluble metal tetrahydroxide $M(OH)_4$, resembling $Si(OH)_4$. The proposed mechanism of metabolic insertion is illustrated in Figure 5. Two vital requirements for this process are (i) initial silicon-starvation of the diatom culture with no soluble Si present, and (ii) co-feeding $Si(OH)_4$ and $M(OH)_4$ to diatom cells to ensure at least one cell division. Metal ions and silicon will be transported inside the protoplast to the SDVs, where the forementioned process of silica deposition into the organic template will be carried out with disposition of these metals in a form of silica-clusters inside the newly synthesized cell wall (Rorrer, 2017; Brzozowska et al., 2020).
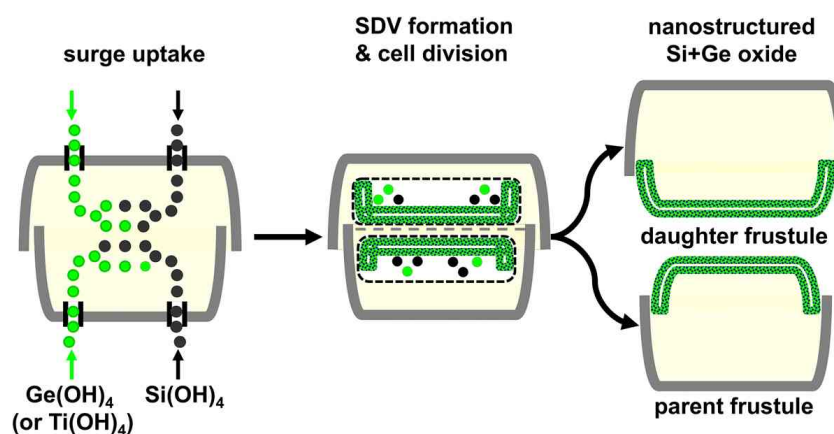
Figure 5. The possible *in vivo* mechanism of metabolic insertion of Ge (or Ti) into the diatom frustule (from Rorrer, 2017) Copyright © 2018, The Royal Society of Chemistry.

There are several reports on the metabolic insertion of titanium for *Pinnularia* sp. Ehrenberg with 2.3 wt % (Jeffryes et al., 2008a), 2.37 wt % (Chauton et al., 2015), 10.4 wt % titanium incorporation (Van Eynde et al., 2016), *Thalassiosira weissflogii* with 34 wt % (Lang et al., 2013), *Synedra acus* Kützin with 0.6 wt % (Basharina et al., 2012), *Coscinodiscus* sp. Ehrenberg with 0.93 wt % (Skolem, 2011), *Pseudostaurosira trainorii* Morales with 8.59 wt % (Brzozowska et al., 2022), and *Fistulifera solaris* Mayama, Matsumoto, Nemoto & Tanaka with 10.6 wt % (Maeda et al., 2018). Research with titanium registered the lack of a cytotoxic

effect of the ions with no change in the fine pore structure (Skolem, 2011; Lang et al., 2013; Chauton et al., 2015).

The chemical similarity of germanium and silicon may result in inhibition of the frustule formation, and it is reported that germanium oxide suppress the diatom growth at only $1.0 \, \mu M$ of GeO_2 in the medium (Lewin, 1966). Several researchers (Werner, 1967; Azam et al., 1973; Basharina et al., 2012) confirmed the cytotoxicity of germanium ions on diatoms. Moreover, there are reported changes in the frustule morphology after germanium doping that includes the removal of fine pore structure of *Pinnularia* sp. with 1.0 wt % germanium incorporation (Jeffryes et al., 2008b), changes in shape and thickness of the frustules of *S. acu*s with 5.1 mol % incorporation (Basharina et al., 2012), gaps between ribs and malformation of pores of *Thalassiosira pseudonana* Hasle & Heimdal with 0.5 wt % (Davis & Hildebrand, 2008), the frustule aberration of *Stauroneis* sp. Ehrenberg (Ali et al., 2011), and reduction of the pore sizes of *Nitzschia frustulum* (Kützing) Grunow with 0.5 wt % (Qin et al., 2008a), and around 5.0 wt % (Rorrer et al., 2005).

There are several reports on the metabolic insertion of other water-soluble metals. Aluminum ions have been successfully incorporated into the frustules of *Stephanopyxis turris* (Greville) Ralfs without any significant changes in the morphology the cell (Machill et al., 2013). The changes in fine pore structure have been observed after nickel doping of *Conscinodiscus wailesii* Gran & Angst with nickel incorporation of 0.1 wt % (Townley et al., 2007). Addition of calcium ions to diatom culture is reported to not influence the shape and structure of *T. weissflogii* with 0.9 wt % incorporation (Leone et al., 2017) and *Coscinodiscus* sp. (Li et al., 2018). Zirconium and tin doping results showed a slight decrease in growth rate and mechanical strength of the frustules of *S. acus* with 3.4 mol % of Zr/Si and 0.91 mol % of Sn/Si (Basharina et al., 2012). Zhang et al. (2013) presented doping of *Navicula* sp. with europium ions which changed the photoluminescence properties of the biosilica.

1.3.2. Decoration of the diatom biosilica with metal nanocomposites

Other techniques propose the frustules as a reducing agent for gold, silver, iron, and other metals. This approach could help to achieve higher concentrations of metals than the metabolic incorporation method. There are several methods to decorate the frustules with nanocomposites. Palladium ($PdCl_2$) nanocomposites were deposited onto *P. trainorii* frustules by dispersing it in ultrasonic bath for 3 h in a mixture of methanol and 1 wt % of $PdCl_2$ (Sprynskyy et al., 2021). Jantschke et al. (2012) demonstrated two strategies, i.e. (i) layer-by-layer deposition based on the bond between negatively charged biosilica – positively charged

polyelectrolyte – negatively charged nanoparticles, and (ii) covalent bonding of nanoparticles to the frustule surface through an amide bond between the amino groups of the biosilica and carboxylic groups on nanoparticles (Figure 6). Both were used for platinum nanoparticles' decoration of *Eucampia zodiacus* Ehrenberg and *Coscinodiscus wailesii* frustules. Resultant platinum concentration for covalent bonding has been 6 times higher than in the layer-by-layer method (6.82 µg and 42.6 µg).
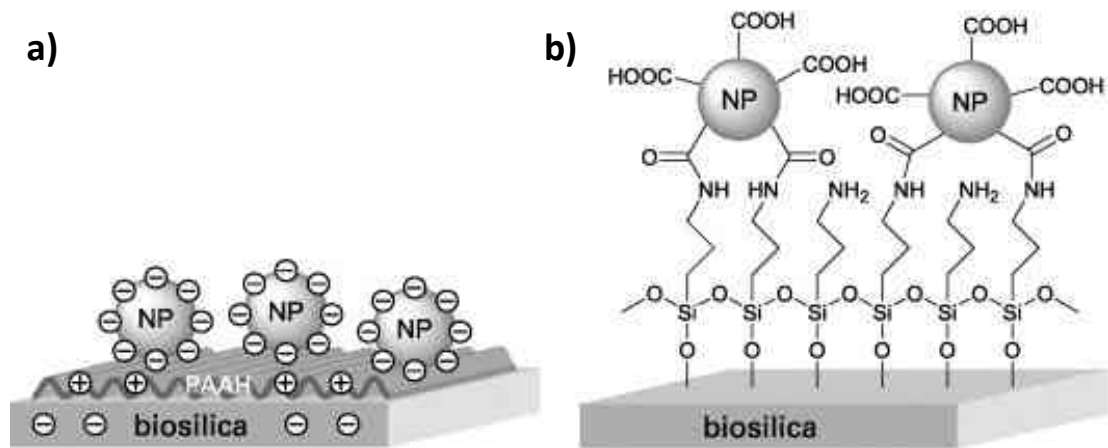
Figure 6. Deposition of nanoparticles on the frustules surface: (a) layer-by-layer and (b) covalent bonding (from Jantschke et al., 2012) Copyright © 2012 Wiley-VCH Verlag GmbH & Co., KGaA.

Covalent coupling has been successfully utilized for decoration of *S. turris, E. zodiacus*, and *T. pseudonana* with gold nanoparticles (Fischer et al., 2016). Good reducing ability for gold was exhibited by the diatoms *Aulacoseira* sp. Thwaites (Briceño et al., 2021), and *Amphora copulata* (Kützing) Schoeman & Archibald (Roychoudhury et al., 2016). Diatom species *Halamphora subturgida* (Hustedt) Levkov*, Gedaniella flavovirens* (Takano) Li, Witkowski & Ashworth, and *Gedaniella mutabilis* Li & Witkowski have been used for biosynthesis of silver nanoconjugates (nanodendrites and nanoflowers) with sodium citrate used as a nano-capping agent (Bose et al., 2021; Roychoudhury et al., 2021). There are a number of reports on metal-silica nanocomposites available: cadmium on the surface of *Pinnularia* sp. (Gutu et al., 2009), zinc deposited on the frustules of *Coscinodiscus lineatus* Ehrenberg (Zhou et al., 2009), titanium oxide decorated frustules of *Cocconeis placentula* Ehrenberg (He et al., 2013), and *Caloneis schroederi* Hustedt (Kumari et al., 2020).

1.4. Techniques utilized for characterization of the diatom biosilica

There are several techniques used to characterize the diatom biosilica. Scanning electron microscopy (SEM), is widely used among the diatomologists and allows to study the diatom surface morphology at micro- and nano-scale level, which supports an identification of its taxonomic status, as well as observation of the characteristic features of the diatom cell wall. Moreover, SEM images will help to identify the presence or absence of any aggregations or composites on the surface after the biosilica modification/functionalization with inorganic and organic compounds. Coupled with an energy-dispersive detector (EDS), SEM could provide information on the elemental composition of the selected frustule surface. Transmission electron microscopy (TEM) and atomic force microscopy (AFM) are usually used for deeper investigation of the porous nature of the nanostructures on the diatom surface (Saoud et al., 2022). Moreover, TEM and confocal fluorescence microscopy images of diatoms from different growth phases allow researchers to study the forementioned process of silica wall synthesis inside the diatom cell (Kröger & Poulsen, 2008). Another tool, to help identify the presence of silica and associated organic compounds inside the frustules (Wisser et al., 2015) as well as to describe and identify the viability of the diatom biosilica for drug delivery is ^{29}Si and ^{13}C nuclear magnetic resonance (NMR) spectroscopy (Saoud et al., 2022). The signals of ^{29}Si centered at $\delta = -92$ ppm, $\delta = -100$ ppm, and $\delta = -108$ ppm correspond to the geminal silanols (Q_2), free silanols (Q_3), and siloxane (Q_4) groups, respectively (Wisser et al., 2015; Johnston et al., 2018). The X-ray powder diffraction (XRD) method is utilized for detection of the amorphous or crystalline structure of the diatom biosilica. The non-modified frustules of *P. trainorii* were identified as an amorphous opal-like silica (Sprynskyy et al., 2017), while the frustules modified with palladium (Sprynskyy et al., 2021), titanium (Brzozowska et al., 2022), silver and ruthenium (Chudzińska et al., 2023) were described as a crystalline material. To identify the functional groups, present on the diatom surface, Fourier-transform infrared spectroscopy (FTIR) is used. The characteristic peaks in the 440 cm^{-1} and the 1040–1060 cm^{-1} regions correspond to the Si–O bond (Camargo et al., 2016). Moreover, FTIR spectra allow the identification of amine and amide groups from organic compounds associated with the diatom cell wall (e.g., silaffins, frustulins, LCPAs) (Otzen, 2012). To measure heavy metal uptake by the diatom frustules, the inductively coupled plasma mass spectroscopy (ICP-MS) (Redan et al., 2019) or atomic adsorption spectroscopy (AAS) (Hernández-Ávila et al., 2017) may be used. Additionally, ICP-MS could help to determine the efficiency of metal modification of the frustules (Lang et al., 2013).

The thermogravimetric analysis (TGA) and differential thermal analysis (DTA) are utilized to assess the thermal stability, decomposition, purity, phase transitions, and melting points (Sprynskyy et al., 2017; Saoud et al., 2022). Unique optical and photonic features of the diatom biosilica can be characterized using spectrofluorometry. The modification and functionalization of the frustules will change its photoluminescence, which is important for biosensing applications (Brzozowska et al., 2022). The low temperature nitrogen adsorption/desorption method is commonly used for the characterization of the biosilica's porosity through the adsorption/desorption isotherm, where IUPAC Type 1 refers to microporous material and Type 2 refers to nonporous or macroporous materials (Thommes et al., 2015). With the N_2 adsorption/desorption data it is possible to calculate the surface area, porosity, and pore diameter distribution, using theoretical models such as Brunauer–Emmett–Teller and Barret–Joyner–Halends (Sprynskyy et al., 2017). Additionally, the zeta potential measurements of the diatom biosilica within a range of pH could help to understand the surface charge and the colloidal stability of the suspension. Literature suggests that stable and non-aggregating systems typically exhibit the absolute zeta potential values greater than +/– 25 mV. Moreover, the zeta potential influences the adsorption properties of the material: a negatively charged surface, for example, tends to have a higher affinity for cationic compounds and vice versa (Gumustas et al., 2017; Pryshchepa et al., 2020). The charge could be manipulated by modification and functionalization of the biosilica (Yu et al., 2012).

1.5. *Application of the diatom biosilica*

1.5.1. Biomedical research

The diatom biosilica has been investigated for its potential use as a drug delivery system. The main advantages of the frustules as a drug carrier are their three-dimensional structures with natural variability of surface architecture, chemical inertia, biocompatibility, nontoxicity, low cost of synthesis, and easy manipulation of pore sizes (Wang et al., 2013; Terracciano et al., 2018; Rogato & De Tommasi, 2020; Tramontano et al., 2020; Roychoudhury et al., 2022a; Zobi, 2022). For a long time, most of the studies were focused on using diatomaceous earth (or diatomite), a natural sediment material accumulated in oceans and large lakes and composed of the frustules of different diatoms, in the field of oral drug delivery (Aw et al., 2013; Zhang et al., 2013; Milović et al., 2014; Vasani et al, 2015). Gnanamoorthy et al. (2014) reported more than 30 wt.% of streptomycin loading capacities for *Coscinodiscus concinnus* Smith frustules *in vitro* with a two-phase release. Functionalized with dopamine and modified with magnetic

iron oxide nanoparticles of *Aulacoseira* sp. showed sustained release of indomethacin (Losic et al., 2010). *Thalassiosira weissflogii*, functionalized with the TEMPO, a scavenger of reactive oxygen species (ROS), demonstrated great potential in loading and release of ciprofloxacin (Cicco et al., 2015). The same specimen has been genetically engineered to enable the attachment of the cell-targeting antibodies, which allows selective targeting and killing of neurblastoma and B-lymphoma cells (Delalat et al., 2015). The chitosan functionalized frustules of *Amphora subtropica* Wachnicka & Gaiser demonstrated a high doxorubicin loading efficiency and low toxicity compared to free doxorubicin (Sasirekha et al., 2019). *Aulacoseira* sp. decorated with gold nanoparticles showed faster gentamicin release and slower loading in *ex-situ* method compared with *in-situ* (Briceño et al., 2021). Encapsulated within the magnetically active frustules of *Nitzschia* sp. Hassall curcumin revealed higher cytotoxicity against tumor cells compared to free curcumin (Javalkote et al., 2015). *Cyclotella cryptica* Reimann, Lewin & Guillard frustules loaded with copper nanoparticles significantly improved the photothermal and photodynamic performance of biomaterial for infected wound therapy and demonstrated almost 100% antibacterial efficiency against *Staphylococcus aureus* and *Escherichia coli* (Cong et al., 2022). Furthermore, the diatom biosilica exhibited high potential in bone regeneration and tissue engineering applications (Reid et al., 2021). The alendronate-doped *T. weissflogii* increased osteoblasts growth, exhibited low toxicity and high antioxidant activity (Cicco et al., 2015; Cicco et al., 2016; Cicco et al., 2019), while calcium doped biosilica of the same species presented high biocompatibility with Saos-2 cell line (Leone et al., 2017). Additionally, some reports indicate the potential of the diatom frustules in hemorrhage control, e.g. *Coscinodiscuss* sp. doped with calcium strengthened the intrinsic blood coagulation pathway (Li et al., 2018).

The biosilica is well known to have photoluminescent capabilities, which could be enhanced by the metal modification, and used as a biosensor for the detection of the target chemical substance (Wang et al., 2013; Rogato & De Tommasi, 2020; Tramontano et al., 2020; De Tommasi & De Luca, 2022; Roychoudhury et al., 2022a; Zobi, 2022). Research on the photoluminescence (PL) of the diatom frustules of *Thalassiosira rotula* Meunier and *Coscinodiscus wailesii* established that this process is greatly influenced by environmental conditions, i.e., the strength of the biosilica's PL signal decreased after exposure to NO_2 (Lettieri et al., 2008). Qin et al. (2008b) reported that the intensity of the PL of *Nitzschia frustulum* correlates with changes in the nanostructure of the frustule during the different growth phases. Moreover, the metabolically doped with germanium biosilica of *Pinnularia* sp.

demonstrated both photoluminescent and electroluminescent properties, while the non-modified biosilica did not emit any detectable electroluminescence (Jeffryes et al., 2008c).

The diatom biosilica is reported to be a photonic crystal (Fuhrmann et al., 2004; De Tommasi & De Luca, 2022), and could therefore be used in the preparation of fluorescence immunoassays. Squire at al. (2018) compared *Pinnularia* sp. composite with rhodamine 6G (R6G) and the R6G-labeled mouse immunoglobulin G (IgG). A 100-fold increase in the detection limit of fluorescence spectroscopy was observed, proving the biosilicas' ability to enhance fluorescence with high sensitivity. Later, Squire et al. (2019) used the same diatom, functionalized with fluorophore-labeled antibodies, for the detection of the cardiovascular disease biomarker – clinically relevant N-terminal prohormone B-type natriuretic peptide (NT-proBNP), and reported excellent specificity, accuracy, and sensitivity of 93%, 78%, and 65%, respectively. Glutaraldehyde crosslinked amine-functionalized *Amphora* sp. Ehrenberg ex Kützing has been successfully utilized in the detection of a *Salmonella typhi* antibody with high specificity (Selvaraj et al., 2018), and magnetic iron oxide nanoparticles coated frustules of *Chaetoceros* sp. Ehrenberg demonstrated great selectivity in targeting and capturing breast cancer cells (SKBR3) in blood (Esfandyari et al., 2020).

Another technique for the discovery of biosensing potential of the material is the surface-enhanced Raman scattering (SERS). The unique structure of diatoms allows them to enhance the localized surface-plasmon resonance (LSPR) resulting in near-field optical amplification of the signal (De Tommasi & De Luca, 2022). Therefore, the diatom biosilica is used as a plasmonic device in biochemical sensing, diagnostics, and therapeutics. *Pinnularia* sp. frustules coated with silver or gold nanoparticles showed enhanced sensitivity for detection of the smallest concentration of biomolecules (Kong et al., 2016). The "sandwich like" functionalized biosilica of *Pseudostaurosira trainorii* with anti-interleukin-8 antibody and conjugated with dithiobis-nitrobenxoic acid (DTNB) – gold nanoparticles reported to have excellent specificity for the detection of IL9 in complex fluids (Kamińska et al., 2017).

1.5.2. Contemporary fields of application of the diatom biosilica

To help chloroplasts to collect more light and improve photosynthesis, diatoms developed unique features, including well known specific light harvesting carotenoid fucoxanthin and a photonic crystal in the form of the silica frustule (Fuhrmann et al., 2004). The strategic location of the chloroplasts near the silica wall in diatom cells allows diatoms to channel and focus light inside. These features make diatoms interesting for exploration of their potential in energy storage application (e.g., batteries and supercapacitors). Although, the diatom biosilica has its

limitation, e.g., high resistivity, which is not favorable for energy storage, conversion, and other optical applications. Therefore, the modification of the diatom biosilica with metals, semiconductors, carbon, and polymers could mitigate the disadvantages of the pure biosilica. Nowak et al. (2019) used the frustules of *Pseudostaurosira trainorii* to develop anode material with a capacity of approximately 400 mAh g^{-1} after 90 cycles. Norberg et al. (2019) obtained a capacity of 723 mAh g^{-1} after 50 cycles for *Coscinodiscus* sp. biosilica with carbon black as an additive. Wang et al. (2021) exploited the diatom frustules of *Chaetoceros* sp., *Navicula* sp. Bory, and *Nitzschia* sp. Hassal as a source of SiO_2 and carbon from organic compounds of diatom cells and obtained carbon-coated anode material with excellent properties, while Luo et al. (2023) modified the biosilica from the same species with aluminum and titanium and this novel composite improved the battery performance. Chen et al. (2023) developed the cobalt nanoparticles coated biosilica material which delivered a capacity of 620 mAh g^{-1} after 270 cycles. Karaman et al. (2019) used the iron oxide coated frustules of *Phaeodactylum tricornutum* Bohlin and observed the functional material after 1000 cycles with 90% of original performance.

The silica based diatomaceous earth has been successfully used in various separation techniques (e.g., column chromatography and thin-layer chromatography), whereas reports about the utilization of the cultured diatom frustules are scarce. Kraai et al. (2019) introduced a new stationary phase for conventional thin-layer chromatography in the form of *Pinnularia* sp. biosilica, which significantly improved separation and mobility of the triphenylmethane dyes malachite green and fast green in comparison to silica gel. The same species of diatom, *Pinnularia* sp., coated with silver nanoparticles has been successfully utilized as a nanostructured thin film for ultrathin layer chromatography during malachite green and Nile red separation (Kraai et al., 2020).

1.5.3. Environmental applications of diatoms and diatom-based materials

To defend themselves from the adverse effects of toxic substances, diatoms developed a natural ability to acquire, reduce, and store compounds into to their frustule. Therefore, they have been extensively studied in the context of water remediation, surpassing green algae and Cyanobacteria in terms of research attention (Lin et al., 2020; Roychoudhury et al., 2022a). Heavy metal uptake by the diatoms has been studied extensively (Lebeau & Robert, 2003; Bello et al., 2014; Marella et al., 2020; Khan et al., 2021; Roychoudhury et al., 2022a; Sodhi et al., 2022). Diatoms have been reported to successfully remove a wide range of metals, e.g. arsenic with 12,500 µg g^{-1} removal by the iron oxide functionalized *Phaeodactylum*

tricornutum frustules (Thakkar et al., 2015), chromium biosorption by *P. tricornutum* and *Navicula pelliculosa* (Kützing) Hilse strains with 1 mg L^{-1} removal efficiency (Hedayatkhah et al., 2018), 70–78% and 96–100% of lead removal by the non-modified and immobilized on calcium-alginate beads frustules of *Nitzschia palea* (Kützing) Smith and *Navicula incerta* Ehrenberg, respectively (Al-Quraishi & Abbas, 2019), 90% of copper biosorption by *Navicula subminuscula* Manguin (Cherifi et al., 2016), cadmium, copper, and zinc metabolic removal by *Planothidium lanceolatum* (Brébisson ex Kützing) Lange-Bertalot (Sbihi et al., 2012), cadmium and zinc biological uptake by *Coscinodiscus granii* (Rabsch & Elbrächter, 1980), cadmium and lead biosorption by *Thalassiosira weissflogii*, *Skeletonema costatum* (Greville) Cleve, *Achnanthidium minutissimum* (Kützing) Czarnecki, and *Navicula minima* Grunow (Gélabert et al., 2007).

Another example of aquatic pollutants is organic dyes. The annual production of dyes exceeds 700,000 tons (Samsami et al., 2020) in which up to 15% remain untreated and lost in emissions (O'Neill et al., 1999). The synthetic dyes, used for coloring purposes in textile, leather, paper, printing, cosmetics, plastic, and pharmaceutical industries, are discarded as an industrial waste and find their way into natural water bodies, transforming clean, colorless water into contaminated, colored water even at low concentrations of the waste material (Liao et al., 2008; Rafatullah et al., 2010; Katheresan et al., 2018). There are numerous classifications of dyes available, although usually they fall into three types. The anionic dyes, which carry a negative charge, are often used in dyeing natural fibers such as cotton or wool (e.g., Acid Red 52, Acid Blue 9, Acid Yellow 23). The cationic dyes are positively charged, therefore used in textile and paper coloring (e.g., Basic Blue 9, Basic Red 9, Basic Yellow 40). The nonionic dyes are not charged and not influenced by the charge of the substrate (e.g., Disperse Red 60, Disperse Blue 79, Disperse Yellow 211). To assess the potential of dye removal, model dyes could be utilized. Methylene blue (MB), widely used in textile coloring, as a staining agent for biological samples, and in adsorption assessment studies, is a cationic water-soluble dye and by chemical origin belongs to the thiazine type. The cationic Crystal Violet (CV) and Malachite Green (MG) both belong to the triphenylmethane type and used as a biological stain, in the textile industry, and as model dyes for removal assessment. Congo Red (CR) is the acidic anionic diazo dye, based on a benzidine, a human carcinogen and used as a model diazo dye for evaluation of adsorption capacity of materials (Figure 7) (Husain, 2006; Benkhaya et al., 2020; Sharma et al., 2021). These dyes are resistant to conventional treatment techniques and pose significant risks to both aquatic organisms and human health (Sarkar et al., 2014). To address this issue, there is a need for innovative methods of water purification. Several methods, including

photocatalytic degradation, sonication, ozonation, oxidation, Fenton process, and biological degradation, have been explored for the removal of different organic pollutants, including dyes and phenols from water. However, these approaches have limitations in terms of efficiency, cost, and design. Among the different methods, adsorption has proven to be the most effective and widely used treatment for dye removal.

The clean frustules of *Pinnularia* sp., treated at 550°C, showed 55.3 mg g^{-1} adsorption capacity against MB (Van Eynde et al., 2014). The frustules of *Cyclotella* sp. (Kützing) Brébisson were treated by sono-Fenton and conventional methods and demonstrated 91.2 mg g^{-1} and 34.8 mg g^{-1} MB removal capability, respectively (Gholami et al., 2020). *Aulocoseira* sp., decorated with silver nanoparticles, successfully removed MB and CV (Pandit et al., 2022). The biosilica of *Pseudostaurosira trainorii* metabolically doped with palladium exhibited high photocatalytic degradation efficiency against methyl orange (Sprynskyy et al., 2021). The flower and spherical silver-silica nanohybrids, synthesized by *Gedaniella flavovirens* and *G. mutabilis*, presented 80% and 50% removal efficiency against MB (Roychoudhury et al., 2021). *Phaeodactylum tricornutum,* decorated with iron oxide nanoparticles, showed excellent photodegradation of rhodamine 6G (Gannavarapu et al., 2018). The titanium oxide coated frustules of *Cocconeis placentula* exhibited high photocatalytic efficiency for degradation of rhodamine B (He et al., 2013), whereas *Coscinodiscus granii* and *C. wailesii* were utilized for production of a luminescent hybrid with rhodamine dyes for photonic applications (Kucki & Fuhrmann-Lieker, 2012). In the presence of chloroform *Caloneis schroederi* frustules decorated with titanium oxide presented high photocatalytic activity against CR (Kumari et al., 2020). *Skeletonema costatum* was utilized for biosorption of CV with 98% efficiency (Ashour et al., 2022).

Phenols are a group of organic pollutants, commonly found in industrial wastewater from various manufacturing processes, such as petroleum refining, chemical production, pharmaceuticals, plastics, fertilizers, construction, explosives, wood processing, etc. Phenols are toxic and can have harmful effects on ecosystems, aquatic organisms, and human health, leading to respiratory problems, skin irritation, and carcinogenic effects. Proper treatment and management of industrial wastewater are necessary to mitigate phenol pollution and protect water quality (Zhang et al., 2020; Hadjar et al., 2021; Das et al., 2022). Live diatoms as well as the modified diatom biosilica showed excellent efficiency in removal of different classes of phenols, e.g. Bisphenol A (BPA) photodegradation using the ruthenium modified frustules of *P. trainorii* (Chudzińska et al., 2023), biodegradation using the diatom *Stephanodiscus hantzschii* Grunow with up to 99% efficiency at low concentrations of BPA (Li et al., 2009),

bioaccumulation of BPA and nonylphenols with 38% and 21% efficiency using the diatom *Navicula incerta* (Liu et al., 2010), biodegradation of 2,4-dichlorophenol using *S. costatum* (Yang et al., 2002), and *Thalassiosira* sp. biodegradation of *p*-xylene with 98% efficiency (Duan et al., 2020).
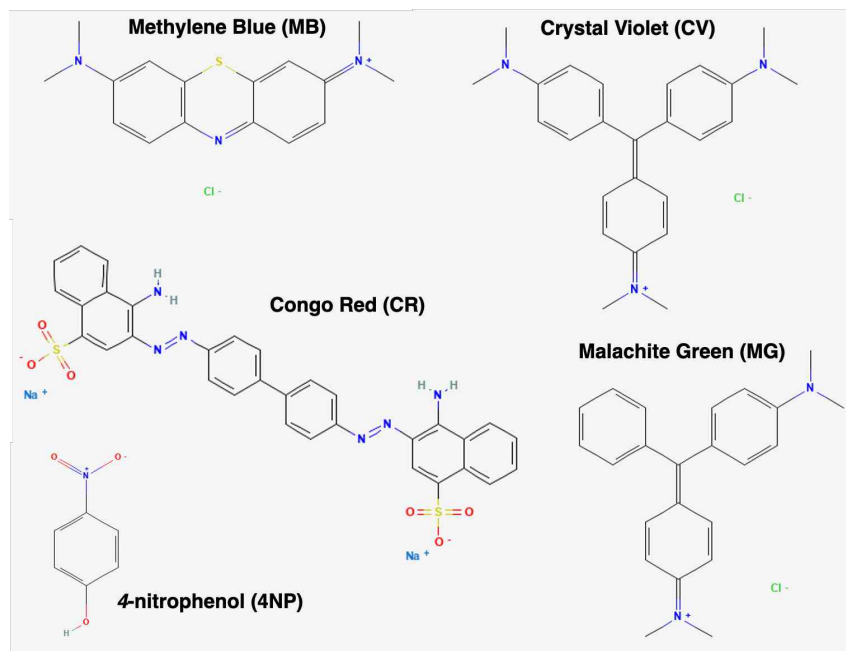
Figure 7. Chemical structure of model dyes and phenols (from PubChem).

AIMS AND HYPOTHESES OF THE THESIS

The extensive overview of the literature highlighted the need for novel bio-originating micro- and nanomaterials, synthesized in an eco-friendly way with high purity and great functionality. Diatomaceous earth (DE) is widely utilized in a number of applications, but the cultured diatom biosilica is pure, naturally functionalized with LCPAs and proteins substitute for DE. The modification and functionalization of the diatom biosilica with noble metals and biomolecules could eradicate the limitation of the intact biosilica. Moreover, it is possible to apply a biorefinery approach in diatom cultivation and synthesize bioactive molecules and the biosilica simultaneously in a cost-effective way. The main purpose of this study was to investigate the potential of the porous diatom biosilica extracted from marine diatoms *Nanofrustulum wachnickianum* Ch.-L Li, Witkowski & Ashworth (strain SZCZCH193), *N. shiloi* (Lee, Reimer & McEnery) Round, Hallsteinsen & Paasche (SZCZM1342), *N.* cf. *shiloi* (Lee, Reimer & McEnery) Round, Hallsteinsen & Paasche (SZCZP1809), *Halamphora* cf. *salinicola* Levkov & Díaz (SZCZM1454), and *Pseudostaurosira trainorii* Morales (BA170) in the field of environmental remediation and dye removal. In order to achieve that, the aims of the study will be to investigate (i) the growth of each strain under various culturing conditions in a laboratory setting for higher biomass yield, (ii) the porous nature of the diatom biosilica by SEM and the low temperature nitrogen adsorption/desorption analyses, (iii) a Fe^{3+} reduction capacity of diatom biomass at the laboratory scale, (iv) the elemental composition and molecular structure of the intact and loaded with iron oxide nanoparticles biosilica by EDS and FTIR spectroscopy, (v) the charge of the biosilica surface under a range of pH, (vi) the crystalline structure, thermal stability, and purity of the diatom biosilica using XRD and TGA/DTA, (vii) adsorption efficiency of the biosilica against the cationic (MB, CV, MG) and the anionic (CR) dyes, (viii) photocatalytic activity of the intact and decorated with iron oxide biosilica against 4-nitrophenol.

The following hypotheses were tested in this PhD thesis:

1. Marine diatoms cultivated under laboratory conditions could accumulate more than 500 mg DW biomass in 1 L of culture.

2. Increased silicon concentration in a culture medium enhances the biomass yield of diatoms.

3. The geographical origin of the diatom strains has a significant impact on their biomass accumulation under laboratory settings.

4. Diatom biomass could reduce Fe^{3+} ions to iron oxide nanoparticles from water solution.

5. The diatom biosilica has high filtration potential due to the presence of macropores (areolae), meso- and micropores on the frustules surface.

6. The various functional groups, including $Si–O^-$, on the surface of the diatom biosilica make it an anionic material with higher affinity to cationic dyes.

7. The diatom frustules decorated with iron oxide nanoparticles exhibit a higher photocatalytic activity against phenols.

MAIN RESULTS

3.1. *Diatom cultivation experiments*

After preliminary screening of diatom cultures from the Szczecin Diatom Culture Collection (SZCZ), Institute of Marine and Environmental Sciences, University of Szczecin, 5 diatom strains were selected for this study. These stains were collected from various habitats, easy to maintain, and demonstrate a high biomass yield (Table S1, Supplementary material). Additionally, the selected species are understudied with only a handful of reports regarding their growth and application. The studied strains showed distinct exponential and stationary phases during their batch culture (Figure 8). Kinetic parameters are presented in Table 1.
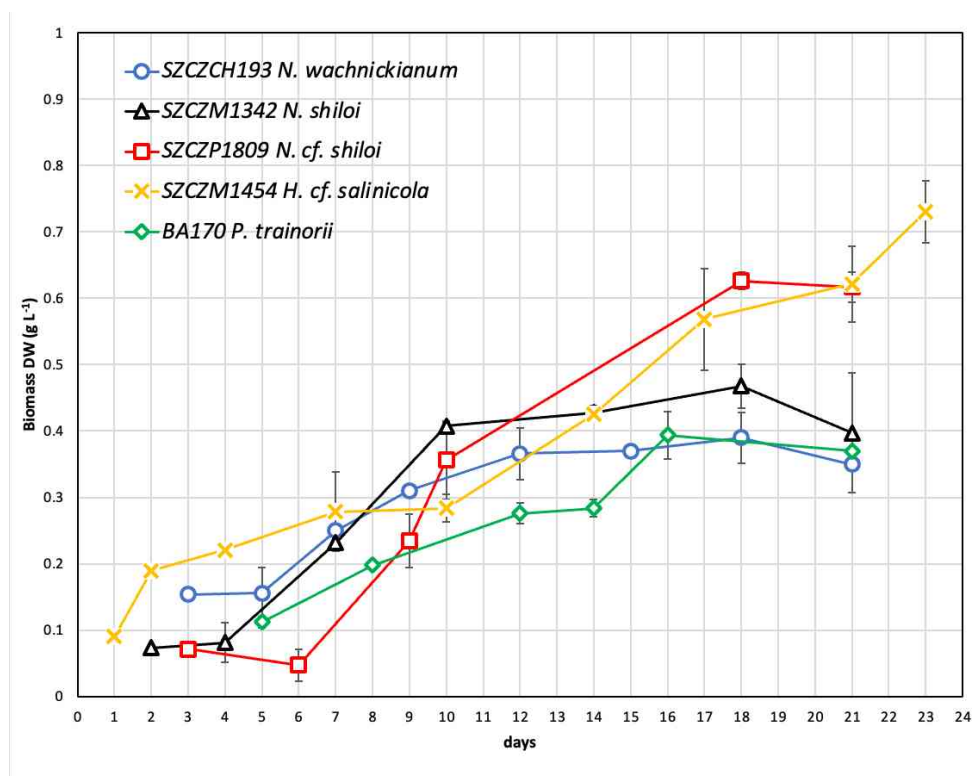
Figure 8. Growth curves for SZCZCH193 *N. wachnickianum*, SZCZM1342 *N. shiloi,* SZCZP1809 *N.* cf. *shiloi*, SZCZM1454 *H.* cf. *salinicola*, and BA170 *P. trainorii* strains (modified from Golubeva et al., 2023a, Golubeva et al., 2023b).

The maximum biomass accumulation was observed for the strains SZCZM1454 *Halamphora* cf. *salinicola* and SZCZP1809 *Nanofrustulum* cf. *shiloi*. The highest growth rate was calculated for the strain SZCZP1809 *N.* cf. *shiloi*. The growth of the strain BA170 *Pseudostaurosira trainorii* corresponds with data published previously (Sprynskyy et al., 2017), while the strain SZCZP1809 *N.* cf. *shiloi* could be considered as the most productive strain of *N. shiloi* (Sahin

et al., 2019; Demirel et al., 2020; Grubišić et al., 2022). To the best of our knowledge no research has been conducted on the growth investigation of *N. wachnickianum* and *H.* cf. *salinicola* species, although the strain SZCZM1454 *H.* cf. *salinicola* showed the highest biomass accumulation among the reported strains of *Halamphora* spp (Martín et al., 2016; Stepanek et al., 2016; Martín et al., 2018; Scodelaro Bilbao et al., 2020; Navarro et al., 2022).

Table 1. Growth kinetic parameters for 5 marine diatom strains tested in this study.

Strain	Growth rate, d^{-1} (R^2)	Maximum biomass DW ± SD, g L^{-1}	Day of maximum growth
SZCZCH193 *N. wachnickianum*	0.115 (0.95)	0.39 ± 0.039	18
SZCZM1342 *N. shiloi*	0.270 (0.97)	0.47 ± 0.033	18
SZCZP1809 *N.* cf. *shiloi*	0.513 (0.99)	0.63 ± 0.013	16
SZCZM1454 *H.* cf. *salinicola*	0.081 (0.93)	0.73 ± 0.047	23
BA170 *P. trainorii*	0.08 (0.92)	0.39 ± 0.035	16

Table 2 presents the biomass yield of the strains grown under various initial silicate concentrations in the medium. The results indicate that increased silicate concentration significantly affect the biomass yield of all the studied strains (one-way ANOVA, p=0.0018, p=0.00008, p=0.015, p=0.0002, and p=0.0012 for SZCZCH193 *N. wachnickianum*, SZCZM1342 *N. shiloi*, SZCZP1809 *N.* cf. *shiloi*, SZCZM1454 *H.* cf. *salinicola*, and BA170 *P. trainorii*, respectively), with the highest accumulation observed in cultures grown in a medium with 20 times higher than standard Guillard's f/2 medium's silicate concentration (Table S2, Table S3, Supplementary material). Previous studies (Chu et al., 1996; Jiang et al., 2015) demonstrated that the presence of an adequate concentration of silicate in the culture medium is essential for diatoms to form their siliceous frustules, and increasing the initial silicon concentration has been found to lead to higher biomass yield.

The effect of temperature on biomass accumulation (Table 3) varied between the strains. For the strains SZCZCH193 *N. wachnickianum*, SZCZM1454 *H.* cf. *salinicola*, and BA170 *P. trainorii* cultivation at a higher temperature (30°C) resulted in higher biomass yield (one-way ANOVA, p=0.0259, p=0.006, p=0.0007, respectively). No significant differences in biomass accumulation were observed for SZCZM1342 *N. shiloi* (one-way ANOVA, p=0.1296).

However, for SZCZP1809 *N*. cf. *shiloi*, cultivation at a lower temperature (15 °C) led to higher biomass yield (one-way ANOVA, p=0.0027) (Table S2, Table S4, Supplementary material).

Table 2. Dry biomass accumulation (g L^{-1}) under a variety of silicate concentrations in Guillard′s f/2 medium in the late exponential phase of batch cultivation of 5 marine diatom strains (mean ± standard deviation).

Strain	Silicate, mM L^{-1}				
	0.11	*0.53*	*1.06*	*1.59*	*2.12*
SZCZCH193 *N. wachnickianum*	0.447 ± 0.089	0.466 ± 0.110	0.711 ± 0.004	0.807 ± 0.030	0.977 ± 0.004
SZCZM1342 *N. shiloi*	0.402 ± 0.003	0.570 ± 0.057	0.636 ± 0.000	0.816 ± 0.040	0.930 ± 0.014
SZCZP1809 *N.* cf. *shiloi*	0.469 ± 0.090	0.600 ± 0.006	0.670 ± 0.059	0.810 ± 0.037	0.989 ± 0.047
SZCZM1454 *H*. cf. *salinicola*	0.501 ± 0.004	0.644 ± 0.027	0.646 ± 0.044	0.825 ± 0.009	0.964 ± 0.047
BA170 *P. trainorii*	0.266 ± 0.018	0.442 ± 0.007	0.594 ± 0.061	0.730 ± 0.064	0.810 ± 0.017

The observed increase in biomass yield at lower temperatures for SZCZP1809 *N*. cf. *shiloi* and higher temperatures for SZCZCH193 *N. wachnickianum* and SZCZM1454 *H*. cf. *salinicola* could be attributed to their geographical origin. SZCZP1809 *N*. cf. *shiloi* was collected from the Atlantic Ocean, Sea Point, Cape Town, South Africa, where the average sea water temperature is around 17 °C, and as a result demonstrated enhanced growth at lower temperatures. SZCZCH193 *N. wachnickianum* originated from the Gulf of Mexico, Marquesas Keys, Florida, USA, with an average sea water temperature of 28 °C and exhibited higher biomass yield at higher temperatures. Moreover, the strain SZCZM1454 *H*. cf. *salinicola* originated from a hot spring in Köyceğiz Lake in Turkey (Avşar et al., 2017), and consequently could be classified as a thermophilic strain, exhibited a preference for higher temperatures during cultivation. These findings conform with similar results obtained from *Halamphora* sp. strain sourced from a thermal spring in Tunisia, where biomass accumulation displayed a positive correlation with increasing temperature (Bouzidi et al., 2020).

Results and statistical analyses on the influence of nitrate, phosphate, salinity, and light intensity are presented in Golubeva et al., 2023a, Golubeva et al., 2023b, and in the Supplementary materials (Table S2, S5–S8).

Table 3. Dry biomass accumulation (g L^{-1}) under different temperatures in the late exponential phase of batch cultivation of 5 marine diatom strains (mean ± standard deviation).

Strain	Temperature, °C		
	15	20	30
SZCZCH193 N. wachnickianum	0.331 ± 0.014	0.352 ± 0.002	0.865 ± 0.187
SZCZM1342 N. shiloi	0.530 ± 0.034	0.568 ± 0.042	0.624 ± 0.011
SZCZP1809 N. cf. shiloi	2.208 ± 0.213	1.178 ± 0.074	0.758 ± 0.025
SZCZM1454 H. cf. salinicola	0.431 ± 0.001	0.480 ± 0.004	0.700 ± 0.035
BA170 P. trainorii	0.492 ± 0.022	0.325 ± 0.010	0.862 ± 0.025

3.2. Characterization of the frustules

The morphology of the frustules of the strains was examined using scanning electron microscopy (SEM), revealing the presence of the pores on both valve faces, confirming the porous nature of the biosilica (Figure 9–13).
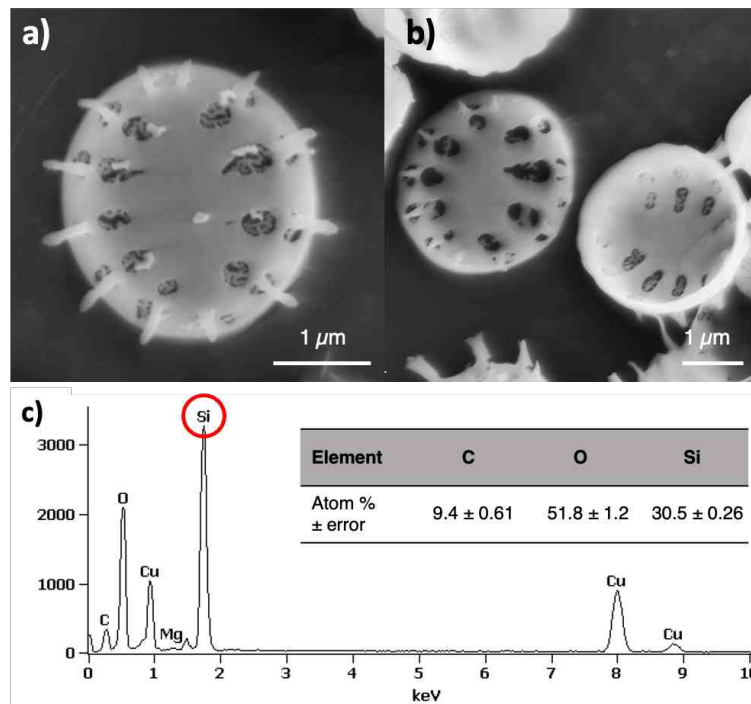
Figure 9. Scanning electron microscopy presents **(a, b)** the morphology and **(c)** EDS spectra revealed the presence of Si, O, and C on the surface of SZCZCH193 *N. wachnickianum* (modified from Golubeva et al., 2023a).

The areolae differed in size (120–615 nm and 120–330 nm for SZCZCH193 *N. wachnickianum* (Figure 9a,b), 150–450 x 120–400 nm for SZCZM1342 *N. shiloi* (Figure 10a,b), 80–510 x 100–330 nm for SZCZP1809 *N.* cf. *shiloi* (Figure 11a,b), 70–230 x 10–340 nm for SZCZM1454 *H.* cf. *salinicola* (Figure 12a,b), and 10–310 nm and 10–230 nm for BA170 *P. trainorii* (Figure 13a,b) in the length and width, respectively) and in number (10–20 for SZCZCH193 *N. wachnickianum,* 30–50 for SZCZM1342 *N. shiloi*, 30–70 for SZCZP1809 *N.* cf. *shiloi*, 200–400 for SZCZM1454 *H.* cf. *salinicola*, and 30–50 for BA170 *P. trainorii* on one valve).
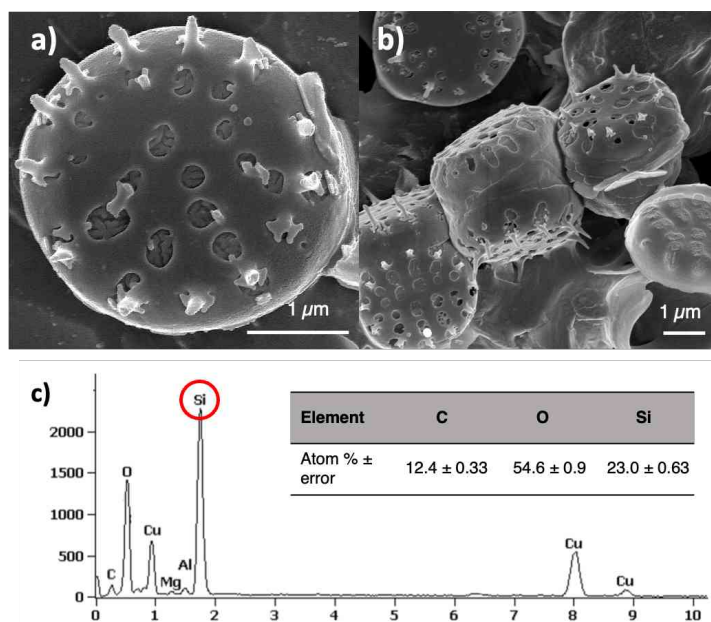
Figure 10. Scanning electron microscopy presents **(a, b)** the morphology and **(c)** EDS spectra revealed the presence of Si, O, and C on the surface of SZCZM1342 *N. shiloi* (modified from Golubeva et al., 2023a).

Following the IUPAC classification (Thommes et al., 2015), pores with a diameter smaller than 2 nm are classified as micropores, pores ranging from 2 to 50 nm are categorized as mesopores, while pores with diameters of 50 nm and above are designated as macropores. Based on this classification, the areolae on the frustule's valve face can be considered as mesopores and macropores since their diameters ranged from 70 to 340 nm.

Analysis of the porous structure of the frustules revealed that they contain other types of pores, ranging from 3 nm to 35 nm in diameter (Table 4, Figure S1, Supplementary material), with an average diameter of 4.22 nm for SZCZCH193 *N. wachnickianum*, 2.07 nm for SZCZM1342 *N. shiloi*, 1.97 nm for SZCZP1809 *N.* cf. *shiloi*, and 3.72 nm for SZCZM1454 *H.* cf. *salinicola*. This indicates that the frustule surface possesses not only macropores (areolae) but also other

micro and mesopores. Previous studies have reported an average pore diameter of 3.93 nm with a pore size distribution of 1–70 nm for BA170 *P. trainorii* (Sprynskyy et al., 2021).
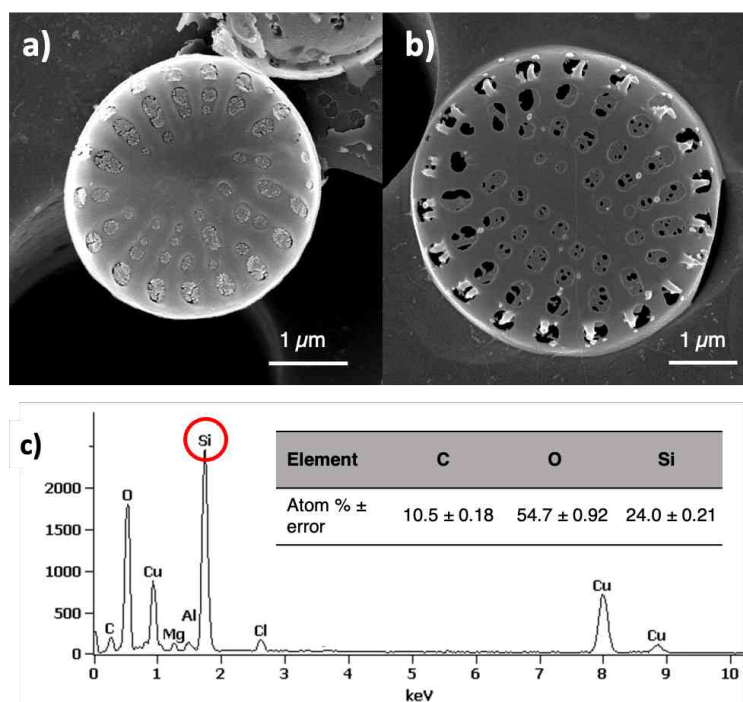
Figure 11. Scanning electron microscopy presents **(a, b)** the morphology and **(c)** EDS spectra revealed the presence of Si, O, and C on the surface of SZCZP1809 *N.* cf *shiloi* (modified from Golubeva et al., 2023a).

These findings were further supported by the low-temperature nitrogen adsorption/desorption isotherms (Golubeva et al., 2023a, Golubeva et al., 2023b), where the frustules exhibited characteristics of both Type I and II isotherms, accompanied by a combination of Type H3 and H4 hysteresis loop, according to the IUPAC classification. Type I signifies a microporous material with a small external surface area, while Type II is indicative of macroporous or nonporous substances. The presence of Type H3 hysteresis loop suggests the presence of a microporous network, while the Type H4 suggests the existence of slit-like pores in the sample (Thommes et al., 2015).

The specific surface area (BET) values for the strains SZCZCH193 *N. wachnickianum*, SZCZM1342 *N. shiloi*, SZCZP1809 *N.* cf. *shiloi*, and SZCZM1454 *H.* cf. *salinicola* are presented in Table 4. The strain BA170 P. *trainorii* has been reported to have a specific surface area value of 30 m^2 g^{-1} (Sprynskyy et al., 2021). Furthermore, Gholami et al. (2020) demonstrated that the specific surface area of diatoms varied depending on the cleaning technique employed. The Sono–Fenton method, utilized in their study, increased the specific surface area of *Cyclotella* sp. from 14.71 m^2 g^{-1} to 132.67 m^2 g^{-1}.
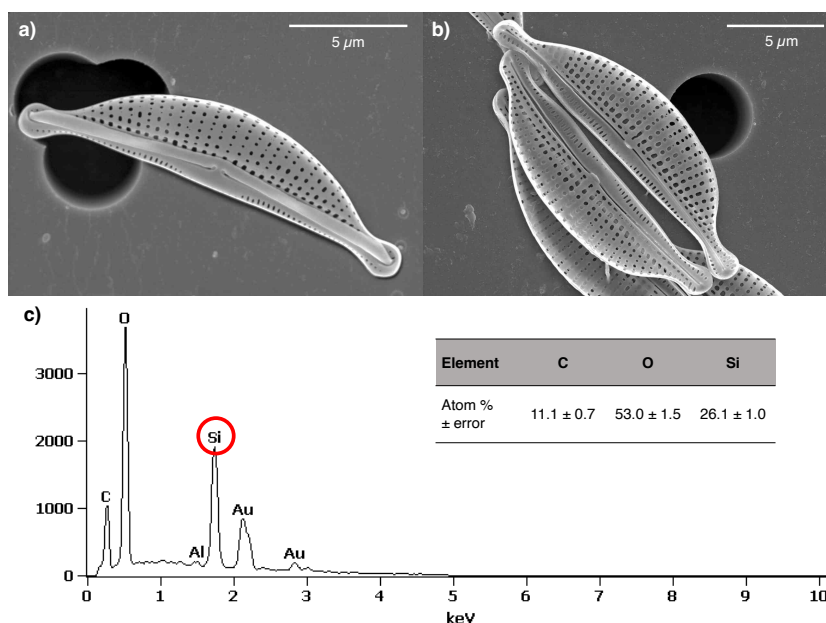
Figure 12. Scanning electron microscopy presents **(a, b)** the morphology and **(c)** EDS spectra revealed the presence of Si, O, and C on the surface of SZCZM1342 *H.* cf *salinicola* (modified from Golubeva et al., 2023b).

The obtained EDS spectra revealed prominent peaks corresponding to silicon (Si) and oxygen (O). The calculated atomic ratio of O:Si was found to be 1.69:1, 2.39:1, 2.27:1, 2.04:1, and 2.26:1 for SZCZCH193 *N. wachnickianum* (Figure 9c), SZCZM1342 *N. shiloi* (Figure 10c), SZCZP1809 *N.* cf. *shiloi* (Figure 11c), SZCZM1454 *H.* cf. *salinicola* (Figure 12c), and BA170 *P. trainorii* (Figure 13c), respectively, indicating that the frustules were primarily composed of SiO_2 (Jeffrey & Humphrey, 1975). However, it is important to note, that oxygen is relatively light and may not be accurately detected by the EDS due to limitations for elements with atomic numbers below sodium (Na). Additionally, a distinct peak of carbon (C) was observed, suggesting the presence of some amount of the organic compounds within the frustules (Tesson & Hildebrand, 2010), although contamination from the SEM oil pump could potentially contribute to the observed carbon peak as well.

Table 4. The porous structure of the frustules for four studied strains.

| Strain	Specific Surface Area (m² g⁻¹)	Pore Volume (cm³ g⁻¹)	Pore Diameter Distribution (nm)
SZCZCH193 *N. wachnickianum*	26.922	0.175	3–35
SZCZM1342 *N. shiloi*	25.319	0.267	3–25
SZCZP1809 *N.* cf. *shiloi*	21.777	0.113	3–15
SZCZM1454 *H.* cf. *salinicola*	35.231	0.174	3–15
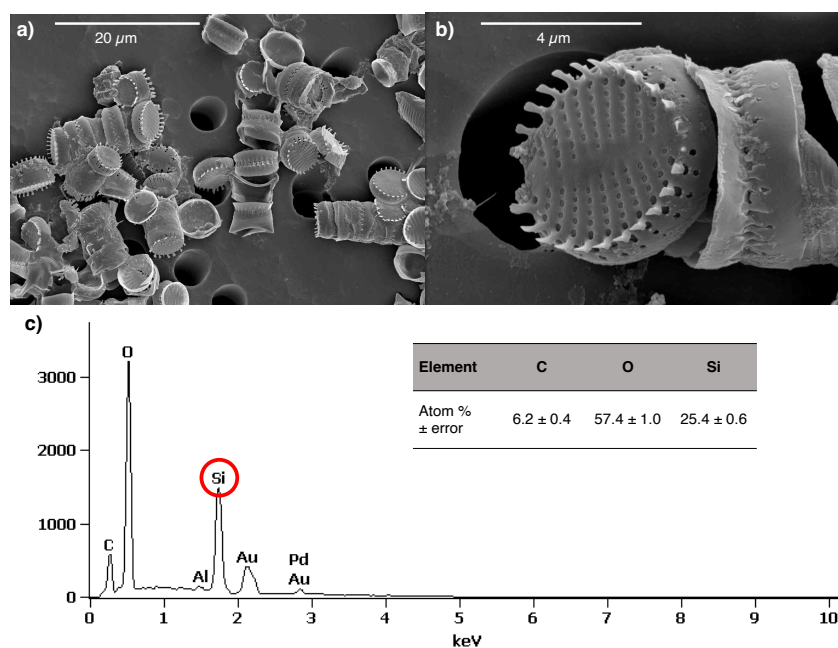
Figure 13. Scanning electron microscopy presents **(a, b)** the morphology and **(c)** EDS spectra revealed the presence of Si, O, and C on the surface of BA170 *P. trainorii* (modified from Roychoudhury et al., 2022b).

The ATR-FTIR spectra exhibited distinctive peaks (Figure 14), indicating the presence of various functional groups on the frustule's surface. According to previous reports (Zhang et al., 2007; Kiraz et al., 2010; Camargo et al., 2016; Sprynskyy et al., 2017), the distinct peaks observed at the 440–446 cm^{-1}, 800–803 cm^{-1}, and 952–1154 cm^{-1} regions are common for siliceous materials and correspond to bending, symmetrical stretching and asymmetrical stretching of Si–O groups, respectively. Karmakar et al (2000) indicated that the small peak visible in the 500–569 cm^{-1} region represent the vibration of siloxane rings. Several studies have identified prominent bands at the 2922–2981 cm^{-1} and 2851–2889 cm^{-1} region corresponding to C–H stretching of –CH$_3$ and –CH$_2$, respectively, while Si–(CH$_3$)$_2$ was present in the 854–856 cm^{-1} region of the FTIR spectra of SZCZM1342 *N. shiloi*, SZCZP1809 *N.* cf. *shiloi*, and SZCZM1454 *H.* cf. *salinicola* (Chen et al., 2015; Camargo et al., 2016). The strong IR vibration was detected in the 1741–1745 cm^{-1} region for all strains except SZCZM1454 *H.* cf. *salinicola* and could be attributed to C=O stretching (Chen et al., 2015; Camargo et al., 2016). Additionally, several peaks at 1378–1576 cm^{-1} region were observed, indicating the bending vibrations of amino groups, which aligns with previous studies (Li, K. M. et al., 2014). As suggested by Otzen (2012), these peaks signify the presence of organic compounds associated with the frustules. The small band at the 3660–3664 cm^{-1} region attributed to the stretching vibration of O–H in Si–OH, while the peak at the 1632–1645 cm^{-1} region and the

broad band spanning from 3500 to 3000 cm^{-1} are associated with molecular water (Musić et al., 2011).
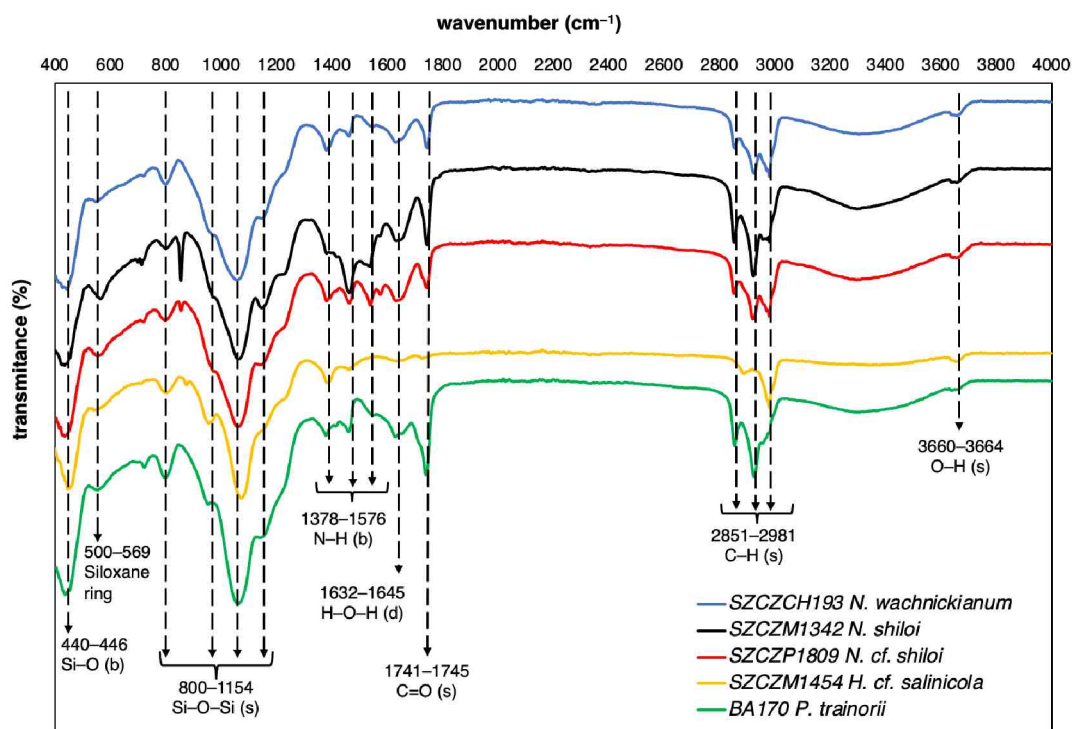
Figure 14. FTIR spectra confirmed the presence of the Si–O, N–H, C–H, C=O, and O–H functional groups on the surface of the frustules of five studied strains (modified from Golubeva et al., 2023a, Golubeva et al., 2023b, Roychoudhury et al., 2022b).

The zeta potential absolute values measured greater than –25 mV at the pH levels higher than 4 (for *Nancfrustulum* spp. strains) and 6 (for SZCZM1454 *H.* cf. *salinicola*), indicate that aggregation does not occur, ensuring suspension stability. Moreover, in the case of the examined samples (Figure 15), the negative charge was observed within the pH range of 2–12 for *Nancfrustulum* spp. strains and 6–12 for SZCZM1454 *H.* cf. *salinicola*. The SZCZM1454 *H.* cf. *salinicola* frustules were charged positively in acidic solutions, which deviates from the typical behavior of the pure silica (Xu et al., 2006). This discrepancy could be attributed to the presence of a significant number of impurities, as indicated by XRD and TGA (Golubeva et al., 2023a; Golubeva et al., 2023b). These findings underscore the differences in sorption behavior. At a pH higher than 3 (for *Nancfrustulum* spp. strains) and a pH higher than 6 (for SZCZM1454 *H.* cf. *salinicola*) the frustule surfaces had a negative charge contributed to the –SiO$^-$, –COO$^-$, and –NH$_2^-$ groups, while at a lower pH the surface was charged positively.
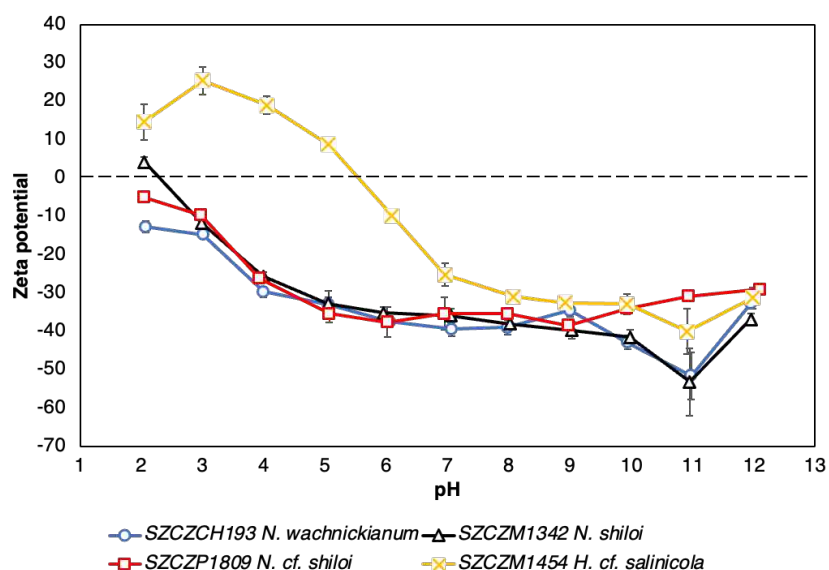
Figure 15. Zeta potential measurements revealed the stable nature of the frustules and their charge under various pH values (modified from Golubeva et al., 2023a, Golubeva et al., 2023b).

3.3. Characterization of the IONPs loaded frustules

The SEM images revealed the presence of nanostructures synthesized and deposited on the surface of BA170 *P. trainorii* following Fe^{3+} treatment (Figure 16a–c). The valves of the examined frustules were completely covered by these nanostructures, which contrasted with the natural surface ornamentation (Figure 13a, b).
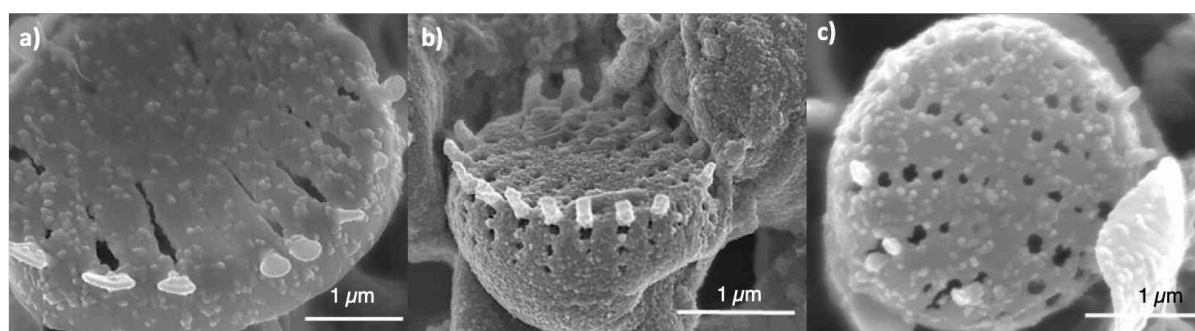
Figure 16. SEM images of the IONPs loaded frustules of BA170 *P. trainorii* (modified from Roychoudhury et al., 2022b).

The EDS analysis (Figure 17g) of the BA170 *P. trainorii* frustules after Fe^{3+} treatment confirmed the presence of silicon, oxygen, and iron throughout the frustules. The elemental mapping (Figure 17a–f) of a single frustule provided a visual representation of the distribution pattern of silicon, oxygen, and iron elements. A strong signal of gold (Au) was also observed due to its use as a coating material for SEM examination.
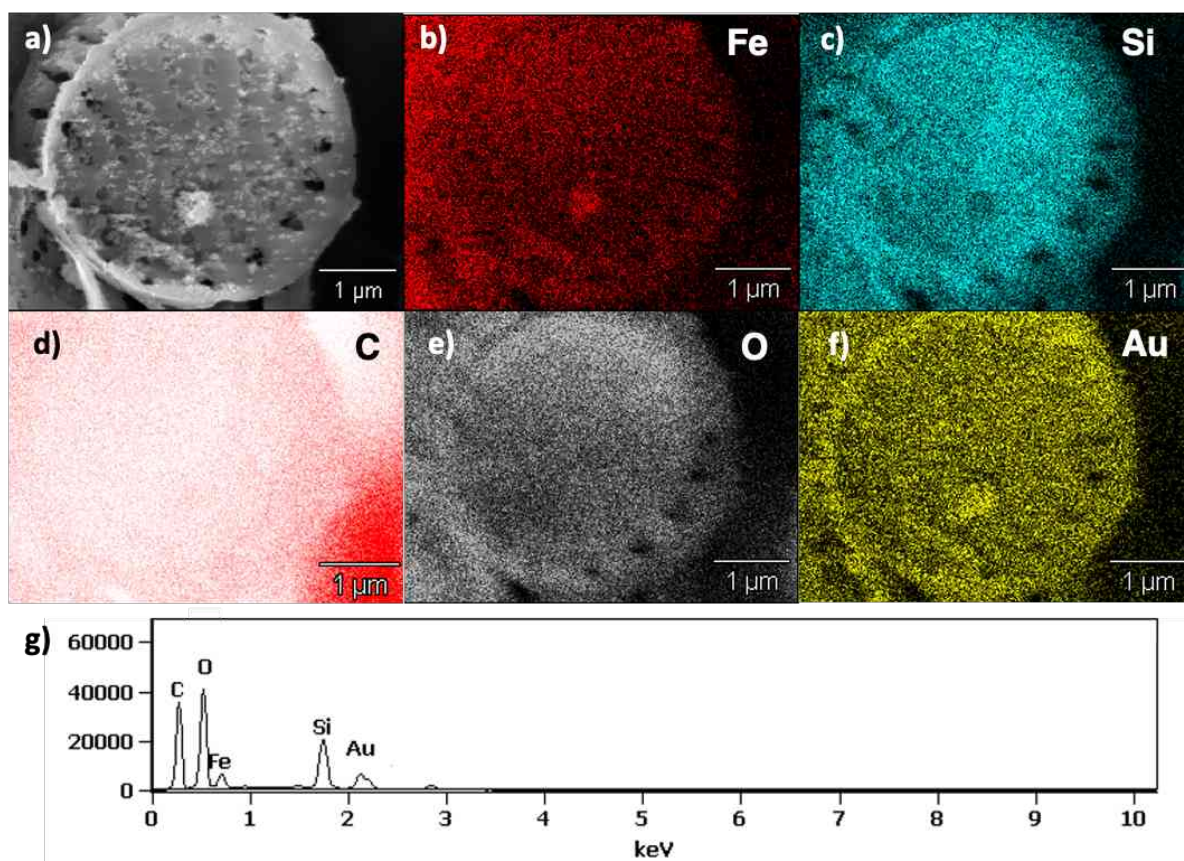
Figure 17. (a-f) The elemental mapping and **(g)** EDAX spectra of the IONPs loaded frustules of BA170 *P. trainorii* revealed the presence of iron, silicon, and oxygen on the surface (from Roychoudhury et al., 2022b).

Figure 18 presents the FTIR spectra of the IONPs loaded frustules of BA170 *P. trainorii*. Similar to the FTIR spectra of the intact frustules of the studied diatom strains, including BA170 *P. trainorii* (Figure 14), there are distinct peaks in the 432 cm^{-1}, 805 cm^{-1}, and 954–1144 cm^{-1} regions, corresponding to Si–O groups' bending, symmetrical and asymmetrical stretching, respectively, as well as a group of peaks at the 1380–1532 cm^{-1} (N–H bending), 2855–2979 cm^{-1} (C–H stretching), 1633 cm^{-1} (deformation of molecular water), 1741 cm^{-1} (C=O stretching) and 3664 cm^{-1} (O–H stretching) regions. However, a distinct broad peak in the 500–560 cm^{-1} region was only observed in the IR spectra of the IONPs loaded frustules of BA170 *P. trainorii*. Yew et al. (2016) reported a peak in the same region and concluded that this bond signifies the appearance of Fe–O groups on the sample surface. Hence, it can be concluded that the identified functional groups, namely N–H, C=O, and C–H, effectively contributed to the stabilization of the fabricated IONPs on the frustule's surface.
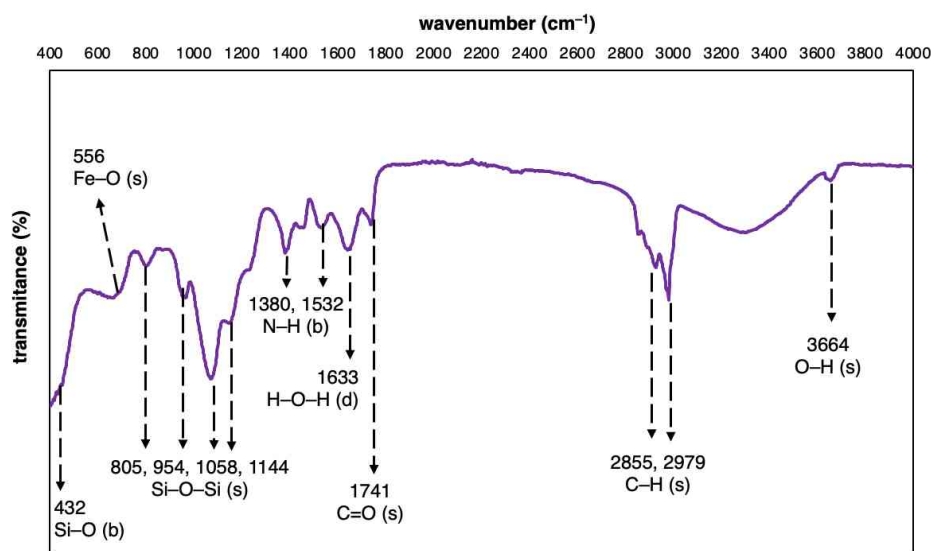
Figure 18. FTIR spectra revealed the presence of the Fe–O functional group on the surface of the IONPs loaded frustules of BA170 *P. trainorii* (modified from Roychoudhury et al., 2022b).

3.4. Removal of dyes from aqueous solutions

The frustules exhibited a positive response in dye discoloration of the aqueous solutions. The spectroscopic analysis demonstrated the percentage of MB removal after 180 minutes as 77.6%, 96.8%, 98.1%, and 92.5% for the frustules of SZCZCH193 *N. wachnickianum*, SZCZM1342 *N. shiloi*, SZCZP1809 *N.* cf. *shiloi*, and BA170 *P. trainorii*, respectively, while the IONPs loaded frustules of BA170 *P. trainorii* removed only 19.9% of MB from solution (Figure 19a, c). The adsorption capacity dependance on time (Figure 19b, d) showed similar dynamics with 5.72, 7.14, 7.23, 8.65, and 1.78 mg g^{-1} value after 180 min of exposure for the SZCZCH193 *N. wachnickianum*, SZCZM1342 *N. shiloi*, SZCZP1809 *N.* cf. *shiloi*, intact and IONPs loaded BA170 *P. trainorii* frustules, respectively.

Moreover, the frustules of SZCZM1454 *H.* cf. *salinicola* demonstrated capability to remove the anionic diazo dye (CR) and the cationic basic dyes (CV, MG). The visible discoloration of the dyes' solutions was observed after 240 minutes of exposure, as shown in Figure 20c–e. The UV-vis measurements confirmed the gradual elimination of the dyes over time (Figure 20a). Among the three dyes, the frustules of SZCZM1454 *H.* cf. *salinicola* exhibited the highest removal efficiency for CV and MG, with 94.02% and 99.81% removal, respectively, after 60 and 240 minutes. The efficiency in removing CR was lower, with 74.9% removal after 240 minutes. The adsorption capacity over time is presented in Figure 20b, with estimated values of 8.81 mg g^{-1}, 10.44 mg g^{-1}, and 11.86 mg g^{-1} for CR, CV, and MG, respectively.
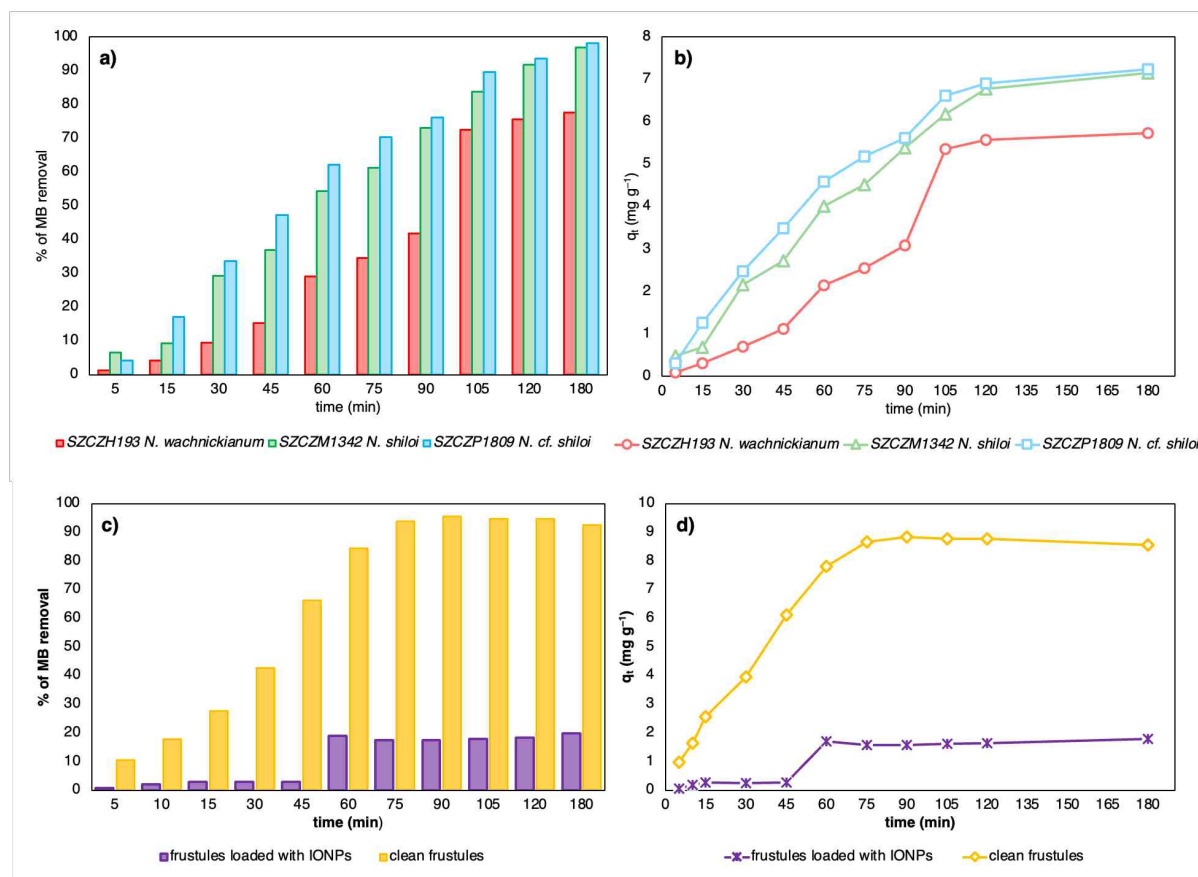
Figure 19. Efficiency of MB removal and adsorption capacity of **(a–b)** the frustules of *Nanofrustulum* spp. strains and **(c–d)** the intact and the IONPs loaded frustules of BA170 *P. trainorii* strain (initial concentration of dye – 20 mg L^{-1}, adsorbent dosage – 20 mg, pH – 7, temperature – 20°C, time – 5–180 min; modified from Golubeva et al., 2023a)

The differences in removal efficiency between different diatom strains could be explained by their morphology and porous structure. Furthermore, it is possible that the IONPs made the meso- and micropores of the frustules surface inaccessible to the dye molecule to interact.

The surface charge is established to have a great impact on the adsorbent affinity to different types of dyes. As we identified earlier, at the pH of 7 the frustules' surface charged negatively, while molecules of the basic dyes (MB, CV, and MG) possess a positive charge from =N$^+$ groups and the diazo dyes (CR) containing the –SO$_3^-$ and –NH$_2^-$ groups charged negatively. Hence, the frustules' surface and the molecules of the basic dyes interact electrostatically, resulting in a higher adsorption efficiency and capacity, while in the case of the diazo dye the frustules' surface experiences electrostatic repulsion with the anionic molecules of the dye. Furthermore, the surface charge of the extracellular IONPs is reported to be highly positive (Roychoudhury et al., 2022b), resulting in lower sorption capacity against the basic dyes. It is

important to note that to confirm this theory, the measurements of the zeta potential for the IONPs loaded frustules is needed.
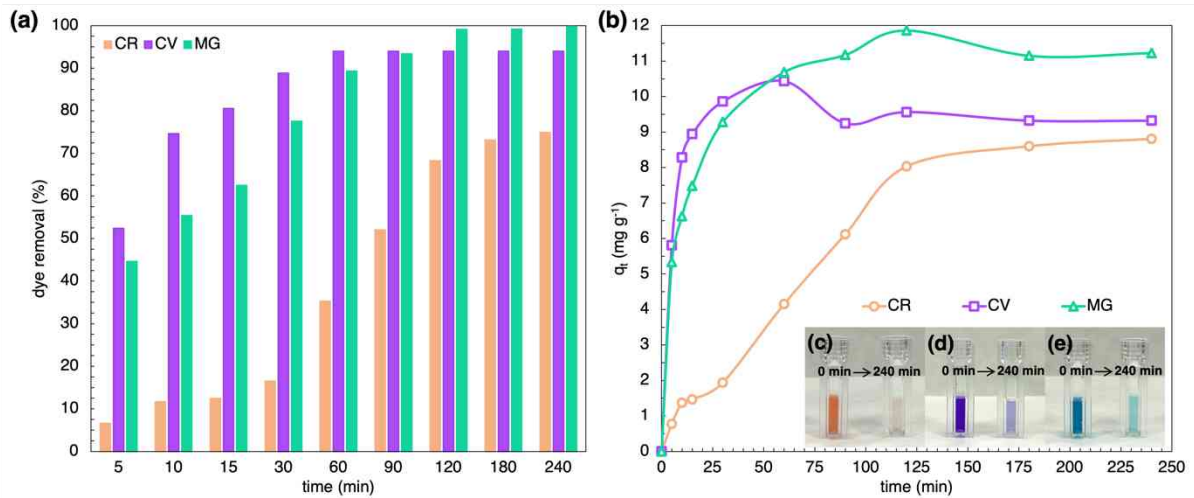
Figure 20. Discoloration of CR, CV, and MG solution after exposure to the frustules of SZCZM1454 *H.* cf. *salinicola*: **(a)** dye removal efficiency and **(b)** adsorption capacity. Changes of solutions' color after 240 min for **(c)** CR, **(d)** CV, and **(e)** MG (initial concentration of dye – 20 mg L^{-1}, adsorbent dosage – 20 mg, pH – 7, temperature – 20°C, time – 5–240 min; from Golubeva et al., 2023b).

The impact of the initial concentration of dye in the water solution was also investigated. Figure 21a illustrates that for SZCZCH193 *N. wachnickianum*, an increase in MB concentration resulted in a notable decrease in the removal efficiency, ranging from 79.48% at 5 mg L^{-1} to 10.69% at 100 mg L^{-1}. In the case of frustules of SZCZM1342 *N. shiloi* exposed to a 100 mg L^{-1} MB solution, the removal efficiency showed a hyperbolic increase, maintaining almost the same efficiency (89.82%) as at lower concentrations. The most effective strain in MB removal, SZCZP1809 *N.* cf. *shiloi*, exhibited a similar trend with the highest removal of 95.95% at 50 mg L^{-1}. The adsorption isotherms (Figure 21b–d) showed a positive correlation between adsorption capacity and the equilibrium concentration of MB for *Nanofrustulum* spp. strains. The adsorption capacities have been established as 6.82 mg g^{-1}, 15.09 mg g^{-1}, and 15.02 mg g^{-1} for the frustules of SZCZCH193 *N. wachnickianum*, SZCZM1342 *N. shiloi*, and SZCZP1809 *N.* cf. *shiloi*, respectively.

33
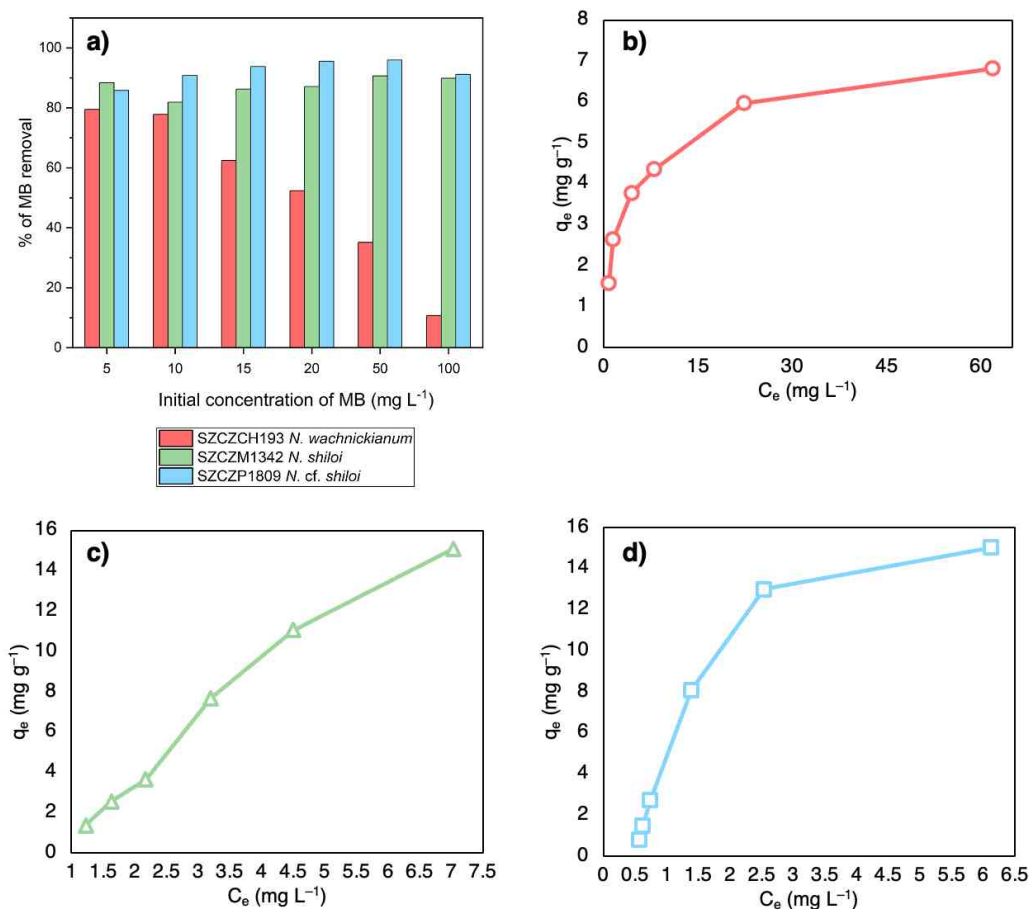
Figure 21. Influence of **(a)** different initial dye concentration on MB removal by the frustules of *Nanofrustulum* spp.; the adsorption isotherms for **(b)** SZCZCH193 *N. wachnickianum*, **(c)** SZCZM1342 *N. shiloi*, and **(d)** SZCZP1809 *N.* cf. *shiloi* (initial concentration of dye – 5–100 mg L^{-1}, adsorbent dosage – 21.40 ± 5.0 mg, pH –7, temperature – 20°C, time – 120 min; modified from Golubeva et al., 2023a).

In case of the SZCM1454 *H.* cf. *salinicola* frustules, an increase in the initial CR concentration resulted in a gradual rise in the removal efficiency, followed by a sharp decline for concentrations exceeding 50 mg L^{-1} (Figure 22a). However, the initial concentration of CV and MG did not significantly affect the removal efficiency of the frustules, as the removal consistently remained above 90% (Figure 22a). Regarding the isotherm, there was a strong positive correlation between the adsorption capacity and the equilibrium concentration of CR, CV, and MG in the solution (Figure 22b–d). The adsorption isotherms indicated that the adsorption capacity of the SZCZM1454 *H.* cf. *salinicola* frustules was lower for the diazo dye

compared to the basic dyes, i.e., 13.04 mg g^{-1} for CR and 41.97 mg g^{-1} and 33.19 mg g^{-1} for CV and MG, respectively.
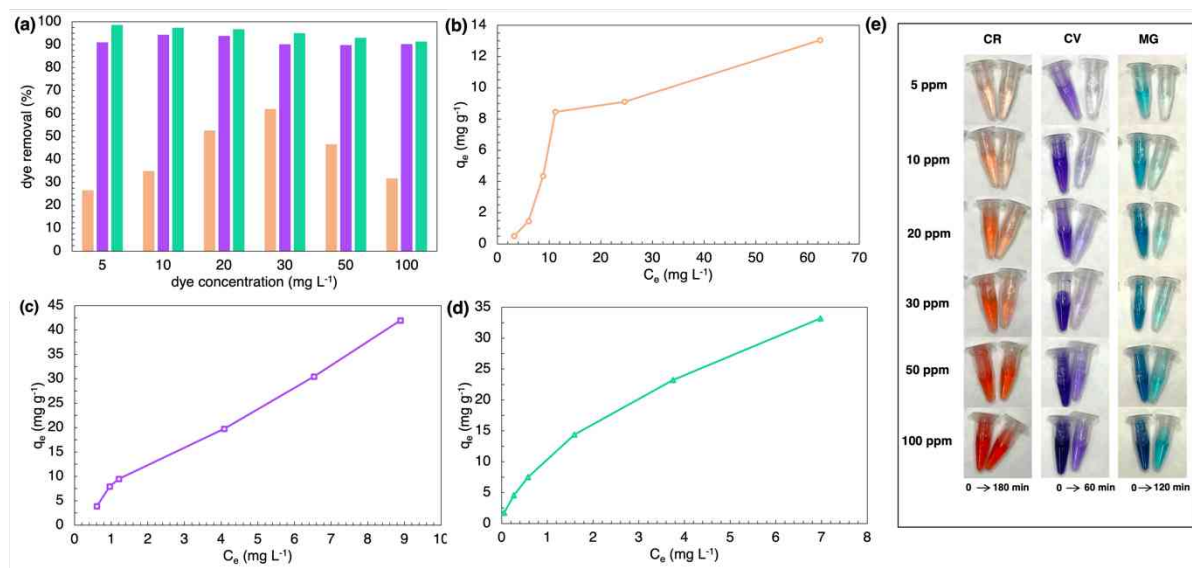
Figure 22. Influence of initial dye concentration on **(a)** dye removal efficiency and adsorption capacity of the frustules of SZCZM1454 *H*. cf. *salinicola* against **(b)** CR, **(c)** CV, and **(d)** MG. **(e)** Discoloration of solutions with different dye concentrations (initial concentration of dye – 5–100 mg L^{-1}, adsorbent dosage – 10 mg, pH – 7, temperature – 20°C, time – 180 min, 60 min, and 120 min for CR, CV, and MG, respectively; from Golubeva et al., 2023b).

To understand the possible mechanisms of adsorption, several kinetic, diffusion, and equilibrium models were applied. Parameters, correlation coefficients, as well as Chi–square values of kinetic and diffusion models are presented in Table 5. Among these models, the pseudo-first order model provided a better fit to the adsorption curves of *Nanofrustulum* spp. strains, as indicated by a higher correlation coefficient and lower Chi–square value, while in case of the frustules of BA170 *P. trainorii* the adsorption curve of MB presented a better fit into the pseudo-second order kinetic model. Thus, we can conclude that the adsorption behavior of MB on the *Nanofrustulum* spp. frustules primarily follows the pseudo-first order kinetic model, which means that the overall rate of the adsorption process was governed by physisorption, where the molecular interaction between MB and the frustules is primarily influenced by van der Waals forces, whereas the BA170 *P. trainorii* exhibited behavior closer to the pseudo-second order model. The adsorption of CV and MG dyes onto the SZCZM1454 *H*. cf. *salinicola* also aligns with the pseudo-second kinetic model with high correlation coefficients and low the Chi–square values. This model indicates that the adsorption rate is governed by chemisorption, involving the sharing or exchange of electrons between the

adsorbent surface and the dye molecules. On the other hand, the adsorption of CR onto the SZCZM1454 *H*. **cf**. *salinicola* frustules predominantly follows the pore diffusion model - modified intraparticle diffusion model. This model suggests that the rate-controlling step in CR adsorption onto the SZCZM1454 *H*. cf. *salinicola* frustules primarily involves the diffusion of dye molecules into the pores within the adsorbent particles.

Table 5. The parameters of kinetic adsorption models for different strains and types of dye.

Sample	Dye	Pseudo First Order				Pseudo Second Order			
		q_1, mg g^{-1}	k_1, min^{-1}	R^2	χ^2	q_2, mg g^{-1}	k_2, g (mg min)$^{-1}$	R^2	χ^2
SZCZCH193 *N. wachnickianum*	MB	19.902	0.002	0.887	0.62	39.671	2.71e^{-5}	0.894	0.58
SZCZM1342 *N. shiloi*	MB	9.445	0.991	0.979	0.14	14.787	4.09e^{-4}	0.964	0.17
SZCZP1809 *N.* cf. *shiloi*	MB	8.458	0.987	0.989	0.07	12.283	7.74e^{-4}	0.973	0.11
BA170 *P. trainorii*	MB	14.28	0.050	0.888	64.98	12.15	0.002	0.931	0.91
SZCZM1454 *H*. **cf**. *salinicola*	CR	10.14	0.009	0.997	59.9	14.62	0.0005	0.993	66.9
	CV	9.85	0.192	0.999	3.62	10.19	0.039	0.998	7.01
	MG	10.92	0.092	0.998	10.13	11.72	0.011	0.999	4.50

Sample	Dye	Intra-particle diffusion				Pore diffusion			
		K_{wm}, mg (g min$^{0.5}$)$^{-1}$	B, mg g^{-1}	R^2	χ^2	$\Delta\beta$	K_β	R^2	χ^2
SZCZCH193 *N. wachnickianum*	MB	0.377	1e^{-16}	0.730	1.48	1.374	0.004	0.972	0.96
SZCZM1342 *N. shiloi*	MB	0.535	1e^{-14}	0.901	0.65	1.025	0.037	0.964	0.78
SZCZP1809 *N.* cf. *shiloi*	MB	0.575	1e^{-14}	0.930	0.91	1.073	0.035	0.985	0.36
BA170 *P. trainorii*	MB	1.236	2.1716	0.979	2.70	0.675	0.0005	0.941	3.21
SZCZM1454 *H*. **cf**. *salinicola*	CR	0.707	1.203	0.935	1.82	0.677	0.0003	0.951	1.37
	CV	0.146	7.813	0.267	1.43	0.088	0.0088	0.479	1.00
	MG	0.441	5.906	0.759	1.25	0.201	0.005	0.907	0.61

MB – methylene blue, CR – congo red, CV – crystal violet, MG – malachite green

Furthermore, the linearity test of the Boyd's model, commonly used to determine the primary resistance to mass transfer, was also applied (Figure 23). The Boyd's plots for MB adsorption

onto frustules of *Nanofrustulum* spp. (R^2 = 0.962, 0.966, 0.995 and χ^2 = 3.91, 2.17, 0.84 for SZCZCH193 *N. wachnickianum*, SZCZM1343 *N. shiloi*, SZCZP1809 *N.* cf. *shiloi*, respectively) and BA170 *P. trainorii* (R^2 = 0.966 and χ^2 = 2.35) strains as well as the sorption of CR onto the SZCZM1454 *H.* cf. *salinicola* frustules (R^2 = 0.947 and χ^2 = 16.91) passed through the origin, while the plots for CV and MG sorption onto SZCZM1454 *H.* cf. *salinicola* did not (R^2 = 0.957, 0.996 and χ^2 = 0.16, 0.51, respectively). According to Hameed & El-Khaiary (2008), if the plot is nonlinear or linear but does not pass through the origin, it indicates that the adsorption rate is controlled by film diffusion or chemical reaction. On the other hand, if the plot is linear and passes through the origin, it suggests that pore diffusion is the main resistance to mass transfer in the adsorption process. Based on these observations, it can be concluded that MB sorption onto *Nanofrustulum* spp. and BA170 *P. trainorii* strains as well as CR adsorption onto the SZCZM1454 *H.* cf. *salinicola* frustules are primarily governed by pore diffusion, while CV and MG adsorption onto SZCZM1454 *H.* cf. *salinicola* involved thin film (boundary layer) diffusion as the main resistance to mass transfer.
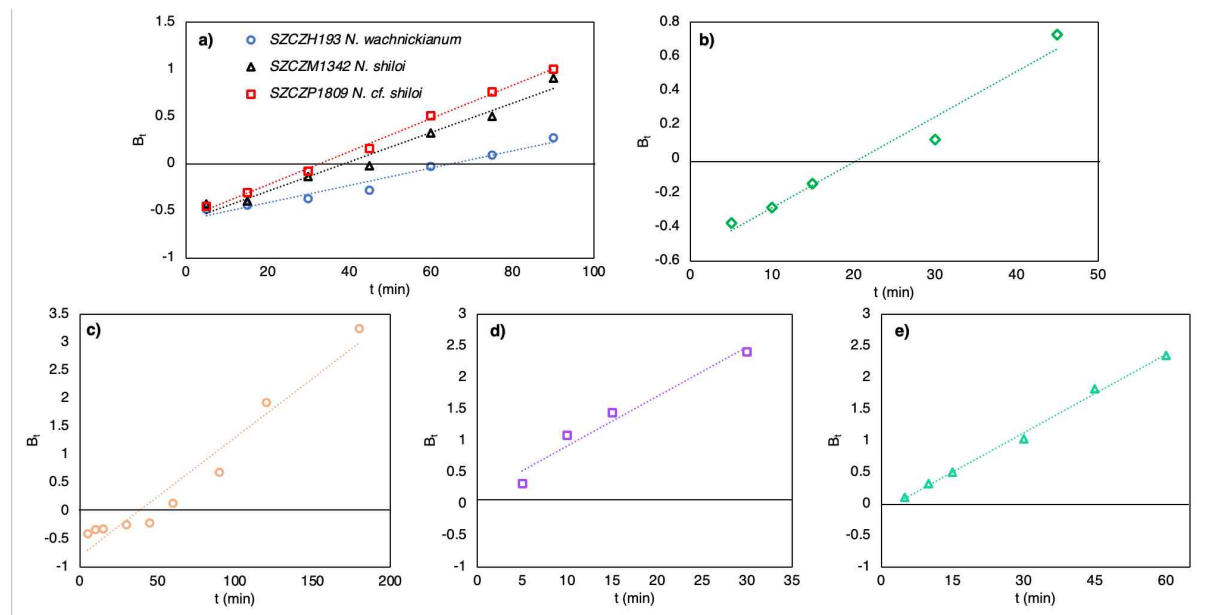
Figure 23. Boyd's plot for adsorption of MB by the frustules of **(a)** *Nanofrustulum* spp. strains, **(b)** BA170 *P. trainorii*, and of **(c)** CR, **(d)** CV, and **(e)** MG by the frustules of SZCZM1454 *H.* cf. *salinicola* (modified from Golubeva et al., 2023a; Golubeva et al., 2023b)

The Langmuir, Freundlich, and Sips models were applied to gain further insights into the potential adsorption mechanisms (Table 6).

Table 6. The parameters of isotherm adsorption models for different strains and types of dye.

Sample	Dye	Langmuir				Freundlich			
		q_{max}, mg g^{-1}	K_L, L mg^{-1}	R^2	χ^2	K_F, (mg g^{-1}) (mg L^{-1})$^{-n}$	n	R^2	χ^2
SZCZCH193 *N. wachnickianum*	MB	6.85	0.31	0.965	0.17	2.37	0.27	0.953	0.23
SZCZM1342 *N. shiloi*	MB	16.18	1.35	0.959	1.47	1.88	1.10	0.965	1.28
SZCZP1809 *N.* cf. *shiloi*	MB	27.09	0.24	0.879	5.70	4.94	0.67	0.820	8.50
SZCZM1454 *H.* cf. *salinicola*	CR	87.72	26.22	0.018	5.05	3.66	0.94	0.786	10.02
	CV	114.9	0.06	0.473	16.82	7.04	1.25	0.977	0.80
	MG	41.5	753.1	0.938	1.31	10.39	1.63	0.999	0.06

Strain	Dye	Sips					q_{exp}, mg g^{-1}
		q_m, mg g^{-1}	K_S [(mg L^{-1})$^{-1/n}$]	n	R^2	χ^2	
SZCZCH193 *N. wachnickianum*	MB	8.39	0.16	0.65	0.992	0.05	6.82
SZCZM1342 *N. shiloi*	MB	19.02	0.26	2.26	0.998	0.08	15.09
SZCZP1809 *N.* cf. *shiloi*	MB	15.17	0.75	2.87	0.999	0.08	15.02
SZCZM1454 *H.* cf. *salinicola*	CR	13.4	0.08	0.47	0.950	1.26	13.04
	CV	42.1	0.53	0.39	0.662	18.92	41.97
	MG	35.0	0.77	0.91	0.900	3.75	33.19

MB – methylene blue, CR – congo red, CV – crystal violet, MG – malachite green

The equilibrium study revealed that different types of dyes exhibited different adsorption characteristics. The Sips model, which combines the Freundlich and Langmuir isotherms and describes the formation of monolayers on both homogeneous and heterogeneous sites (Kalam et al., 2021), demonstrated better suitability for MB (*Nanofrustulum* spp. strains) and CR (SZCZM1454 *H.* cf. *salinicola*) adsorption data, as evidenced by higher values of R^2 close to unity and lower Chi-square values. On the other hand, the Freundlich model was found to be the most appropriate for describing the adsorption of CV and MG onto the SZCZM1454 *H.* cf. *salinicola* frustules, with R^2 values exceeding 0.95. This model suggests the formation of multiple layers of the basic dye on the heterogeneous sites of the SZCZM1454 *H.* cf. *salinicola* surface. According to the Freundlich model, adsorption is considered favorable when $1 < n < 10$, and higher values of n indicate stronger adsorption. Therefore, CV (n = 1.18) and MG (n =

1.63) were favorably adsorbed onto the SZCZM1454 *H.* cf. *salinicola* frustules (Lu et al., 2010).

3.5. *Degradation of 4-nitrophenol in water solution*

The frustules of SZCZM1454 *H.* cf. *salinicola* exhibited minimal response to 4-nitrophenol, with the maximum removal rate of only 39.3% ± 0.612 (Figure 24a), whereas the IONPs loaded frustules of BA170 *P. trainorii* showed a positive response with 94% ± 0.157 degradation of 4-nitrophenol under the visible light after 180 minutes of reaction (Figure 24b).
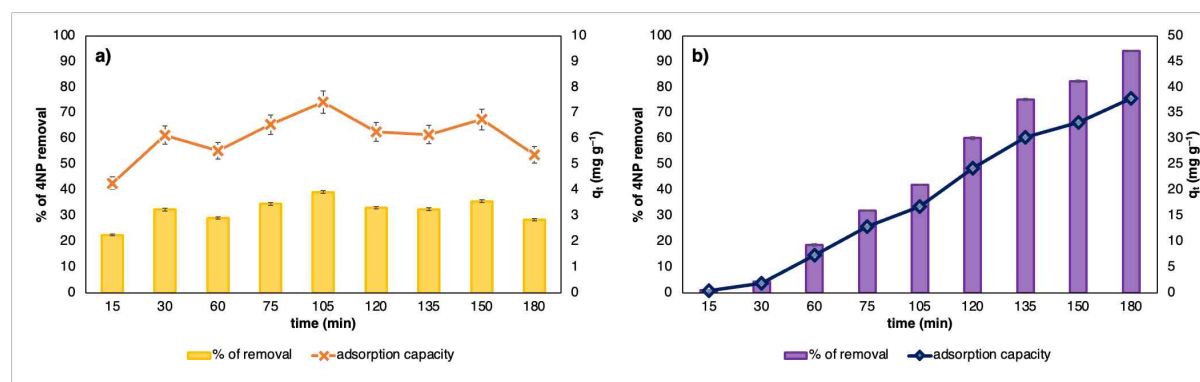
Figure 24. (a) Adsorption of 4NP by the frustules of SZCZM1454 *H*. cf. *salinicola* and **(b)** the photocatalytic removal of 4NP by the IONPs loaded frustules of BA170 *P. trainorii* (initial concentration of 4NP – 20 mg L^{-1}, adsorbent/catalyst dosage – 5 mg, illumination – 200 μmol s^{-1} m^{-2}, pH – 7, temperature – 20°C, time – 15–180 min; modified from Roychoudhury et al., 2022b).

One explanation for this difference suggests that the IONPs loaded frustules can generate highly oxidizing species, such as HO$^{\bullet}$ and O$_2^{\bullet-}$ radicals, through the interaction with emitted photons under the visible light excitation, whereas in case of SZCZM1454 *H.* cf. *salinicola* frustules, there is either lower generation of the radicals or the removal process is mostly adsorption, which is reported to be less effective against phenolic compounds (Banat et al., 2000; Djebbar et al., 2012).

CONCLUSIONS

The study of growth kinetic revealed that some marine diatom strains could accumulate more than 500 mg L^{-1} of biomass DW under standard culture conditions: 720 mg L^{-1} DW after 23 days for *Halamphora* cf. *salinicola* (SZCZM1454) and 630 mg L^{-1} after 16 days for *Nanofrustulum* cf. *shiloi* (SZCZP1809). Other strains managed to achieve higher biomass accumulation under various conditions, i.e., 0.18 mM L^{-1} phosphate in medium resulted in 633 mg L^{-1} for *N. wachnickianum* (SZCZCH193) and 701 mg L^{-1} for *N. shiloi* (SZCZM1342), whereas for *Pseudostraurosira trainorii* (BA170) 678 mg L^{-1} biomass yield was achieved under 50 μmol s^{-1} m^{-2} white light. These results, partially published in Golubeva et al., 2023a and Golubeva et al., 2023b (Annex I and Annex II), confirmed the hypothesis 1: 'Marine diatoms cultivated under laboratory conditions could accumulate more than 500 mg DW biomass in 1 L of culture'.

Moreover, the increased concentration of silicon in a culture medium significantly (one-way ANOVA, $p < 0.05$) enhanced the biomass yield for all five strains up to 977 mg L^{-1} for *N. wachnickianum* (SZCZCH193), 930 mg L^{-1} for *N. shiloi* (SZCZM1342), 989 mg L^{-1} for *N.* cf. *shiloi* (SZCZP1809), 964 mg L^{-1} for *H.* cf. *salinicola* (SZCZM1454), and 810 mg L^{-1} for *P. trainorii* (BA170), therefore confirming the hypothesis 2: 'Increased silicon concentration in a culture medium enhances the biomass yield of diatoms'. These results were published in Golubeva et al., 2023a and Golubeva et al., 2023b as well (Annex I and Annex II).

To confirm the hypothesis 3: 'The geographical origin of the diatom strains has a significant impact on their biomass accumulation under laboratory settings', I studied the growth of the strains under different temperature, salinity, and light intensity. *N. wachnickianum* (SZCZCH193) originated from Marquesas Keys in Gulf of Mexico, Florida, USA, where the average sea water temperature of 28 °C accumulated 865 mg L^{-1} under 30 °C in laboratory setting, which is significantly higher (one-way ANOVA, $p < 0.05$) compared to other temperatures impacts. Similar dynamics were observed for *H.* cf. *salinicola* (SZCZM1454), originated from hot spring in Turkey, with higher biomass yield of 700 mg L^{-1} under 30 °C in laboratory setting, and for *N.* cf. *shiloi* (SZCZP1809), which was sampled in Cape Town in South Africa with average sea water temperature of 17 °C and accumulated 2,210 mg L^{-1} of DW biomass, which makes this strain the most productive one. Moreover, the lower salinity tends to increase the biomass yield of *P. trainorii* (BA170), due to lower salinity in its original habitat – the Baltic Sea. Thus, hypothesis 3 has been confirmed.

SEM images as well as EDS study revealed the presence of iron particles on the surface of the frustule of *P. trainorii* (BA170). Moreover, the FTIR study demonstrated bonds, corresponding to Fe–O, Si–O, and O–H groups, confirming the reduction of Fe^{3+} ions by Si–O– or O–H– groups on the frustule surface. Therefore, the hypothesis 4: 'Diatom biomass could reduce Fe^{3+} ions to iron oxide nanoparticles from water solution' has been proved. The results were published in Roychoudhury et al., 2022b (Annex III).

The intact biosilica is composed of the amorphous SiO_2 nH_2O similar to opal (atomic ratio of O:Si close to 2:1) with some impurities as confirmed by UV-vis spectra, EDS, XRD, and TGA/DTA analyses. SEM image and the low temperature nitrogen adsorption/desorption demonstrated the presence of macro-, meso-, and micropores on the surface of the diatom frustule. As demonstrated by modeling of MB and CR adsorption, published in Golubeva et al., 2023a and Golubeva et al., 2023b (Annex I and Annex II), the rate-controlling step is pore diffusion within the particle of biosilica, therefore the hypothesis 5: 'The diatom biosilica has high filtration potential due to the presence of macropores (areolae), meso- and micropores on the frustules surface', has been confirmed.

The Si–O, N–H, C–H, and O–H functional groups, present on the diatom frustule surface, are accountable for the negative charge on the surface as demonstrated by FTIR and zeta potential analyses. It is important to note, that *H.* cf. *salinicola* (SZCZM1454) biosilica demonstrated the positive charge under a pH lower than 6. This could be explained be the impact of impurities, detected by XRD and TGA. The adsorption efficiency of the diatom biosilica was higher against the cationic dyes (MB, CV, and MG) due to the formation of a strong electrostatic bond, while the anionic dye was repulsed by the negative charge on the surface of the frustule. These results, published in Golubeva et al., 2023a and Golubeva et al., 2023b, prove the hypothesis 6: 'The various functional groups, including Si–O⁻, on the surface of the diatom biosilica make it an anionic material with higher affinity to the cationic dyes'.

The photocatalytic activity of the diatom biosilica against 4-nitrophenol significantly increased (from 40% to 95% removal after 180 min of exposure) after the decoration of their surface with iron oxide nanoparticle. Therefore, the hypothesis 7: 'The diatom frustules decorated with iron oxide nanoparticles exhibit a higher photocatalytic activity against phenols' has been confirmed and results were published in Roychoudhury et al., 2022b (Annex III).

Thus, the non-modified diatom biosilica could be used as a novel eco-friendly bio-originated adsorbent of the cationic and anionic dyes, while controlled green modification of the frustule presents a high potential for photocatalytic degradation of phenolic compounds.

MATERIALS AND METHODS

5.1. Chemical reagents

Methylene blue (>99%, MW 319.89) has been purchased from Aqua-Med® (Łódź, Poland). Malachite Green (99%, MW 364.911 Da), crystal violet (99%, MW 407.99 Da), and congo red (99%, MW 696.69 Da) were purchased from Hadron Scientific (Kielce, Poland). Thiamine hydrochloride (99%, MW 337.27), biotin (>99%, MW 244.31), vitamin B12 (>98%, MW 1355.37), sodium hydroxide (>98%, MW 40.00), hydrochloric acid (37%, MW 36.46), 4-nitrophenol (>99%, MW 139.11), and standard buffered solutions pH 2.0, 7.0 and 10.0 have been supplied by Sigma-Aldrich (St. Louis, MO, USA). Hydrogen peroxide (30%, MW 34.01), sodium nitrate (>99%, MW 84.99), sodium dihydrogen phosphate monohydrate (>99%, MW 137.99), sodium molybdate dihydrate (>99%, MW 241.95), manganese (II) chloride tetrahydrate (>99%, MW 197.91), and cobalt (II) chloride hexahydrate (>99%, DW 237.93) have been obtained from Chempur® (Piekary Śląskie, Poland). Zinc sulfate heptahydrate (>99%, MW 287.54), iron (III) chloride hexahydrate (>99%, MW 270.32), EDTA disodium dihydrate (>99%, MW 372.24), and copper (II) sulfate pentahydrate (>99%, MW 249.68) have been purchased from Scharlab (Barcelona, Spain). Non-anhydrate sodium metasilicate (44-47.5% total solids, MW 284.19) has been supplied by Acros Organics, ThermoFisher Scientific (Waltham, MA, USA). The PhosVer® 3 Phosphate Reagent Powder Pillow, Amino Acid F Reagent Powder Pillow, Citric Acid Powder Pillow, and Molybdate 3 Reagent Solution have been provided by HACH-Lange (Loveland, CO, USA). Deionized water was obtained by using a Milli-Q® purification system (Millipore Co., Bedford, MA, USA).

5.2. The diatom strains

The diatom strains *Nanofrustulum wachickanium* Chunlian, Witkowski & Ashworth (SZCZCH193) – collected from Marquesas, Florida, USA, isolated and identified by Li C., *N. shiloi* (Lee, Reimer & McEnery) Round, Hallsteinsen & Paasche (SZCZM1342) – collected from Mediterranean Sea Cost, Turkey, isolated and identified by Krzywda M., *N.* cf. *shiloi* (Lee, Reimer & McEnery) Round, Hallsteinsen & Paasche (SZCZP1809) – collected from Sea Point, Cape Town, South Africa, isolated and identified by Dąbek P., *Halampora.* cf. *salinicola* Levkov & Díaz (SZCZM1454) – collected from thermal spring in Köyceğiz Lake, Turkey, isolated and identified by Krzywda M. were obtained from the Szczecin Diatom Culture Collection (SZCZ), University of Szczecin (Poland), and *Pseudostraurosira trainorii* Morales

(BA170) – collected from Gulf of Gdańsk, Baltic Sea, was obtained the Culture Collection of Baltic Algae, University of Gdańsk (Poland).

5.3. Batch cultivation of the diatom strains

5.3.1. Standard culturing conditions

The monoclonal cultures were maintained in standard artificial seawater 7 ‰ (*Pseudostaurosira* strain) and 35 ‰ (*Nanofrustulum* and *Halamphora* strains) Guillard′s f/2 medium: 880 µM L^{-1} $NaNO_3$, 36 µM L^{-1} NaH_2PO_4 H_2O, 106 µM L^{-1} Na_2SiO_3 $9H_2O$, trace metal: 0.08 µM L^{-1} $ZnSO_4$ $7H_2O$, 0.9 µM L^{-1} $MnSO_4$ H_2O, 0.03 µM L^{-1} Na_2MoO_4 $2H_2O$, 0.05 µM L^{-1} $CoCl_2$ $6H_2O$, 0.04 µM L^{-1} $CuCl_2$ $2H_2O$, 11.7 µM L^{-1} $FeCl_3$ $6H_2O$, 11.7 µM L^{-1} Na_2EDTA $2H_2O$, vitamin B_{12}, biotin and thiamine (Guillard, 1975), at constant temperature (20°C) and illumination (100 µmol s^{-1} m^{-2} white light) under a 12:12h day:night light cycle in a plant growth chamber (FITO1400i, Biogenet, Poland). The diatom strains were observed under the inverted Olympus CKX41 microscope (Olympus- Shinjuku, Tokyo, Japan) at 400× magnification.

5.3.2. Growth curve and kinetic parameters

For each strain the growth curve and kinetic parameters were obtained. 25 ml of monoclonal culture of the strain was put in 100 ml Erlenmeyer flask with 25 ml of standard f/2 medium, and the strains were cultivated under standard condition for 22–24 days with biomass harvested every other day. After, biomass was centrifuged at 3,000 rpm and pellet was heat dried for 3 days at 50°C. The growth curves were built for each strain. The growth rates were determined by dry biomass weight: the regression curve for each strain was built and the specific growth rate (µ) was calculated following the equation 1 (Kirchman, 2002):

$$B_t = B_0 e^{\mu t} \tag{1}$$

where B_t – the biomass concentration at any time (t) and B_0 – the initial biomass concentration.

5.3.3. Nutrients concentration determination

The nutrients concentrations in f/2 medium were determined before and after cultivation as follows: culture was harvested, centrifuged at 3,000 rpm for 15 min, and supernatant was used for nutrients measurements.

The nitrate concentration in medium was measured by UV screening method (HACH-Lange), based on nitrate and organic substances adsorption at 220 nm and only organic adsorption at 275 nm. To prevent hydroxide ions or carbonate ions from interfering at these wavelengths 20 µl of 0.1 M HCl was added to 9.98 ml of sample, readings were performed using the UV-Vis DR 6000 spectrophotometer (HACH-Lange).

The orthophosphate concentration in medium was measured by ascorbic acid method (PhosVer 3 ® powder pillows, HACH-Lange), based on molybdate interaction with orthophosphate to form a phosphate/molybdate complex, later reduced by ascorbic acid, which gives intense molybdenum blue color (absorbance at 880 nm). 10 ml of sample was exposed to one PhosVer 3 ® powder pillow for 2 min, readings were performed with use of the UV-Vis DR 6000 spectrophotometer (HACH-Lange).

The silica content was checked by Heteropoly Blue method (Molybdate 3, Citric acid and Amino acid powder pillows, HACH-Lange). Similar to orthophosphate measurements, this method is based on molybdate ion interaction with silica and phosphate, forming yellow silicomolybdic acid complexes and phosphomolybdic acid complexes. Addition of citric acid destroys the phosphate complexes, and amino acid is added to reduce the yellow silicomolybdic acid to an intense blue color (absorbance at 815 nm). 10 ml of sample was exposed to 14 drops of Molybdate 3 reagent for 4 min, following with Citric Acid Reagent powder pillow for 1 min and later Amino Acid F Reagent powder pillow for 2 min, reading was performed with use of the UV-Vis DR 6000 spectrophotometer (HACH-Lange).

5.3.4. Optimization of culturing conditions

For every optimization experiment 10 ml of the monoclonal culture (with concentration approximately 2000 cells µl^{-1} for *Nanofrustulum* strains, 200 cells µl^{-1} for *Halamphora* strain, and 1000 cells µl^{-1} for *Pseudostaurosira* strain) was placed in 100 ml Erlenmeyer flask with 40 ml of medium. The variable conditions were set as mentioned below, while other conditions were kept standard. All experiments were carried out in a plant growth chamber (FITO1400i, Biogenet, Poland). Biomass was harvested in the late exponential growth phase by centrifugation at 3,000 rpm for 15 min, supernatant was used for nutrients measurements, and pellets were heat dried under 50°C for several days, and the total biomass yield was evaluated by dry weight.

5.3.4.1. Experiments with different salinity of medium

The influence of salinity on the dry biomass yield was evaluated. *Pseudostaurosira* strain was cultivated under standard conditions in 7 ‰ (control), 10 ‰, 15 ‰, and 20 ‰ artificial seawater standard f/2 medium, while *Nanofrustulum* and *Halamphora* strains were cultivated in 15 ‰, 20 ‰, 35 ‰ (control), and 45 ‰ artificial seawater standard f/2 medium.

5.3.4.2. Experiments with different temperature of cultivation

The effect of the variation of cultivation temperature was studied. The strains were maintained under standard culturing conditions and 15°C, 20°C (control), and 30°C temperature.

5.3.4.3. Experiments with different illumination intensity

The change in biomass accumulation under different illumination intensity was evaluated. The strains were cultivated under 10 µmol s^{-1} m^{-2}, 50 µmol s^{-1} m^{-2}, 100 µmol s^{-1} m^{-2} (control), and 150 µmol s^{-1} m^{-2} white light.

5.3.4.4. Experiments with a variation of nutrients in medium

The concentration of nutrients in medium is important for growth and metabolism of diatoms. Due to diatoms' ability to synthesize the siliceous cell frustule it is crucial to provide diatom with silicate for this process. Thus, the strains were cultivated in f/2 medium enriched with silicate: 0.11 mM L^{-1} (control), 0.53 mM L^{-1}, 1.06 mM L^{-1}, 1.59 mM L^{-1}, and 2.12 mM L^{-1}. Moreover, nitrate and phosphate in medium are used by diatoms for all major metabolic processes, hence their influence on biomass yield was studied. The strains were cultivated first in f/2 medium enriched with nitrate (0.88 mM L^{-1} (control), 4.41 mM L^{-1}, 8.82 mM L^{-1}, 13.23 mM L^{-1}, and 17.64 mM L^{-1}) and second in f/2 medium enriched with phosphate (0.04 mM L^{-1} (control), 0.18 mM L^{-1}, 0.36 mM L^{-1}, 0.54 mM L^{-1}, and 0.72 mM L^{-1}).

5.3.5. Scale-up cultivation of diatoms

For the biosilica production, the strains were cultivated in 2 L bottles with aeration system and in closed vertical tubular 70 L photobioreactors (PBRs) for three weeks. The biomass was harvested by sedimentation, decantated, and later used for the frustule's purification and biosynthesis of the IONPs.

5.4. *The purification of the diatom frustules*

To obtain the frustules the harvested biomass was centrifuged at 3,000 rpm for 15 min, and pellets were exposed to 30% H$_2$O$_2$ solution at 110°C for 2 days following a thorough cleaning

with double distilled water (ddH$_2$O). The colorless cleaned silica was dried at 50°C for 3 days and later used for characterization experiments.

5.5. *Diatom mediated biosynthesis of the IONPs*

The entire biomass of the diatom strain BA170 *P. trainorii* was utilized as a reducing agent for the synthesis of the biogenic IONPs. To prepare the biomass, healthy cells of BA 170 *P. trainorii* were subjected to centrifugation at 6,000 rpm for 10 minutes. Then the collected cells were washed three times with ddH$_2$O to remove any residual salts from the medium. After the washing steps, the biomass was collected again through centrifugation at 6,000 rpm for 10 minutes. The thoroughly washed biomass, 300 mg wet weight (WW), was exposed to a 400 mL 0.01 M Fe^{3+} solution with a pH of 2. The entire experiment was conducted in the dark at room temperature for a duration of 3 days. The resulting golden yellow biomass was then collected by centrifugation at 8,000 rpm for 20 minutes. To remove any residual substances, the harvested biomass was rinsed 3–4 times with ddH$_2$O. Finally, the biomass was stored at a temperature of 4°C for further investigation.

5.6. *Characterization techniques*

5.6.1. SEM imaging and EDS study

The morphologies of the intact and IONPs loaded frustules were studied by scanning electron microscopy (SEM) using a Hitachi SU8020 (Hitachi, Tokyo, Japan). For the SEM study, 40 µL of sample was dried on Nuclepore™ 5.0 µm Track-Etch Membrane (Whatman™, Cytiva, Germany) at room temperature. The dried samples were mounted on an M4 cylinder SEM sample aluminum stub (Hitachi, Tokyo, Japan) using black conductive carbon adhesive tape and coated with a 10 nm thick gold layer. For the elemental analysis of *Nanofrustulum* spp. frustules, the drop was placed on the carbon-coated copper grid (Sigma-Aldrich, USA), and the analysis was carried out by a Hitachi STEM S5500 attached with EDAX (Hitachi, Tokyo, Japan). The measurements were performed with an accelerating energy 30.0 kV.

5.6.2. UV-vis spectroscopy

The control biomass, intact and IONPs loaded frustules were sonicated with water using a Hielscher UP100H ultrasonic processor (Teltow, Germany) for 20 min at 60% amplitude. After sonication, the suspensions were centrifuged at 3,000 rpm for 5 min and the supernatants were added to 10 mm quartz cuvette and subjected to the UV-Vis DR 6000 spectrophotometer (HACH-Lange) for optical measurements in the wavelength range of 200–900 nm against

ddH$_2$O (blank). For absorbances higher than 2, the solution was diluted with ddH$_2$O, the dilution factors were considered in the presented graphs.

5.6.3. Fourier transform infrared spectroscopy (FITR)

FTIR spectra of the intact and IONPs loaded frustules were obtained in the mid-infrared range (4,000 – 400 cm^{-1}) with the utilization of attenuated total reflection (ATR) mode on Alpha FTIR spectrometer (Bruker Daltonics, Bremen, Germany).

5.6.4. The low-temperature nitrogen adsorption/desorption

Adsorption/desorption experiments using nitrogen were carried out at 77.35 K on a Autosorb iQ Quantachrome. Before each measurement, the intact frustules (200 ± 50 mg) were outgassed at 120°C for 3.5 h in vacuum. The N$_2$ isotherm were used to determine the specific surface areas using the standard Brunauer–Emmett–Teller (BET) equation 2:

$$\frac{1}{X\left[\left(P_0/P\right) - 1\right]} = \frac{1}{X_m C} + \frac{C - 1}{X_m C}\left(\frac{P}{P_0}\right) \tag{2}$$

where X_m – the number of gas molecules needed to form a monolayer of adsorbed gas on a solid surface, X – the number of gas molecules adsorbed at a given relative pressure (P/P_0), C – a second parameter related to the heat of adsorption.

Pore volume and sizes were obtained from the N$_2$ adsorption branch, using the Barrete–Joynere–Halenda (BJH) method (Eq. 3):

$$V_p = \left(\frac{r_p}{r_K + \Delta t/2}\right)^2 \left(\Delta V - \Delta t \sum_{j=1}^{n-1} Ac_j\right) \tag{3}$$

where r_p – pore radius, V_p – pore volume, r_K – inner capillary radius, Δt – thickness of adsorbed layer of nitrogen, Ac_j – area exposed by the pore from which the physically adsorbed gas is desorbed.

5.6.5. Zeta potential

Zeta potential measurements were carried out with Malvern Zetasizer NanoZS (Malvern) using DTS1070 cuvette (Malvern). The analysis was performed in the automatic selection mode of voltage and number of runs. The results consider the Smoluchowski approximation (Eq. 4):

$$\zeta = {}^{\eta\mu_e}\!/_{\varepsilon_r\varepsilon_0} \qquad (4)$$

where η - solution viscosity; μ_e - electrophoretic mobility; ε_0 - electric permeability in vacuum, and ε_r - dielectric constant of the solution.

Each measurement was repeated three times. Zeta potential was measured in 2.0 – 12.0 pH range. To maintain the pH 0.1M NaOH and 0.1M HCl solutions were used. FiveEasy Plus pH-meter (Mettler Toledo) with a combined electrode with glass membrane and Ag/AgCl reference system (Mettler Toledo) was applied to measure pH of suspensions. The pH-meter was calibrated using standard buffered solutions with pH of 2.0, 7.0, 10.0 before carrying out measurements.

5.6.6. X-ray diffraction (XRD)

The X-ray diffraction was performed with X'Pert Pro Analytical diffractometer (Phillips, Erlangen, Germany) with CuKa radiation source and Ni filter. The X-ray diffraction pattern analysis was obtained from XRD Malvern Panalytical software (version 1.5a, Almelo, The Netherlands) in the 2θ range from 5 to 120º and scan step size 0.0167º.

5.6.7. Thermogravimetric analysis (TA/TGA)

TA/TGA of the biosilica samples was performed with TA Instruments type SDT 2960 (Artisan Technology, Champaign, IL, USA) using 0 – 1,100°C temperature range, 100 mL min^{-1} air flow rate and 10°C min^{-1} heating rate. The analysis data for TA/DTA was proceed with the use of TA Universal Analysis software (TA Instruments, New Castle, DE, USA).

5.7. *Dye adsorption experiments*

5.7.1. The calibration curves

The absorbance of methylene blue (MB, 665 nm), congo red (CR, 499 nm), crystal violet (CV, 586 nm), malachite green (MG, 616 nm), and 4-nitrophenol (4NP, 400 nm) was measured for known concentrations (from 100 mg L^{-1} to 0.5 mg L^{-1}). The calibration curves as well as the calibration equations with the correlation coefficients are presented in Supplementary Materials, Figure S2.

5.7.2. The influence of time on dye removal

Four types of the model dyes – methylene blue (MB), congo red (CR), crystal violet (CV) and malachite green (MG) – were used in batch adsorption experiments. The dried frustules (20 ±

0.5 mg) were exposed to 10.0 ml of 14.0 mg L^{-1} MB, 20 mg L^{-1} of CR, CV, and MG solutions with the pH of 7 in a 15 ml Falcon tube. The mixture was mechanically stirred at 3,000 rpm at 23°C for 4 hours. The removal of dye was recorded by a UV-Vis DR 6000 (HACH-Lange) spectrophotometer in the wavelength range from 300 to 800 nm at different time points: 5, 10, 15, 30, 45, 60, 90, 105, 120, 180, and 240 min.

5.7.3. The influence of initial dye concentration on dye removal

Similarly, the study of the effects of initial dye concentration on adsorption process was performed by measuring 20 ± 0.5 mg of the cleaned frustules into 15 ml Falcon tubes containing varying initial concentrations (5, 10, 15, 20, 50, and 100 mg L^{-1}) of MB. The mixture was stirred at 3,000 rpm under 23°C for 120 min, which is necessary to attain equilibrium, and the absorbance value at 665 nm was used for further calculations. For CR, CV, and MG dyes the influence of initial concentration was investigated by measuring 10 mg of cleaned frustules in Falcon tubes containing various dyes' concentrations (5, 10, 15, 20, 50, and 100 mg L^{-1}). After the mixture reached equilibrium (120 min for CR and MG, 60 min for CV), the removal was recorded spectrophotometrically at 499 nm (CR), 586 nm (CV), and 616 nm (MG).

5.7.4. The influence of pH of solution on dye removal

The effects of different pH of the initial MB solution (14.0 mg L^{-1}) were recorded for the pH of 3, 7, and 11 after 120 min of exposure. The initial pH of the solution was adjusted with 1 M HCl and 1 M NaOH solutions. The absorbance value at 665 nm was used for further calculations.

5.8. Photocatalytic degradation of 4-nitrophenol

The spectroscopic analysis was employed to investigate the degradation of 4-nitrophenol (4NP) using the intact and IONPs loaded frustules. In order to determine the 4NP degradation, 5 mg of the intact and IONPs loaded frustules were added to a 10 mL aqueous solution containing 20 mg L^{-1} of 4NP at pH 7.0. The resulting suspension was stirred under white light at room temperature for a duration of 3 hours. The decolorization of 4NP was measured using a spectrophotometer at 400 nm, at various time intervals including 15, 30, 60, 75, 105, 120, 135, 150, and 180 minutes. Before each measurement, the reaction mixture was centrifuged at 4,000 rpm for 3 minutes to eliminate any interference from the frustules. A control set consisting of 4NP without IONPs-loaded frustules was also maintained under the same reaction conditions.

5.9. Calculations and modeling

The quantity of adsorbed dye and 4NP by the frustules was calculated by the equation 5:

$$q_t = \frac{(C_0 - C_t) \times V}{m} \tag{5}$$

where q_t – dye or phenol amount adsorbed on the frustules (mg g^{-1}) at a given time (t); C_0 and C_t – the concentrations of the dye or phenol at the start and at the given timepoint (mg L^{-1}), respectively; V – the solution volume (L); m – the frustules dosage (g).

The percentage of dye and 4NP removal (%) was calculated by the equation 6:

$$removal\ \% = \frac{(C_0 - C_t) \times 100\%}{C_0} \tag{6}$$

where C_0 and C_t – the initial concentration and concentration at the given time (t), respectively (mg L^{-1}).

To understand the possible mechanisms and rate controlling steps of adsorption, several kinetic, diffusion and isotherm models were applied (Table 7).

5.10. Data analysis

The batch cultivation experiments were conducted in duplicates. The figures show mean values and standard deviations. The significance of differences between different groups was analyzed using a one–way ANOVA analysis with Tukey's post-hoc test, the alpha level of 0.05. The batch growth experiment figures, UV-Vis, FTIR spectra, batch adsorption spectra were plotted using MS Excel software (version 16.73). The EDS spectra were obtained using NSS ThermoScientific software (version 1.0). The analysis data for TA/DTA was proceed with the use of TA Universal Analysis software (TA Instruments, New Castle, DE, USA). The X-ray diffraction pattern analysis was obtained from XRD Malvern Panalytical software (version 1.5a, Almelo, The Netherlands).

The applicability of the kinetic, diffusion and isotherm models was validated using the Chi-square (χ^2), which is defined by equation 7:

$$\chi^2 = \sum \frac{(q_{cal} - q_{exp})^2}{q_{exp}} \tag{7}$$

where q_{exp} and q_{cal} (mg g^{-1}) the experimental and calculated adsorption capacity value, respectively.

Table 7. Linearized forms of kinetic and isotherm models' equations and parameters

Models	Equation		Description of parameters	Ref.
Kinetic study				
Pseudo-first order	$\ln(q_1 - q_t) = \ln q_1 - k_1 t$	(8)	q_t (mg g^{-1}) – amount adsorbed at given time (t, min)	(Lagergren, 1898)
			q_1 (mg g^{-1}) – adsorbent capacity at equilibrium	
Pseudo-second order	$\dfrac{t}{q_t} = \dfrac{1}{k_2 q_2^2} + \dfrac{1}{q_2} t$	(9)	k_1 (min^{-1}) – Pseudo-first order constant rate	(Blanchard et al., 1984)
			q_2 (mg g^{-1}) – adsorbent capacity at equilibrium	
			k_2 (g (mg min)$^{-1}$) – Pseudo-second order constant rate	
			α (mg (g min)$^{-1}$) – initial adsorption rate	
			β (mg g^{-1}) – desorption constant	
Diffusion study				
Boyd's	$B_t = -0.4977 - \ln(1 - \dfrac{q_t}{q_e})$	(10)	q_e (mg g^{-1}) – amount adsorbed at equilibrium	(Boyd et al., 1947)
			B_t – mathematical function of F	
Intra particle diffusion	$q_t = k_{wm} t^{0.5} + B$	(11)	F – the fraction of metal ion adsorbed at any time (t)	(Weber & Morris, 1963)
			q_t (mg g^{-1}) – amount adsorbed at given time (t, min)	
Pore diffusion	$\log \log \left(\dfrac{C_0}{C_0 - m q_t} \right)$ $= \log \left(\dfrac{m K_\beta}{2.303 V} \right) + \Delta \beta \log t$	(12)	K_{wm} (mg (g min$^{0.5}$)$^{-1}$)– Intra-particle diffusion rate constant	(Bangham et al., 1965)
			B (mg g^{-1}) – intercept	
			C_0 (mg L^{-1}) – initial concentration of MB	
			m (g) – mass of adsorbent g	
			$\Delta \beta$ and K_β - Bangham constants	
			V (mL)– volume of solution	
Equilibrium study (isotherms)				
Langmuir	$\dfrac{C_e}{q_e} = \dfrac{1}{K_L Q_{max}} + \dfrac{C_e}{Q_{max}}$	(13)	q_e (mg g^{-1}) – adsorption capacity at equilibrium	(Langmuir, 1918)
Freundlich	$\ln q_e = \ln K_F + \dfrac{1}{n} \ln C_e$	(14)	C_e (mg L^{-1}) – concentration of MB dye at equilibrium	(Freundlich, 1906)
Sips	$\ln \left(\dfrac{q_e}{q_m - q_e} \right) = \dfrac{1}{n} \ln C_e + \ln K_S^{\frac{1}{n}}$	(15)	q_{max} (mg g^{-1}) – maximum monolayer adsorption capacity of Langmuir	(Sips, 1948)
			K_L (L mg^{-1}) – Langmuir constant	
			K_F [(mg g^{-1}) (mg L^{-1})$^{-n}$] – Freundlich constant	
			n – dimensionless Freundlich intensity parameter	
			q_m (mg g^{-1}) – the Sips maximum adsorption capacity	
			K_S [(mg L^{-1})$^{-1/n}$] – the Sips equilibrium constant	
			n – the exponent of Sips where 0<1/n≤1	

REFERENCES

Al-Quraishi, D. O., & Abbas, I. K. (2019). Removing heavy metals by diatoms *Nitzschia palea* and *Navicula incerta* in their aqueous solutions. *Plant Archives*, *19*, 272–278.

Ali, D. M., Divya, C., Gunasekaran, M., & Thajuddin, N. (2011). Biosynthesis and characterization of silicon-germanium oxide nanocomposite by diatom. *Digest Journal of Nanomaterials Biostructures*, *6*, 117–120.

Allen, A. E., Dupont, C. L., Oborník, M., Horák, A., Nunes-Nesi, A., McCrow, J. P., Zheng, H., Johnson, D. A., Hu, H., Fernie, A. R., & Bowler, C. (2011). Evolution and metabolic significance of the urea cycle in photosynthetic diatoms. *Nature*, *473*, 203–207. https://doi.org/10.1038/nature10074

Ashour, M., Alprol, A. E., Khedawy, M., Abualnaja, K. M., & Mansour, A. T. (2022). Equilibrium and Kinetic Modeling of Crystal Violet Dye Adsorption by a Marine Diatom, *Skeletonema costatum*. *Materials*, *15*, 6375. https://doi.org/10.3390/ma15186375

Avşar, Ö., Avşar, U., Arslan, Ş., Kurtuluş, B., Niedermann, S., & Güleç, N. (2017). Subaqueous hot springs in Köyceğiz Lake, Dalyan Channel and Fethiye-Göcek Bay (SW Turkey): Locations, chemistry and origins. *Journal of Volcanology and Geothermal Research*, *345*, 81–97. https://doi.org/10.1016/j.jvolgeores.2017.07.016

Aw, M. S., Bariana, M., Yu, Y., Addai-Mensah, J., & Losic, D. (2013). Surface-functionalized diatom microcapsules for drug delivery of water-insoluble drugs. *Journal of Biomaterials Applications*, *28*, 163–174. https://doi.org/10.1177/0885328212441846

Azam, F., Hemmingsen, B. B., & Volcani, B. E. (1973). Germanium incorporation into the silica of diatom cell walls. *Archiv für Mikrobiologie*, *92*, 11–20. https://doi.org/10.1007/BF00409507

Banat, F. A., Al-Bashir, B., Al-Asheh, S., & Hayajneh, O. (2000). Adsorption of phenol by bentonite. *Environmental Pollution*, *107*, 391–398. https://doi.org/10.1016/s0269-7491(99)00173-6

Bangham, A. D., Standish, M. M., & Watkins, J. C. (1965). Diffusion of univalent ions across the lamellae of swollen phospholipids. *Journal of Molecular Biology*, *13*, 238–252. https://doi.org/10.1016/s0022-2836(65)80093-6

Basharina, T. N., Danilovtseva, E. N., Zelinskiy, S. N., Klimenkov, I. V., Likhoshway, Y. V., & Annenkov, V. V. (2012). The effect of titanium, zirconium and tin on the growth of diatom

Synedra acus and morphology of its silica valves. *Silicon*, *4*, 239–249. https://doi.org/10.1007/s12633-012-9119-x

Bello, O. S., Adegoke, K. A., & Oyewole, R. O. (2014). Insights into the adsorption of heavy metals from wastewater using diatomaceous earth. *Separation Science and Technology*, *49*, 1787–1806. https://doi.org/10.1080/01496395.2014.910223

Benkhaya, S., M'rabet, S., & El Harfi, A. (2020). A review on classifications, recent synthesis and applications of textile dyes. *Inorganic Chemistry Communications*, *115*, 107891. https://doi.org/10.1016/j.inoche.2020.107891

Blanchard, G., Maunaye, M., & Martin, G. (1984). Removal of heavy metals from waters by means of natural zeolites. *Water Research*, *18*, 1501–1507. https://doi.org/10.1016/0043-1354(84)90124-6

Bose, R., Roychoudhury, P., & Pal, R. (2021). In-situ green synthesis of fluorescent silica-silver conjugate nanodendrites using nanoporous frustules of diatoms: an unprecedented approach. *Bioprocess and Biosystems Engineering*, *44*, 1263–1273. https://doi.org/10.1007/s00449-021-02536-4

Bouzidi, N., Zili, F., García-Maroto, F., Alonso, D. L., & Ouada, H. B. (2020). Impact of temperature and growth phases on lipid composition and fatty acid profile of a thermophilic Bacillariophyta strain related to the genus *Halamphora* from north-eastern Tunisia. *Journal of the Marine Biological Association of the United Kingdom*, *100*, 529–536. https://doi.org/10.1017/S002531542000048X

Bowler, C., Vardi, A., & Allen, A. E. (2010). Oceanographic and biogeochemical insights from diatom genomes. *Annual Review of Marine Science*, *2*, 333–365. https://doi.org/10.1146/annurev-marine-120308-081051

Boyd, G. E., Adamson, A. W., & Myers, I. S. (1947). The exchange adsorption of ions from aqueous solutions by organic zeolites; kinetics. *Journal of the American Chemical Society*, *69*, 2836–2848. https://doi.org/10.1021/ja01203a066

Branco-Vieira, M., San Martin, S., Agurto, C., Freitas, M. A., Martins, A. A., Mata, T. M., & Caetano, N. S. (2020). Biotechnological potential of *Phaeodactylum tricornutum* for biorefinery processes. *Fuel*, *268*, 117357. https://doi.org/10.1016/j.fuel.2020.117357

Briceño, S., Chavez-Chico, E. A., & González, G. (2021). Diatoms decorated with gold nanoparticles by *In-situ* and *Ex-situ* methods for *in vitro* gentamicin release. *Materials Science & Engineering. C*, *123*, 112018. https://doi.org/10.1016/j.msec.2021.112018

Brunner, E., Gröger, C., Lutz, K., Richthammer, P., Spinde, K., & Sumper, M. (2009). Analytical studies of silica biomineralization: towards an understanding of silica

processing by diatoms. *Applied Microbiology and Biotechnology*, *84*, 607–616. https://doi.org/10.1007/s00253-009-2140-3

Brzozowska, W., Sprynskyy, M., Wojtczak, I., Dąbek, P., Witkowski, A., & Buszewski, B. (2020). "Outsourcing" Diatoms in Fabrication of Metal-Doped 3D Biosilica. *Materials*, *13*, 2576. https://doi.org/10.3390/ma13112576

Brzozowska, W., Sprynskyy, M., Wojtczak, I., Dąbek, P., Markuszewski, M. J., Witkowski, A., & Buszewski, B. (2022). Metabolically Doping of 3D Diatomaceous Biosilica with Titanium. *Materials*, *15*, 5210. https://doi.org/10.3390/ma15155210

Camargo, E., Jaime, P. C. J., Lin, C. F., Lin, M. S., Yu, T. Y., Wu, M. C., Lai, S.Y., & Wang, M. Y. (2016). Chemical and optical characterization of *Psammodictyon panduriforme* (Gregory) Mann comb. nov.(Bacillariophyta) frustules. *Optical Materials Express*, *6*, 1436–1443. https://doi.org/10.1364/OME.6.001436

Chauton, M. S., Skolem, L. M., Olsen, L. M., Vullum, P. E., Walmsley, J., & Vadstein, O. (2015). Titanium uptake and incorporation into silica nanostructures by the diatom *Pinnularia* sp. (Bacillariophyceae). *Journal of Applied Phycology*, *27*, 777–786. https://doi.org/10.1007/s10811-014-0373-8

Chen, C., Jia, Z., Wang, X., Lu, H., Guan, Z., & Yang, C. (2015). Micro characterization and degradation mechanism of liquid silicone rubber used for external insulation. *IEEE Transactions on Dielectrics and Electrical Insulation*, *22*, 313–321. https://doi.org/10.1109/TDEI.2014.004188.

Chen, Y. X., Liu, H. C., Xie, W. Q., Shen, Z., Xia, J. L., Nie, Z. Y., & Xie, J. P. (2023). Diatom Frustules Decorated with Co Nanoparticles for the Advanced Anode of Li-Ion Batteries. *Small*, 2300707. https://doi.org/10.1002/smll.202300707

Cherifi, O., Sbihi, K., Bertrand, M., & Cherifi, K. (2016). The removal of metals (Cd, Cu and Zn) from the Tensift river using the diatom *Navicula subminuscula* Manguin: A laboratory study. *International Journal of Advanced Research in Biological Sciences*, *3*, 177–187. http://doi.org/10.22192/ijarbs.2016.03.10.024

Chu, W. L., Phang, S. M., & Goh, S. H. (1996). Environmental effects on growth and biochemical composition of *Nitzschia inconspicua* Grunow. *Journal of Applied Phycology*, *8*, 389–396. https://doi.org/10.1007/BF02178582

Chudzińska, J., Woźniak, B., Sprynskyy, M., Nowak, I., & Feliczak-Guzik, A. (2023). Photoremoval of Bisphenol A Using Hierarchical Zeolites and Diatom Biosilica. *International Journal of Molecular Sciences*, *24*, 2878. https://doi.org/10.3390/ijms24032878

Cicco, S. R., Vona, D., De Giglio, E., Cometa, S., Mattioli-Belmonte, M., Palumbo, F., Ragni, R., & Farinola, G. M. (2015). Chemically Modified Diatoms Biosilica for Bone Cell Growth with Combined Drug-Delivery and Antioxidant Properties. *ChemPlusChem*, *80*, 1104–1112. https://doi.org/10.1002/cplu.201402398

Cicco, S. R., Vona, D., Gristina, R., Sardella, E., Ragni, R., Lo Presti, M., & Farinola, G. M. (2016). Biosilica from Living Diatoms: Investigations on Biocompatibility of Bare and Chemically Modified *Thalassiosira weissflogii* Silica Shells. *Bioengineering*, *3*, 35. https://doi.org/10.3390/bioengineering3040035

Cicco, S. R., Vona, D., Leone, G., De Giglio, E., Bonifacio, M. A., Cometa, S., Fiore, S., Palumbo, F., Ragni, R., & Farinola, G. M. (2019). *In vivo* functionalization of diatom biosilica with sodium alendronate as osteoactive material. *Materials Science & Engineering. C, 104*, 109897. https://doi.org/10.1016/j.msec.2019.109897

Cong, X., Mu, Y., Qin, D., Sun, X., Su, C., Chen, T., Wang, X., Chen, X., & Feng, C. (2022). Copper deposited diatom-biosilica with enhanced photothermal and photodynamic performance for infected wound therapy. *New Journal of Chemistry*, *46*, 2140–2154. https://doi.org/10.1039/D1NJ05283G

Das, B., Deka, S., & Patra, S. (2022). Algae mediated technologies in biotreatment of phenolic wastewaters. In M. Shah, S. Rodriguez-Couto, C. B. V. De La Cruz, J. Biswas (Eds), *An Integration of Phycoremediation Processes in Wastewater Treatment* (pp. 103–120). Elsevier. https://doi.org/10.1016/B978-0-12-823499-0.00016-X

Davis, A. K., & Hildebrand, M. (2008). A self-propagating system for Ge incorporation into nanostructured silica. *Chemical Communications*, *37*, 4495–4497. https://doi.org/10.1039/b804955f

De Tommasi, E., & De Luca, A. C. (2022). Diatom biosilica in plasmonics: applications in sensing, diagnostics and therapeutics [Invited]. *Biomedical Optics Express*, *13*, 3080–3101. https://doi.org/10.1364/BOE.457483

Delalat, B., Sheppard, V. C., Rasi Ghaemi, S., Rao, S., Prestidge, C. A., McPhee, G., Rogers, M. L., Donoghue, J. F., Pillay, V., Johns, T. G., Kröger, N., & Voelcker, N. H. (2015). Targeted drug delivery using genetically engineered diatom biosilica. *Nature Communications*, *6*, 8791. https://doi.org/10.1038/ncomms9791

Demirel, Z., Imamoglu, E., & Dalay, M. C. (2020). Growth kinetics of *Nanofrustulum shiloi* under different mixing conditions in flat-plate photobioreactor. *Brazilian Archives of Biology and Technology*, *63*. https://doi.org/10.1590/1678-4324-2020190201

Djebbar, M., Djafri, F., Bouchekara, M., & Djafri, A. (2012). Adsorption of phenol on natural clay. *Applied Water Science*, *2*, 77–86. https://doi.org/10.1007/s13201-012-0031-8

Dorrell, R. G., Gile, G., McCallum, G., Méheust, R., Bapteste, E. P., Klinger, C. M., Brillet-Guéguen, L., Freeman, K. D., Richter, D. J., & Bowler, C. (2017). Chimeric origins of Ochrophytes and Haptophytes revealed through an ancient plastid proteome. *eLife*, *6*, e23717. https://doi.org/10.7554/eLife.23717

Drum, R. W., & Pankratz, H. S. (1964). Post mitotic fine structure of *Gomphonema parvulum*. *Journal of Ultrastructure Research*, *10*, 217–223. https://doi.org/10.1016/s0022-5320(64)80006-x

Duan, W., Du, S., Meng, F., Peng, X., Peng, L., Lin, Y., Wang, G., & Wu, J. (2020). The pathways by which the marine diatom *Thalassiosira* sp. OUC2 biodegrades p-xylene, combined with a mechanistic analysis at the proteomic level. *Ecotoxicology and Environmental Safety*, *198*, 110687. https://doi.org/10.1016/j.ecoenv.2020.110687

Esfandyari, J., Shojaedin-Givi, B., Hashemzadeh, H., Mozafari-Nia, M., Vaezi, Z., & Naderi-Manesh, H. (2020). Capture and detection of rare cancer cells in blood by intrinsic fluorescence of a novel functionalized diatom. *Photodiagnosis and Photodynamic Therapy*, *30*, 101753. https://doi.org/10.1016/j.pdpdt.2020.101753

Falkowski, P. G., Katz, M. E., Milligan, A. J., Fennel, K., Cramer, B. S., Aubry, M. P., Berner, R. A., Novacek, M. J., & Zapol, W. M. (2005). The rise of oxygen over the past 205 million years and the evolution of large placental mammals. *Science*, *309*, 2202–2204. https://doi.org/10.1126/science.1116047

Fischer, C., Adam, M., Mueller, A. C., Sperling, E., Wustmann, M., van Pée, K. H., Kaskel, S., & Brunner, E. (2016). Gold Nanoparticle-Decorated Diatom Biosilica: A Favorable Catalyst for the Oxidation of d-Glucose. *ACS Omega*, *1*, 1253–1261. https://doi.org/10.1021/acsomega.6b00406

Freundlich, H. M. F. (1906). Over the adsorption in solution. *Journal of Physical Chemistry*, *57*, 1100–1107.

Fuhrmann, T., Landwehr, S., El Rharbi-Kucki, M., & Sumper, M. (2004). Diatoms as living photonic crystals. *Applied Physics B*, *78*, 257–260. https://doi.org/10.1007/s00340-004-1419-4

Gannavarapu, K. P., Thakkar, M., Veerapaga, S., Wei, L., Dandamudi, R. B., & Mitra, S. (2018). Novel diatom-FeOx composite as highly active catalyst in photodegradation of Rhodamine-6G. *Nanotechnology Reviews*, *7*, 247–255. https://doi.org/10.1515/ntrev-2017-0218

Gélabert, A., Pokrovsky, O. S., Schott, J., Boudou, A., & Feurtet-Mazel, A. (2007). Cadmium and lead interaction with diatom surfaces: a combined thermodynamic and kinetic approach. *Geochimica et Cosmochimica Acta*, *71*, 3698–3716. https://doi.org/10.1016/j.gca.2007.04.034

Gholami, P., Khataee, A., & Bhatnagar, A. (2020). Environmentally superior cleaning of diatom frustules using sono-Fenton process: Facile fabrication of nanoporous silica with homogeneous morphology and controlled size. *Ultrasonics Sonochemistry*, *64*, 105044. https://doi.org/10.1016/j.ultsonch.2020.105044

Gnanamoorthy, P., Anandhan, S., & Prabu, V. A. (2014). Natural nanoporous silica frustules from marine diatom as a biocarrier for drug delivery. *Journal of Porous Materials*, *21*, 789–796. https://doi.org/10.1007/s10934-014-9827-2

Golubeva, A., Roychoudhury, P., Dąbek, P., Pałczyńska, J., Pryshchepa, O., Piszczek, P., Pomastowski, P., Gloc, M., Dobrucka, R., Feliczak-Guzik, A., Nowak, I., Kurzydłowski, K. J., Buszewski, B., & Witkowski, A. (2023a). A novel effective bio-originated methylene blue adsorbent: the porous biosilica from three marine diatom strains of *Nanofrustulum* spp. (Bacillariophyta). *Scientific Reports*, *13*, 9168. https://doi.org/10.1038/s41598-023-36408-6

Golubeva, A., Roychoudhury, P., Dąbek, P., Pryshchepa, O., Pomastowski, P., Pałczyńska, J., Piszczek, P., Gloc, M., Dobrucka, R., Feliczak-Guzik, A., Nowak, I., Buszewski, B., & Witkowski, A. (2023b). Removal of the Basic and Diazo Dyes from Aqueous Solution by the Frustules of *Halamphora* cf. *salinicola* (Bacillariophyta). *Marine Drugs*, *21*, 312. https://doi.org/10.3390/md21050312

Grachev, M. A., Bedoshvili, Y. D., Gerasimov, E. Y., Zaikovskii, V. I., Gneusheva, K. V., & Likhoshway, Y. V. (2017). Silica-containing inclusions in the cytoplasm of diatom *Synedra acus*. *Doklady: Biochemistry and biophysics*, *472*, 44–48. https://doi.org/10.1134/S1607672917010124

Gröger, C., Lutz, K., & Brunner, E. (2008a). Biomolecular self-assembly and its relevance in silica biomineralization. *Cell Biochemistry and Biophysics*, *50*, 23–39. https://doi.org/10.1007/s12013-007-9003-2

Gröger, C., Sumper, M., & Brunner, E. (2008b). Silicon uptake and metabolism of the marine diatom *Thalassiosira pseudonana*: Solid-state 29Si NMR and fluorescence microscopic studies. *Journal of Structural Biology*, *161*, 55–63. https://doi.org/10.1016/j.jsb.2007.09.010

Grubišić, M., Šantek, B., Zorić, Z., Čošić, Z., Vrana, I., Gašparović, B., Čož-Rakovac, R., & Ivančić Šantek, M. (2022). Bioprospecting of Microalgae Isolated from the Adriatic Sea: Characterization of Biomass, Pigment, Lipid and Fatty Acid Composition, and Antioxidant and Antimicrobial Activity. *Molecules*, *27*, 1248. https://doi.org/10.3390/molecules27041248

Guillard, R. R. (1975). Culture of phytoplankton for feeding marine invertebrates. In W. L. Smith, M. H. Chanley (Eds), *Culture of Marine Invertebrate Animals,* (pp. 29–60). Springer US. https://doi.org/10.1007/978-1-4615-8714-9_3

Gumustas, M., Sengel-Turk, C. T., Gumustas, A., Ozkan, S. A., & Uslu, B. (2017). Effect of polymer-based nanoparticles on the assay of antimicrobial drug delivery systems. In A. M. Grumezescu (Ed), *Multifunctional Systems for Combined Delivery, Biosensing and Diagnostics* (pp. 67–108). Elsevier. https://doi.org/10.1016/B978-0-323-52725-5.00005-8

Gutu, T., Gale, D. K., Jeffryes, C., Wang, W., Chang, C. H., Rorrer, G. L., & Jiao, J. (2009). Electron microscopy and optical characterization of cadmium sulphide nanocrystals deposited on the patterned surface of diatom biosilica. *Journal of Nanomaterials*, *2009*, 1–7. https://doi.org/10.1155/2009/860536

Hadjar, H., Hamdi, B., Bachiller-Baeza, B., & Doña-Rodríguez, J. M. (2021). Efficient sorption performance of carbon-diatomaceous silica compounds towards phenol. *Surfaces and Interfaces*, *24*, 101101. https://doi.org/10.1016/j.surfin.2021.101101

Hameed, B. H., & El-Khaiary, M. I. (2008). Malachite green adsorption by rattan sawdust: isotherm, kinetic and mechanism modeling. *Journal of Hazardous Materials*, *159*, 574–579. https://doi.org/10.1016/j.jhazmat.2008.02.054

He, J., Chen, D., Li, Y., Shao, J., Xie, J., Sun, Y., Yan, Z., & Wang, J. (2013). Diatom-templated TiO 2 with enhanced photocatalytic activity: Biomimetics of photonic crystals. *Applied Physics A*, *113*, 327–332. https://doi.org/10.1007/s00339-013-7970-2

Hedayatkhah, A., Cretoiu, M. S., Emtiazi, G., Stal, L. J., & Bolhuis, H. (2018). Bioremediation of chromium contaminated water by diatoms with concomitant lipid accumulation for biofuel production. *Journal of Environmental Management*, *227*, 313–320. https://doi.org/10.1016/j.jenvman.2018.09.011

Hernández-Ávila, J., Salinas-Rodríguez, E., Cerecedo-Sáenz, E., Reyes-Valderrama, M. I., Arenas-Flores, A., Román-Gutiérrez, A. D., & Rodríguez-Lugo, V. (2017). Diatoms and their capability for heavy metal removal by cationic exchange. *Metals*, *7*, 169. https://doi.org/10.3390/met7050169

Hildebrand, M. (2004). Silicic Acid Transport and its Control During Cell Wall Silicification in Diatoms. In E. Bäuerlein (Ed), *Biology to Biotechnology and Medical Application* (pp. 159–176). Wiley-VCH Verlag GmbH & Co. KGaA, https://doi.org/10.1002/3527604138.ch10

Hildebrand, M., Davis, A. K., Smith, S. R., Traller, J. C., & Abbriano, R. (2012). The place of diatoms in the biofuels industry. *Biofuels*, *3*, 221–240. https://doi.org/10.4155/bfs.11.157

Husain Q. (2006). Potential applications of the oxidoreductive enzymes in the decolorization and detoxification of textile and other synthetic dyes from polluted water: a review. *Critical Reviews in Biotechnology*, *26*, 201–221. https://doi.org/10.1080/07388550600969936

Jantschke, A., Herrmann, A. K., Lesnyak, V., Eychmüller, A., & Brunner, E. (2012). Decoration of diatom biosilica with noble metal and semiconductor nanoparticles (<10 nm): assembly, characterization, and applications. *Chemistry, an Asian journal*, *7*, 85–90. https://doi.org/10.1002/asia.201100563

Javalkote, V. S., Pandey, A. P., Puranik, P. R., & Deshmukh, P. K. (2015). Magnetically responsive siliceous frustules for efficient chemotherapy. *Materials Science & Engineering. C*, *50*, 107–116. https://doi.org/10.1016/j.msec.2015.01.079

Jeffrey, S. T., & Humphrey, G. F. (1975). New spectrophotometric equations for determining chlorophylls a, b, c1 and c2 in higher plants, algae and natural phytoplankton. *Biochemie und Physiologie der Pflanzen*, *167*, 191–194. https://doi.org/10.1016/S0015-3796(17)30778-3

Jeffryes, C., Gutu, T., Jiao, J., & Rorrer, G. L. (2008a). Metabolic insertion of nanostructured TiO2 into the patterned biosilica of the diatom *Pinnularia* sp. by a two-stage bioreactor cultivation process. *ACS Nano*, *2*, 2103–2112. https://doi.org/10.1021/nn800470x

Jeffryes, C., Gutu, T., Jiao, J., & Rorrer, G. L. (2008b). Two-stage photobioreactor process for the metabolic insertion of nanostructured germanium into the silica microstructure of the diatom *Pinnularia* sp. *Materials Science & Engineering: C*, *28*, 107–118. https://doi.org/10.1016/j.msec.2007.01.002

Jeffryes, C., Solanki, R., Rangineni, Y., Wang, W., Chang, C. H., & Rorrer, G. L. (2008c). Electroluminescence and photoluminescence from nanostructured diatom frustules containing metabolically inserted germanium. *Advanced Materials*, *20*, 2633–2637. https://doi.org/10.1002/adma.200800292

Jiang, Y., Laverty, K. S., Brown, J., Brown, L., Chagoya, J., Burow, M., & Quigg, A. (2015). Effect of silicate limitation on growth, cell composition, and lipid production of three

native diatoms to Southwest Texas desert. *Journal of Applied Phycology*, *27*, 1433–1442. https://doi.org/10.1007/s10811-014-0463-7

Johnston, M. R., Gascooke, J. R., Ellis, A. V., & Leterme, S. C. (2018). Diatoms response to salinity changes: investigations using single pulse and cross polarisation magic angle spinning ^{29}Si NMR spectra. *The Analyst*, *143*, 4930–4935. https://doi.org/10.1039/c8an00948a

Kalam, S., Abu-Khamsin, S. A., Kamal, M. S., & Patil, S. (2021). Surfactant Adsorption Isotherms: A Review. *ACS Omega*, *6*, 32342–32348. https://doi.org/10.1021/acsomega.1c04661

Kamińska, A., Sprynskyy, M., Winkler, K., & Szymborski, T. (2017). Ultrasensitive SERS immunoassay based on diatom biosilica for detection of interleukins in blood plasma. *Analytical and Bioanalytical Chemistry*, *409*, 6337–6347. https://doi.org/10.1007/s00216-017-0566-5

Karaman, E. S., Wang, Z., Di Benedetto, G., Zunino III, J. L., Meng, X., & Mitra, S. (2019). Fabrication of supercapacitors and flexible electrodes using biosilica from cultured diatoms. *Materials Today Energy*, *11*, 166–173. https://doi.org/10.1016/j.mtener.2018.11.004

Karmakar, B., De, G., & Ganguli, D. (2000). Dense silica microspheres from organic and inorganic acid hydrolysis of TEOS. *Journal of Non-crystalline Solids*, *272*, 119–126. https://doi.org/10.1016/S0022-3093(00)00231-3

Katheresan, V., Kansedo, J., & Lau, S. Y. (2018). Efficiency of various recent wastewater dye removal methods: A review. *Journal of Environmental Chemical Engineering*, *6*, 4676–4697. https://doi.org/10.1016/j.jece.2018.06.060

Khan, M. J., Rai, A., Ahirwar, A., Sirotiya, V., Mourya, M., Mishra, S., Schoefs, B., Marchand, J., Bhatia, S. K., Varjani, S., & Vinayak, V. (2021). Diatom microalgae as smart nanocontainers for biosensing wastewater pollutants: recent trends and innovations. *Bioengineered*, *12*, 9531–9549. https://doi.org/10.1080/21655979.2021.1996748

Kiraz, N., Kesmez, Ö., Burunkaya, E., Budama, L., Acar, B., Asiltürk, M., Camurlu, H.E., & Arpaç, E. (2010). Antibacterial glass films prepared on metal surfaces by sol–gel method. *Journal of Sol-Gel Science and Technology*, *56*, 227–235. https://doi.org/10.1007/s10971-010-2298-2

Kirchman, D. L. (2002). Calculating microbial growth rates from data on production and standing stocks. *Marine Ecology Progress Series*, *233*, 303–306. https://doi.org/10.3354/meps233303

Kolbe, F., & Brunner, E. (2022). Silicic Acid Uptake and Storage by Diatoms. In A. Falciatore & T. Mock (Eds), *The Molecular Life of Diatoms* (pp. 345–365). Springer. https://doi.org/10.1007/978-3-030-92499-7_13

Kong, X., Squire, K., Li, E., LeDuff, P., Rorrer, G. L., Tang, S., Chen, B., McKay, C. P., Navarro-Gonzalez, R., & Wang, A. X. (2016). Chemical and Biological Sensing Using Diatom Photonic Crystal Biosilica With In-Situ Growth Plasmonic Nanoparticles. *IEEE Transactions on Nanobioscience*, *15*, 828–834. https://doi.org/10.1109/TNB.2016.2636869

Kraai, J. A., Rorrer, G. L., & Wang, A. X. (2019). Highly-porous diatom biosilica stationary phase for thin-layer chromatography. *Journal of Chromatography A*, *1591*, 162–170. https://doi.org/10.1016/j.chroma.2019.01.037

Kraai, J. A., Wang, A. X., & Rorrer, G. L. (2020). Photonic crystal enhanced sers detection of analytes separated by ultrathin layer chromatography using a diatom frustule monolayer. *Advanced Materials Interfaces*, *7*, 2000191. https://doi.org/10.1002/admi.202000191

Kröger, N., Lorenz, S., Brunner, E., & Sumper, M. (2002). Self-assembly of highly phosphorylated silaffins and their function in biosilica morphogenesis. *Science*, *298*, 584–586. https://doi.org/10.1126/science.1076221

Kröger, N., & Poulsen, N. (2008). Diatoms-from cell wall biogenesis to nanotechnology. *Annual Review of Genetics*, *42*, 83–107. https://doi.org/10.1146/annurev.genet.41.110306.130109

Kucki, M., & Fuhrmann-Lieker, T. (2012). Staining diatoms with rhodamine dyes: control of emission colour in photonic biocomposites. *Journal of the Royal Society, Interface*, *9*, 727–733. https://doi.org/10.1098/rsif.2011.0424

Kumar, S., Rechav, K., Kaplan-Ashiri, I., & Gal, A. (2020). Imaging and quantifying homeostatic levels of intracellular silicon in diatoms. *Science Advances*, *6*, eaaz7554. https://doi.org/10.1126/sciadv.aaz7554

Kumari, S., Min, K. H., Kanth, B. K., Jang, E. K., & Pack, S. P. (2020). Production of TiO 2-deposited diatoms and their applications for photo-catalytic degradation of aqueous pollutants. *Biotechnology and Bioprocess Engineering*, *25*, 758–765. https://doi.org/10.1007/s12257-020-0019-4

Lagergren, S. (1898). Zur theorie der sogenannten adsorption geloster stoffe. *Kungliga Svenska Vetenskapsakademiens. Handlingar*, *24*, 1–39.

Lang, Y., del Monte, F., Rodriguez, B. J., Dockery, P., Finn, D. P., & Pandit, A. (2013). Integration of TiO2 into the diatom *Thalassiosira weissflogii* during frustule synthesis. *Scientific Reports*, *3*, 3205. https://doi.org/10.1038/srep03205

Langmuir, I. (1918). The adsorption of gases on plane surfaces of glass, mica and platinum. *Journal of the American Chemical society*, *40*, 1361–1403. https://doi.org/10.1021/ja02242a004

Lebeau, T., & Robert, J. M. (2003). Diatom cultivation and biotechnologically relevant products. Part II: current and putative products. *Applied Microbiology and Biotechnology*, *60*, 624–632. https://doi.org/10.1007/s00253-002-1177-3

Lee, R. E. (2018). *Phycology*. Cambridge University Press

Leone, G., Vona, D., Presti, M. L., Urbano, L., Cicco, S., Gristina, R., Palumbo, F., Ragni, R., & Farinola, G. M. (2017). Ca^{2+}-*in vivo* doped biosilica from living *Thalassiosira weissflogii* diatoms: Investigation on Saos-2 biocompatibility. *Mrs Advances*, *2*, 1047–1058. https://doi.org/10.1557/adv.2017.49

Lettieri, S., Setaro, A., De Stefano, L., De Stefano, M., & Maddalena, P. (2008). The gas-detection properties of light-emitting diatoms. *Advanced Functional Materials*, *18*, 1257–1264. https://doi.org/10.1002/adfm.200701124

Lewin J. C. (1953). Heterotrophy in diatoms. *Journal of General Microbiology*, *9*, 305–313. https://doi.org/10.1099/00221287-9-2-305

Lewin, J. (1966). Silicon metabolism in diatoms. V. Germanium dioxide, a specific inhibitor of diatom growth. *Phycologia*, *6*, 1-12. https://doi.org/10.2216/i0031-8884-6-1-1.1

Li, H. Y., Lu, Y., Zheng, J. W., Yang, W. D., & Liu, J. S. (2014). Biochemical and genetic engineering of diatoms for polyunsaturated fatty acid biosynthesis. *Marine Drugs*, *12*, 153–166. https://doi.org/10.3390/md12010153

Li, J., Han, J., Sun, Q., Wang, Y., Mu, Y., Zhang, K., Dou, X., Kong, M., Chen, X., & Feng, C. (2018). Biosynthetic calcium-doped biosilica with multiple hemostatic properties for hemorrhage control. *Journal of Materials Chemistry B*, *6*, 7834–7841. https://doi.org/10.1039/c8tb00667a

Li, K. M., Jiang, J. G., Tian, S. C., Chen, X. J., & Yan, F. (2014). Influence of silica types on synthesis and performance of amine–silica hybrid materials used for CO_2 capture. *The Journal of Physical Chemistry C*, *118*, 2454–2462. https://doi.org/10.1021/jp408354r

Li, R., Chen, G. Z., Tam, N. F., Luan, T. G., Shin, P. K., Cheung, S. G., & Liu, Y. (2009). Toxicity of bisphenol A and its bioaccumulation and removal by a marine microalga

Stephanodiscus hantzschii. Ecotoxicology and Environmental Safety, *72*, 321–328. https://doi.org/10.1016/j.ecoenv.2008.05.012

Liao, Q., Sun, J., & Gao, L. (2008). The adsorption of resorcinol from water using multi-walled carbon nanotubes. *Colloids and Surfaces A*, *312*, 160–165. https://doi.org/10.1016/j.colsurfa.2007.06.045

Lin, Z., Li, J., Luan, Y., & Dai, W. (2020). Application of algae for heavy metal adsorption: A 20-year meta-analysis. *Ecotoxicology and Environmental Safety*, *190*, 110089. https://doi.org/10.1016/j.ecoenv.2019.110089

Liu, Y., Guan, Y., Gao, Q., Tam, N. F., & Zhu, W. (2010). Cellular responses, biodegradation and bioaccumulation of endocrine disrupting chemicals in marine diatom *Navicula incerta*. *Chemosphere*, *80*, 592–599. https://doi.org/10.1016/j.chemosphere.2010.03.042

Losic, D., Yu, Y., Aw, M. S., Simovic, S., Thierry, B., & Addai-Mensah, J. (2010). Surface functionalisation of diatoms with dopamine modified iron-oxide nanoparticles: toward magnetically guided drug microcarriers with biologically derived morphologies. *Chemical Communications*, *46*, 6323–6325. https://doi.org/10.1039/c0cc01305f

Lu, Z., Maroto-Valer, M. M., & Schobert, H. H. (2010). Catalytic effects of inorganic compounds on the development of surface areas of fly ash carbon during steam activation. *Fuel*, *89*, 3436–3441. https://doi.org/10.1016/j.fuel.2010.05.024

Luo, J., Liu, P., Peng, G., & Tao Zhang, J. (2023). Basic Characterization and Sputtering Processing of Diatom-Based Anode Materials. *ChemistrySelect*, *8*, e202204313. https://doi.org/10.1002/slct.202204313

Machill, S., Köhler, L., Ueberlein, S., Hedrich, R., Kunaschk, M., Paasch, S., Schulze, R., & Brunner, E. (2013). Analytical studies on the incorporation of aluminium in the cell walls of the marine diatom *Stephanopyxis turris*. *BioMetals*, *26*, 141–150. https://doi.org/10.1007/s10534-012-9601-3

Maeda, Y., Niwa, Y., Tang, H., Kisailus, D., Yoshino, T., & Tanaka, T. (2018). Development of Titania-Integrated Silica Cell Walls of the Titanium-Resistant Diatom, *Fistulifera solaris*. *ACS Applied Bio Materials*, *1*, 2021–2029. https://doi.org/10.1021/acsabm.8b00520

Marella, T.K., Saxena, A., & Tiwari, A. (2020). Diatom mediated heavy metal remediation: A review. *Bioresource Technology*, *305*, 123068. https://doi.org/10.1016/j.biortech.2020.123068

Martin-Jézéquel, V., Hildebrand, M., & Brzezinski, M. A. (2000). Silicon metabolism in diatoms: implications for growth. *Journal of Phycology*, *36*, 821–840. https://doi.org/10.1046/j.1529-8817.2000.00019.x

Martín, L. A., Popovich, C. A., Martinez, A. M., Damiani, M. C., & Leonardi, P. I. (2016). Oil assessment of *Halamphora coffeaeformis* diatom growing in a hybrid two-stage system for biodiesel production. *Renewable Energy*, *92*, 127–135. https://doi.org/10.1016/j.renene.2016.01.078

Martín, L. A., Popovich, C. A., Martínez, A. M., Bilbao, P. G. S., Damiani, M. C., & Leonardi, P. I. (2018). Hybrid two-stage culture of *Halamphora coffeaeformis* for biodiesel production: Growth phases, nutritional stages and biorefinery approach. *Renewable Energy*, *118*, 984–992. https://doi.org/10.1016/j.renene.2017.10.086

Milligan, A. J., & Morel, F. M. (2002). A proton buffering role for silica in diatoms. *Science*, *297*, 1848–1850. https://doi.org/10.1126/science.1074958

Milović, M., Simović, S., Lošić, D., Dashevskiy, A., & Ibrić, S. (2014). Solid self-emulsifying phospholipid suspension (SSEPS) with diatom as a drug carrier. *European Journal of Pharmaceutical Dciences*, *63*, 226–232. https://doi.org/10.1016/j.ejps.2014.07.010

Musić, S., Filipović-Vinceković, N., & Sekovanić, L. (2011). Precipitation of amorphous SiO_2 particles and their properties. *Brazilian Journal of Chemical Engineering*, *28*, 89–94. https://doi.org/10.1590/S0104-66322011000100011

Navarro, F. E., Damiani, M. C., Leonardi, P. I., & Popovich, C. A. (2022). Temperature and Salinity Effect on Tolerance and Lipid Accumulation in *Halamphora coffeaeformis*: an Approach for Outdoor Bioenergy Cultures. *BioEnergy Research*, 1–10. https://doi.org/10.1007/s12155-021-10349-2

Norberg, A. N., Wagner, N. P., Kaland, H., Vullum-Bruer, F., & Svensson, A. M. (2019). Silica from diatom frustules as anode material for Li-ion batteries. *RSC Advances*, *9*, 41228–41239. https://doi.org/10.1039/c9ra07271c

Nowak, A. P., Sprynskyy, M., Brzozowska, W., & Lisowska-Oleksiak, A. (2019). Electrochemical behavior of a composite material containing 3D-structured diatom biosilica. *Algal Research*, *41*, 101538. https://doi.org/10.1016/j.algal.2019.101538

O'Neill, C., Hawkes, F. R., Hawkes, D. L., Lourenço, N. D., Pinheiro, H. M., & Delée, W. (1999). Colour in textile effluents–sources, measurement, discharge consents and simulation: a review. *Journal of Chemical Technology & Biotechnology*, *74*, 1009–1018. https://doi.org/10.1002/(SICI)1097-4660(199911)74:11<1009::AID-JCTB153>3.0.CO;2-N

Otzen D. (2012). The role of proteins in biosilicification. *Scientifica*, *2012*, 867562. https://doi.org/10.6064/2012/867562

Pandit, P., Rananaware, P., D'Souza, A., Kurkuri, M. D., & Brahmkhatri, V. (2022). Functionalized diatom biosilica decorated with nanoparticles: synthesis, characterization, catalytic oxidation, and dye scavenging applications. *Journal of Porous Materials*, *29*, 1369–1383. https://doi.org/10.1007/s10934-022-01262-w

Peng, J., Yuan, J. P., Wu, C. F., & Wang, J. H. (2011). Fucoxanthin, a marine carotenoid present in brown seaweeds and diatoms: metabolism and bioactivities relevant to human health. *Marine Drugs*, *9*, 1806–1828. https://doi.org/10.3390/md9101806

Petersen, J., Teich, R., Brinkmann, H., & Cerff, R. (2006). A "green" phosphoribulokinase in complex algae with red plastids: evidence for a single secondary endosymbiosis leading to Haptophytes, Cryptophytes, Heterokonts, and Dinoflagellates. *Journal of Molecular Evolution*, *62*, 143–157. https://doi.org/10.1007/s00239-004-0305-3

Poulsen, N., Scheffel, A., Sheppard, V. C., Chesley, P. M., & Kröger, N. (2013). Pentalysine clusters mediate silica targeting of silaffins in *Thalassiosira pseudonana*. *The Journal of biological chemistry*, *288*, 20100–20109. https://doi.org/10.1074/jbc.M113.469379

Pryshchepa, O., Pomastowski, P., & Buszewski, B. (2020). Silver nanoparticles: Synthesis, investigation techniques, and properties. *Advances in Colloid and Interface Science*, *284*, 102246. https://doi.org/10.1016/j.cis.2020.102246

Qin, T., Gutu, T., Jiao, J., Chang, C. H., & Rorrer, G. L. (2008a). Biological fabrication of photoluminescent nanocomb structures by metabolic incorporation of germanium into the biosilica of the diatom *Nitzschia frustulum*. *ACS Nano*, *2*, 1296–1304. https://doi.org/10.1021/nn800114q

Qin, T., Gutu, T., Jiao, J., Chang, C. H., & Rorrer, G. L. (2008b). Photoluminescence of silica nanostructures from bioreactor culture of marine diatom *Nitzschia frustulum*. *Journal of Nanoscience and Nanotechnology*, *8*, 2392–2398. https://doi.org/10.1166/jnn.2008.241

Rabsch, U., & Elbrächter, M. (1980). Cadmium and zinc uptake, growth, and primary production in *Coscinodiscus granii* cultures containing low levels of cells and dissolved organic carbon. *Helgoländer Meeresuntersuchungen*, *33*, 79–88. https://doi.org/10.1007/BF02414737

Rafatullah, M., Sulaiman, O., Hashim, R., & Ahmad, A. (2010). Adsorption of methylene blue on low-cost adsorbents: a review. *Journal of Hazardous Materials*, *177*, 70–80. https://doi.org/10.1016/j.jhazmat.2009.12.047

Raven, J. A. (1983). The transport and function of silicon in plants. *Biological Reviews*, *58*, 179–207. https://doi.org/10.1111/j.1469-185X.1983.tb00385.x

Redan, B. W., Jablonski, J. E., Halverson, C., Jaganathan, J., Mabud, M. A., & Jackson, L. S. (2019). Factors Affecting Transfer of the Heavy Metals Arsenic, Lead, and Cadmium from Diatomaceous-Earth Filter Aids to Alcoholic Beverages during Laboratory-Scale Filtration. *Journal of Agricultural and Food Chemistry*, *67*, 2670–2678. https://doi.org/10.1021/acs.jafc.8b06062

Reid, A., Buchanan, F., Julius, M., & Walsh, P. J. (2021). A review on diatom biosilicification and their adaptive ability to uptake other metals into their frustules for potential application in bone repair. *Journal of Materials Chemistry. B*, *9*, 6728–6737. https://doi.org/10.1039/d1tb00322d

Roche H. M. (1999). Unsaturated fatty acids. *The Proceedings of the Nutrition Society*, *58*, 397–401. https://doi.org/10.1017/s002966519900052x

Rogato, A., & De Tommasi, E. (2020). Physical, chemical, and genetic techniques for diatom frustule modification: applications in nanotechnology. *Applied Sciences*, *10*, 8738. https://doi.org/10.3390/app10238738

Rorrer, G. L., Chang, C. H., Liu, S. H., Jeffryes, C., Jiao, J., & Hedberg, J. A. (2005). Biosynthesis of silicon-germanium oxide nanocomposites by the marine diatom *Nitzschia frustulum*. *Journal of nanoscience and nanotechnology*, *5*, 41–49. https://doi.org/10.1166/jnn.2005.005

Rorrer, G. L. (2017). Functionalization of frustules from diatom cell culture for optoelectronic properties. In D. Losic (Ed), *Diatom Nanotechnology: Progress and Emerging Applications* (pp. 79–110). The Royal Society of Chemistry. https://doi.org/10.1039/9781788010160-00079

Round, F. E., Crawford, R. M., & Mann, D. G. (1990). *Diatoms: biology and morphology of the genera*. Cambridge University Press.

Roychoudhury, P., Nandi, C., & Pal, R. (2016). Diatom-based biosynthesis of gold-silica nanocomposite and their DNA binding affinity. *Journal of Applied Phycology*, *28*, 2857–2863. https://doi.org/10.1007/s10811-016-0809-4

Roychoudhury, P., Golubeva, A., Dąbek, P., Gloc, M., Dobrucka, R., Kurzydłowski, K., & Witkowski, A. (2021). Diatom Mediated Production of Fluorescent Flower Shaped Silver-Silica Nanohybrid. *Materials*, *14*, 7284. https://doi.org/10.3390/ma14237284

Roychoudhury, P., Bose, R., Dąbek, P., & Witkowski, A. (2022a). Photonic Nano-/Microstructured Diatom Based Biosilica in Metal Modification and Removal-A Review. *Materials*, *15*, 6597. https://doi.org/10.3390/ma15196597

Roychoudhury, P., Golubeva, A., Dąbek, P., Pryshchepa, O., Sagandykova, G., Pomastowski, P., Gloc, M., Dobrucka, R., Kurzydłowski, K., Buszewski, B., & Witkowski, A. (2022b). Study on Biogenic Spindle-Shaped Iron-Oxide Nanoparticles by *Pseudostaurosira trainorii* in Field of Laser Desorption/Ionization Applications. *International Journal of Molecular Sciences*, *23*, 11713. https://doi.org/10.3390/ijms231911713

Sahin, M. S., Khazi, M. I., Demirel, Z., & Dalay, M. C. (2019). Variation in growth, fucoxanthin, fatty acids profile and lipid content of marine diatoms *Nitzschia* sp. and *Nanofrustulum shiloi* in response to nitrogen and iron. *Biocatalysis and Agricultural Biotechnology*, *17*, 390–398. https://doi.org/10.1016/j.bcab.2018.12.023

Samsami, S., Mohamadizaniani, M., Sarrafzadeh, M. H., Rene, E. R., & Firoozbahr, M. (2020). Recent advances in the treatment of dye-containing wastewater from textile industries: Overview and perspectives. *Process Safety and Environmental Protection*, *143*, 138–163. https://doi.org/10.1016/j.psep.2020.05.034

Saoud, H. A. A., Sprynskyy, M., Pashaei, R., Kawalec, M., Pomastowski, P., & Buszewski, B. (2022). Diatom biosilica: Source, physical-chemical characterization, modification, and application. *Journal of Separation Science*, *45*, 3362–3376. https://doi.org/10.1002/jssc.202100981

Sarkar, A. K., Pal, A., Ghorai, S., Mandre, N. R., & Pal, S. (2014). Efficient removal of malachite green dye using biodegradable graft copolymer derived from amylopectin and poly(acrylic acid). *Carbohydrate Polymers*, *111*, 108–115. https://doi.org/10.1016/j.carbpol.2014.04.042

Sasirekha, R., Sheena, T. S., Sathiya Deepika, M., Santhanam, P., Townley, H. E., Jeganathan, K., Dinesh Kumar, S., & Premkumar, K. (2019). Surface engineered *Amphora subtropica* frustules using chitosan as a drug delivery platform for anticancer therapy. *Materials Science & Engineering. C, 94*, 56–64. https://doi.org/10.1016/j.msec.2018.09.009

Sbihi, K., Cherifi, O., El Gharmali, A., Oudra, B., & Aziz, F. (2012). Accumulation and toxicological effects of cadmium, copper and zinc on the growth and photosynthesis of the freshwater diatom *Planothidium lanceolatum* (Brébisson) Lange-Bertalot: a laboratory study. *Journal of Materials and Environmental Science*, *3*, 497–506.

Schmid, A. M. M., & Schulz, D. (1979). Wall morphogenesis in diatoms: deposition of silica by cytoplasmic vesicles. *Protoplasma*, *100*, 267–288. https://doi.org/10.1007/BF01279316

Scodelaro Bilbao, P. G., Martín, L. A., Popovich, C. A., Almeyda, M. D., Chamorro, V., & Leonardi, P. I. (2020). Assessment of *Halamphora coffeaeformis* growth and biochemical composition for aquaculture purposes. *Journal of Marine Science and Engineering*, *8*, 282. https://doi.org/10.3390/jmse8040282

Selvaraj, V., Muthukumar, A., Nagamony, P., & Chinnuswamy, V. (2018). Detection of typhoid fever by diatom-based optical biosensor. *Environmental Science and Pollution Research International*, *25*, 20385–20390. https://doi.org/10.1007/s11356-017-9362-1

Sharma, J., Sharma, S., & Soni, V. (2021). Classification and impact of synthetic textile dyes on Aquatic Flora: A review. *Regional Studies in Marine Science*, *45*, 101802. https://doi.org/10.1016/j.rsma.2021.101802

Sibbald, S. J., & Archibald, J. M. (2020). Genomic Insights into Plastid Evolution. *Genome Biology and Evolution*, *12*, 978–990. https://doi.org/10.1093/gbe/evaa096

Sips, R. (1948). On the structure of a catalyst surface. *The Journal of Chemical Physics*, *16*, 490–495. https://doi.org/10.1063/1.1746922

Skolem, L.M.B. (2011). *Biosynthesis and Characterization of Ti- Doped Silica-Based Nanostructures Formed by the Diatoms Pinnularia sp. and Coscinodiscus wailesii* [Master thesis, Norwegian University of Science and Technology] Norwegian University of Science and Technology Repository. http://hdl.handle.net/11250/245760

Smetacek V. (1999). Diatoms and the ocean carbon cycle. *Protist*, *150*, 25–32. https://doi.org/10.1016/S1434-4610(99)70006-4

Sodhi, K. K., Mishra, L. C., Singh, C. K., & Kumar, M. (2022). Perspective on the heavy metal pollution and recent remediation strategies. *Current Research in Microbial Sciences*, *3*, 100166. https://doi.org/10.1016/j.crmicr.2022.100166

Sprynskyy, M., Pomastowski, P., Hornowska, M., Król, A., Rafińska, K., & Buszewski, B. (2017). Naturally organic functionalized 3D biosilica from diatom microalgae. *Materials & Design*, *132*, 22–29. https://doi.org/10.1016/j.matdes.2017.06.044

Sprynskyy, M., Szczyglewska, P., Wojtczak, I., Nowak, I., Witkowski, A., Buszewski, B., & Feliczak-Guzik, A. (2021). Diatom Biosilica Doped with Palladium(II) Chloride Nanoparticles as New Efficient Photocatalysts for Methyl Orange Degradation. *International Journal of Molecular Sciences*, *22*, 6734. https://doi.org/10.3390/ijms22136734

Squire, K., Kong, X., LeDuff, P., Rorrer, G. L., & Wang, A. X. (2018). Photonic crystal enhanced fluorescence immunoassay on diatom biosilica. *Journal of Biophotonics*, *11*, e201800009. https://doi.org/10.1002/jbio.201800009

Squire, K. J., Zhao, Y., Tan, A., Sivashanmugan, K., Kraai, J. A., Rorrer, G. L., & Wang, A. X. (2019). Photonic Crystal-Enhanced Fluorescence Imaging Immunoassay for Cardiovascular Disease Biomarker Screening with Machine Learning Analysis. *Sensors and Actuators. B*, *290*, 118–124. https://doi.org/10.1016/j.snb.2019.03.102

Stepanek, J. G., Fields, F. J., & Kociolek, J. P. (2016). A comparison of lipid content metrics using six species from the genus *Halamphora* (Bacillariophyta). *Biofuels*, *7*, 521–528. https://doi.org/10.1080/17597269.2016.1163216

Stiller, J. W., Schreiber, J., Yue, J., Guo, H., Ding, Q., & Huang, J. (2014). The evolution of photosynthesis in chromist algae through serial endosymbioses. *Nature Communications, 5*, 5764. https://doi.org/10.1038/ncomms6764

Sumper M. (2004). Biomimetic patterning of silica by long-chain polyamines. *Angewandte Chemie*, *43*, 2251–2254. https://doi.org/10.1002/anie.200453804

Terracciano, M., De Stefano, L., & Rea, I. (2018). Diatoms Green Nanotechnology for Biosilica-Based Drug Delivery Systems. *Pharmaceutics*, *10*, 242. https://doi.org/10.3390/pharmaceutics10040242

Tesson, B., & Hildebrand, M. (2010). Extensive and intimate association of the cytoskeleton with forming silica in diatoms: control over patterning on the meso- and micro-scale. *PloS One*, *5*, e14300. https://doi.org/10.1371/journal.pone.0014300

Thakkar, M., Randhawa, V., Mitra, S., & Wei, L. (2015). Synthesis of diatom-FeOx composite for removing trace arsenic to meet drinking water standards. *Journal of Colloid and Interface Science*, *457*, 169–173. https://doi.org/10.1016/j.jcis.2015.07.003

Thommes, M., Kaneko, K., Neimark, A. V., Olivier, J. P., Rodriguez-Reinoso, F., Rouquerol, J., & Sing, K. S. (2015). Physisorption of gases, with special reference to the evaluation of surface area and pore size distribution (IUPAC Technical Report). *Pure and Applied chemistry*, *87*, 1051–1069. https://doi.org/10.1515/pac-2014-1117

Townley, H. E., Woon, K. L., Payne, F. P., White-Cooper, H., & Parker, A. R. (2007). Modification of the physical and optical properties of the frustule of the diatom *Coscinodiscus wailesii* by nickel sulfate. *Nanotechnology*, *18*, 295101. https://doi.org/10.1088/0957-4484/18/29/295101

Tramontano, C., Chianese, G., Terracciano, M., de Stefano, L., & Rea, I. (2020). Nanostructured biosilica of diatoms: From water world to biomedical applications. *Applied Sciences*, *10*, 6811. https://doi.org/10.3390/app10196811

Van Eynde, E., Lenaerts, B., Tytgat, T., Verbruggen, S. W., Hauchecorne, B., Blust, R., & Lenaerts, S. (2014). Effect of pretreatment and temperature on the properties of *Pinnularia* biosilica frustules. *Rsc Advances*, *4*, 56200–56206. https://doi.org/10.1039/C4RA09305D

Van Eynde, E., Hu, Z. Y., Tytgat, T., Verbruggen, S. W., Watté, J., Van Tendeloo, G., Van Driessche, I., Blust, R., & Lenaerts, S. (2016). Diatom silica–titania photocatalysts for air purification by bio-accumulation of different titanium sources. *Environmental Science: Nano*, *3*, 1052–1061. https://doi.org/10.1039/C6EN00163G

Vasani, R. B., Losic, D., Cavallaro, A., & Voelcker, N. H. (2015). Fabrication of stimulus-responsive diatom biosilica microcapsules for antibiotic drug delivery. *Journal of Materials Chemistry. B*, *3*, 4325–4329. https://doi.org/10.1039/c5tb00648a

Wang, Y., Cai, J., Jiang, Y., Jiang, X., & Zhang, D. (2013). Preparation of biosilica structures from frustules of diatoms and their applications: current state and perspectives. *Applied Microbiology and Biotechnology*, *97*, 453–460. https://doi.org/10.1007/s00253-012-4568-0

Wang, Z., Zhao, J., Liu, S., Cui, F., Luo, J., Wang, Y., Zhang, S., Zhang, C., & Yang, X. (2021). Cultured diatoms suitable for the advanced anode of lithium ion batteries. *ACS Sustainable Chemistry & Engineering*, *9*, 844–852. https://doi.org/10.1021/acssuschemeng.0c07484

Weber W. J., & Morris, J. C. (1963). Kinetics of adsorption on carbon from solution. *Journal of the Sanitary Engineering Division*, *89*, 31–59.

Werner, D. (1967). Hemmung der Chlorophyllsynthese und der NADP$^+$-abhängigen Glycerinaldehyd-3-Phosphat-Dehydrogenase durch Germaniumsäure bei *Cyclotella cryptica*. *Archives of Microbiology*, *57*, 51–60.

Wisser, D., Brückner, S. I., Wisser, F. M., Althoff-Ospelt, G., Getzschmann, J., Kaskel, S., & Brunner, E. (2015). (1)H-(13)C-(29)Si triple resonance and REDOR solid-state NMR-A tool to study interactions between biosilica and organic molecules in diatom cell walls. *Solid State Nuclear Magnetic Resonance*, *66*, 33–39. https://doi.org/10.1016/j.ssnmr.2014.12.007

Xu, P., Wang, H., Tong, R., Du, Q., & Zhong, W. (2006). Preparation and morphology of SiO 2/PMMA nanohybrids by microemulsion polymerization. *Colloid and Polymer Science*, *284*, 755–762. https://doi.org/10.1007/s00396-005-1428-9

Yang, S., Wu, R. S., & Kong, R. Y. (2002). Biodegradation and enzymatic responses in the marine diatom *Skeletonema costatum* upon exposure to 2,4-dichlorophenol. *Aquatic Toxicology*, *59*, 191–200. https://doi.org/10.1016/s0166-445x(01)00252-1

Yew, Y. P., Shameli, K., Miyake, M., Kuwano, N., Bt Ahmad Khairudin, N. B., Bt Mohamad, S. E., & Lee, K. X. (2016). Green Synthesis of Magnetite (Fe_3O_4) Nanoparticles Using Seaweed (*Kappaphycus alvarezii*) Extract. *Nanoscale Research Letters*, *11*, 276. https://doi.org/10.1186/s11671-016-1498-2

Yu, Y., Addai-Mensah, J., & Losic, D. (2012). Functionalized diatom silica microparticles for removal of mercury ions. *Science and Technology of Advanced Materials*, *13*, 015008. https://doi.org/10.1088/1468-6996/13/1/015008

Zhang, C., Wang, X., Ma, Z., Luan, Z., Wang, Y., Wang, Z., & Wang, L. (2020). Removal of phenolic substances from wastewater by algae. A review. *Environmental Chemistry Letters*, *18*, 377–392. https://doi.org/10.1007/s10311-019-00953-2

Zhang, G., Jiang, W., Wang, L., Liao, X., Liu, P., Deng, X., & Li, J. (2013). Preparation of silicate-based red phosphors with a patterned nanostructure via metabolic insertion of europium in marine diatoms. *Materials Letters*, *110*, 253–255. https://doi.org/10.1016/j.matlet.2013.08.045

Zhang, X., Wu, Y., He, S., & Yang, D. (2007). Structural characterization of sol–gel composites using TEOS/MEMO as precursors. *Surface and Coatings Technology*, *201*, 6051–6058. https://doi.org/10.1016/j.surfcoat.2006.11.012

Zhou, H., Fan, T., Li, X., Ding, J., Zhang, D., Li, X., & Gao, Y. (2009), Bio-Inspired Bottom-Up Assembly of Diatom-Templated Ordered Porous Metal Chalcogenide Meso/Nanostructures. *European Journal of Inorganic Chemistry, 2009*, 211–215. https://doi.org/10.1002/ejic.200800764

Zobi, F. (2022). Diatom Biosilica in Targeted Drug Delivery and Biosensing Applications: Recent Studies. *Micro*, *2*, 342–360. https://doi.org/10.3390/micro2020023

SUPPLEMENTARY MATERIAL

Table S1. Preliminary screening of diatom cultures from Szczecin Diatom Culture Collection with growth parameters and place of sampling.

Strain	Growth rate, d^{-1} (R^2)	Time of maximum growth, d	Maximum biomass DW, g L^{-1}	Biomass productivity DW, mg L^{-1} d^{-1}	Origin of the strain
NCC340 *Phaeodactylum tricornutum*	0.347 (0.99)	14	1.15	82.1	Nantes Culture Collection, France
SZCZM1454 *Halamphora* cf. *salinicola*	0.081 (0.97)	23	0.72	31.3	Hot spring in Köyceğiz Lake,Turkey
SZCZP1809 *Nanofrustulum* cf. *shiloi*	0.513 (0.99)	16	0.63	39.4	Sea Point, Cape Town, South Africa
SZCZCH1268 *Gedaniella flavovirens*	0.380 (0.82)	16	0.58	36.2	Resko Lake, Poland
SZCZP1020 *Nitzschia* cf. *laevis*	0.351 (0.97)	14	0.56	40.0	Tsaarbank, Langebaan, South Africa
SZCZM1342 *N. shiloi*	0.270 (0.97)	18	0.47	26.1	Mediterranean Sea coast, Turkey
BA170 *Pseudostaurosira trainorii*	0.08 (0.92)	16	0.39	24.4	Gulf of Gdańsk, Baltic Sea, Poland
SZCZCH193 *N. wachnickianum*	0.115 (0.95)	18	0.39	21.7	Marquesas, Florida, USA
SZCZP599 *Biremis panamae*	0.12 (0.97)	14	0.38	27.1	Playa Monagre, Panama, Pacific Ocean
SZCZCH153 *G. mutabilis*	0.144 (0.99)	14	0.24	17.1	Gdańsk, Orle, Baltic Sea

Table S2. One-way ANOVA results for different growth parameters

Phosphate

SZCZCH193 *N. wachnickianum*

One-way ANOVA of your $k=5$ independent treatments:

source	sum of squares SS	degrees of freedom ν	mean square MS	F statistic	p-value
treatment	0.0448	4	0.0112	1.9727	0.2371
error	0.0284	5	0.0057		
total	0.0732	9			

SZCZM1342 *N. shiloi*

One-way ANOVA of your $k=5$ independent treatments:

source	sum of squares SS	degrees of freedom ν	mean square MS	F statistic	p-value
treatment	0.0158	4	0.0040	3.1187	0.1219
error	0.0063	5	0.0013		
total	0.0221	9			

SZCZP1809 *N.*cf. *shiloi*

One-way ANOVA of your $k=5$ independent treatments:

source	sum of squares SS	degrees of freedom ν	mean square MS	F statistic	p-value
treatment	0.0087	4	0.0022	0.7939	0.5765
error	0.0137	5	0.0027		
total	0.0225	9			

SZCZM1454 *H.* cf. *salinicola*

One-way ANOVA of your $k=5$ independent treatments:

source	sum of squares SS	degrees of freedom ν	mean square MS	F statistic	p-value
treatment	0.0155	4	0.0039	2.0622	0.2237
error	0.0094	5	0.0019		
total	0.0249	9			

BA170 *P. trainorii*

One-way ANOVA of your $k=5$ independent treatments:

source	sum of squares SS	degrees of freedom ν	mean square MS	F statistic	p-value
treatment	0.0474	4	0.0118	1.0105	0.4815
error	0.0586	5	0.0117		
total	0.1060	9			

Nitrate

SZCZCH193 *N. wachnickianum*

One-way ANOVA of your $k=5$ independent treatments:

source	sum of squares SS	degrees of freedom ν	mean square MS	F statistic	p-value
treatment	0.0053	4	0.0013	1.0313	0.4734
error	0.0064	5	0.0013		
total	0.0118	9			

SZCZM1342 *N. shiloi*

One-way ANOVA of your $k=5$ independent treatments:

source	sum of squares SS	degrees of freedom ν	mean square MS	F statistic	p-value
treatment	0.0313	4	0.0078	2.4619	0.1749
error	0.0159	5	0.0032		
total	0.0472	9			

SZCZP1809 *N.*cf. *shiloi*

One-way ANOVA of your $k=5$ independent treatments:

source	sum of squares SS	degrees of freedom ν	mean square MS	F statistic	p-value
treatment	0.1796	4	0.0449	5.4570	0.0455
error	0.0411	5	0.0082		
total	0.2207	9			

SZCZM1454 *H.* cf. *salinicola*

One-way ANOVA of your $k=5$ independent treatments:

source	sum of squares SS	degrees of freedom ν	mean square MS	F statistic	p-value
treatment	0.0142	4	0.0036	1.4401	0.3442
error	0.0123	5	0.0025		
total	0.0265	9			

BA170 *P. trainorii*

One-way ANOVA of your $k=5$ independent treatments:

source	sum of squares SS	degrees of freedom ν	mean square MS	F statistic	p-value
treatment	0.0326	4	0.0081	0.4036	0.8000
error	0.1009	5	0.0202		
total	0.1335	9			

Silicate

SZCZCH193 *N. wachnickianum*

One-way ANOVA of your *k*=5 independent treatments:

source	sum of squares SS	degrees of freedom ν	mean square MS	F statistic	p-value
treatment	0.4106	4	0.1026	24.4685	0.0018
error	0.0210	5	0.0042		
total	0.4315	9			

SZCZM1342 *N. shiloi*

One-way ANOVA of your *k*=5 independent treatments:

source	sum of squares SS	degrees of freedom ν	mean square MS	F statistic	p-value
treatment	0.3438	4	0.0859	86.3609	8.4236e-05
error	0.0050	5	0.0010		
total	0.3488	9			

SZCZP1809 *N.*cf. *shiloi*

One-way ANOVA of your *k*=5 independent treatments:

source	sum of squares SS	degrees of freedom ν	mean square MS	F statistic	p-value
treatment	0.3192	4	0.0798	26.5493	0.0015
error	0.0150	5	0.0030		
total	0.3342	9			

SZCZM1454 *H.* cf. *salinicola*

One-way ANOVA of your *k*=5 independent treatments:

source	sum of squares SS	degrees of freedom ν	mean square MS	F statistic	p-value
treatment	0.2600	4	0.0650	64.6078	0.0002
error	0.0050	5	0.0010		
total	0.2650	9			

BA170 *P. trainorii*

One-way ANOVA of your *k*=5 independent treatments:

source	sum of squares SS	degrees of freedom ν	mean square MS	F statistic	p-value
treatment	0.3851	4	0.0963	28.5736	0.0012
error	0.0168	5	0.0034		
total	0.4020	9			

Salinity

SZCZCH193 *N. wachnickianum*

One-way ANOVA of your $k=4$ independent treatments:

source	sum of squares SS	degrees of freedom ν	mean square MS	F statistic	p-value
treatment	0.0463	3	0.0154	8.6592	0.0319
error	0.0071	4	0.0018		
total	0.0535	7			

SZCZM1342 *N. shiloi*

One-way ANOVA of your $k=4$ independent treatments:

source	sum of squares SS	degrees of freedom ν	mean square MS	F statistic	p-value
treatment	0.2088	3	0.0696	103.2903	0.0003
error	0.0027	4	0.0007		
total	0.2115	7			

SZCZP1809 *N.*cf. *shiloi*

One-way ANOVA of your $k=4$ independent treatments:

source	sum of squares SS	degrees of freedom ν	mean square MS	F statistic	p-value
treatment	0.3129	3	0.1043	39.2130	0.0020
error	0.0106	4	0.0027		
total	0.3236	7			

SZCZM1454 *H.* cf. *salinicola*

One-way ANOVA of your $k=4$ independent treatments:

source	sum of squares SS	degrees of freedom ν	mean square MS	F statistic	p-value
treatment	0.4793	3	0.1598	7.2168	0.0432
error	0.0885	4	0.0221		
total	0.5678	7			

BA170 *P. trainorii*

One-way ANOVA of your $k=4$ independent treatments:

source	sum of squares SS	degrees of freedom ν	mean square MS	F statistic	p-value
treatment	0.0740	3	0.0247	1.2136	0.4128
error	0.0813	4	0.0203		
total	0.1552	7			

Temperature

SZCZCH193 *N. wachnickianum*

One-way ANOVA of your $k=3$ independent treatments:

source	sum of squares SS	degrees of freedom ν	mean square MS	F statistic	p-value
treatment	0.3668	2	0.1834	15.6490	0.0259
error	0.0352	3	0.0117		
total	0.4020	5			

SZCZM1342 *N. shiloi*

One-way ANOVA of your $k=3$ independent treatments:

source	sum of squares SS	degrees of freedom ν	mean square MS	F statistic	p-value
treatment	0.0089	2	0.0045	4.3558	0.1296
error	0.0031	3	0.0010		
total	0.0120	5			

SZCZP1809 *N.*cf. *shiloi*

One-way ANOVA of your $k=3$ independent treatments:

source	sum of squares SS	degrees of freedom ν	mean square MS	F statistic	p-value
treatment	1.9145	2	0.9573	76.2974	0.0027
error	0.0376	3	0.0125		
total	1.9522	5			

SZCZM1454 *H.* cf. *salinicola*

One-way ANOVA of your $k=3$ independent treatments:

source	sum of squares SS	degrees of freedom ν	mean square MS	F statistic	p-value
treatment	0.0822	2	0.0411	43.7626	0.0060
error	0.0028	3	0.0009		
total	0.0850	5			

BA170 *P. trainorii*

One-way ANOVA of your $k=3$ independent treatments:

source	sum of squares SS	degrees of freedom ν	mean square MS	F statistic	p-value
treatment	0.3026	2	0.1513	190.2109	0.0007
error	0.0024	3	0.0008		
total	0.3049	5			

Light intensity

SZCZCH193 *N. wachnickianum*

One-way ANOVA of your $k=4$ independent treatments:

source	sum of squares SS	degrees of freedom ν	mean square MS	F statistic	p-value
treatment	0.0141	3	0.0047	0.6019	0.6473
error	0.0312	4	0.0078		
total	0.0452	7			

SZCZM1342 *N. shiloi*

One-way ANOVA of your $k=4$ independent treatments:

source	sum of squares SS	degrees of freedom ν	mean square MS	F statistic	p-value
treatment	0.1611	3	0.0537	3.6045	0.1237
error	0.0596	4	0.0149		
total	0.2207	7			

SZCZP1809 *N.*cf. *shiloi*

One-way ANOVA of your $k=4$ independent treatments:

source	sum of squares SS	degrees of freedom ν	mean square MS	F statistic	p-value
treatment	0.8341	3	0.2780	13.0766	0.0155
error	0.0850	4	0.0213		
total	0.9192	7			

SZCZM1454 *H.* cf. *salinicola*

One-way ANOVA of your $k=4$ independent treatments:

source	sum of squares SS	degrees of freedom ν	mean square MS	F statistic	p-value
treatment	0.1550	3	0.0517	18.5785	0.0082
error	0.0111	4	0.0028		
total	0.1661	7			

BA170 *P. trainorii*

One-way ANOVA of your $k=4$ independent treatments:

source	sum of squares SS	degrees of freedom ν	mean square MS	F statistic	p-value
treatment	0.2115	3	0.0705	22.3283	0.0058
error	0.0126	4	0.0032		
total	0.2242	7			

Table S3. Post-hoc test: Tukey's HSD for silicate concentration

SZCZCH193, N. wachickianum	0.11	0.53	1.06	1.59	2.21
0.11					
0.53	0.8999947				
1.06	0.0472728*	0.0621420*			
1.59	0.0135091*	0.0169507*	0.6080312		
2.21	0.0023999**	0.0028320**	0.0458097*	0.2001009	
SZCZM1342, N. shiloi	**0.11**	**0.53**	**1.06**	**1.59**	**2.21**
0.11					
0.53	0.0161578*				
1.06	0.0037594**	0.3469723			
1.59	0.0010053**	0.0029894**	0.0120501*		
2.21	0.0010053**	0.0010053**	0.0013018**	0.0731735	
SZCZM1809 N. cf. shiloi	**0.11**	**0.53**	**1.06**	**1.59**	**2.21**
0.11					
0.53	0.2556397				
1.06	0.0695203	0.7040614			
1.59	0.0082758**	0.0593770	0.2155356		
2.21	0.0011985**	0.0045982**	0.01100757*	0.1034915	
SZCZM1454 H. cf. salinicola	**0.11**	**0.53**	**1.06**	**1.59**	**2.21**
0.11					
0.53	0.0316509*				
1.06	0.0304112*	0.8999947			
1.59	0.0010053**	0.0120532*	0.0124769*		
2.21	0.0010053**	0.0010053**	0.0010053**	0.0354286*	
BA170, P. trainorii	**0.11**	**0.53**	**1.06**	**1.59**	**2.21**
0.11					
0.53	0.1311601				
1.06	0.0125641*	0.2014198			
1.59	0.0026694**	0.0216935*	0.2683216		
2.21	0.0012699**	0.0076107**	0.0659369	0.6566852	

* $p < 0.05$; ** $p < 0.01$

Table S4. Post-hoc test: Tukey's HSD for temperature

SZCZCH193, N. wachickianum	15	20	30
15			
20	0.8999947		
30	0.0320137*	0.0357364*	
SZCZM1809 N. cf. shiloi	**15**	**20**	**30**
15			
20	0.0074323**		
30	0.002513**	0.0656481	
SZCZM1454 H. cf. salinicola	**15**	**20**	**30**
15			
20	0.3691884		
30	0.0063471**	0.0113256*	
BA170, P. trainorii	**15**	**20**	**30**
15			
20	0.0195562*		
30	0.0019526**	0.0010053**	

* $p < 0.05$; ** $p < 0.01$

Table S5. Post-hoc test: Tukey's HSD for salinity

SZCZCH193, N. wachickianum	15	20	35	45
15				
20	0.4087059			
35	0.7058779	0.1441450		
45	0.1021474	0.0257183*	0.2839445	
SZCZM1342, N. shiloi	15	20	35	45
15				
20	0.2145430			
35	0.0010053**	0.0010594**		
45	0.0010053**	0.0016672**	0.6117027	
SZCZM1809 N. cf. shiloi	15	20	35	45
15				
20	0.3965940			
35	0.0180139*	0.0662861		
45	0.0019652**	0.0041484**	0.0360781*	
SZCZM1454 H. cf. salinicola	15	20	35	45
15				
20	0.8999947			
35	0.5382717	0.4426575		
45	0.0569181	0.0478407*	0.2063421	

* $p < 0.05$; ** $p < 0.01$

Table S6. Post-hoc test: Tukey's HSD for light intensity

SZCZM1809 N. cf. shiloi	10	50	100	150
10				
50	0.095841			
100	0.2290149	0.7762922		
150	0.0119221*	0.1378448	0.0608016	
SZCZM1454 H. cf. salinicola	10	50	100	150
10				
50	0.0074969**			
100	0.0577910	0.1110210		
150	0.0160843*	0.5925836	0.3922733	
BA170, P. trainorii	10	50	100	150
10				
50	0.004902**			
100	0.0210509*	0.1811152		
150	0.0156458*	0.2826787	0.8999947	

* $p < 0.05$; ** $p < 0.01$

Table S7. Post-hoc test: Tukey's HSD for nitrate

| SZCZP1809 N. cf. shiloi	0.88	4.41	8.82	13.23	17.64
0.88					
4.41	0.2109006				
8.82	0.8999947	0.1774637			
13.23	0.4562040	0.0354621*	0.5298723		
17.64	0.8339776	0.0761166*	0.8999947	0.8999947	

* $p < 0.05$

Table S8. Dry biomass accumulation (g L^{-1}) under different culturing conditions in the late exponential phase of batch cultivation of BA170 *P. trainorii* strain (mean ± standard deviation).

Nitrate, mM L^{-1}					Phosphate, mM L^{-1}				
0.88	*4.41*	*8.82*	*13.23*	*17.64*	*0.04*	*0.18*	*0.36*	*0.54*	*0.72*
0.225 ± 0.007	0.393 ± 0.075	0.317 ± 0.202	0.323 ± 0.004	0.264 ± 0.062	0.355 ± 0.052	0.350 ± 0.116	0.197 ± 0.103	0.347 ± 0.047	0.226 ± 0.017

Light intensity, µmol s^{-1} m^{-2}				Salinity, ‰			
10	*50*	*100*	*150*	*7*	*10*	*15*	*20*
0.236 ± 0.051	0.678 ± 0.044	0.532 ± 0.025	0.558 ± 0.034	0.588 ± 0.116	0.405 ± 0.016	0.327 ± 0.052	0.402 ± 0.155
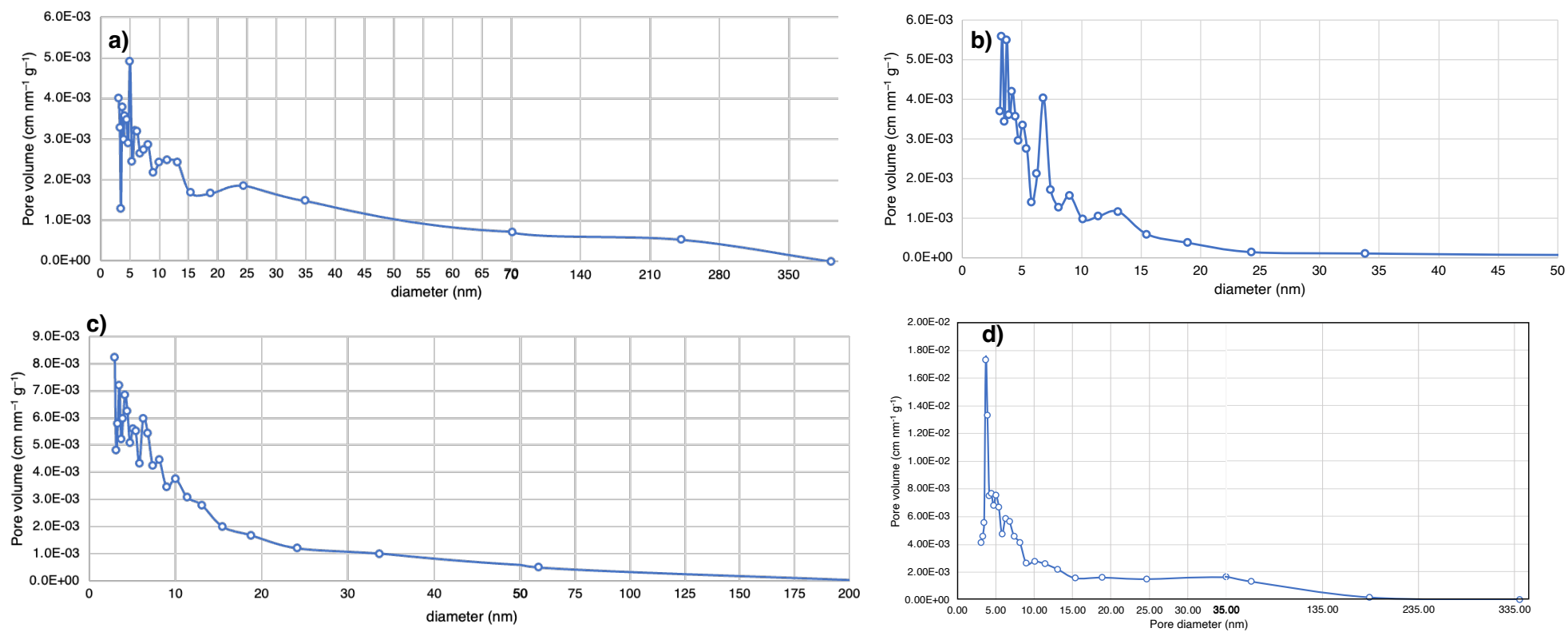
Figure S1. Pore distribution for **(a)** SZCZCH193 *N. wachnickianum*, **(b)** SZCZM1342 *N. shiloi*, **(c)** SZCZP1809 *N.* cf. *shiloi*, and **(d)** SZCZM1454 *H.* cf. *salinicola.*
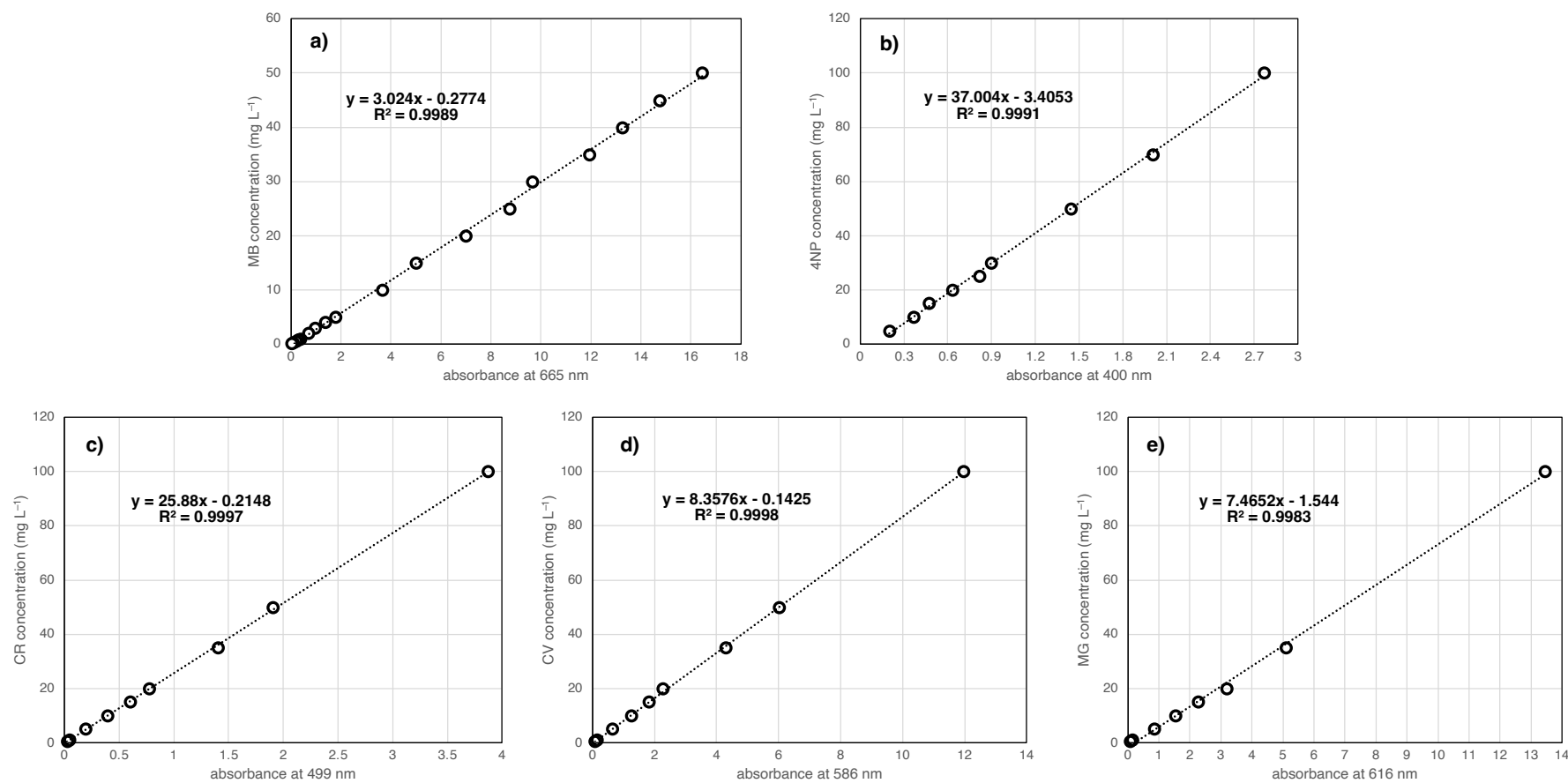
Figure S2. Calibration curves for **(a)** MB, **(b)** 4NP, **(c)** CR, **(d)** CV, and **(e)** MG

ANNEX I

Golubeva, A., Roychoudhury, P., Dąbek, Pałczyńska, J., P., Pryshchepa, O., Piszczek, P., Pomastowski, P., Gloc, M., Dobrucka, R., Feliczak-Guzik, A., Nowak, I., Kurzydłowski, K.J., Buszewski, B., & Witkowski, A. (2023a) A novel effective bio-originated methylene blue adsorbent: the porous biosilica from three marine diatom strains of *Nanofrustulum* spp. (Bacillariophyta). *Scientific Reports*, *13*, 9168.

scientific reports

OPEN

A novel effective bio-originated methylene blue adsorbent: the porous biosilica from three marine diatom strains of *Nanofrustulum* spp. (Bacillariophyta)

Aleksandra Golubeva[1]✉, Piya Roychoudhury[1], Przemysław Dąbek[1], Jagoda Pałczyńska[2], Oleksandra Pryshchepa[3], Piotr Piszczek[2], Paweł Pomastowski[3], Michał Gloc[4], Renata Dobrucka[4,5], Agnieszka Feliczak-Guzik[6], Izabela Nowak[6], Krzysztof J. Kurzydłowski[7], Bogusław Buszewski[8,9] & Andrzej Witkowski[1]

In the present paper, for the first time the ability of the porous biosilica originated from three marine diatom strains of '*Nanofrustulum* spp.' viz. *N. wachnickianum* (SZCZCH193), *N. shiloi* (SZCZM1342), *N.* cf. *shiloi* (SZCZP1809), to eliminate MB from aqueous solutions was investigated. The highest biomass was achieved under silicate enrichment for *N. wachnickianum* and *N. shiloi* (0.98 g L^{-1} DW and 0.93 g L^{-1} DW respectively), and under 15 °C for *N.* cf. *shiloi* (2.2 g L^{-1} DW). The siliceous skeletons of the strains were purified with hydrogen peroxide and characterized by SEM, EDS, the N$_2$ adsorption/desorption, XRD, TGA, and ATR-FTIR. The porous biosilica (20 mg DW) obtained from the strains i.e. SZCZCH193, SZCZM1342, SZCZP1809, showed efficiency in 77.6%, 96.8%, and 98.1% of 14 mg L^{-1} MB removal under pH 7 for 180 min, and the maximum adsorption capacity was calculated as 8.39, 19.02, and 15.17 mg g^{-1}, respectively. Additionally, it was possible to increase the MB removal efficiency in alkaline (pH = 11) conditions up to 99.08% for SZCZP1809 after 120 min. Modelling revealed that the adsorption of MB follows Pseudo-first order, Bangham's pore diffusion and Sips isotherm models.

Diatoms (Bacillariophyta), representing a major group of photosynthetic microorganisms, are unicellular eukaryotic microalgae that live within cell walls composed of 3D structured porous biosilica (SiO$_2$). They play an essential role in global carbon and silicon cycles in the ocean and their photosynthetic activity accounts for almost one-fifth of the Earth's primary productivity[1,2]. Diatoms attract increasing attention in the applied sciences due to their potential for producing a variety of bioactive compounds and fine chemicals for industrial applications: fucoxanthin is known for its antioxidant effect and can be used in pharmaceuticals and cosmetics[3]; unsaturated fatty acids have been used as food supplements[4]; triacylglycerols (TAG) provide a carbon feedstock for conversion

[1]Institute of Marine and Environmental Sciences, University of Szczecin, Mickiewicza 16a, 70-383 Szczecin, Poland. [2]Department of Inorganic and Coordination Chemistry, Faculty of Chemistry, Nicolaus Copernicus University, Gagarina 7, 87-100 Toruń, Poland. [3]Centre for Modern Interdisciplinary Technologies, Nicolaus Copernicus University, Wileńska 4, 87-100 Toruń, Poland. [4]Faculty of Materials Science and Engineering, Warsaw University of Technology, Wołoska 141, 02-507 Warsaw, Poland. [5]Department of Industrial Products and Packaging Quality, Institute of Quality Science, Poznań University of Economics and Business, al. Niepodległości 10, 61-875 Poznan, Poland. [6]Department of Applied Chemistry, Faculty of Chemistry, Adam Mickiewicz University, Uniwersytetu Poznańskiego 8, 61-614 Poznań, Poland. [7]Faculty of Mechanical Engineering, Bialystok University of Technology, ul. Wiejska 45 c, 15-351 Bialystok, Poland. [8]Department of Environmental Chemistry and Bioanalysis, Faculty of Chemistry, Nicolaus Copernicus University, Gagarina 7, 87-100 Toruń, Poland. [9]Prof. Jan Czochralski Kuyavian-Pomeranian Research and Development Centre, Krasińskiego 4, 87-100 Toruń, Poland. ✉email: alexandra.golubeva@phd.usz.edu.pl

to biofuels[5]. The natural porous architecture of diatomaceous frustules gained the attention in a field of drug delivery[6], biosensing[7], and metal recovery[8]. Diatoms have enormous biotechnological potential for biorefinery processes[9], thereby their biomass could be used in the production of various compounds in a cost-effective way.

The widespread use of various organic pollutants, e.g. drugs[10], antibiotics[11], phenols[12], and dyes[13], in industry has resulted in the problem of water pollution. They are stored as industrial wastes and then purged into environmental water bodies, changing colorless clean water into contaminated colored wastes. Water-soluble basic dyes are commonly used in paper, polyester, silk, cotton, and wool coloration[14]. This contamination is highly toxic and could negatively affect humans, causing breathing problems, eye damage, and methemoglobinemia[15–17]. Methylene blue (MB) is known as a model dye that is used to evaluate the removal capacity of different materials and an indicator of the mesoporous nature of adsorbents[18].

Currently, numerous studies have been done to find an efficient green dye removal method, so that the dye in wastewater could be recovered. One of the most promising degradation methods is adsorption, which gives better results, could be used for different types of dyes, does not require highly sophisticated equipment, insensitive to toxic co-pollutants in wastewaters, and does not produce toxic substances[19]. Activated carbon, the most commonly applied natural adsorbent, has been used in numerous studies and showed high adsorption capacity in the removal of MB, although the high cost and difficult regeneration process resulted in a further search to find low-cost and highly effective adsorbents[20]. Many non-conventional adsorbents, especially those based on natural products, have been proposed as adsorption agents. High adsorption capacities have been shown for bioadsorbents (dead and live biomass of bacteria[21], algae[22], fungi[23], plants[24], and agricultural wastes[25]), zeolites[26] and diatomite[27]. To the best of our knowledge, only a few studies have been performed with pure diatomaceous biosilica extracted from *Punnularia* sp.[28] and *Cyclotella* sp.[29], with a greater focus on metal-doped diatomaceous silica[30,31], diatomaceous earth[27,32] and chemically synthesized mesoporous silica[33,34]. Although chemically synthesized silica demonstrates high adsorption efficiency, some investigations suggested that this material can show cytotoxicity[35,36], while diatom-originated biosilica reported to be non-cytotoxic material[37], therefore could be used in non-damaging way. In the present study, porous biosilica from three different marine diatom strains of the genus *Nanofrustulum* Round, Hallsteinsen & Paasche grown in the Szczecin Diatom Culture Collection (SZCZ), University of Szczecin, Institute of Marine and Environmental Sciences, Poland, has been for the first time characterized and identified as highly effective and cheap MB adsorbent.

Results

Batch cultivation of diatom cultures. Three strains of *Nanofrustulum* spp. showed distinct lag, exponential, and stationary phases during batch culture (Fig. 1a,b). The lag phase of the strain SZCZCh193 *N. wachnickianum* was observed until the 5th day of cultivation, with exponential growth for 7 days from the 5th to 12th day, and a stationary phase starting from the 12th day of growth. The maximum specific growth rate of the exponential phase was calculated as $0.115 \, d^{-1}$ ($R^2 = 0.95$). The growth of strain SZCZM1342 *N. shiloi* showed a lag (until the 4th day), exponential (for 6 days, from 4 to 10th day), and stationary (from 10th day) phases, and the maximum specific growth rate of the exponential phase was calculated as $0.270 \, d^{-1}$ ($R^2 = 0.97$) 6 days after inoculation, SZCZP1809 *N.* cf. *shiloi* showed exponential growth for 10 days (to the 16th day of cultivation), with a following stationary phase of growth. The maximum specific growth rate during the exponential phase was calculated as $0.513 \, d^{-1}$ ($R^2 = 0.99$). Therefore, it can be said that the maximum biomass yields for SZCZCh193 *N. wachnickianum* ($0.39 \pm 0.039 \, g \, L^{-1}$ DW), and SZCZM1342 *N. shiloi* ($0.47 \pm 0.033 \, g \, L^{-1}$ DW) were obtained on the 18th day, and for SZCZP1809 *N.* cf. *shiloi* ($0.63 \pm 0.013 \, g \, L^{-1}$ DW) on the 16th day of cultivation.

Experiments with different salinities of artificial seawater Guillard's f/2 medium (Table 1, Supplementary Figure S1a) showed that low salinities (15 and 20‰) resulted in lower biomass accumulation than high salinities (35 and 45‰). The highest dry biomass yield was observed with 45‰ for SZCZCH193 *N. wachnickianum* (n = 8, one-way ANOVA $p = 0.0319$; Turkey HSD $p = 0.0251$ between 35 and 45‰) and strains SZCZP1809 *N.*
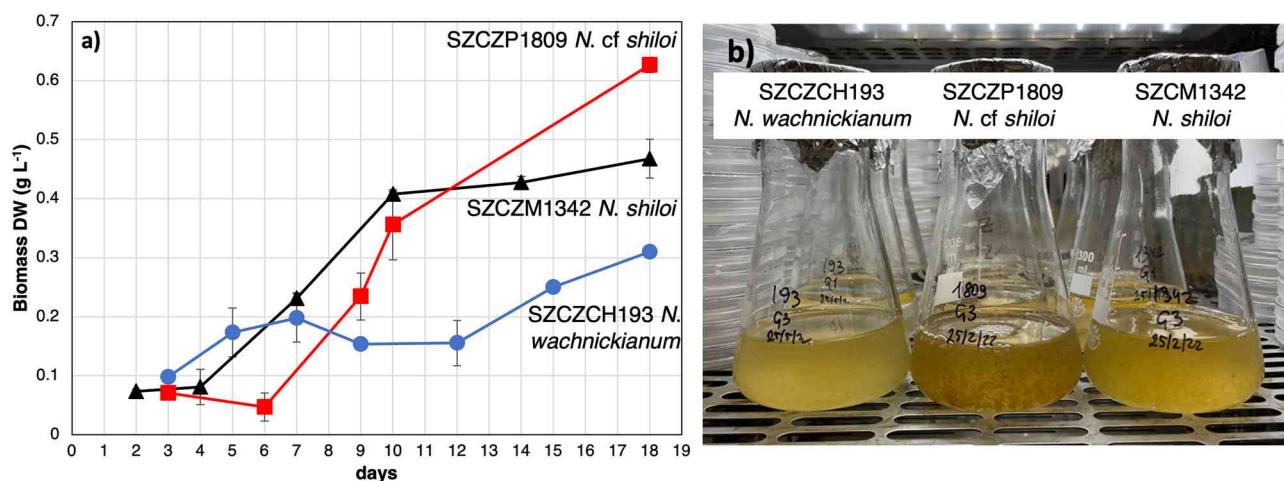
Figure 1. Batch culture of SZCZCH193 *N. wachnickianum*, SZCZM1342 *N. shiloi*, SZCZP1809 *N.* cf. *shiloi*: (**a**) growth dynamics of biomass DW; (**b**) cultivation flasks.

Cultivation parameter	Nitrate, mM L^{-1}					Phosphate, mM L^{-1}				
	0.88	4.41	8.82	13.23	17.64	0.04	0.18	0.36	0.54	0.72
SZCZCH193	0.499 ± 0.064	0.473 ± 0.023	0.463 ± 0.037	0.452 ± 0.021	0.430 ± 0.004	0.531 ± 0.137	0.633 ± 0.077	0.445 ± 0.004	0.491 ± 0.057	0.463 ± 0.017
SZCZM1342	0.502 ± 0.091	0.591 ± 0.080	0.524 ± 0.019	0.623 ± 0.029	0.647 ± 0.007	0.622 ± 0.007	0.701 ± 0.025	0.710 ± 0.056	0.742 ± 0.014	0.686 ± 0.048
SZCZP1809	0.774 ± 0.058	1.01 ± 0.095	0.759 ± 0.169	0.609 ± 0.016	0.683 ± 0.006	0.735 ± 0.026	0.699 ± 0.013	0.791 ± 0.093	0.732 ± 0.063	0.735 ± 0.000

Cultivation parameter	Silicate, mM L^{-1}					Temperature, °C				
	0.11	0.53	1.06	1.59	2.12	15	20	30		
SZCZCH193	0.447 ± 0.089	0.466 ± 0.110	0.711 ± 0.004	0.807 ± 0.030	0.977 ± 0.004	0.331 ± 0.014	0.352 ± 0.002	0.865 ± 0.187		
SZCZM1342	0.402 ± 0.003	0.570 ± 0.057	0.636 ± 0.000	0.816 ± 0.040	0.930 ± 0.014	0.530 ± 0.034	0.568 ± 0.042	0.624 ± 0.011		
SZCZP1809	0.469 ± 0.090	0.600 ± 0.006	0.670 ± 0.059	0.810 ± 0.037	0.989 ± 0.047	2.208 ± 0.213	1.178 ± 0.074	0.758 ± 0.025		

Cultivation parameter	Light intensity, μmol s^{-1} m^{-2}				Salinity, ‰					
	10	50	100	150	15	20	35	45		
SZCZCH193	0.308 ± 0.009	0.329 ± 0.050	0.383 ± 0.141	0.413 ± 0.093	0.306 ± 0.042	0.232 ± 0.041	0.352 ± 0.003	0.442 ± 0.059		
SZCZM1342	0.395 ± 0.116	0.718 ± 0.195	0.733 ± 0.088	0.718 ± 0.019	0.053 ± 0.007	0.116 ± 0.051	0.421 ± 0.001	0.387 ± 0.002		
SZCZP1809	0.557 ± 0.014	1.037 ± 0.043	0.900 ± 0.038	1.458 ± 0.286	0.282 ± 0.017	0.374 ± 0.039	0.566 ± 0.008	0.798 ± 0.093		

Table 1. Dry biomass accumulation (g L^{-1}) under a variety of cultivation parameters (temperature, light intensity, salinity, and nitrate, phosphate, silicate concentrations in Guillard′s f/2 medium) in the late exponential phase of batch cultivation of three *Nanofrustulum* spp strains (mean ± standard deviation).

cf. *shiloi*, (n = 8, one-way ANOVA $p = 0.002$; Turkey HSD $p = 0.0361$ between 35 and 45%) and no significant increase in biomass yield for SZCZM1342 *N. shiloi* (n = 8, one-way ANOVA $p = 0.0003$; Turkey HSD $p = 0.6117$ between 35 and 45%).

The following set of experiments (Table 1, Supplementary Figure S1b) showed a tendency of *Nanofrustulum* spp. to increase their biomass yield with increasing silicate concentration in Guillard's f/2 medium 20 times (2.12 mM) for all three strains (SZCZCH193: n = 10, one-way ANOVA $p = 0.0018$, Turkey HSD $p = 0.0024, 0.0028, 0.608, 0.2001$ (between 2.12 and 0.11, 0.53, 1.06, 1.59 respectively); SZCZM1342: n = 10, one-way ANOVA $p = 0.0008$, Turkey HSD $p = 0.001$ (between 2.12 mM and 0.11, 0.53 or 1.06 mM) and $p = 0.0731$ (between 2.12 and 1.59 mM); SZCZP1809: n = 10, one-way ANOVA $p = 0.0015$, Turkey HSD $p = 0.0012, 0.0046, 0.0111, 0.1035$ (between 2.12 and 0.11, 0.53, 1.06, 1.59 respectively)).

Experiments with different illumination intensities (Table 1, Supplementary Figure S1e) showed that the high light intensity (150 μmol s^{-1} m^{-2}) did not result in different biomass yields for SZCZCH193 *N. wachnickianum* and SZCZM1342 *N. shiloi*, and increased biomass accumulation for SZCZP1809 *N. cf. shiloi*. (SZCZCH193: n-8, one-way ANOVA $p = 0.6473$; SZCZM1342: n = 8, one-way ANOVA $p = 0.1237$; SZCZP1809: n = 8, one-way ANOVA $p = 0.0155$, Turkey HSD $p = 0.0119$ between 10 and 150 μmol s^{-1} m^{-2}).

The impact of temperature (Table 1, Supplementary Figure S1f) on biomass accumulation was different for each strain. For SZCZCH193 *N. wachnickianum*, the high temperature of cultivation (30 °C) increased the biomass yield (n = 6, one-way ANOVA $p = 0.0259$, Turkey HSD $p = 0.032, 0.0357$ between 20 and 15, 30 °C respectively); no differences in biomass accumulation for SZCZM1342 *N. shiloi* were observed (n = 6, one-way ANOVA $p = 0.1296$); and for SZCZP1809 *N. cf. shiloi* the low temperature of cultivation (15 °C) increased biomass yield (n = 6, one-way ANOVA $p = 0.0027$, Turkey HSD $p = 0.0074, 0.0025$ between 15 and 20, 30 °C respectively).

The variation in nitrate (Table 1, Supplementary Figure S1c) and phosphate (Table 1, Supplementary Figure S1d) concentrations in Guillard's f/2 medium did not show differences in dry biomass yield for SZCZCH193 *N. wachnickianum* (nitrate: n = 10, one-way ANOVA $p = 0.4732$; phosphate: n = 10, one-way ANOVA $p = 0.2371$), SZCZM1342 *N. shiloi* (nitrate: n = 10, one-way ANOVA $p = 0.1749$; phosphate: n = 10, one-way ANOVA $p = 0.1219$), and SZCZP1809 *N. cf. shiloi* (nitrate: n = 10, one-way ANOVA $p = 0.0455$, Turkey HSD $p = 0.0355$ between 4.41 and 13.23 mM; phosphate: n = 10, one-way ANOVA $p = 0.5765$).

Morphology and characterization of diatomaceous biosilica.

Scanning electron microscopy (SEM) revealed the similarities and differences in the morphology of the frustules of the three *Nanofrustulum* strains (Fig. 2a–d,g,h). The valves of all three strains' frustules are oval. The length of the frustules slightly varies from 2.6–2.9 μm (SZCZCH193 *N. wachnickianum*) and 3.1–3.3 μm (SZCZM1342 *N. shiloi*) to 3.9–4.2 μm (SZCZP1809 *N. cf. shiloi*), and the width varies from 2.9–3.1 μm (SZCZCH193 *N. wachnickianum,* SZCZM1342 *N. shiloi*) to 3.6–4.0 μm (SZCZP1809 *N. cf. shiloi*). The sternum is broadly-lanceolate for SZCZCH193 *N. wachnickianum*, and narrow-linear for the other two strains. The pores on a valve face, called areolae, are slightly elongated towards the valve mantle, length and width were measured as 120–615 nm and 120–330 nm (SZCZCH193 *N. wachnickianum*); 150–450 nm and 120–400 nm (SZCZM1342 *N. shiloi*); 80–510 nm and 100–330 nm (SZCZP1809 *N. cf. shiloi*). There is only one row of areolae on the valve face of SZCZCH193 *N. wachnickianum* (Fig. 2a,b), then there are two rows on the valve face of SZCZM1342 *N. shiloi* (Fig. 2c,d) and up to four rows on the valve of SZCZP1809 *N. cf. shiloi* (Fig. 2g,h).

The energy-dispersive X-ray spectra (Fig. 2e,f,i) of the three strains showed distinct peaks for silicon (Si), oxygen (O), carbon (C), and copper (Cu), which is an effect of copper grids use in STEM imaging. The atomic percentage of major elements were recorded as 30.55, 24.03, and 23.00% of silicon, 51.77, 54.69, and 54.67%
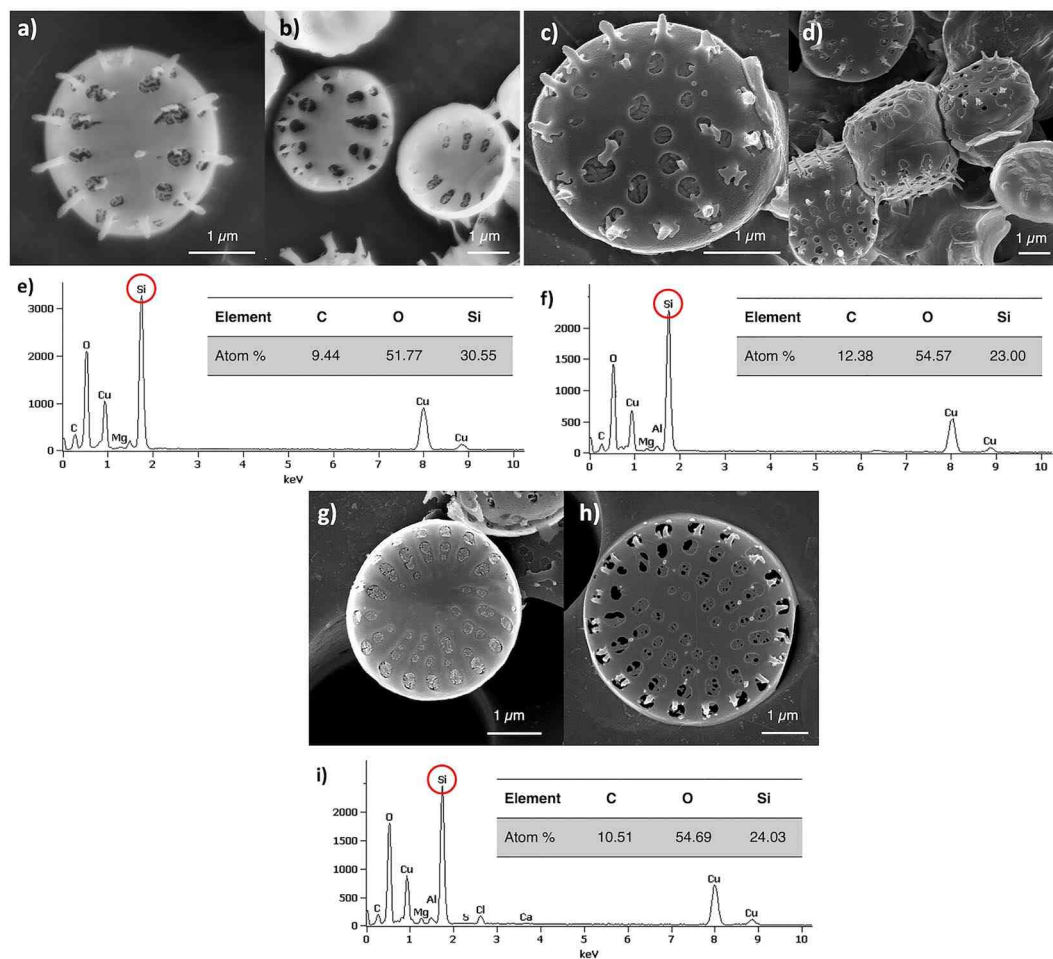
Figure 2. SEM images showing surface morphology of (**a**, **b**) SZCZCH193 *N. wachnickianum*, (**c**, **d**) SZCZM1342 *N. shiloi*, (**g**, **h**) SZCZP1809 *N.* cf. *shiloi*, and EDS spectra confirmed presence of Si and O on surface of (**e**) SZCZCH193 *N. wachnickianum*, (**f**) SZCZM1342 *N. shiloi*, (**i**) SZCZP1809 *N.* cf. *shiloi* (scale bar—1 μm, red circles show the presence of Si).

of oxygen, and 9.44, 10.51, and 12.38% of carbon for SZCZCH193 *N. wachickianum*, SZCZM1342 *N. shiloi*, SZCZP1809 *N.* cf. *shiloi* and respectively.

The specific surface area, pore volume, and pore diameter (Supplementary Table S1) of *Nanofrustulum* spp. strains frustules were estimated from the low-temperature N_2 adsorption/desorption isotherms, presented in Fig. 3a–c, as 25.32 m^2 g^{-1}, 0.267 cm^3 g^{-1}, 4.22 nm respectively for SZCZCH193 *N. wachnickianium*, 21.78 m^2 g^{-1}, 0.113 cm^3 g^{-1}, 2.07 nm respectively for SZCZM1342 *N. shiloi*, and 35.23 m^2 g^{-1}, 0.174 cm^3 g^{-1}, 1.97 nm respectively for SZCZP1809 *N.* cf. *shiloi*.

The UV–vis spectroscopy of sonicated biomass showed a distinct peak at 230 nm and small peaks at 270, 430, 495 and 676 nm (Fig. 3d–f, green line). The pure, sonicated biosilica showed only one distinct peak at 230 nm (Fig. 3d–f, gray line).

The biosilica Tauc's plot (Fig. 4a) showed a steep linear increase in light absorption with increasing energy. The x-axis intersection point of the linear fit of the Tauc plot gives an estimate of the band gap energy of 4.40 eV for SZCZCH193 *N. wachnickianum*, 4.05 eV for SZCZM1342 *N. shiloi*, and 4.10 eV for SZCZP1809 *N.* cf. *shiloi*.

On the Fig. 4b XRD the results of X-ray diffraction analysis are presented. On the XRD pattern of all samples the broad peak at $2\theta \approx 15°$–32°. However, for sample SZCZCH193 *N. wachnickianum* intense signals at $2\theta \approx 26.4°$, 27.4°, 36.6°, 37.5°, 38.1°, 38.6°, 41.4°, 43.1°, 46.0°, 50.4°, 59.4°, 61.9°, 77.2° were distinguished, while the presence of low intensity signals at $2\theta \approx 26.4°$, 36.4°, 46.2°, 48.7°, 60.7° were noticed for sample SZCZP1809 *N.* cf. *shiloi*.

ATR-FTIR spectra revealed distinct peaks (Fig. 4c) indicating the presence of O–H, C–H, C=O, N–H, and Si–O functional groups on the surface of frustules: 3,660 cm^{-1}; 2981, 2922, and 2851 cm^{-1}; 1748 cm^{-1}; 1630, 1540, 1450, and 1395 cm^{-1}; and 1150, 1050, 805, and 442 cm^{-1}, respectively.

The PZC was calculated as the intercept between initial pH and change in pH value after 24 h of incubation and was estimated as $pH_{pzc} = 6.0$ for SZCZCH193 *N. wachnickianum* and $pH_{pzc} = 5.3$ for SZCZM1342 *N. shiloi* and SZCZP1809 *N.* cf. *shiloi* (see Supplementary Figure S2a).
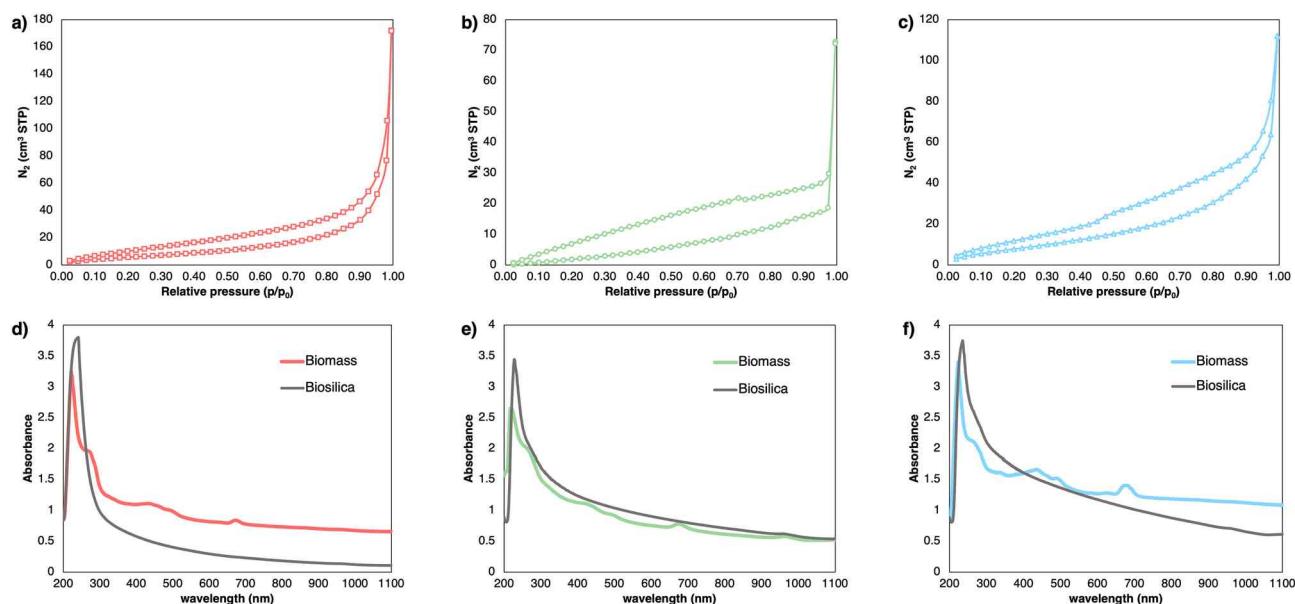
Figure 3. The N_2 adsorption/desorption isotherms for (**a**) SZCZCH193 *N. wachnickianum*, (**b**) SZCZM1342 *N. shiloi*, (**c**) SZCZP1809 *N.* cf. *shiloi*; and the UV–vis spectroscopy of biomass (colored line) and biosilica (gray line) for (**d**) SZCZCH193 *N. wachnickianum*, (**e**) SZCZM1342 *N. shiloi*, (**f**) SZCZP1809 *N.* cf. *shiloi*.
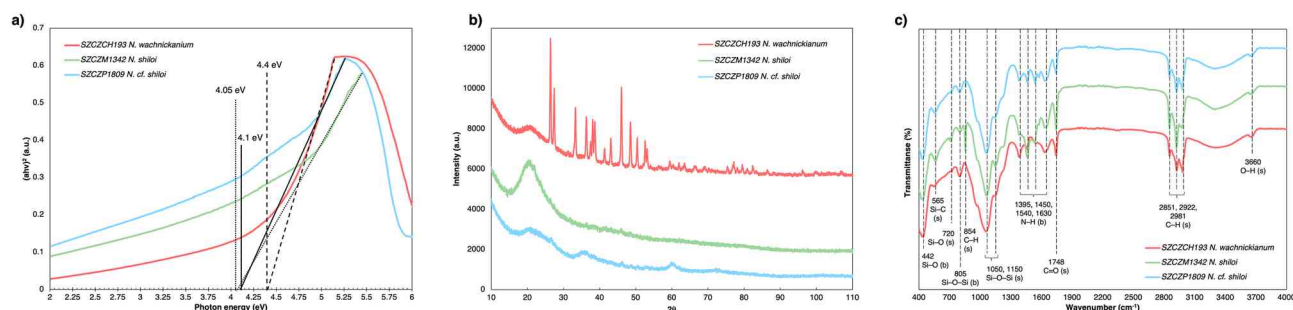
Figure 4. Characterization of pure diatomaceous biosilica with (**a**) Tauc's plot—presented biosilica bandgaps; (**b**) XRD—showed amorphous structure of biosilica as well as the presence of quartz or inorganic salts; (**c**) FTIR spectra—revealed the presence of functional groups surrounding the surfaces of biosilica of SZCZCH193 *N. wachnickianum*, SZCZM1342 *N. shiloi*, SZCZP1809 *N.* cf. *shiloi* (s—stretching, b—bending; spectra are offset to aid comparison).

The low zeta potential values in the range of 2.0 – 4.0 pH for each sample can be seen on the graph (see Supplementary Figure S2b). In the pH range of 4.0 to 12.0 an increase of zeta potential is observed (zeta potential > –25 mV).

Figure 5a–c presents the results of TGA analysis for all three biosilica samples. The plot of the mass loss against temperature did not allow us to derive more specific information about individual stage of the process. Thus, the differential thermal analysis (DTA) was performed which showed three main stages of the process
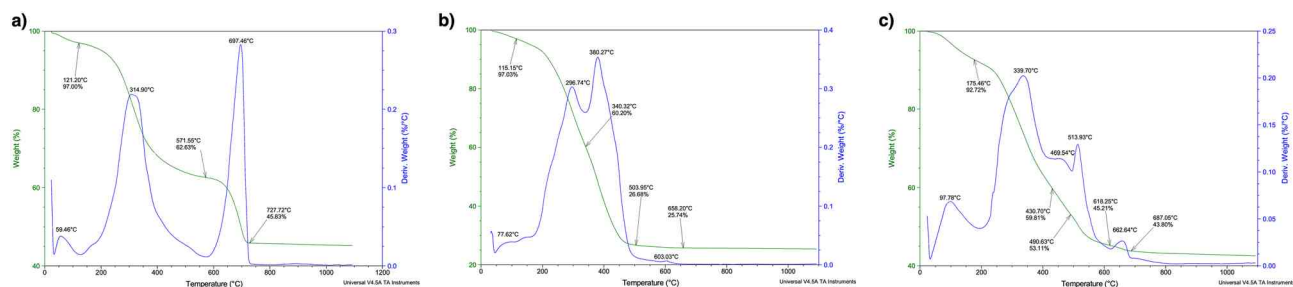
Figure 5. Thermal stability and transformation of pure diatomaceous biosilica (**a**) SZCZCH193 *N. wachnickianum*, (**b**) SZCZM1342 *N. shiloi*, (**c**) SZCZP1809 *N.* cf. *shiloi*.

(Fig. 5a–c). SZCZCH193 *N. wachnickianum* biosilica sample (Fig. 5a) showed three distinguished peaks on the DTA analysis plot appeared with maxima at 59.5, 314.9 and 697 °C. First stage ends up at 121.2 °C and mass loss of 3%, second one at 571.5 °C with mass loss of 34.6%, and third one at 727.72 °C with mass loss of 54.17%. Similarly, SZCZM1342 *N. shiloi* plot (Fig. 5b) revealed three stages in process with first one ending at 115 °C (mass loss of about 3%), second one at 340.32 °C with mass loss of 39.8%, and third one at 503 °C with mass loss of 73.32%. The DTA analysis revealed peaks at 77.62, 296.74, 380.27, and 603.03 °C. For sample SZCZP1809 *N.* cf. *shiloi* the most complex plot of DTA analysis has been observed (Fig. 5c) with peaks at 97.78, 339.70, 469.54, 513.93, and 662.64 °C. First stage ends at 175.46 °C with mass loss of 7.28%, second one at 490.6 °C with 46.89% mass loss, and third one at 687.05 °C with 56.92% mass loss.

Methylene blue batch adsorption. The pure porous diatomaceous biosilica of the three strains showed a positive response in the discoloration of MB in aqueous solution. Spectroscopy showed a sharp decrease in the MB peak with exposure time (Figure S3a-c), which confirmed the removal of the dye. The adsorption of MB onto the biosilica from SZCZCH193 *N. wachnickianum* strain progressed slowly with a sharp increase after 90 min of exposure until it reached equilibrium after 120 min. For frustules of SZCZCH193 *N. wachnickianum*, the percentage of MB removal after 180 min was 77.6%. The adsorption of MB onto the frustules of SZCZM1342 *N. shiloi* and SZCZP1809 *N.* cf. *shiloi* gradually increased with time until the systems reached equilibrium after 120 min of exposure. The percentage of MB removal after 180 min was calculated as 96.8% for SZCZM1342 *N. shiloi* and 98.1% for SZCZP1809 *N.* cf. *shiloi* (Fig. 6a).

Furthermore, the effect of different pH of MB solutions was investigated with exposure of biosilica to acidic (pH = 3), neutral (pH = 7), and alkaline (pH = 11) aqueous solutions of MB as shown in Fig. 6b. In acidic solutions, the removal of MB was lower than in neutral and alkaline conditions: 71.33% for SZCZCH193 *N. wachnickianum*, 91.90% for SZCZM1342 *N. shiloi*, and 97.23% for SZCZP1809 *N.* cf. *shiloi*. An increase in pH resulted in higher removal efficiencies: up to 77.27% for SZCZCH193 *N. wachnickianum*, up to 96.03% for SZCZM1342 *N. shiloi*, and up to 99.08% for SZCZP1809 *N.* cf. *shiloi*.

The influence of different MB concentrations in the initial solution was also examined. Figure 6c shows that, for SZCZCH193 *N. wachnickianum*, an increase in MB concentration resulted in a significant decrease in the removal efficiency—from 79.48% at 5 mg L^{-1} to 10.69% at 100 mg L^{-1}. Frustules of SZCZM1342 *N. shiloi*, exposed to a 100 mg L^{-1} solution of MB, showed an hyperbolic increase with concentrations almost of the same efficiency (89.82%) as at lower concentrations—88.35% at 5 mg L^{-1}, 81.92% at 10 mg L^{-1}, 86.26% at 15 mg L^{-1}, 87.13% at 20 mg L^{-1}, 90.69% at 50 mg L^{-1}, and 89.82% of removal at 100 mg L^{-1}. The most efficient strain in the removal of MB, SZCZP1809 *N. wachnickianum*, showed a similar tendency—85.82% of removal at 5 mg L^{-1}, 90.78% at 10 mg L^{-1}, 93.77% at 15 mg L^{-1}, 95.59% at 20 mg L^{-1}, 95.95% at 50 mg L^{-1}, and 91.15% at 100 mg L^{-1}.

Batch adsorption kinetics and isotherm studies. A pseudo-first order (Supplementary Figure S4a) model showed higher correlation coefficients for SZCZM1342 *N. shiloi* and SZCZP1809 *N.* cf. *shiloi* than Elovich (Supplementary Figure S4b) and pseudo-second order (Supplementary Figure S4c) kinetic models and the normalized standard deviation value for pseudo-first order was the lowest. For SZCZCH193 *N. wachnickianum*, the correlation coefficients for pseudo-second and Elovich models were higher than for the pseudo-first order model, but not close to unity and with very small constant values. The standard deviation value was higher than 50% for all three models (Table 2).

For the three tested strains, the Boyd's linear graph was a straight line passing through the origin (see Supplementary Figure S4e), and the test showed high correlation coefficients ($R^2 = 0.962$, 0.966 and 0.995 for SZCZCH193 *N. wachnickianum*, SZCZM1342 *N. shiloi*, and SZCZP1809 *N.* cf. *shiloi* respectively) and low standard deviation values for SZCZM1342 *N. shiloi* (14.5%) and SZCZP1809 *N.* cf. *shiloi* (35.2%), but higher than 50% for SZCZCH193 *N. wachnickianum*.
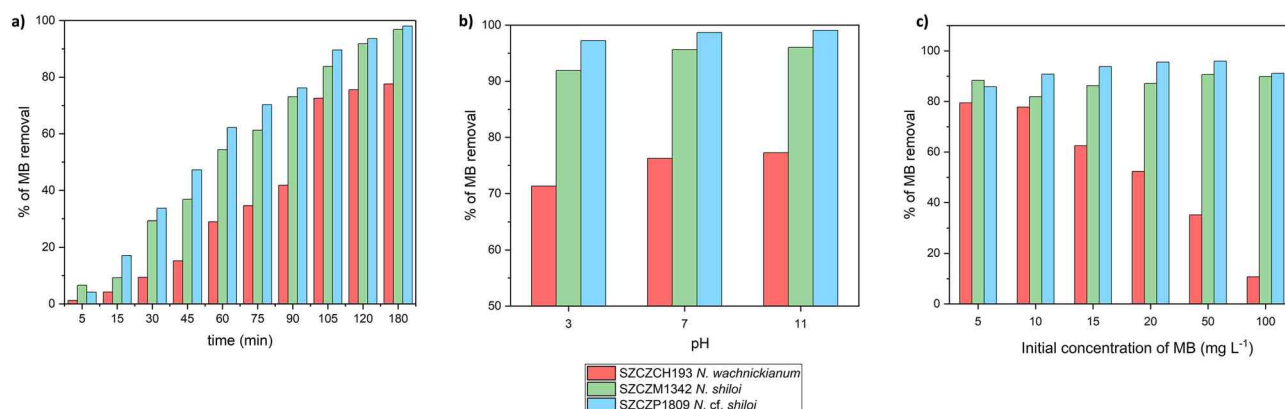
Figure 6. Effect of (**a**) time; (**b**) different pH and (**c**) different initial MB concentrations on the efficiency of MB adsorption onto pure biosilica of SZCZCH193 *N. wachnickianum*, SZCZM1342 *N. shiloi*, SZCZP1809 *N.* cf. *shiloi*, (initial concentration of MB—(**a**, **b**) 14.31 mg L^{-1}; (**c**) 5–100 mg L^{-1}; adsorbent dosage—21.40 ± 5.0 mg; pH—(**a**–**c**) 7, (**b**) 3, 7, 10; temperature—20 °C; time—(**a**) 5–180 min; (**b**, **c**) 120 min).

Kinetic model	Pseudo-first order				Pseudo-second order				Elovich				
	q_1, mg g^{-1}	k_1, min^{-1}	R^2	Δq, %	q_2, mg g^{-1}	k_2, g (mg min)$^{-1}$	R^2	Δq, %	α, g (mg min)$^{-1}$	β, mg g^{-1}	R^2	Δq, %	
SZCZCH193	19.902	0.002	0.887	52.2	39.671	$2.71e^{-5}$	0.894	65.4	0.042	0.051	0.893	64.7	
SZCZM1342	9.445	0.991	0.979	26.9	14.787	$4.09e^{-4}$	0.964	28.2	0.094	0.178	0.969	29.6	
SZCZP1809	8.458	0.987	0.989	24.1	12.283	$7.74e^{-4}$	0.973	28.9	0.130	0.237	0.976	32.3	

Diffusion model	Intra-particle (Weber-Morris)				Bangham's pore diffusion								
	K_{wm}, mg (g min$^{0.5}$)$^{-1}$	B, mg g^{-1}	R^2	Δq, %	$\Delta\beta$	K_β	R^2	Δq, %					
SZCZCH193	0.377	$1e^{-16}$	0.730	52.2	1.374	0.004	0.972	18.2					
SZCZM1342	0.535	$1e^{-14}$	0.901	26.9	1.025	0.037	0.964	13.9					
SZCZP1809	0.575	$1e^{-14}$	0.930	24.1	1.073	0.035	0.985	19.2					

Isotherm	Langmuir				Freundlich				Sips				
	Q^0_{max}, mg g^{-1}	K_L, L mg^{-1}	R^2	Δq, %	K_F (mg g^{-1}) (mg L^{-1})$^{-n}$	n	R^2	Δq, %	q_m, mg g^{-1}	K_{S_i} [(mg L^{-1})$^{-1/n}$]	n	R^2	Δq, %
SZCZCH193	6.85	0.31	0.965	11.9	2.37	0.27	0.953	19.6	8.39	0.16	0.65	0.992	7.2
SZCZM1342	16.18	1.35	0.959	48.9	1.88	1.10	0.965	36.3	19.02	0.26	2.26	0.998	6.5
SZCZP1809	27.09	0.24	0.879	>100	4.94	0.67	0.820	>100	15.17	0.75	2.87	0.999	20.9

Table 2. Adsorption kinetic and diffusion model constants for MB removal using pure diatomaceous mesoporous biosilica.

To understand the rate-controlling step of the adsorption, Weber-Morris Intra-Particle Diffusion and Bangham's Pore Diffusion models were used (Supplementary Figure S4d, f). The highest and closest to unity coefficient for SZCZCH193 *N. wachnickianum*, SZCZM1342 *N. shiloi*, and SZCZP1809 *N.* cf. *shiloi* were calculated for the Bangham's Pore Diffusion model. The standard deviation values for Bangham's Pore Diffusion model for all three strains were lower than 20% (Table 2).

According to the isotherms models' constants and coefficients of correlation, the Sips Isotherm model is the most suitable for SZCZCH193 *N. wachnickianum*, SZCZM1342 *N. shiloi*, and SZCZP1809 *N.* cf. *shiloi* (Table 2, Supplementary Figure S5a–c).

Discussion

Several studies reported specific growth rate and biomass productivities for *Nanofrustulum shiloi* strains as 0.099 d^{-1}[38], 0.305 d^{-1}[39], 0.457 d^{-1}[40], which correspond to 12.8 mg L^{-1} d^{-1}[38], 31.29 mg L^{-1} d^{-1}[40], respectively. In the present study, the specific growth rate and biomass productivity of SZCZM1342 *N. shiloi* and SZCZP1809 *N.* cf. *shiloi* were observed as 0.270 d^{-1}, 0.513 d^{-1}, which correspond to 26.12 mg L^{-1} d^{-1}, 39.37 mg L^{-1} d^{-1}, respectively. Thus, SZCZP1809 could be considered the most productive strain of *N. shiloi*. To the best of our knowledge no work has been done on the growth investigation of *Nanofrustulum wachnickianum*. A significant increase of biomass yield at lower temperatures for SZCZP1809 *N.* cf. *shiloi* and higher temperature for SZCZCH193 *N. wachnickianum* could be explained by the origin of the strains: SZCZP1809 was collected from the Atlantic Ocean, Sea Point, Cape Town, South Africa, where the average sea water temperature amounts to 17 °C, and SZCZCH193 *N. wachnickianum*—from the Gulf of Mexico, Marquesas Keys, Florida, USA (an average sea water temperature of 28 °C). Silica is a major limiting nutrient for diatom growth because of their need to build silicon-based frustules. The strains of *Nanofrustulum* spp. showed that biomass yield can be significantly enhanced with an increased silicon source up to almost 1 g L^{-1} DW, which correlated with previous studies[41].

Pictures from scanning electron microscopy revealed that the valve faces of strains SZCZP1809 *N.* cf. *shiloi* and SZCZM1342 *N. shiloi* contain more than one row of areolae whereas the valves of SZCZCH193 *N. wachnickianum* contain only one row. The differences in areolation of the valve face make frustules of SZCZM1342 *N. shiloi* and SZCZP1809 *N.* cf. *shiloi* more porous than those of SZCZCH193 *N. wachnickianum*. Li et al.[42] described a new species of *N. wachnickianum* and observed that this species could be differentiated from *N. shiloi* by the number of areolae on the valve face. In the case of MB removal, the pore size and number are crucial. Thus, SZCZCH193 *N. wachnickianum* has less potential as an adsorbing agent of MB due to a lower number of areolae, unlike SZCZM1342 *N. shiloi* and SZCZP1809 *N.* cf. *shiloi*. The areolae (width 80 nm and higher) of *Nanofrustulum* spp. strains could be considered macropores[43]. However, the N$_2$ adsorption/desorption revealed presence of micro and mesopores, with average diameter 4.217 nm (SZCZCH193 *N. wachnickianum*), 2.073 nm (SZCZM1342 *N. shiloi*), and 1.971 nm (SZCZP1809 *N.* cf. *shiloi*). Previous studies reported the similar values of average pore diameter of diatomaceous frustules: 3.93 nm for *Pseudostraurosira trainorii*[44], 3–10 nm for *Thalassiosira punctigera* and 3.6–3.7 nm for *T. weissflogii*[45], and 4.61 nm for *Navicula australoshetlandica*[46]. Additionally, the porous nature of material could be described by the shape of the N$_2$ adsorption/desorption isotherm. According to IUPAC classification the isotherms of *Nanofrustulum* spp. biosilica follow the Type I (microporous nature) and Type II (macroporous material), with combination of Type H3 and H4 hysteresis loop, where Type H3 shows presence of the macropores network and Type H4 indicates the existence of slit-like micropores in sample[43].

Specific surface area of different strains of *NanofrusItulum* spp. differs slightly. Previous reports showed that different diatomaceous frustules have diverse S$_{BET}$ value: from 2 m^2 g^{-1} for *Skeletonema* sp.[47] and 30 m^2 g^{-1} for *P.*

trainorii[44], to 401.45 $m^2 g^{-1}$ for *N. australoshetlandica*[46]. However, it is important to note, that cleaning method could influence enormously in surface area: Gholami et al.[29] demonstrated the possibility to increase SBET for *Cyclotella* sp. frustules from 14.71 $m^2 g^{-1}$ to 132.67 $m^2 g^{-1}$ with change of cleaning method from traditional to Sono-Fenton.

The appearance of peaks at 430, 495, and 676 nm in UV–vis spectra of sonicated biomass, according to interpretations in several reports[48,49], confirmed the presence of chlorophyll and carotenoids. A peak at 270 nm could indicate the presence of polysaccharides as reported by Trabelsi et al.[50]. Sonicated, purified frustules showed only one peak at 230 nm, revealing the presence of silica in the samples[51,52].

First stage of thermal analysis is connected with water desorption, second stage—could be connected to oxidative degradation of organic compounds (i.e. lipids), while third stage revealed degradation of inorganic matter (i.e. magnesium and sodium salts)[53–55]. The highest mass loss (almost 75%) of the sample during the thermal analysis (TGA/DTA) was observed for the sample of SZCZM1342 *N. shiloi*. In comparison for samples SZCZCH193 *N. wachnickianum* and SZCZP1809 *N.* cf. *shiloi* the overall mass loss was 45.8% and 43.8%. This could be explained by presence of high amount of organic matter in sample SZCM1342 *N. shiloi*, considering that this sample had slightly brown color in comparison to other samples (see Supplementary Figure S6).

The EDS study confirmed the presence of silica and oxygen in the frustules. The atomic ratio of O:Si was calculated as 1.69:1, 2.39:1, and 2.27:1 for SZCZCH193, SZCZM1342, and SZCZP1809, respectively, which confirmed that diatom frustules are made from silica mostly in the form of $SiO_2 \cdot nH_2O$—very similar to opal[56]. The distinct peak of carbon (C) could be explained by the presence of the remaining organic compounds surrounding the frustules and chitin template within the diatomaceous silica[57]. The oocccurrence of copper (Cu) is the result of using copper TEM grids.

X-ray diffraction analysis for all strains showed the broad peak indicating the presence of amorphous from of the silica. Thus, it can be concluded that studied samples mostly comprised from amorphous silica. For SZC-ZCH193 N. wachnickianum intense signals are most likely originating from quartz and cristobalite[58]. Alternatively, these signals could indicate the inclusions of magnesium inorganic salts[53]. For SZCZP1809 *N.* cf. *shiloi* the low intensity signals may come from the inclusions of alpha-quartz.

The calculated Tauc plot energy bandgaps (4.40 eV for SZCZCH193 *N. wachnickianum*, 4.05 eV for SZCZM1342 *N. shiloi*, and 4.10 eV for SZCZP1809 *N.* cf. *shiloi*) showed that pure porous biosilica has the properties to be an ultrawide semiconductor[59]. Analysis for amorphous silica[60] revealed a band gap of 3.35 eV. A previous study confirmed that amorphous and crystalline silica has a lower band gap than a porous one[61] and the difference in values for strains could be explained by their differences in pore sizes.

In order to identify the potential functional groups on the surface of the frustules, ATR-FTIR analysis was performed. According to several reports[12,62], the appearance of strong bands at 1150, 1050, 805 and 442 cm^{-1} presented asymmetrical stretching, symmetrical stretching, and bending vibrations of Si–O–Si groups, respectively. There are strong bands recognised by several studies[12,62,63] as C–H stretching at 2981, 2922 (CH_3), 2851 (CH_2), and 854 cm^{-1} (Si–$(CH_3)_2$), and C=O stretching at 1748 cm^{-1}. Four strong peaks at 1630, 1540, 1450, and 1395 cm^{-1} showed the bending vibrations of amino groups, corresponding to a previous study[64]. According to Otzen[65], these peaks indicate the presence of organic compounds surrounding the biosilica. The band at 3660 cm^{-1} is related to a stretching vibration of O–H from SiOH[62], moreover, the broad band from 3500 to 3000 cm^{-1} is related to molecular water[66].

The surface charge of the particles determines the ability of the particles to aggregate. The value of zeta potential is dependent on the properties of the given particles as well as from the pH and ionic strength of the solution. Particles with zeta potential close to zero will aggregate. In turn, stable and non-aggregating systems are characterized by absolute zeta potential values greater than $+/- 25 - +/- 30$ mV[67,68]. The results of zeta potential measurments for pure biosilica samples indicate that at pH greater than 4 aggregation is not occurring and suspensions are stable. The respective results can be confirmed by the photos taken of diatom solutions at different pH (2.0, 3.0, > 4.0) (see Supplementary Figure S7a-c). In the lowest pH a significant aggregation and sample precipitation can be observed. At pH around 3.0 the aggregation is still visible but in lower extend. At pH higher than 4.0 no visible aggregation occurs, the suspension is stable. It is noteworthy to mention, that obtained results differ from the results obtained for pure synthetically prepared silica described by Xu et al.[69]. The different shape of zeta potential plot of examined samples in comparison to Peng Zu's can be explained by the presence of carboxyl (COOH) and amine (NH_2) groups on surface of the biosilica. The presence of respective functional groups was confirmed by FTIR analysis. Moreover, TA/DTA analysis also revealed the presence of high amount of organic matter on the surface of the biosilica. The difference is also notable between the samples of biosilica, for instance, for SZCM1342 *N. shiloi* the positive charge of the surface was observed. The respective difference more likely is due to higher amount of organic matter on the surface of SZCZM1342 *N. shiloi* sample, (i.e. proteins).

The point zero charge (PZC) allows us to find the pH at which the charge at the surface is neutral, therefore in pH less than pH_{pzc} the surface is charged positively, and at pH higher than pH_{pzc} the charge of the surface is negative[70]. Pure biosilica showed a PZC value of $pH_{pzc} = 6.0$ (SZCZCH193 *N. wachnickianum*), and $pH_{pzc} = 5.3$ (SZCZM1342 *N. shiloi*, SZCZP1809 *N.* cf. *shiloi*), which corresponds with several studies of diatomaceous earth: the residual (RDE) and pure (PDE) from Brazil ($pH_{pzc} = 6.75$ and $pH_{pzc} = 6.59$ respectively)[70], from the mine El Pino ($pH_{pzc} = 5.0$)[71], from East Jordan ($pH_{pzc} = 5.4$)[72], from Egypt ($pH_{pzc} = 6.21$)[73]. The results from the PZC study of pure diatomaceous biosilica confirm the presence of O–H groups on the surface and suggest that these hydroxyl groups can gain or lose a proton by changing the pH. Therefore, in acidic media ($pH < pH_{pzc}$), the Si–OH group of biosilica gains a proton and produces Si–OH_2^+, and in basic media ($pH > pHpzc$) the Si–OH group loses a proton and produces Si–O^-[74].

The percentage of MB removal from aqueous solution in all experiments for SZCZCH193 *N. wachnickianum* was lower than for the two remaining strains of *N. shiloi*, these differences could be explained by differences in morphology, pore density, specific surface area, and pore diameter between the *Nanofrustulum* spp. strains.

Nevertheless diatomaceous biosilica showed good removal efficiency compared with other bioadsorbents: 80% for pine tree needles after 240 min of incubation and at pH = 9.2[75], 53% for bacteria[21], up to 90% for fungi *Phellinus adamantinus*[23], up to 90% for sugarcane bagasse[25]. Cleaned frustules of SZCZP1809 *N*. cf. *shiloi* demonstrated an efficiency close to activated carbon prepared from rice husk—98.43% at a flow rate of 1.0 ml min^{-1}[76]. Natural diatomite, a more explored adsorbent than cleaned diatom biosilica (frustules), showed a similar removal efficiency—95.2% at pH = 10[73], 90.75% and 100 mg L^{-1} MB concentration[77], 96.5% for modified diatomite[78], and 100% at 50 mg L^{-1} of MB[79].

Abdelrahman et al.[80] noticed a decrease in the removal of MB under increased concentrations for metal–silica amorphous adsorbents, similar to the removal observed for SZCZCH193 *N. wachnickianum*. However, the hyperbolic increase with concentration for SZCZM1342 *N. shiloi* and SZCZP1809 *N*. cf. *shiloi* was noticed as for MB absorbance onto fava bean peel[81].

Even though the frustules of *Nanofrustulum* spp. showed a high percentage of MB removal, comparable to the efficiency of well-known adsorbents such as natural diatomite and activated carbon, the MB adsorption capacity of *Nanofrustulum* spp. frustules was reported almost 10 times less than diatomite[32], algae *Gellidium* sp.[22], little less than amorphous silica[82], brown algae biomass[83], and almost the same as some zeolites[26] and dead biomass of *Aspergillus niger*[84] (see Supplementary Table S2). Pre-treated frustules of *Pinnularia* showed a higher adsorption capacity[28] than frustules of *Nanofrustulum* spp., which could be explained by morphology and specific surface area of *Pinnularia* and *Nanofrustulum*, as well as by the cleaning method.

The pH of adsorbate solution is considered to be one of the most important parameters in water adsorption processes[74]. The pKa of MB is reported to be 3.8, thus at pH less than 3.8 the surface of MB molecule is not charged, and at pH higher than 3.8—positively charged[85]. Therefore, in pH less than pH$_{pzc}$ of biosilica, the main interaction between MB and frustules are hydrogen bonds and the adsorption process is slower because of repulsive forces between positive sites on the diatomaceous biosilica surface and the cationic dye. In pH higher than pH$_{pzc}$ of biosilica, the positively charged MB and negatively charge frustules interact electrostatically, and the adsorption process is stronger than in acidic media[73]. In our study, an increase in pH resulted in increased removal up to 99.08% for SZCZP1809 *N*. cf. *shiloi*. Similar results reported for diatomite from China[79], diatomaceous earth from Egypt[80], East Jordan[72] and Brazil[71], palygorskite[74]. To achieve desirable pH, trace amounts of 1 M HCl and 1 M NaOH solutions were added and could negatively affect the adsorption as an ionic species (Na$^+$ and Cl$^-$), because in presence of inorganic salts the adsorbent surface becomes not easily accessible for MB. However, there were no influence of these ionic species on the dye uptake observed, presumably due to their low concentrations (less than 0.005 M) in dye solution[86].

Moreover, several kinetic, diffusion, and equilibrium models were applied for better understanding of the possible MB sorption mechanism. The kinetic curve fitted the pseudo-first order model better (with a higher correlation coefficient and lower standard deviation value), therefore we can conclude that the adsorption behaviour of MB on biosilica predominantly followed the pseudo-first order kinetic model: the overall rate of adsorption process was controlled by physisorption, meaning that the molecular interaction between MB and biosilica is governed by van der Waals froces[87]. In order to determine whether the main resistance to mass transfer was in the thin film (boundary layer) surrounding the adsorbent particle, or in the resistance to diffusion inside the particles, Boyd's model was applied. The straight line passing through the origin indicated that the MB adsorption rate is governed by diffusion inside the particles[88]. The high correlation coefficients for Bangham's pore diffusion model indicated that the diffusion of MB molecules onto pores inside biosilica is a rate-controlling step in mass transfer for adsorption process[89]. The adsorption isotherms of SZCZM1342 and SZCZP1809 were characterized as slightly LS-shaped and the isotherm of SZCZCH193 as L-shaped[90], which suggests that the studied diatomaceous biosilica exhibit a high adsorption affinity towards MB dye. Isotherms for *Nanofrustulum* spp. showed a higher affinity to the Sips equation due to high correlation coefficients and low standard deviation values. Based on that, we can conclude that the mechanism of MB sorption onto biosilica predominantly follows the Sips model, which combines the Freundlich and Langmuir isotherms and describes monolayer MB formation onto homogenous and heterogenous sites on biosilica surface[90].

The present research introduced a novel environmentally friendly adsorbent of basic dyes from wastewaters—the porous biosilica originated from marine diatom *Nanofrustulum*. The diatom genus could be considered the most productive microalgae with the highest biomass productivity. The biomass could be further used for extraction of bio-active molecules, e.g. fucoxanthin, known by its antioxidant activity, polyunsaturated fatty acids, with anti-inflammatory properties, and neutral lipids for biodiesel production, while unused diatomaceous biosilica can be purified and efficiently applied in wastewater treatment, due to its porous architecture, the negative surface charge, and relatively high the specific surface area. Several researchers reported the ability of diatomaceous silica to remove heavy metals from aqueous solutions, although the present paper for the first time introduced biosilica as a novel efficient adsorbent of basic dyes from wastewaters. In the future, more intensive research should focus on evaluation of biorefinery potential of these three species, with special focus on co-production of fucoxanthin, fatty acid, and biosilica in economically desirable and eco-friendly way, and adsorption capacity to remove different types of organic pollutants in presence of inorganic salts, which could decrease dye uptake.

Materials and methods

Chemicals.   Methylene blue (> 99%, MW 319.89 Da) was purchased from Aqua-Med® (Łódź, Poland). Thiamine hydrochloride (99%, MW 337.27 Da), biotin (> 99%, MW 244.31 Da), vitamin B12 (> 98%, MW 1355.37 Da) were supplied by Sigma-Aldrich (St. Louis, MO, USA). Hydrogen peroxide (30%, MW 34.01 Da), sodium nitrate (> 99%, MW 84.99 Da), sodium dihydrogen phosphate monohydrate (> 99%, MW 137.99 Da), sodium molybdate dihydrate (> 99%, MW 241.95 Da), manganese (II) chloride tetrahydrate (> 99%, MW 197.91 Da), and cobalt (II) chloride hexahydrate (> 99%, DW 237.93 Da) were obtained from Chempur® (Piekary

Śląskie, Poland). Zinc sulfate heptahydrate (> 99%, MW 287.54 Da), iron (III) chloride hexahydrate (> 99%, MW 270.32 Da), EDTA disodium dihydrate (> 99%, MW 372.24 Da), and copper (II) sulfate pentahydrate (> 99%, MW 249.68 Da) were purchased from Scharlab (Barcelona, Spain). Nonahydrate sodium metasilicate (44–47.5% total solids, MW 284.19 Da) was supplied by Acros Organics, ThermoFisher Scientific (Waltham, MA, USA). Sodium hydroxide, hydrochloric acid and standard buffered solutions pH 2.0, 7.0 and 10.0 were purchased from Sigma-Aldrich. Deionized water was obtained by using a Milli-Q® purification system (Millipore Co., Bedford, MA, USA).

Batch culturing optimization.

Three diatom strains belonging to the genus *Nanofrustulum* were selected as follows: SZCZCH193 *N. wachnickianum* Chunlian Li, A.Witkowski & M.P.Ashworth; SZCZM1342 *N. shiloi* (J.J.Lee, Reimer & McEnery) Round, Hallsteinsen & Paasche[42]; and strain SZCZP1809 morphologically identified by P. Dąbek as *N. cf. shiloi* (sampled from Sea Point, Cape Town, South Africa) were obtained from the Szczecin Diatom Culture Collection (SZCZ), University of Szczecin, Institute of Marine and Environmental Sciences, Poland. Monoclonal cultures were maintained in standard 35‰ Guillard's artificial seawater f/2 medium[91] (880 µM L^{-1} NaNO$_3$, 36 µM L^{-1} NaH$_2$PO$_4$ H$_2$O, 106 µM L^{-1} Na$_2$SiO$_3$ 9H$_2$O, trace metal: 0.08 µM L^{-1} ZnSO$_4$ 7H$_2$O, 0.9 µM L^{-1} MnSO$_4$ H$_2$O, 0.03 L^{-1} µM Na$_2$MoO$_4$ 2H$_2$O, 0.05 µM L^{-1} CoCl$_2$ 6H$_2$O, 0.04 µM L^{-1} CuCl$_2$ 2H$_2$O, 11.7 µM L^{-1} FeCl$_3$ 6H$_2$O, 11.7 µM L^{-1} Na$_2$EDTA 2H$_2$O, vitamin B12, biotin and thiamine) at constant temperature (20 °C) and illumination (100 µmol s^{-1} m^{-2} white light) under a 12:12 day/night light cycle in a plant growth chamber (FITO1400i, Biogenet, Poland). The growth rates were determined by dry biomass weight harvested by centrifugation at 3000 rpm speed and heat drying for 3 days at 50 °C. The regression curve for each strain was built and the specific growth rate (µ) was calculated using the following Eq. (1)[92]:

$$B_t = B_0 \times e^{\mu t} \tag{1}$$

where B_t is the biomass concentration at any time (t) and B_0 is the initial biomass concentration. The diatom strains were observed under an Olympus CKX41 inverted microscope (Olympus- Shinjuku, Tokyo, Japan) at 400 × magnification.

The influence of nutrient enrichment (5, 10, 15, 20 times higher concentration of NO$_3^-$, PO$_4^{3-}$, SiO$_3^{2-}$), salinity (15, 20, and 45%), temperature (15 and 30 °C), and illumination intensity (10, 50, and 150 µmol photons m^{-2} s^{-1}) on biomass accumulation in the late exponential phase was studied for each strain.

Characterization of the diatomaceous biosilica.

Diatoms were harvested in the late exponential phase, centrifuged at 3000 rpm for 15 min, and pellets were purified by 30% H$_2$O$_2$ solution at 110 °C for 2 days following a thorough cleaning with ddH$_2$O. The colorless, cleaned silica was dried at 50 °C for 3 days and later used for characterization experiments. The morphology of the clean diatom frustules was imaged by scanning electron microscopy (SEM) using a Hitachi SU8000 (Hitachi, Tokyo, Japan). For the SEM study, 40 µL of frustules were dried on a Nuclepore™ 5.0 µm Track-Etch Membrane (Whatman™, Cytiva, Germany) at room temperature, later mounted on a M4 cylinder SEM holder, and sputtered with a 10 nm thick gold layer. For the elemental analysis of biosilica, a drop of frustules were placed on a carbon-coated copper grid (Sigma-Aldrich, USA), and the analysis was carried out by a Hitachi STEM S5500 equipped with an EDS detector (Hitachi, Tokyo, Japan). The measurements were performed with an accelerating energy of 30.0 kV and analyzed using NSS ThermoScientific software.

After sonication of the biomass and the cleaned frustules (using Hielscher UP100H ultrasonic processor (Teltow, Germany) for 20 min at 60% amplitude), the suspensions were subjected to the UV–Vis DR 6000 spectrophotometer (HACH-Lange) for optical measurements in the wavelength range of 200–900 nm in 10 mm cuvettes against ddH$_2$O (blank). For absorbances higher than 2, the solution was diluted with ddH$_2$O, the dilution factors were considered in the presented graphs.

FTIR spectra of dried biosilica were obtained in the mid-infrared range (4000–400 cm^{-1}) with the utilization of attenuated total reflection (ATR) mode on an Alpha FTIR spectrometer (Bruker Daltonics, Bremen, Germany).

The low-temperature nitrogen adsorption/desorption isotherms were recorded on Quantachrome Autosorb iQ at 77.35 K.

Thermogravimetric analysis (TA/TGA) of biosilica samples was performed with TA Instruments type SDT 2960 (Artisan Technology, Champaign, IL, USA) using 0–1100 °C temperature range, 100 mL min^{-1} air flow rate and 10 °C min^{-1} heating rate.

Zeta potential measurements were carried out with Malvern Zetasizer NanoZS (Malvern) using DTS1070 cuvette (Malvern). The analysis was performed in the automatic selection mode of voltage and number of runs. Each measurement was repeated three times. Zeta potential was measured in 2.0–12.0 pH range. To maintain the pH 0.1 M NaOH and 0.1 M HCl solutions were used. FiveEasy Plus pH-meter (Mettler Toledo) with a combined electrode with glass membrane and Ag/AgCl reference system (Mettler Toledo) was applied to measure pH of suspensions. The pH-meter was calibrated using standard buffered solutions with pH of 4.0, 7.0, 10.0 before carrying out measurements.

The X-ray diffraction (XRD) spectra were recorded with an X'Pert Pro Analytical X-ray diffractiometer (Phillips, Würzburg, Germany) with Cu-Kα radiation (λ = 0.1541 nm, 40 kV, 30 mA); 1 mL of dried on glass slide sample was scanned in the 2θ range between 5° and 120° with step sizes of 0.0167.

The salt addition method was used to find the PZC of dried biosilica. An aliquot of 20 ml of 0.1 M NaCl was collected in 6 Erlenmeyer flasks and a 2–10 pH range was set by adding 1 M HCl and 1 M NaOH solutions using a pH meter (Voltcraft PH-100ATC). Then in each flask 20 mg of the dried biosilica were added and shaken at speed 100 rpm on an orbital shaker at temperature 23 °C for 24 h. After equilibrium, the contents were filtered,

and the pH values of filtrates were recorded. The PZC value was determined by plotting the graph of initial pH against the change in pH.

Methylene blue (MB) batch sorption. The cleaned frustules (20 ± 0.5 mg DW) were exposed to 10.0 ml of 14.0 mg L^{-1} MB in a 15 ml Falcon tube. The mixture (pH = 7) was mechanically stirred at 3000 rpm at 23 °C for 3 h. The removal of dye was recorded by a UV–Vis DR 6000 (HACH-Lange) spectrophotometer in the wavelength range from 500 to 800 nm at different time points: 5, 15, 30, 45, 60, 75, 90, 105, 120, and 180 min.

Similarly, isotherm studies were performed by measuring 20 ± 0.5 mg of cleaned frustules into 15 ml Falcon tubes containing varying initial concentrations (5, 10, 15, 20, 50, and 100 mg L^{-1}) of MB. The mixture was stirred at 3000 rpm under 23 °C for 120 min, which is necessary to attain equilibrium. The effect of different pH of the initial MB solution (14.0 mg L^{-1}) was recorded for pH = 3, 7, and 11 after 120 min of exposure. The initial pH of the solution was adjusted with 1 M HCl and 1 M NaOH solutions. The absorbance value at 665 nm was used for further calculations.

The quantity of adsorbed MB by biosilica was calculated as follows:

$$q_t = \frac{(C_0 - C_t) \times V}{m} \quad (2)$$

where q_t is the MB adsorbed on the biosilica (mg g^{-1}) at a given time (t); C_0 and C_t are the concentrations of the MB at the start and at the given timepoint (mg L^{-1}), respectively; V is the solution volume (L); m is the biosilica dosage (g).

The percentage of MB removal (%) was calculated by Eq. (3):

$$removal\% = \frac{(C_0 - C_t) \times 100\%}{C_0} \quad (3)$$

where C_0 and C_t are the concentrations of the MB at the start and at the given time (t), respectively (mg L^{-1}).

To understand the possible mechanisms and rate controlling steps of adsorption, several kinetic, diffusion and isotherm models were applied (see Supplementary Table S3).

Furthermore, the applicability of the kinetic and isotherm models was validated by the normalized standard deviation, Δq (%), Eq. (4)

$$\Delta q = 100 \times \sqrt{\frac{\sum \left[\frac{q_{exp} - q_{cal}}{q_{exp}}\right]^2}{(N-1)}} \quad (4)$$

where N is the number of data points, q_{exp} and q_{cal} (mg g^{-1}) are the experimental and calculated adsorption capacity value, respectively.

Data analysis. The batch cultivation experiments were conducted in duplicate. The figures show mean values and standard errors. The significance of differences between different groups was analyzed using a one–way ANOVA analysis with Tukey's post-hoc test, the alpha level 0.05. The batch growth experiment figures, UV–Vis, FTIR spectra, batch adsorption spectra were plotted using MS Excel software. The EDS spectra were obtained using NSS ThermoScientific software. The zeta potential results take into account the Smoluchowski approximation. The analysis data for TA/DTA was proceed with the use of TA Universal Analysis software (TA Instruments, New Castle, DE, USA). The X-ray diffraction pattern analysis was obtained from XRD Malvern Panalytical software (version 1.5a, Almelo, The Netherlands). Modeling of adsorption were performed in OriginPro 2022 software.

Data availability
The authors confirm that the data supporting the findings of this study are available within the article and its Supplementary material. Raw data that supports the fundings of this study are available from the corresponding author, upon reasonable request.

References
1. Armbrust, E. The life of diatoms in the world's oceans. *Nature* **459**, 185–192 (2009).
2. Yool, A. & Tyrrell, T. Role of diatoms in regulating the ocean's silicon cycle. *Global Biogeochem. Cycles* https://doi.org/10.1029/2002GB002018 (2003).
3. Peng, J., Yuan, J. P., Wu, C. F. & Wang, J. H. Fucoxanthin, a marine carotenoid present in brown seaweeds and diatoms: Metabolism and bioactivities relevant to human health. *Mar. Drugs* **9**, 1806–1828. https://doi.org/10.3390/md9101806 (2011).
4. Li, H. Y., Lu, Y., Zheng, J. W., Yang, W. D. & Liu, J. S. Biochemical and genetic engineering of diatoms for polyunsaturated fatty acid biosynthesis. *Mar. Drugs.* **12**, 153–166. https://doi.org/10.3390/md12010153 (2014).
5. Hildebrand, M., Davis, A. K., Smith, S. R., Traller, J. C. & Abbriano, R. The place of diatoms in the biofuels industry. *Biofuels* **3**, 221–240. https://doi.org/10.4155/bfs.11.157 (2012).
6. Uthappa, U. T. *et al.* Nature engineered diatom biosilica as drug delivery systems. *J. Control. Release* **281**, 70–83 (2018).
7. Gale, D. K., Gutu, T., Jiao, J., Chang, C. H. & Rorrer, G. L. Photoluminescence detection of biomolecules by antibody-functionalized diatom biosilica. *Adv. Funct. Mater.* **19**, 926–933. https://doi.org/10.1002/adfm.200801137 (2009).

8. Roychoudhury, P., Bose, R., Dąbek, P. & Witkowski, A. Photonic nano-/microstructured diatom based biosilica in metal modification and removal—A review. *Materials* **15**, 6597. https://doi.org/10.3390/ma15196597(2022) (2022).

9. Branco-Vieira, M. *et al.* Biotechnological potential of *Phaeodactylum tricornutum* for biorefinery processes. *Fuel* **268**, 117357. https://doi.org/10.1016/j.fuel.2020.117357 (2020).

10. Rhoden, C. R. B., da Silva Bruckmann, F., da Rosa Salles, T., Junior, C. G. K. & Mortari, S. R. Study from the influence of magnetite onto removal of hydrochlorothiazide from aqueous solutions applying magnetic graphene oxide. *J. Water Process Eng.* **43**, 102262. https://doi.org/10.1016/j.jwpe.2021.102262 (2021).

11. da Rosa Salles, T. *et al.* Magnetic nanocrystalline cellulose: Azithromycin adsorption and in vitro biological activity against melanoma cells. *J. Polym. Environ.* **30**, 2695–2713 (2022).

12. Roychoudhury, P. *et al.* Study on biogenic spindle-shaped iron-oxide nanoparticles by *Pseudostaurosira trainorii* in field of laser desorption/ionization applications. *Int. J. Mol. Sci.* **23**, 11713. https://doi.org/10.3390/ijms231911713 (2022).

13. Oviedo, L. R. *et al.* Synthesis and characterization of nanozeolite from (agro)industrial waste for application in heterogeneous photocatalysis. *Environ. Sci. Pollut. Res.* **29**, 3794–3807 (2022).

14. Samsami, S., Mohamadizaniani, M., Sarrafzadeh, M. H., Rene, E. R. & Firoozbahr, M. Recent advances in the treatment of dye-containing wastewater from textile industries: Overview and perspectives. *Process Saf. Environ. Prot.* **143**, 138–163 (2020).

15. Balarak, D., Mahdavi, Y., Gharibi, F. & Sadeghi, S. Removal of hexavalent chromium from aqueous solution using canola biomass: Isotherms and kinetics studies. *J. Adv. Environ. Health Res.* **2**, 234–241 (2014).

16. Malatji, N. *et al.* Removal of methylene blue from wastewater using hydrogel nanocomposites: A review. *Nanomater. Nanotechnol.* **11**, 18479804211039424. https://doi.org/10.1177/18479804211039425 (2021).

17. Harvey, J. W. & Keitt, A. S. Studies of the efficacy and potential hazards of methylene blue therapy in aniline-induced methaemoglobinaemia. *Br. J. Haematol.* **54**, 29–41 (1983).

18. El-Bery, H. M., Saleh, M., El-Gendy, R. A., Saleh, M. R. & Thabet, S. M. High adsorption capacity of phenol and methylene blue using activated carbon derived from lignocellulosic agriculture wastes. *Sci. Rep.* **12**, 1–17 (2022).

19. Katheresan, V., Chanced, J. & Lau, S. Y. Efficiency of various recent wastewater dye removal methods: A review. *J. Environ. Chem. Eng.* **6**, 4676–4697. https://doi.org/10.1016/j.jece.2018.06.060 (2018).

20. Ravikumar, K., Deebika, B. & Balu, K. Decolourization of aqueous dye solutions by a novel adsorbent: Application of statistical designs and surface plots for the optimization and regression analysis. *J. Hazard. Mater.* **122**, 75–83 (2005).

21. Kilany, M. Isolation, screening and molecular identification of novel bacterial strain removing methylene blue from water solutions. *Appl. Water. Sci.* **7**, 4091–4098. https://doi.org/10.1007/s13201-017-0565-x (2017).

22. Vilar, V. J., Botelho, C. M. & Boaventura, R. A. Methylene blue adsorption by algal biomass based materials: Biosorbents characterization and process behaviour. *J. Hazard. Mater.* **147**, 120–132 (2007).

23. Sintakindi, A. & Ankamwar, B. Uptake of methylene blue from aqueous solution by naturally grown *Daedalea africana* and *Phellinus adamantinus* fungi. *ACS Omega* **5**, 12905–12914. https://doi.org/10.1021/acsomega.0c00673 (2020).

24. Ponnusami, V., Rajan, K. S. & Srivastava, S. N. Application of film-pore diffusion model for methylene blue adsorption onto plant leaf powders. *Chem. Eng. J.* **163**, 236–242 (2010).

25. Meili, L. *et al.* Adsorption of methylene blue on agroindustrial wastes: Experimental investigation and phenomenological modelling. *Prog. Biophys. Mol. Biol.* **141**, 60–71 (2019).

26. Han, R. *et al.* Study of equilibrium, kinetic and thermodynamic parameters about methylene blue adsorption onto natural zeolite. *Chem. Eng. J.* **145**, 496–504 (2009).

27. Al-Ghouti, M. A., Khraisheh, M. A., Ahmad, M. N. & Allen, S. Adsorption behaviour of methylene blue onto Jordanian diatomite: A kinetic study. *J. Hazard. Mater.* **165**, 589–598 (2009).

28. Van Eynde, E. *et al.* Effect of pretreatment and temperature on the properties of *Pinnularia biosilica* frustules. *RSC Adv.* **4**, 56200–56206. https://doi.org/10.1039/C4RA09305D (2014).

29. Gholami, P., Khataee, A. & Bhatnagar, A. Environmentally superior cleaning of diatom frustules using sono-Fenton process: Facile fabrication of nanoporous silica with homogeneous morphology and controlled size. *Ultrason. Sonochem.* **64**, 105044. https://doi.org/10.1016/j.ultsonch.2020.105044 (2020).

30. Roychoudhury, P. *et al.* Diatom mediated production of fluorescent flower shaped silver-silica nanohybrid. *Materials* **14**, 7284. https://doi.org/10.3390/ma14237284 (2021).

31. Gola, D. *et al.* Silver nanoparticles for enhanced dye degradation. *Curr. Res. Green Sustain. Chem.* **4**, 100132. https://doi.org/10.1016/j.crgsc.2021.100132 (2021).

32. Touina, A. *et al.* Characterization and efficient dye discoloration of Algerian diatomite from Ouled Djilali-Mostaganem. *SN Appl. Sci.* **3**, 1–13 (2021).

33. Liu, S., Chen, X., Ai, W. & Wei, C. A new method to prepare mesoporous silica from coal gasification fine slag and its application in methylene blue adsorption. *J. Clean. Prod.* **212**, 1062–1071. https://doi.org/10.1016/j.jclepro.2018.12.060 (2019).

34. Lyu, R. *et al.* Efficient adsorption of methylene blue by mesoporous silica prepared using sol-gel method employing hydroxyethyl cellulose as a template. *Colloids Surf. A Physiochem. Eng. Asp.* **606**, 125425. https://doi.org/10.1016/j.colsurfa.2020.125425 (2020).

35. Bruckmann, F. D. S. *et al.* Biological applications of silica-based nanoparticles. *Magnetochemistry* **8**, 131. https://doi.org/10.3390/magnetochemistry8100131 (2022).

36. Bruckmann, F. D. S. *et al.* Synthesis, characterization and cytotoxicity evaluation of magnetic nanosilica in L929 cell line. *Discip. Sci. Nat. Tecnol.* **21**, 1–14 (2020).

37. Delasoie, J. & Zobi, F. Natural diatom biosilica as microshuttles in drug delivery systems. *Pharmaceutics* **11**, 537. https://doi.org/10.3390/pharmaceutics11100537 (2019).

38. Grubišić, M. *et al.* Bioprospecting of microalgae isolated from the Adriatic Sea: Characterization of biomass, pigment, lipid and fatty acid composition, and antioxidant and antimicrobial activity. *Molecules* **27**, 1248. https://doi.org/10.3390/molecules27041248 (2022).

39. Sahin, M. S., Khazi, M. I., Demirel, Z. & Dalay, M. C. Variation in growth, fucoxanthin, fatty acids profile and lipid content of marine diatoms *Nitzschia* sp. and Nanofrustulum shiloi in response to nitrogen and iron. *Biocatal. Agric. Biotechnol.* **17**, 390–398 (2019).

40. Demirel, Z., Imamoglu, E. & Dalay, M. C. Growth kinetics of *Nanofrustulum shiloi* under different mixing conditions in flat-plate photobioreactor. *Braz. Arch. Biol. Technol.* https://doi.org/10.1590/1678-4324-2020190201 (2020).

41. Jiang, Y. *et al.* Effect of silicate limitation on growth, cell composition, and lipid production of three native diatoms to Southwest Texas desert. *J. Appl. Phycol.* **27**, 1433–1442. https://doi.org/10.1007/s10811-014-0463-7 (2015).

42. Li, C. L. *et al.* The morphology and molecular phylogenetics of some marine diatom taxa within the Fragilariaceae, including twenty undescribed species and their relationship to Nanofrustulum, Opephora and Pseudostaurosira. *Phytotaxa* **355**, 1–104 (2018).

43. Thommes, M. *et al.* Physisorption of gases, with special reference to the evaluation of surface area and pore size distribution (IUPAC Technical Report). *Pure Appl. Chem.* **87**, 1051–1069 (2015).

44. Sprynskyy, M. *et al.* Diatom biosilica doped with palladium (II) chloride nanoparticles as new efficient photocatalysts for methyl orange degradation. *Int. J. Mol. Sci.* **22**, 6734. https://doi.org/10.3390/ijms22136734 (2021).

45. Vrieling, E. G. *et al.* Salinity-dependent diatom biosilicification implies an important role of external ionic strength. *Proc. Natl. Acad. Sci. U.S.A.* **104**, 10441–10446 (2017).

46. Luo, Y. *et al.* Study on the hemostasis characteristics of biomaterial frustules obtained from diatom *Navicula australoshetlandica* sp.. *Materials* **14**, 3752. https://doi.org/10.3390/ma14133752 (2021).
47. Dalagan, E. G. & Enriquez, E. P. Interaction of diatom silica with graphene. *Philipp. Sci. Lett.* **6**, 119–127 (2013).
48. Jeffrey, S. W. & Humphrey, G. F. New spectrophotometric equations for plants, algae and natural phytoplankton. *Biochem. Physiol. Pflanzen* **167**, 191–194 (1975).
49. Haryatfrehni, R., Dewi, S. C., Meilianda, A., Rahmawati, S. & Sari, I. Z. R. Preliminary study the potency of macroalgae in yogyakarta: Extraction and analysis of algal pigments from common gunungkidul seaweeds. *Proc. Chem.* **14**, 373–380 (2015).
50. Trabelsi, L., M'sakni, N. H., Ben Ouada, H., Bacha, H. & Roudesli, S. Partial characterization of extracellular polysaccharides produced by cyanobacterium *Arthrospira platensis*. *Biotechnol. Bioprocess Eng.* **14**, 27–31 (2009).
51. Verma, J. & Bhattacharya, A. Analysis on synthesis of silica nanoparticles and its effect on growth of T. Harzianum & Rhizoctonia species. *Biomed. J. Sci. Technol. Res.* **10**, 7890–7897. https://doi.org/10.26717/BJSTR.2018.10.001972 (2018).
52. Prasetyanto, E. A., Sujandi, S., Lee, S. C. & Park, S. E. Highly dispersed CuO nanoparticles on SBA-16 type mesoporous silica with cyclam SBA-16 as a precursor. *Bull. Korean Chem. Soc.* **28**, 2359–2362. https://doi.org/10.5012/bkcs.2007.28.12.2359 (2007).
53. Choi, S. B., Kim, N. W., Lee, D. K. & Yu, H. Growth mechanism of cubic MgO granule via common ion effect. *J. Nanosci. Nanotechnol.* **13**, 7577–7580. https://doi.org/10.1166/jnn.2013.7882 (2013).
54. Chen, W. H., Chu, Y. S., Liu, J. L. & Chang, J. S. Thermal degradation of carbohydrates, proteins and lipids in microalgae analyzed by evolutionary computation. *Energy Convers. Manag.* **160**, 209–219. https://doi.org/10.1016/j.enconman.2018.01.036 (2018).
55. Dong, B., Xu, Y., Lin, S. & Dai, X. Characterizing and exploring the formation mechanism of salt deposition by reusing advanced-softened, silica-rich, oilfield-produced water (ASOW) in superheated steam pipeline. *Sci. Rep.* **5**, 17274. https://doi.org/10.1038/srep17274 (2015).
56. Desikachary, T. V. & Dweltz, N. E. The chemical composition of the diatom frustule. *Proc. Indian Acad. Sci.* **53**, 157–165 (1961).
57. Brunner, E. *et al.* Chitin-based organic networks: an integral part of cell wall biosilica in the diatom *Thalassiosira pseudonana*. *Angew. Chem. Int. Ed. Engl.* **48**, 9724–9727. https://doi.org/10.1002/anie.200905028 (2009).
58. Nowak, A. P. *et al.* Diatoms biomass as a joint source of biosilica and carbon for lithium-ion battery anodes. *Materials* **13**, 1673. https://doi.org/10.3390/ma13071673 (2020).
59. Higashiwaki, M., Kaplar, R., Pernot, J. & Zhao, H. Ultrawide bandgap semiconductors. *Appl. Phys. Lett.* **118**, 200401. https://doi.org/10.1063/5.0055292 (2021).
60. Jyoti, A., Singh, R. K., Kumar, N., Aman, A. K. & Kar, M. Synthesis and properties of amorphous nanosilica from rice husk and its composites. *Mater. Sci. Eng. B Solid. State Mater. Adv. Technol.* **263**, 114871. https://doi.org/10.1016/j.mseb.2020.114871 (2021).
61. Chen, Z., Lee, T. Y. & Bosman, G. Electrical band gap of porous silicon. *Appl. Phys. Lett.* **64**, 3446–3448 (1994).
62. Camargo, E. *et al.* Chemical and optical characterization of Psammodictyon panduriforme (Gregory) Mann comb. nov. (Bacillariophyta) frustules. *Opt. Mater. Express* **6**, 1436–1443. https://doi.org/10.1364/OME.6.001436 (2016).
63. Chen, C. *et al.* Micro characterization and degradation mechanism of liquid silicone rubber used for external insulation. *IEEE Trans. Dielectr. Electr. Insul.* **22**, 313–321 (2015).
64. Li, K. M., Jiang, J. G., Tian, S. C., Chen, X. J. & Yan, F. Influence of silica types on synthesis and performance of amine–silica hybrid materials used for CO_2 capture. *J. Phys. Chem. C.* **118**, 2454–2462. https://doi.org/10.1021/jp408354r (2014).
65. Otzen, D. The role of proteins in biosilicification. *Scientifica* **2012**, 867562. https://doi.org/10.6064/2012/867562 (2012).
66. Musić, S., Filipović-Vinceković, N. & Sekovanić, L. Precipitation of amorphous SiO_2 particles and their properties. *Braz. J. Chem. Eng.* **28**, 89–94 (2011).
67. Pryshchepa, O., Pomastowski, P. & Buszewski, B. Silver nanoparticles: Synthesis, investigation techniques, and properties. *Adv. Colloid Interface Sci.* **284**, 102246. https://doi.org/10.1016/j.cis.2020.102246 (2020).
68. Gumustas, M., Sengel-Turk, C. T., Gumustas, A., Ozkan, S. A. & Uslu, B. Effect of polymer-based nanoparticles on the assay of antimicrobial drug delivery systems. In *Multifunctional Systems for Combined Delivery, Biosensing and Diagnostics* (ed. Grumezescu, A. M.) (Elsevier, 2017).
69. Xu, P., Wang, H., Tong, R., Du, Q. & Zhong, W. Preparation and morphology of SiO_2/PMMA nanohybrids by microemulsion polymerization. *Colloid Polym. Sci.* **284**, 755–762. https://doi.org/10.1007/s00396-005-1428-9 (2006).
70. Semiao, M. A., Haminiuk, C. W. I. & Maciel, G. M. Residual diatomaceous earth as a potential and cost effective biosorbent of the azo textile dye Reactive Blue 160. *J. Environ. Chem. Eng.* **8**, 103617. https://doi.org/10.1016/j.jece.2019.103617 (2020).
71. Bautista, M. M. C. *et al.* Evaluation of diatomaceous earth in the removal of crystal violet dye in solution. *J. Appl. Res. Technol.* **20**, 387–398 (2022).
72. Khraisheh, M. A. M., Al-Ghouti, M. A., Allen, S. J. & Ahmad, M. N. Effect of OH and silanol groups in the removal of dyes from aqueous solution using diatomite. *Water Res.* **39**, 922–932 (2005).
73. Mohamed, E. A. *et al.* Enhancing adsorption capacity of Egyptian diatomaceous earth by thermo-chemical purification: Methylene blue uptake. *J. Colloid Interface Sci.* **534**, 408–419 (2019).
74. Zhang, J. *et al.* Adsorption of methylene blue from aqueous solution onto multiporous palygorskite modified by ion beam bombardment: Effect of contact time, temperature, pH and ionic strength. *Appl. Clay Sci.* **83**, 137–143 (2013).
75. Yagub, M. T., Sen, T. K. & Ang, H. M. Equilibrium, kinetics, and thermodynamics of methylene blue adsorption by pine tree leaves. *Wat. Air Soil Poll.* **223**, 5267–5282. https://doi.org/10.1007/s11270-012-1277-3 (2012).
76. Rahman, M. A., Amin, S. R. & Alam, A. S. Removal of methylene blue from waste water using activated carbon prepared from rice husk. *Dhaka Univ. J. Sci.* **60**, 185–189 (2012).
77. Zhang, J., Ping, Q., Niu, M., Shi, H. & Li, N. Kinetics and equilibrium studies from the methylene blue adsorption on diatomite treated with sodium hydroxide. *Appl. Clay Sci.* **83**, 12–16 (2013).
78. Ebrahimi, P. & Kumar, A. Diatomite chemical activation for effective adsorption of methylene blue dye from model textile wastewater. *Int. J. Environ. Sci. Dev.* **12**, 23–28 (2021).
79. Al-Ghouti, M. A., Khraisheh, M. A. M., Allen, S. J. & Ahmad, M. N. The removal of dyes from textile wastewater: A study of the physical characteristics and adsorption mechanisms of diatomaceous earth. *J. Environ. Manage* **69**, 229–238 (2003).
80. Abdelrahman, E. A., Hegazey, R. M. & El-Azabawy, R. E. Efficient removal of methylene blue dye from aqueous media using Fe/Si, Cr/Si, Ni/Si, and Zn/Si amorphous novel adsorbents. *J. Mater. Res. Technol.* **8**, 5301–5313. https://doi.org/10.1016/j.jmrt.2019.08.051 (2019).
81. Bayomie, O. S. *et al.* Novel approach for effective removal of methylene blue dye from water using fava bean peel waste. *Sci. Rep.* **10**, 1–10 (2020).
82. Ahmed, M. N. & Ram, R. N. Removal of basic dye from waste-water using silica as adsorbent. *Environ. Pollut.* **77**, 79–86 (1992).
83. Caparkaya, D. & Cavas, L. Biosorption of methylene blue by a brown alga *Cystoseira barbatula* Kützing. *Acta Chim. Slov.* **55**, 547–553 (2008).
84. Fu, Y. & Viraraghavan, T. Removal of a dye from an aqueous solution by the fungus *Aspergillus niger*. *Water Qual. Res. J.* **35**, 95–112 (2000).
85. Kim, J. R., Santiano, B., Kim, H. & Kan, E. Heterogeneous oxidation of methylene blue with surface-modified iron-amended activated carbon. *Am. J. Analyt. Chem.* **4**, 34470. https://doi.org/10.4236/ajac.2013.47A016 (2013).
86. Boumediene, M., Benaïssa, H., George, B., Molina, S. & Merlin, A. Effects of pH and ionic strength on methylene blue removal from synthetic aqueous solutions by sorption onto orange peel and desorption study. *J. Mater. Environ. Sci.* **9**, 1700–1711 (2018).
87. Liu, Y. & Liu, Y. J. Biosorption isotherms, kinetics and thermodynamics. *Sep. Purif. Technol.* **61**, 229–242 (2008).

88. Eba, F. *et al.* Evaluation of the absorption capacity of the natural clay from Bikougou (Gabon) to remove Mn(II) from aqueous solution. *Int. J. Eng. Thechnol.* **2**, 5001–5016 (2010).
89. Pourhakkak, P., Taghizadeh, A., Taghizadeh, M., Ghaedi, M. & Haghdoust, S. Fundamentals of adsorption technology. In *Adsorption: Fundamental Processes and Application* (ed. Chaedi, M.) (Elsevier, 2021).
90. Kalam, S., Abu-Khamsin, S. A., Kamal, M. S. & Patil, S. Surfactant adsorption isotherms: A review. *ACS Omega* **6**, 32342–32348. https://doi.org/10.1021/acsomega.1c04661 (2021).
91. Guillard, R. R. Culture of phytoplankton for feeding marine invertebrates. In *Culture of Marine Invertebrate Animals* (eds Smith, W. L. & Chanley, M. H.) (Springer, 1975).
92. Kirchman, D. L. Calculating microbial growth rates from data on production and standing stocks. *Mar. Ecol. Prog. Ser.* **233**, 303–306 (2002).

Acknowledgements

Author contributions

A.G. and P.R. conceptualized and designed the work. A.G., P.R., P.D., P.P., P.P., M.G. and I.N. developed methodology. A.G. performed growth and biosilica characterization experiments, made kinetic and isotherm modeling, interpreted the data, prepared Figures and Tables, and drafted the work. A.G. and P.R. performed MB removal experiments. A.G. and O.P. performed ATR-FTIR analysis. A.G. and M.G. performed SEM and EDS investigation. O.P. performed zeta potential measurements. J.P. and P.P. performed TGA/DTA and XRD analysis and described the results. A.F.G. performed the N_2 adsorption/desorption experiments. P.R., P.D., J.P., O.P., P.P., P.P., M.G., R.D., A.F.G., I.N., K.J.K., B.B., and A.W. reviewed and edited the work. A.W. supervise the work. B.B. acquired the funding. All the authors approved the manuscript.

Competing interests

The authors declare no competing interests.

Additional information

Supplementary Information The online version contains supplementary material available at https://doi.org/10.1038/s41598-023-36408-6.

Correspondence and requests for materials should be addressed to A.G.

Reprints and permissions information is available at www.nature.com/reprints.

Publisher's note Springer Nature remains neutral with regard to jurisdictional claims in published maps and institutional affiliations.

A novel effective bio-originated methylene blue adsorbent – the porous biosilica from three marine diatom strains of *Nanofrustulum* spp. (Bacillariophyta)

Aleksandra Golubeva[1*], Piya Roychoudhury[1], Przemysław Dąbek[1], Jagoda Pałczyńska[2], Oleksandra Pryshchepa[3], Piotr Piszczek[2], Paweł Pomastowski[3], Michał Gloc[4], Renata Dobrucka[4,5], Agnieszka Feliczak-Guzik[6], Izabela Nowak[6], Krzysztof J. Kurzydłowski[7], Bogusław Buszewski[8,9] and Andrzej Witkowski[1]

Supplementary material

Supplementary Table S1. Surface porous structure for SZCZCH193 *N. wachnickianum*, SZCZM1342 *N. shiloi*, SZCZP1809 *N.* cf. *shiloi* frustules.

Strain	Specific Surface Area ($m^2 g^{-1}$)	Pore Volume ($cm^3 g^{-1}$)	Average Pore Diameter (nm)
SZCZCH193 *N. wachnickianum*	25.319	0.267	4.217
SZCZM1342 *N. shiloi*	21.777	0.113	2.073
SZCZP1809 *N.* cf. *shiloi*	35.231	0.174	1.971

Supplementary Table S2. Adsorption capacity of different adsorbents

Adsorbent	Adsorption capacity ($mg g^{-1}$)	Reference
Defatted *Scenedesmus* sp. biomass	7.73	[1]
Amorphous silica	22.66	[2]
Zeolite	19.94	[3]
Diatomite	116.59	[4]

Brown algae *Cystoseira barbatula*	38.61	[5]
Dead fungus *Aspergillus niger*	18.54	[6]
Algae *Gelidium* **sp.**	171	[7]
Pre-treated *Pinnularia* **frustules**	26.2	[8]
Diatomaceous mesoporous biosilica *Nanofrustulum* **spp.**		
SZCZCH193 *N. wachnickianum*	8.39	
SZCZM1342 *N. shiloi*	19.02	
SZCZP1809 *N.* **cf.** *shiloi*	15.17	

Supplementary Table S3. Kinetic, diffusion and isotherm models used in this study

Models	Equation	Description of parameters	References
Kinetic study			
Pseudo-first order (nonlinear)	$q_t = q_1(1 - e^{-kt})$ (4)	q_t (mg g^{-1}) – amount adsorbed at given time (t, min)	[9]
Pseudo-second order (nonlinear)	$q_t = \dfrac{k_2 q_2^2 t}{1 + k_2 q_2 t}$ (5)	q_1 (mg g^{-1}) – adsorbent capacity at equilibrium k (min^{-1}) – Pseudo-first order constant rate	[10]
Elovich (nonlinear)	$q_t = {}^1\!/_\beta \ln(1 + \alpha\beta t)$ (6)	q_2 (mg g^{-1}) – adsorbent capacity at equilibrium k_2 (g (mg min)$^{-1}$) – Pseudo-second order constant rate α (mg (g min)$^{-1}$) – initial adsorption rate β (mg g^{-1}) – desorption constant	[11]
Diffusion study			
Intra-particle diffusion (nonlinear)	$q_t = k_{wm} t^{0.5} + B$ (7)	q_t (mg g^{-1}) – amount adsorbed at given time (t, min)	[12]
Boyd (linear)	$B_t = -0.4977 - \ln(1 - \dfrac{q_t}{q_e})$ (8) *B_t vs. t plot*	K_{wm} (mg (g min$^{0.5}$)$^{-1}$)– Intra-particle diffusion rate constant B (mg g^{-1}) – intercept q_e (mg g^{-1}) – amount adsorbed at equilibrium	[13]

Bangham's pore diffusion (linear)	$\log\log\left(\dfrac{C_0}{C_0 - mq_t}\right)$ $= \log\left(\dfrac{mK_\beta}{2.303V}\right)$ $+ \Delta\beta\log t$	(9)	B_t – mathematical function of F		[14]
			F – the fraction of metal ion adsorbed at any time (t)		
	$\log\log\left(\dfrac{C_0}{C_0 - mq_t}\right)$ v.s $\log t$ plot		C_0 (mg L^{-1}) – initial concentration of MB		
			m (g) – mass of adsorbent g		
			$\Delta\beta$ and K_β - Bangham constants		
			V (mL)– volume of solution		

Equilibrium study (isotherms)

Langmuir (nonlinear)	$q_e = \dfrac{Q^0_{max}K_LC_e}{1 + K_LC_e}$	(10)	q_e (mg g^{-1}) – adsorption capacity at equilibrium		[15]
Freundlich (nonlinear)	$q_e = K_FC_e^n$	(11)	C_e (mg L^{-1}) – concentration of MB dye at equilibrium		[16]
Sips (nonlinear)	$q_t = \dfrac{q_m(K_SC_e)^n}{1 + (K_SC_e)^n}$	(12)	Q^0_{max} (mg g^{-1}) – maximum monolayer adsorption capacity of Langmuir		[17]
			K_L (L mg^{-1}) – Langmuir constant		
			K_F [(mg g^{-1}) (mg L^{-1})$^{-n}$] – Freundlich constant		
			n – dimensionless Freundlich intensity parameter		
			q_m (mg g^{-1}) – the Sips maximum adsorption capacity		

K_S [(mg L^{-1})$^{-1/n}$] – the Sips equilibrium constant

n – the exponent of Sips where $0 < 1/n \leq 1$
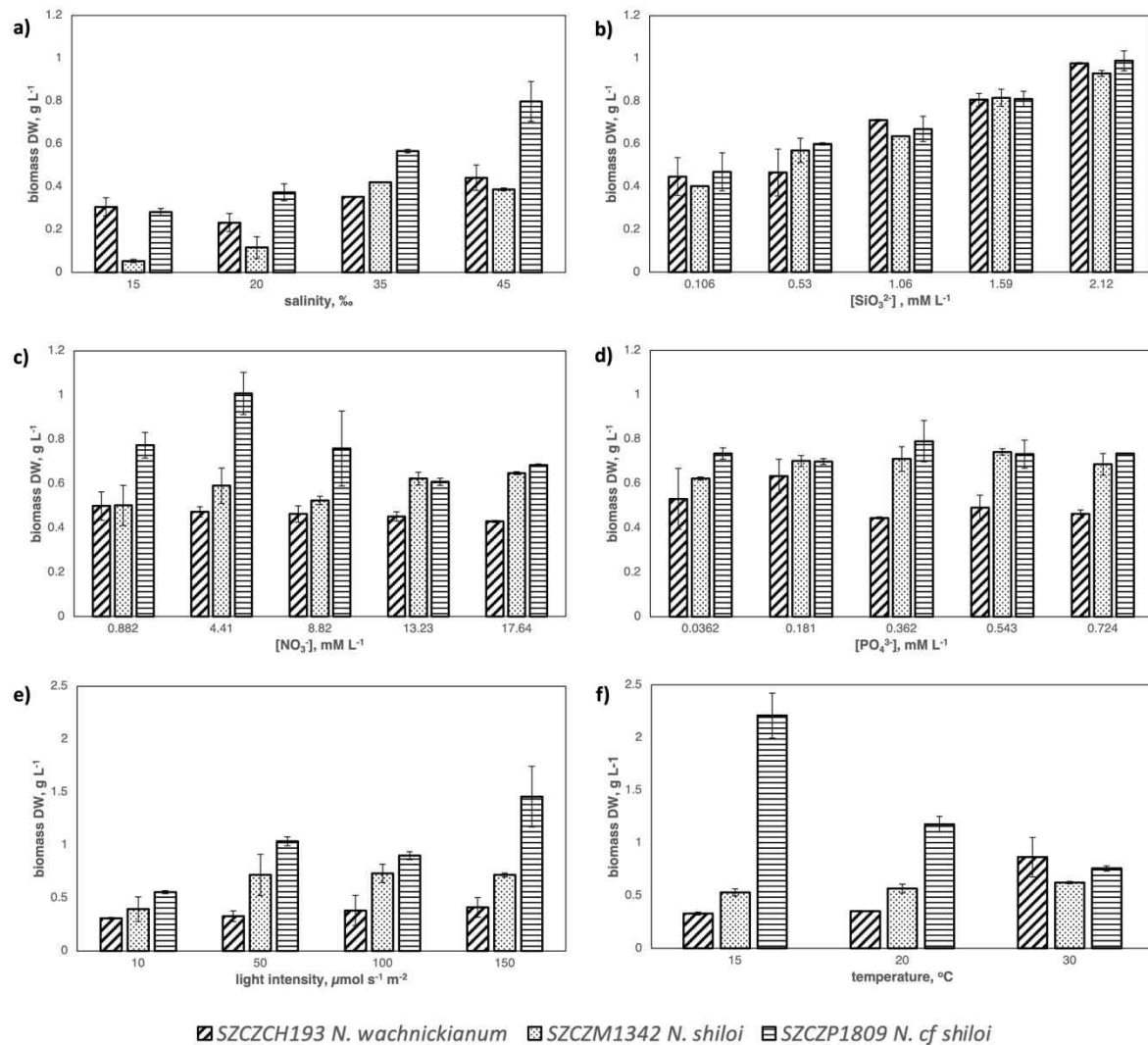
Supplementary Figure S1. Optimization of batch cultivation of SZCZCH193 *N. wachnickianum*, SZCZM1342 *N. shiloi*, SZCZP1809 *N.* cf. *shiloi*: the influence of salinity (a), silicate (b), nitrate (c), and phosphate (d) concentrations in f/2 medium, light intensity (e), and temperature (f) on biomass DW accumulation.
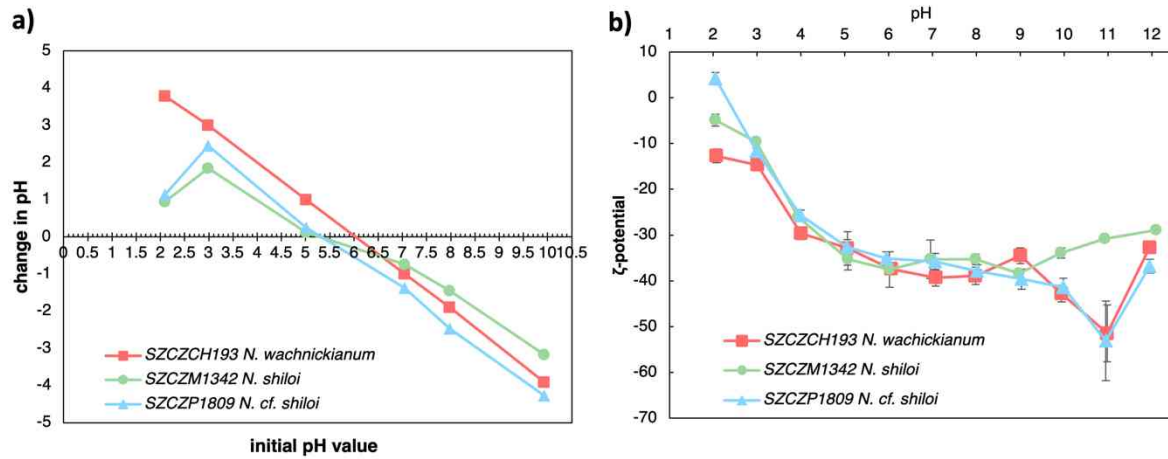
Supplementary Figure S2. (a) The point zero charge (PZC) and (b) the zeta potential of pure diatomaceous biosilica of SZCZCH193 *N. wachnickianum*, SZCZM1342 *N. shiloi*, SZCZP1809 *N.* cf. *shiloi*
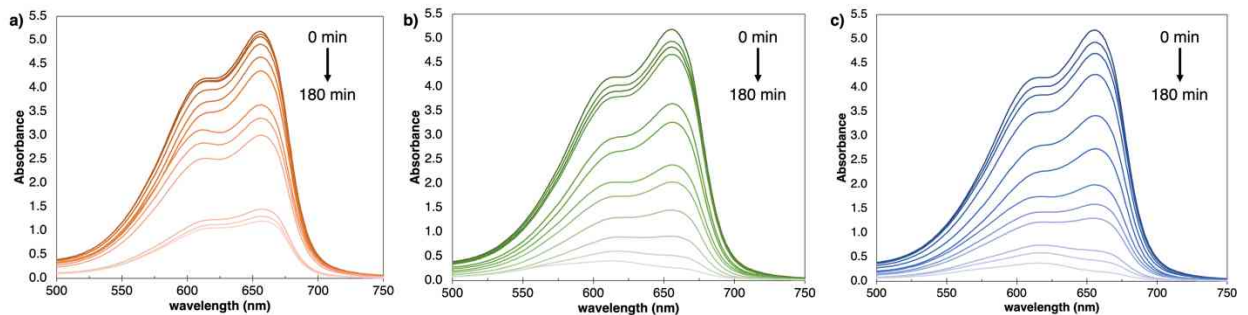
Supplementary Figure S3. The UV-vis spectra showing MB removal with time onto pure biosilica of (a) SZCZCH193 *N. wachnickianum*, (b) SZCZM1342 *N. shiloi*, (c) SZCZP1809 *N.* cf. *shiloi*
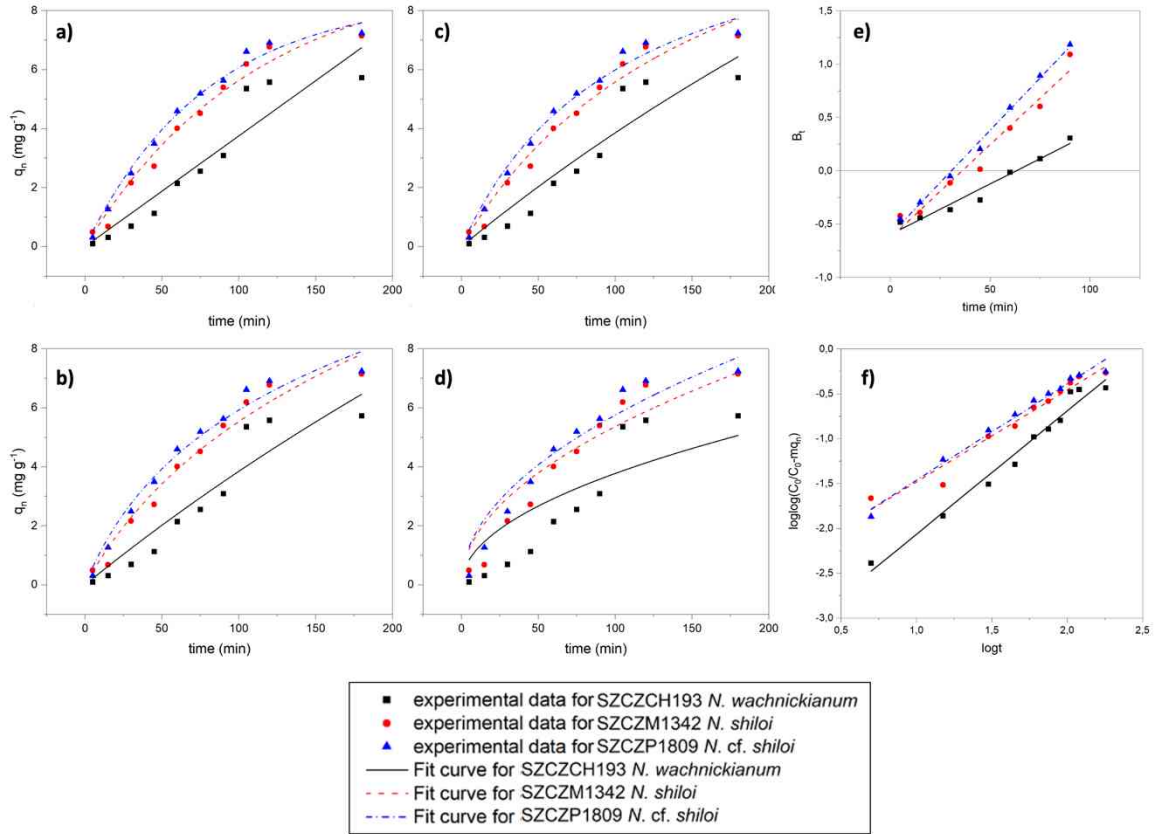
Supplementary Figure S4. Adsorption kinetic study: (a) pseudo-first order, (b) Elovich, and (c) pseudo-second order models, and diffusion study: (d) Intra-particle diffusion (Webber-Morris), (e) Boyd's and (f) Bangham's pore diffusion models (experimental data: black squares – SZCZCH193 *N. wachnickianum*, red circles – SZCZM1342 *N. shiloi*, blue triangles – SZCZP1809 *N.* cf. *shiloi;* calculated modeling data: black line for SZCZCH193 *N. wachnickianum*, red line for SZCZM1342 *N. shiloi*, blue line for SZCZP1809 *N.* cf. *shiloi*).
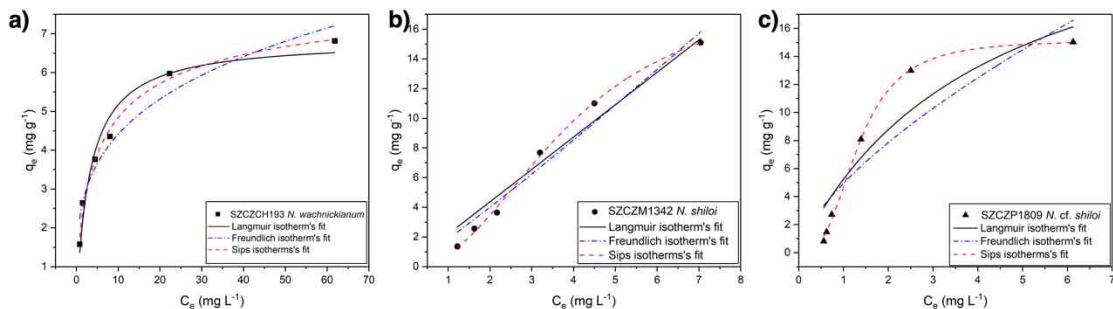
Supplementary Figure S5. Adsorption isotherms of MB onto pure biosilica of (a) SZCZCH193 *N. wachnickianum*, (b) SZCZM1342 *N. shiloi*, (c) SZCZP1809 *N.* cf. *shiloi*
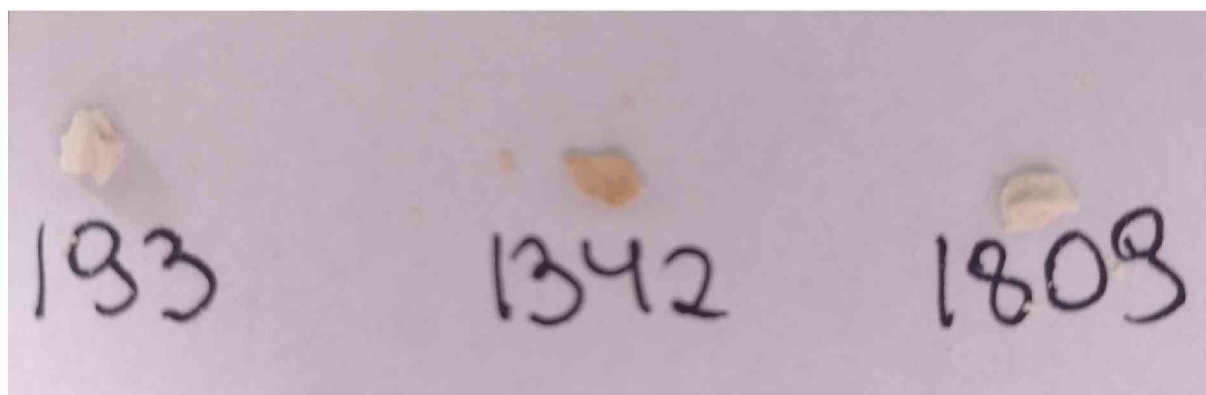
Supplementary Figure S6. Color of dried biosilica samples for TGA/DTA analysis: SZCZCH193 *N. wachnickianum*, SZCZM1342 *N. shiloi*, and SZCZP1809 *N.* cf. *shiloi*
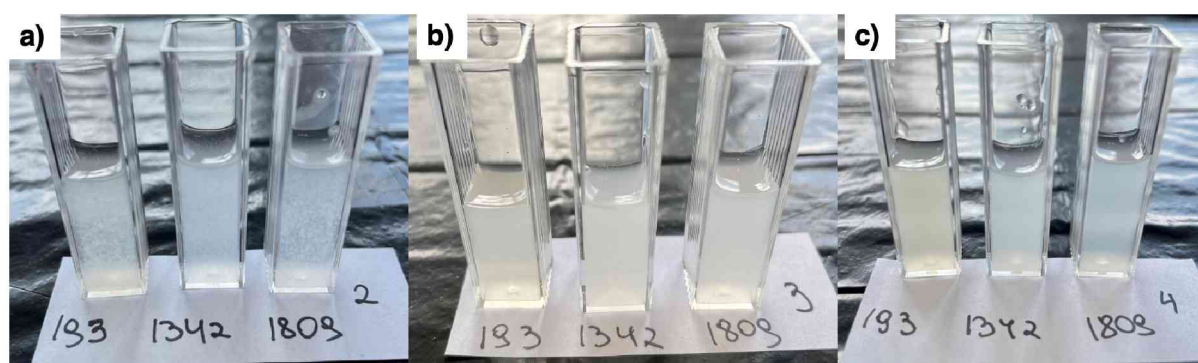
Supplementary Figure S7. Agglomeration of biosilica samples under (a) 2, (b) 3, (c) >4 pH in zeta potential measurements: SZCZCH193 *N. wachnickianum*, SZCZM1342 *N. shiloi*, and SZCZP1809 *N.* cf. *shiloi*

Supplementary References

1. Chandra, T.S. *et al.* Defatted algal biomass as a non-conventional low-cost adsorbent: surface characterization and methylene blue adsorption characteristics. *Bioresour. Technol.* **184**, 395-404 (2015).

2. Ahmed, M.N. & Ram, R.N. Removal of basic dye from waste-water using silica as adsorbent. *Environ. Pollut.* **77**, 79-86 (1992).

3. Han, R. *et al.* Study of equilibrium, kinetic and thermodynamic parameters about methylene blue adsorption onto natural zeolite. *Chem. Eng. J.* **145**, 496-504 (2009).

4. Touina, A. *et al.* Characterization and efficient dye discoloration of Algerian diatomite from Ouled Djilali-Mostaganem. *SN Appl. Sci.* **3**, 1-13 (2021).

5. Caparkaya, D. & Cavas, L. Biosorption of Methylene Blue by a Brown Alga Cystoseira barbatula Kützing. *Acta Chim. Slov.* **55**, 547-553 (2008).

6. Fu, Y. & Viraraghavan, T.Removal of a dye from an aqueous solution by the fungus Aspergillus niger. *Water Qual. Res. J.* **35**, 95-112 (2000).

7. Vilar, V.J., Botelho, C.M., & Boaventura, R.A. Methylene blue adsorption by algal biomass based materials: biosorbents characterization and process behaviour. *J. Hazard. Mater.* **147**, 120-132 (2007).

8. Van Eynde, E. *et al.* Effect of pretreatment and temperature on the properties of *Pinnularia* biosilica frustules. *RSC Adv.* **4**, 56200-56206; 10.1039/C4RA09305D (2014).

9. Lagergren, S. Zur theorie der sogenannten adsorption geloster stoffe. *Kungliga svenska vetenskapsakademiens. Handlingar* **24**, 1-39 (1898).

10. Blanchard, G., Maunaye, M., & Martin, G. Removal of heavy metals from waters by means of natural zeolites. *Water Res. 18*, 1501-1507 (1984).

11. Aharoni, C. & Tompkins, F.C. Kinetics of adsorption and desorption and the Elovich equation, in *Advances in Catalysis, 21 (eds.* Eley, D.D., Pines, H., Weisz, P.B.) 1-49 (Academic Press Inc., 1970).

12. Weber Jr, W.J. & Morris, J.C. Kinetics of adsorption on carbon from solution. *J. Sanit. Eng. Div.* **89**, 31-59 (1963).

13. Boyd, G.E., Adamson, A.W. & Myers Jr, L.S. The exchange adsorption of ions from aqueous solutions by organic zeolites. II. Kinetics. *J. Am. Chem. Soc.* **69**, 2836-2848 (1947).

14. Bangham, A.D., Standish, M.M. & Watkins, J.C. Diffusion of univalent ions across the lamellae of swollen phospholipids. *J. Mol. Biol.* **13**, 238-252 (1965).

15. Langmuir, I. The adsorption of gases on plane surfaces of glass, mica and platinum. *J. Am. Chem. Soc.* **40**, 1361-1403 (1918).

16. Freundlich, H.M.F. Over the adsorption in solution. *J. Phys. Chem. 57*, 385-471 (1906).

17. Sips, R. On the structure of a catalyst surface. *J. Phys. Chem. 16*, 490-495 (1948).

Aleksandra Golubeva

Institute of Marine and Environmental Sciences

University of Szczecin

Mickiewicza 16a, 70-383 Szczecin, Poland

Declaration

I hereby declare that my contribution in the preparation of article: "A novel effective bio-originated methylene blue adsorbent: the porous biosilica from three marine diatom strains of *Nanofrustulum* spp. (Bacillariophyta)" published in Scientific Reports, 13: 9168, of which I am co-author with Roychoudhury P., Dąbek P., Pałczyńska J., Pryshchepa O., Piszczek P., Pomastowski P., Gloc M., Dobrucka R., Feliczak-Guzik A., Nowak I., Kurzydłowski, K.J., Buszewski B., and Witkowski A. equals to 65% (percent). For the purpose of the study, I conceptualized the study, performed the experiments, interpreted the data, performed statistical analysis and mathematical modeling, prepared figures and tables, drafted original manuscript, revised it after co-authors suggestions, led the revision process after the peer review, and submitted final version.

Aleksandra Golubeva

Instytut Nauk o Morzu i Środowisku: ul. Adama Mickiewicza 16, 70-383 Szczecin
Sekretariat: tel. 914442461, e-mail sekretariat.nms@usz.edu.pl
Dyrektor Instytutu: tel. 91 4442462, e-mail: dyrektor.nms@usz.edu.pl

Dr Piya Roychoudhury

Institute of Marine and Environmental Sciences

University of Szczecin

Mickiewicza 16a, 70-383 Szczecin, Poland

Declaration

I hereby declare that my contribution in the preparation of article: "A novel effective bio-originated methylene blue adsorbent: the porous biosilica from three marine diatom strains of *Nanofrustulum* spp. (Bacillariophyta)" published in Scientific Reports, 13: 9168, of which I am co-author with Golubeva A., Dąbek P., Pałczyńska J., Pryshchepa O., Piszczek P., Pomastowski P., Gloc M., Dobrucka R., Feliczak-Guzik A., Nowak I., Kurzydłowski, K.J., Buszewski B., and Witkowski, A. equals to 10% (percent). For the purpose of the study, I took part in conceptualization, methodology, SEM, EDS, UV-vis, FTIR, and batch adsorption experiments, and reviewed the original draft.

Piya Roychoudhury

Instytut Nauk o Morzu i Środowisku: ul. Adama Mickiewicza 16, 70-383 Szczecin
Sekretariat: tel. 914442461, e-mail sekretariat.nms@usz.edu.pl
Dyrektor Instytutu: tel. 91 4442462, e-mail: dyrektor.nms@usz.edu.pl

Dr Przemysław Dąbek

Institute of Marine and Environmental Sciences

University of Szczecin

Mickiewicza 16a, 70-383 Szczecin, Poland

Declaration

I hereby declare that my contribution in the preparation of article: "A novel effective bio-originated methylene blue adsorbent: the porous biosilica from three marine diatom strains of *Nanofrustulum* spp. (Bacillariophyta)" published in Scientific Reports, 13: 9168, of which I am co-author with Golubeva A., Roychoudhury P., Pałczyńska J., Pryshchepa O., Piszczek P., Pomastowski P., Gloc M., Dobrucka R., Feliczak-Guzik A., Nowak I., Kurzydłowski, K.J., Buszewski B., and Witkowski, A. equals to 2% (percent). For the purpose of the stu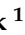dy, I supervised the work of PhD student Golubeva A., and took part in methodology development and revision of the original draft.

Przemysław Dąbek

Instytut Nauk o Morzu i Środowisku: ul. Adama Mickiewicza 16, 70-383 Szczecin
Sekretariat: tel. 914442461, e-mail sekretariat.nms@usz.edu.pl
Dyrektor Instytutu: tel. 91 4442462, e-mail: dyrektor.nms@usz.edu.pl

UNIWERSYTET
MIKOŁAJA KOPERNIKA
W TORUNIU
Interdyscyplinarne Centrum
Nowoczesnych Technologii

Dr. Paweł Pomastowski, DSc., Prof. NCU

Centre for Modern Interdisciplinary Technologies

Nicolaus Copernicus University in Toruń

Wileńska 4, 87-100, Toruń, Poland

Declaration

I hereby declare that my contribution in the preparation of article: "A novel effective bio-originated methylene blue adsorbent: the porous biosilica from three marine diatom strains of *Nanofrustulum* spp. (Bacillariophyta)" published in Scientific Reports, 13: 9168, of which I am co-author with Golubeva A., Roychoudhury P., Dąbek P., Pałczyńska J., Pryshchepa O., Piszczek P., Gloc M., Dobrucka R., Feliczak-Guzik A., Nowak I., Kurzydłowski K.J., Buszewski B., and Witkowski A. equals to 3% (percent). For the purpose of the study, I took part in conceptualization of the study, reviewed the original draft, and helped with revision in peer-review process.

Prof. Dr hab. Andrzej Witkowski

Institute of Marine and Environmental Sciences

University of Szczecin

Mickiewicza 16a, 70-383 Szczecin, Poland

Declaration

I hereby declare that my contribution in the preparation of article: "A novel effective bio-originated methylene blue adsorbent: the porous biosilica from three marine diatom strains of *Nanofrustulum* spp. (Bacillariophyta)" published in Scientific Reports, 13: 9168, of which I am co-author with Golubeva A., Roychoudhury P., Dąbek P., Pałczyńska J., Pryshchepa O., Piszczek P., Pomastowski P., Gloc M., Dobrucka R., Feliczak-Guzik A., Nowak I., Kurzydłowski, K.J., and Buszewski B. equals to 1% (percent). For the purpose of the study, I supervised the work of PhD student Golubeva A., and revised of the original draft.

Andrzej Witkowski

ANNEX II

Golubeva, A., Roychoudhury, P., Dąbek, P., Pryshchepa, O., Pomastowski, P., Pałczyńska, J., Piszczek, P., Gloc, M., Dobrucka, R., Feliczak-Guzik, A., Nowak, I., Buszewski, B. & Witkowski, A. (2023b) Removal of the Basic and Diazo Dyes from Aqueous Solution by the Frustules of *Halamphora* cf. *salinicola* (Bacillariophyta). *Marine Drugs*, *21*, 312.

Removal of the Basic and Diazo Dyes from Aqueous Solution by the Frustules of *Halamphora* cf. *salinicola* (Bacillariophyta)

Aleksandra Golubeva [1,*], Piya Roychoudhury [1], Przemysław Dąbek [1], Oleksandra Pryshchepa [2], Paweł Pomastowski [2], Jagoda Pałczyńska [3], Piotr Piszczek [3], Michał Gloc [4], Renata Dobrucka [4,5], Agnieszka Feliczak-Guzik [6], Izabela Nowak [6], Bogusław Buszewski [7,8] and Andrzej Witkowski [1,*]

[1] Institute of Marine and Environmental Sciences, University of Szczecin, Mickiewicza 16a, 70-383 Szczecin, Poland; przemyslaw.dabek@usz.edu.pl (P.D.)

[2] Centre for Modern Interdisciplinary Technologies, Nicolaus Copernicus University, Wileńska 4, 87-100 Toruń, Poland; 503144@doktorant.umk.pl (O.P.); p.pomastowski@umk.pl (P.P.)

[3] Department of Inorganic and Coordination Chemistry, Faculty of Chemistry, Nicolaus Copernicus University, Gagarina 7, 87-100 Toruń, Poland; 296600@stud.umk.pl (J.P.); piszczek@umk.pl (P.P.)

[4] Faculty of Materials Science and Engineering, Warsaw University of Technology, Wołoska 141, 02-507 Warsaw, Poland; michalgloc@wp.pl (M.G.); renata.dobrucka@pw.edu.pl (R.D.)

[5] Department of Industrial Products and Packaging Quality, Institute of Quality Science, Poznań University of Economics and Business, al. Niepodległości 10, 61-875 Poznan, Poland

[6] Department of Applied Chemistry, Faculty of Chemistry, Adam Mickiewicz University, Uniwersytetu Poznańskiego 8, 61-614 Poznań, Poland; agnieszka.feliczak-guzik@amu.edu.pl (A.F.-G.); nowakiza@amu.edu.pl (I.N.)

[7] Department of Environmental Chemistry and Bioanalysis, Faculty of Chemistry, Nicolaus Copernicus University, Gagarina 7, 87-100 Toruń, Poland; bbusz@umk.pl

[8] Prof. Jan Czochralski Kuyavian-Pomeranian Research & Development Centre, Krasińskiego 4, 87-100 Toruń, Poland

* Correspondence: alexandra.golubeva@phd.usz.edu.pl (A.G.); andrzej.witkowski@usz.edu.pl (A.W.); Tel.: +48-534-030-336 (A.G.)

Abstract: Industrial wastes with hazardous dyes serve as a major source of water pollution, which is considered to have an enormous impact on public health. In this study, an eco-friendly adsorbent, the porous siliceous frustules extracted from the diatom species *Halamphora* cf. *salinicola*, grown under laboratory conditions, has been identified. The porous architecture and negative surface charge under a pH of 7, provided by the various functional groups via Si–O, N–H, and O–H on these surfaces, revealed by SEM, the N_2 adsorption/desorption isotherm, Zeta-potential measurement, and ATR-FTIR, respectively, made the frustules an efficient mean of removal of the diazo and basic dyes from the aqueous solutions, 74.9%, 94.02%, and 99.81% against Congo Red (CR), Crystal Violet (CV), and Malachite Green (MG), respectively. The maximum adsorption capacities were calculated from isotherms, as follows: 13.04 mg g^{-1}, 41.97 mg g^{-1}, and 33.19 mg g^{-1} against CR, CV, and MG, respectively. Kinetic and isotherm models showed a higher correlation to Pore diffusion and Sips models for CR, and Pseudo-Second Order and Freundlich models for CV and MG. Therefore, the cleaned frustules of the thermal spring-originated diatom strain *Halamphora* cf. *salinicola* could be used as a novel adsorbent of a biological origin against anionic and basic dyes.

Keywords: biosilica; adsorption; congo red; crystal violet; malachite green

1. Introduction

Diatoms (*Bacillariophyceae*) are photosynthetic unicellular eukaryotes with unique three-dimensional perforated shells surrounding the cells—the so-called frustules. They are responsible for 20% of global primary production and play an essential role in the silicon cycle, due to their ability to uptake silicic acid from the environment and deposit it within their cell walls in the form of opal (SiO_2 nH_2O) [1]. Their adaptable metabolism allows

them to grow in any kind of environment, from marine and fresh waters to thermal geysers and polar glaciers [2]. In recent years a great selection of various diatom taxa have been studied for their industrial potential [3].

Halamphora spp. has gained attention due to its ability to accumulate a high amount of triglycerides (TAG) for biodiesel production [4–7], fatty acids for the aquaculture [8,9] and cosmetics industries [10], as well as fucoxanthin and chrysolaminarin with antioxidant, anticancer, and immunomodulatory capacities for pharmaceutical purposes [11,12]. Thus, *Halamphora* strains can be cultivated on an industrial scale for biodiesel, while wastes from lipid extraction may be purified and clean biosilica can be used in different applications. A single report of *Halamphora* spp. mediated biosynthesis of hybrid SiO_2–Ag nanodendrites is available [13], while other pennate diatoms have shown promising results in metal nanoparticles biosynthesis (*Gedaniella flavovirens*, *G. mutabilis*, and *Nanofrustulum shiloi*) [14,15], drug delivery (*Amphora subtropica* and *Nitzschia* sp.) [16,17], biosensing (*Amphora* sp., *Pinnularia* sp., and *Pseudostaurosira trainorii*) [18–21], and heavy metal remediation (*Nitzschia* spp., *Navicula* spp., and *Pheodactylum tricornutum*) [22,23]. Furthermore, the growth rate and morphology of *H. veneta* have been proposed for the toxicological assessment of copper and mercury in aquatic environments [24].

Water pollution is recognized to have an enormous impact on public health, and the discharge from dye-based industries serves as a major source of contamination: up to 15% of the total dyes used in the textile industry remain untreated and are lost in emissions [25]. Synthetic dyes, released into waters by textile, leather, paper, printing, cosmetics, plastic, and pharmaceutical industries, usually resist ordinary treatment techniques and can have a negative influence on both aquatic organisms and human health [26]. Dyes are classified according to their chemical structure and application: acidic, basic, direct, reactive, etc. [27]. Crystal Violet (CV) and Malachite Green (MG) are water soluble basic cationic dyes and belong to the triphenylmethane type, whereas Congo Red (CR) is an acidic anionic diazo dye, based on a benzidine—a well-known human carcinogen [28]. These dyes are used as models for evaluation of the adsorption ability of different adsorbents. A variety of techniques have been used for the removal of CR, CV, and MG from aqueous solutions: photocatalytic degradation [29–31], sonication [32–34], ozonation [35–37], oxidation [38–40], Fenton process [41–43], and biological degradation [44–46]. However, all these approaches have limitations in terms of efficiency, cost, and design [47]. The most effective and widely used treatment for dye removal from aqueous solutions is adsorption. Various adsorbents of diverse origins have been used in the basic and anionic dye adsorption processes, namely activated carbon [48–50], nanoparticles [51–53], nanotubes [54–56], waste materials [57–59], naturally occurring materials such as clays [60–62], zeolites and diatomite [63–65], and bio-adsorbents [66–68]. To the best of our knowledge, reports about the utilization of pure diatom frustules in the dye adsorption procedure are limited [69,70]. The main difference between the purified frustules from diatom culture and diatomaceous earth is the presence of organic compounds on the frustule surface, whose functional groups play an important role in the adsorption process.

This study presents a novel eco-friendly adsorbent of biological origin, derived from the diatom strain *Halamphora* cf. *salinicola* Levkov and Díaz, produced under laboratory conditions, characterized morphologically and functionally for the first time, and which could perform against anionic and basic dyes with a high removal efficiency and adsorption capacity.

2. Results

2.1. Batch Cultivation of SZCZM1454 H. cf. salinicola

Figure 1 presents the growth of strain SZCZM1454 *H.* cf. *salinicola*. From the second day of cultivation this strain grew exponentially until it reached its maximum on the 22nd day. The maximum biomass yield DW ($m_{max} = 0.73 \pm 0.047$ g L^{-1}) and the maximum cell density ($C_{max} = 2.46 \pm 0.004 \times 10^6$ cells per ml) were observed after 23 days. By the end of the cultivation period, uptake of nitrate was 79.5% and silicate was 30% (0.7 mM

and 0.033 mM of nitrate and silicate, respectively), whereas phosphate uptake was the highest at 99.9% (0.0359 mM). The maximum specific growth rate was calculated as 0.081 d^1 (R^2 = 0.935) for the biomass yield and 0.113 div d^{-1} (R^2 = 0.949) for cell density. After the 22 days, the biomass yield and cell density had not changed for several days, which indicated the start of the stationary growth phase.
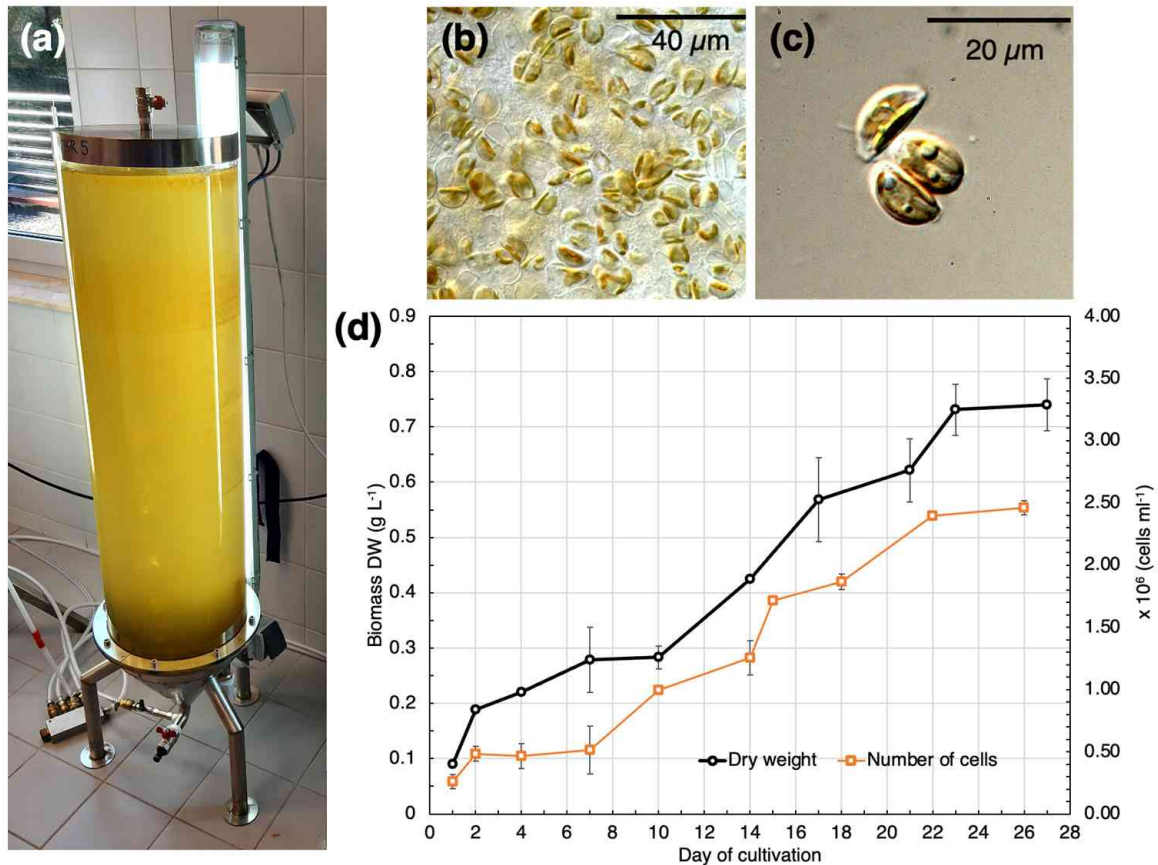
Figure 1. Growth of SZCZM1454 *H.* cf. *salinicola*: (**a**) photobioreactor (PBR) for batch cultivation; (**b**,**c**) cell culture under light microscope (LM) with different magnification; and (**d**) growth curve for the dry biomass yield and the number of cells.

Table 1 shows the dry biomass yield of strain SZCZM1454 *H.* cf. *salinicola* grown under a variety of nutrient concentrations, salinity, illumination intensity, and temperature. The increased concentration of silicates in the f/2 medium resulted in a significant change in the dry biomass yield (one-way ANOVA, *p* = 0.0002): the highest biomass accumulation was observed for samples grown in medium with 20 times higher silicate concentration (Turkey HSD, *p* = 0.001 between 2.12 and 0.11, 0.53, or 1.06 mM; and *p* = 0.035 between 2.12 and 1.59 mM). Likewise, a significant difference in the biomass yield was observed for samples cultivated in a medium with a higher salinity (one-way ANOVA, *p* = 0.043; Turkey HSD, *p* = 0.0082 between 20 ppt and 45 ppt). Furthermore, a higher cultivation temperature (30 °C) of cultivation resulted in a higher biomass yield (one-way ANOVA, *p* = 0.006; Turkey HSD, *p* = 0.0063, 0.0113 between 30 °C and 15 °C, 20 °C, respectively), whereas low light intensity (10 µmol s^{-1} m^{-2}) decreased the biomass accumulation in comparison with a higher illumination (one-way ANOVA, *p* = 0.0082; Turkey HSD, *p* = 0.0075, 0.016 between 10 and 50, 150 µmol s^{-1} m^{-2}, respectively). No significant differences were observed in the biomass yield for samples grown in a medium with higher concentrations of nitrate (one-way ANOVA *p* = 0.344) and phosphate (one-way ANOVA *p* = 0.224).

Table 1. The dry biomass yield (g L^{-1} DW) of SZCZM1454 *H.* cf. *salinicola* under different cultivation parameters.

| Nitrate, mM					Phosphate, mM				
0.88	4.41	8.82	13.23	17.64	0.04	0.18	0.36	0.54	0.72
0.610 ± 0.0206	0.556 ± 0.0295	0.627 ± 0.0300	0.670 ± 0.0899	0.641 ± 0.0457	0.646 ± 0.0321	0.631 ± 0.0226	0.604 ± 0.0707	0.701 ± 0.0074	0.704 ± 0.0530
Silicate, mM					Temperature, °C			
0.11	0.53	1.06	1.59	2.12	15	20	30	
0.501 ± 0.0045	0.644 ± 0.0274	0.646 ± 0.0442	0.825 ± 0.0093	0.964 ± 0.0471	0.431 ± 0.0015	0.480 ± 0.00402	0.700 ± 0.0346	
Light, μmol s^{-1} m^{-2}				Salinity, ppt				
10	50	100	150	15	20	35	45	
0.342 ± 0.0619	0.712 ± 0.0527	0.547 ± 0.0511	0.641 ± 0.0436	0.388 ± 0.0779	0.355 ± 0.1576	0.603 ± 0.0751	0.969 ± 0.0228	

2.2. Characterization of the Frustule Surface

The SEM images (Figure 2a,b) revealed the surface topography of the SZCZM1454 *Halamphora* cf. *salinicola* frustules. The siliceous frustule is composed of two valves which are semi-lunate in shape and dorsiventral with slightly capitate apices. The dorsal margin of the valve is gently arched, and its ventral margin is straight. The length and width of the valves were measured as 14.0–19.0 mm and 3.0–4.15 mm, respectively. Pores, called areolae, are spherical in the center of the valve face and become elliptical on each side of a slit, called the raphe. The size of the areolae decrease towards the dorsal margin, and the length and width of the areolae were calculated as 0.07–0.23 mm and 0.1–0.34 mm, respectively. The areolae are arranged in rows, the transapical striae, and consist of 1–2 to 7–9 areolae. The number of striae was calculated as 39–48.
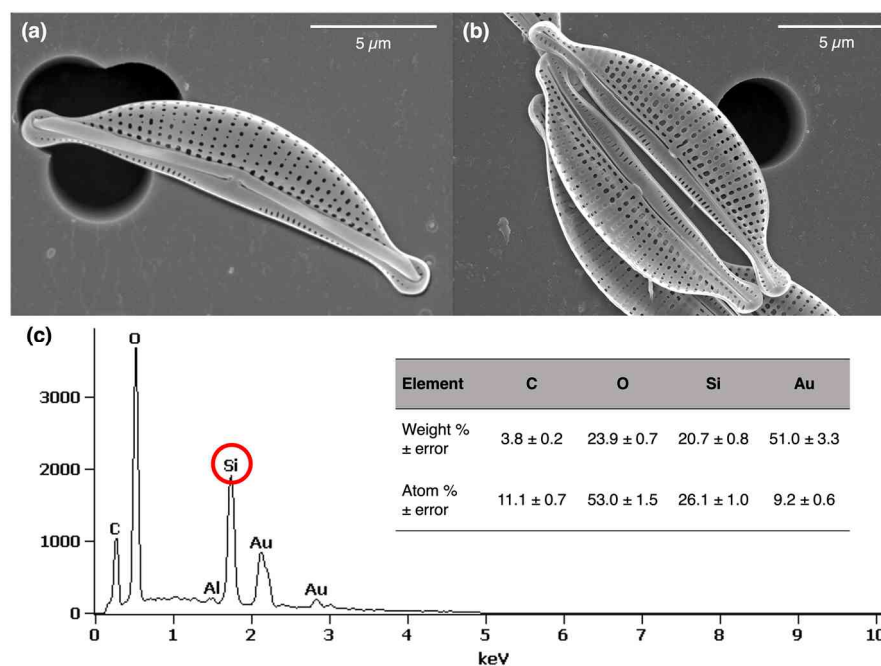
Figure 2. Morphology and the elemental analysis of the SZCZM1454 *H.* cf. *salinicola* frustules: (**a**,**b**) SEM images revealed the surface topography of the frustules and (**c**) the EDS spectra detected the presence of silicon (Si) on the surface of the frustules.

The elemental composition analysis of the frustules (Figure 2c), demonstrated by the Energy dispersive X-ray spectroscopy, demonstrated the presence of silica (Si), carbon (C), oxygen (O), and gold (Au) on the sample's surface. The weight percentage was calculated as 20.7, 3.8, 23.9, and 51.0%, respectively, and the atomic percentage was estimated as 26.1, 11.1, 53.0, and 9.2%, respectively. Au peaks indicate a gold layer from sample preparation for SEM and EDS analyses.

Demonstrated in Figure 3a, the UV–vis spectra of the sonicated biomass (green line) showed several distinct peaks at 230, 270, 430, 495, and 676 nm. The UV–vis spectra of the sonicated frustules (black line) revealed only one distinct peak at 230 nm.
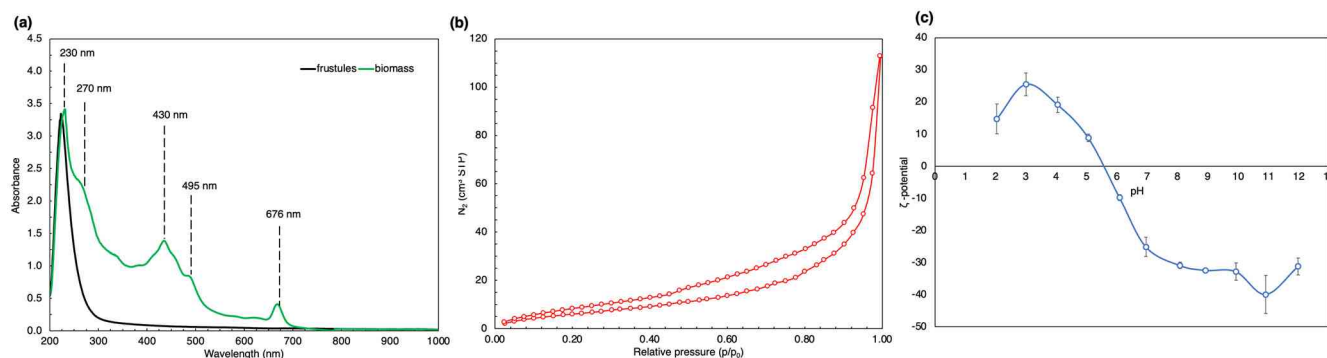
Figure 3. Surface characterization of the SZCZM1454 *H.* cf. *salinicola* frustules: (**a**) the UV–vis spectroscopy revealed the presence of one peak for the cleaned frustules and several peaks for the biomass; (**b**) the low temperature N_2 adsorption/desorption isotherm; and (**c**) the zeta potential values recorded for the different pH.

The results of low-temperature N_2 adsorption/desorption were analysed using the BET (Brunauer–Emmett–Teller) method to determine the specific surface area of the frustules and the BJH (Barrett–Joyner–Halenda) algorithm was used for the calculation of pore volume and diameter, presented in Table 2. Figure 3b shows the N_2 adsorption/desorption isotherm.

Table 2. Porous structure of the surface of the SZCZM1454 *H.* cf. *salinicola* frustules.

Specific Surface Area (m^2 g^{-1})	Pore Volume (cm^3 g^{-1})	Pore Diameter Distribution (nm)
26.922	0.175	3–35

Figure 3c presents the measured zeta potential values as a function of pH. The biosiliceous frustules revealed the positive charge in a pH range of 2–5.5, and at a pH higher than 7, the negative charge.

On the X-ray powder diffractogram (Figure 4a) the signals at $2\theta \approx 23.4°$, $29.7°$, $36.84°$, $39.8°$, $43.6°$, $47.8°$, $48.6°$, $56.9°$, and $57.8°$ can be distinguished. Furthermore, there is a continuous elevation in the 2θ range from $10°$ to $35°$.

The ATR-FTIR spectra, presented in Figure 4b, demonstrates several distinct peaks, confirming the existence of O–H, C–H, C = O, N–H, and Si–O functional groups on the surface of the frustules: 3660 and 1670 cm^{-1}; 2980 and 2890 cm^{-1}; 1720 cm^{-1}; 1470 and 1380 cm^{-1}; and 1150, 1075, 956, 805, and 445 cm^{-1}, respectively.
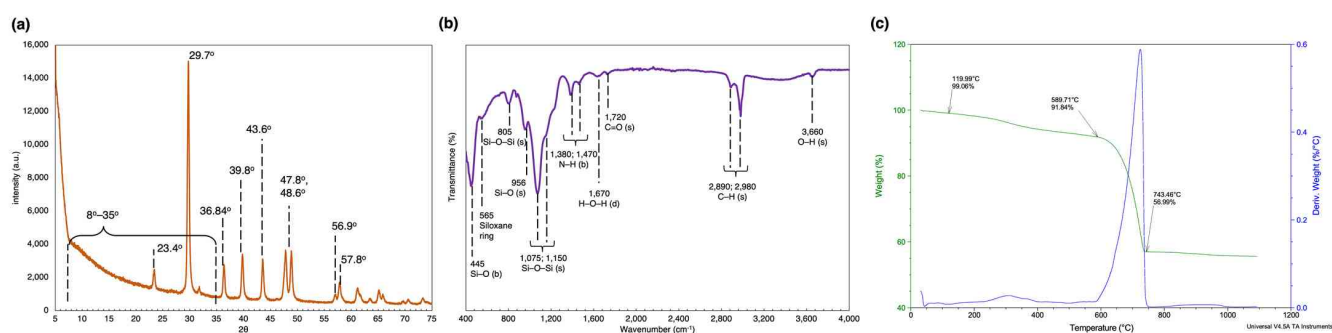
Figure 4. Characterization of the SZCZM1454 *H.* cf. *salinicola* frustules: (**a**) the X-ray powder diffractogram; (**b**) the FTIR spectra; and (**c**) the TGA/DTA analysis.

Thermogravimetric analysis (Figure 4c) showed the overall weight loss of the sample as almost 45%. The TGA curve revealed a gradual decrease in the temperature range of 0–600 °C with an overall mass loss of nearly 18.16%. Using differential thermal analysis (DTA) it was possible to distinguish two main steps in the relevant range. The first one that ended at nearly 120 °C was about 1%. The second, in the range of 150–400 °C, showed a mass loss of 7.2%. At temperatures higher than 600 °C, drastic weight loss occurred.

2.3. Batch Adsorption Study

The frustules of SZCZM1454 *H.* cf. *salinicola* showed good removal activity for the diazo dyes—Congo Red (CR), and the basic dyes—Crystal Violet (CV) and Malachite Green (MG). Figure 5c–e shows visible discoloration of the aqueous dye solutions after 240 min of exposure. The UV–vis measurements confirmed the elimination of dyes over time—Figure 5a shows rapid removal of CV in the first five minutes of exposure, followed by a gradual increase until the system reached equilibrium at 60 min. The removal of MG shows a similar pattern, but at a slower rate with 50% removal achieved after 10 min of exposure, and the system only reached equilibrium after 120 min. CR removal gradually increased after 30 min until it reached equilibrium after 180 min. The frustules of SZCZM1454 *H.* cf. *salinicola* exhibited the highest removal efficiency against the basic dyes with 94.02% and 99.81% removal of CV and MG, respectively, after 60 min and 240 min. However, their efficiency against the diazo dye was lower, with 74.9% removal of CR after 240 min of exposure. The change in adsorption capacity over time is presented in Figure 5b. The adsorption capacity is estimated to be 8.81, 10.44, and 11.86 mg g $^{-1}$ for CR, CV, and MG, respectively.

Linear kinetic and diffusion models (Figure S1) were applied to investigate possible mechanisms behind sorption of different types of dyes onto SZCZM1454 *H.* cf. *salinicola*. Table 3 shows the kinetic parameters for each model. The closest to a unity correlation coefficient R^2 (higher than 0.93) was observed for the Pseudo-First Order, Intra particle diffusion, and Pore diffusion models for the adsorption of the diazo dye CR (Figure S1a,c,d). However, the Chi-square values were considerably lower for the Intra particle and Pore diffusion models. Figure S1b presents the Pseudo-Second Order model as the best fit for the experimental data of CV and MG adsorption onto the SZCZM1454 *H.* cf. *salinicola* frustules, with the highest correlation coefficient (higher than 0.95 and 0.99, respectively) and the lowest Chi-square value (around 3 and 0.2, respectively).
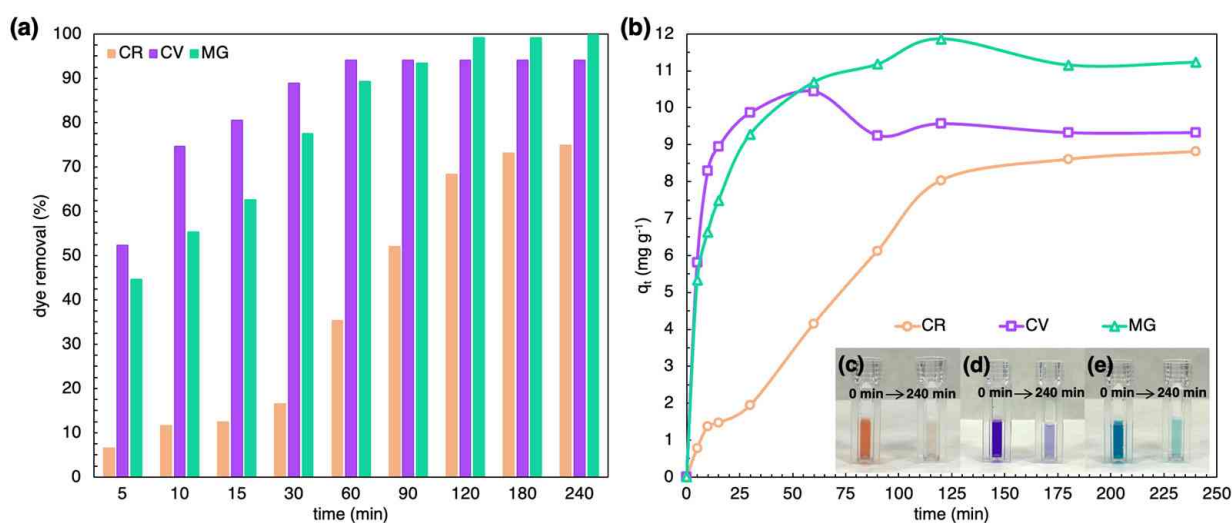
Figure 5. Discoloration of CR, CV, and MG solution after exposure to the SZCZM1454 *H.* cf. *salinicola* frustules: (**a**) dye removal efficiency and (**b**) adsorption capacity. Changes of solutions' color after 240 min for (**c**) CR, (**d**) CV, and (**e**) MG (initial concentration of dye–20 mg L^{-1}, adsorbent dosage–20 mg, pH–7, temperature–20 °C, time–5–240 min).

Table 3. Parameters of kinetic and diffusion models for CR, CV, and MG adsorption onto the SZCZM1454 *H.* cf. *salinicola* frustules.

Type of Dye	Pseudo First Order				Pseudo Second Order				Boyd's	
	q_1, mg g^{-1}	k_1, min^{-1}	R^2	χ^2	q_2, mg g^{-1}	k_2, g (mg min)$^{-1}$	R^2	χ^2	R^2	χ^2
CR	11.95	0.008	0.947	32.41	14.64	0.0005	0.859	1.47	0.947	16.91
CV	1.64	0.003	0.142	75.5	9.36	0.4491	0.954	3.15	0.957	0.16
MG	3.87	0.010	0.720	57.59	11.64	0.0145	0.999	0.25	0.996	0.51

Type of dye	Intra particle diffusion				Pore diffusion				q_{exp}, mg g^{-1}
	K_{wm}, mg (g min$^{0.5}$)$^{-1}$	B, mg g^{-1}	R^2	χ^2	$\Delta\beta$	k_β	R^2	χ^2	
CR	0.707	1.203	0.935	1.82	0.677	0.0003	0.951	1.37	8.81
CV	0.146	7.813	0.267	1.43	0.088	0.0088	0.479	1.00	10.44
MG	0.441	5.906	0.759	1.25	0.201	0.005	0.907	0.61	11.86

To determine the main resistance to mass transfer, the Boyd's model was used (Figure 6). Graphs for all three dyes were straight lines (correlation coefficients higher than 0.95), although only the plot for CR adsorption passed through the origin (Figure 6a), while CV and MG (Figure 6b,c) did not.

Figure 7a shows the effect of different initial concentrations on removal efficiency. For the diazo dye CR, increasing the concentration of the solution resulted in a gradual increase in the removal percentage, followed by a sharp decrease for solutions with concentrations higher than 50 mg L^{-1}. The initial concentration of CV and MG did not affect the removal efficiency of the frustules; in both cases, the removal was always higher than 90% (Figure 7a). For the isotherm, there was a strong positive correlation between adsorption capacity and equilibrium concentration of CR, CV, and MG in the solution (Figure 7b–d). Adsorption isotherms showed that the maximum adsorption capacity (q_{max}) of the SZCZM1454 *H.* cf. *salinicola* frustules against the diazo dye is lower than against the basic dyes: 13.04 mg g^{-1} for CR and 41.97, 33.19 mg g^{-1} for CV and MG, respectively.
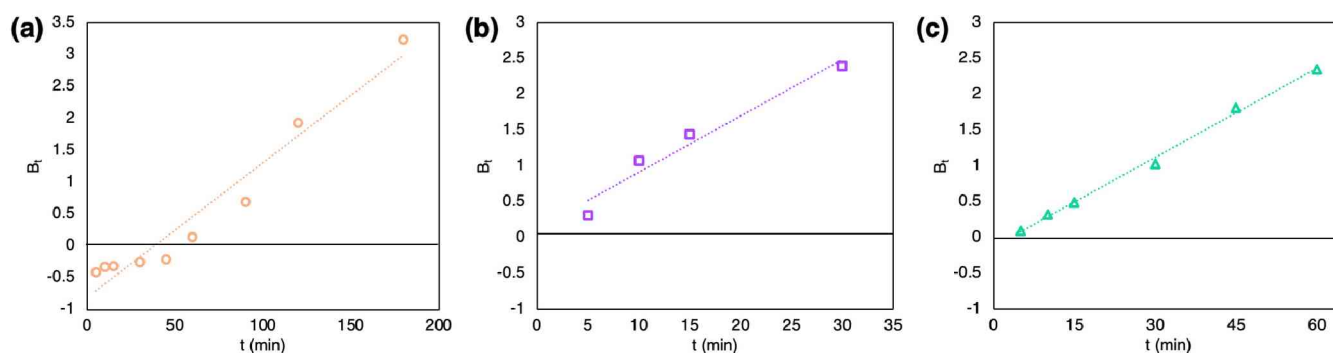
Figure 6. Boyd's plot for adsorption of (**a**) CR, (**b**) CV, and (**c**) MG onto the SZCZM1453 *H.* cf. *salinicola* frustules.
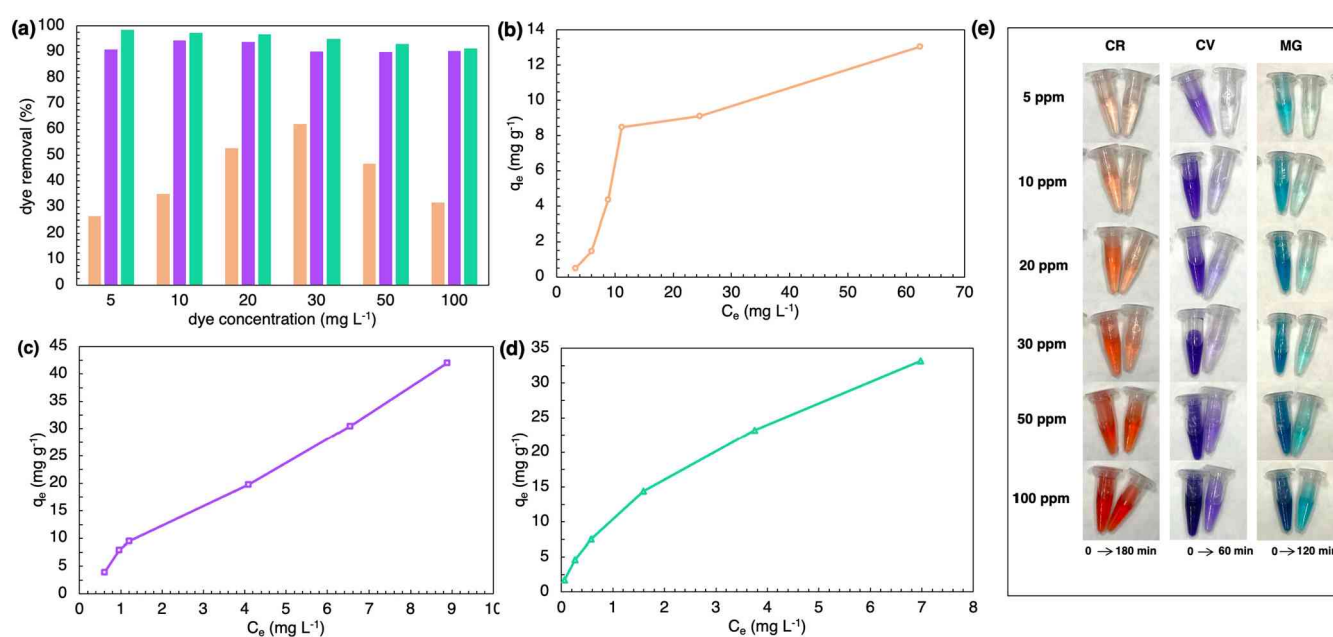
Figure 7. Influence of initial dye concentration on removal: (**a**) dye removal efficiency; adsorption isotherms of (**b**) CR, (**c**) CV, and (**d**) MG; and (**e**) discoloration of solutions with different dye concentrations (initial concentration of dye–5–100 mg L^{-1}; adsorbent dosage–20 mg, pH–7, temperature–20 °C, time–180 min, 60 min, and 120 min for CR, CV, and MG, respectively).

Linear forms of Langmuir, Freundlich, Temkin, and Sips models (Figure S2) were applied to further understanding the possible adsorption mechanisms. The isotherm parameters as well as the coefficients of correlation and the normalized standard deviation are presented in Table 4. The equilibrium study showed that adsorption of different types of dyes follows different models: the Sips model is more applicable to CR adsorption data with closer to unity R^2 and the lowest Chi-square values, while the most suitable model for the CV and MG adsorption onto the SZCZM1454 *H.* cf. *salinicola* frustules is the Freundlich model with R^2 higher than 0.95 and χ^2 less than 0.8.

Table 4. Parameters of four linear isotherm models for CR, CV, and MG adsorption onto the SZCZM1454 *H.* cf. *salinicola* frustules.

Type of Dye	Langmuir				Freundlich				Temkin				Sips					q_{exp}, mg g^{-1}
	q_{max}, mg g^{-1}	K_L, L mg^{-1}	R^2	χ^2	K_F, (mg g^{-1}) (mg L^{-1})$^{-n}$	n	R^2	χ^2	b, J mol^{-1}	K_m, L g^{-1}	R^2	χ^2	q_m, mg g^{-1}	K_S [(mg L^{-1})$^{-1/n}$]	n	R^2	χ^2	
CR	87.72	26.22	0.018	5.05	3.66	0.94	0.786	10.02	549.6	0.33	0.916	2.69	13.4	0.08	0.47	0.950	1.26	13.04
CV	114.9	0.06	0.473	16.82	7.04	1.25	0.977	0.80	189.9	1.86	0.923	3.74	42.1	0.53	0.39	0.662	18.92	41.97
MG	41.5	753.1	0.938	1.31	10.39	1.63	0.999	0.06	384.4	11.0	0.874	19.02	35.0	0.77	0.91	0.900	3.75	33.19

3. Discussion

Table 5 shows the difference in growth parameters between different *Halamphora* spp. strains. The strain SZCZM1454 *H.* cf. *salinicola* has a lower specific growth rate and longer cultivation time, but the highest dry biomass yield and cell density than other strains reported (slightly lower than *H. coffeaeformis* from Argentina [6]). Furthermore, an increase in silicate concentration and salinity enhanced the biomass accumulation up to almost 1 g L^{-1} DW (Table 1), which is the highest biomass yield reported for any *Halamphora* spp. strain. The ability of diatoms to build the silicon frustules requires a sufficient concentration of silicate in the medium, and previous studies showed that silicon enrichment of the medium results in higher biomass yields [71,72].

Table 5. Growth parameters of different *Halamphora* strains cultivated under standard conditions.

Strain	Origin of Strain	Cell Density per mL	Biomass DW (g L^{-1})	Specific Growth Rate	Days of Cultivation	Ref.
H. coffeaeformis		1.40×10^5		1.47 div d^{-1}	7 days	[4]
H. coffeaeformis			0.3		22 days	[7]
H. coffeaeformis		10.0×10^5	0.43	2.03 div d^{-1}	13 days	[12]
H. coffeaeformis	Bahía Blanca Estuary, Argentina	7.8×10^5	0.18	0.92 div d^{-1}	6 days	[8]
H. coffeaeformis		37.0×10^5 in PBR	0.64	0.4 div d^{-1}	11 days	[6]
H. luciae		417 cells in mm^{-2}		0.29 div d^{-1}	18 days	[73]
UTCC58 *H. coffeaeformis*		2.51×10^5		Max: 2.01 div d^{-1} Mean: 1.04 div d^{-1}	8 days	[74]
H. coffeaeformis	Kelley's Slough, ND, USA			1.01 div d^{-1}		
H. subturgida	Sawhill Pond, CO, USA			0.26 div d^{-1}	The growth rate was calculated after 48 h	[5]
H. pertusa	Blue Lake, UT, USA			1.33 div d^{-1}		
H. turgida	Blue Lake, UT, USA			1.16 div d^{-1}		
H. oligotraphenta	Sawhil Pond, CO, USA			0.33 div d^{-1}		
H. cf. *borealis*	Guana River, FL, USA			0.98 div d^{-1}		
SB1 MK575516.1 *Halamphora* sp.	Sfax Solar Saltern pond, Tunisia	8×10^5			10 days	[75]
SZCZM1454 *H.* cf. *salinicola*	Köyceğiz Lake, Turkey	$24.6 \pm 0.04 \times 10^5$	0.73 ± 0.047	0.081 d^{-1} 0.113 div d^{-1}	27 days	This study

Cultivation experiments with different temperature treatments revealed a significant difference in the biomass yield cultivated under 30 °C (Table 1). The SZCZM1454 *H.* cf. *salinicola* originates from Köyceğiz Lake in Turkey [10], which contains subaqueous hot springs [76]. Therefore, the strain could be considered thermophilic, hence the higher temperature requirements for cultivation. Similar results were obtained for a *Halamphora* sp. strain from a thermal spring in Tunisia, where the biomass accumulation increases with increasing temperature [9].

Scanning electron microscopy provided the surface topography of the frustules. Each frustule consists of two valves, and every valve has more than 200 areolae, thereby confirming the porous nature of the biosilica material. According to the IUPAC classification [77], pores with a diameter less than 2 nm are interpreted as micropores, pores with a diameter in the range of 2–50 nm are considered to be mesopores, and pores with diameters of 50 nm and larger are identified as macropores. The areolae could be considered as mesopores and macropores as they were 50–200 nm in diameter [78]. To study the microporous and mesoporous structure of the frustules, the BJH (Barrett–Joyner–Halenda) algorithm was applied. Pore diameter distribution (Figure S3) showed that the frustules have pores with a diameter from 3 nm to 35 nm, with an average pore diameter of 3.72 nm. Therefore, the frustule surface not only has areolae, but other micro and mesopores. Previous reports showed that the average pore diameter of biosilica was calculated as 3.93 nm for *P. trainorii* [79], 3–10 nm for *Thalassiosira punctigera*, 3.6–3.7 nm for *T. weissflogii* [80], and 4.61 nm for *Navicula australoshetlandica* [81]. These findings were confirmed by the low temperature nitrogen adsorption/desorption results: the isotherm for the SZCZM1454 *H.* cf. *salinicola* frustules could be classified as a combination of Type I and Type II isotherms with a Type H4 hysteresis loop, according to the IUPAC codification. Type I describes a microporous material with a small external surface, while Type II corresponds to macroporous or nonporous substances. The presence of the Type H4 hysteresis loop indicates the existence of slit-like pores in the sample [77].

Several authors have demonstrated that the specific surface area (BET) of different species of diatoms differs drastically, from $2 \, \text{m}^2 \, \text{g}^{-1}$ and $4 \, \text{m}^2 \, \text{g}^{-1}$ for *Skeletonema* sp. and *N. ramossisima*, respectively [82], and a $12–32 \, \text{m}^2 \, \text{g}^{-1}$ range for *T. weissflogii* and *T. punctigera* [80], $30 \, \text{m}^2 \, \text{g}^{-1}$ for *P. trainorii* [79] and $401.45 \, \text{m}^2 \, \text{g}^{-1}$ for *N. australoshetlandica* [81]. Furthermore, [70] demonstrated that the specific surface area of the diatom frustules corresponds to the cleaning technique used and proposed the Sono–Fenton method, which increased the specific surface area from $14.71 \, \text{m}^2 \, \text{g}^{-1}$ to $132.67 \, \text{m}^2 \, \text{g}^{-1}$ for the *Cyclotella* sp. frustules.

The presence of silica on the surface of diatoms was demonstrated by UV–vis spectroscopy. The same peak at 230 nm was recorded in both the sonicated biomass and the clean frustules. According to several reports [83–85], this peak reveals the presence of silica in both samples. The bands at 430, 495, and 676 nm shown in the sonicated biomass spectra indicate the presence of carotenoids and chlorophyll in the sample [86]. The band at 270 nm in the sonicated biomass sample could be explained by the presence of carbohydrates [87].

In order to determine the elemental composition of the frustules, an EDS analysis was performed. The spectra confirmed the UV–vis spectroscopy results and demonstrated distinct peaks of silicon (Si) and oxygen (O). The calculated atomic ratio O/Si of the frustules was 2.04; therefore, we can conclude that the SZCZM1454 *H.* cf. *salinicola* frustules were made of SiO_2 [88]. The distinct peak of carbon (C) could indicate the presence of organic compounds within the frustules [89]. However, it is important to note that oxygen is too light to be properly indicated by EDS (there is a limitation for the elements with an atomic number below Na), and SEM oil pump contamination could also contribute to the observed carbon peak.

To analyse the frustule structure, the identification of functional groups on the surface is important. ATR-FTIR spectra showed a series of bands in the fingerprint region, which according to several reports [85,90–92], indicates bending ($445 \, \text{cm}^{-1}$), symmetrical stretching ($805 \, \text{cm}^{-1}$), and asymmetrical stretching ($956, 1075$, and $1150 \, \text{cm}^{-1}$) of the Si–O groups. According to [93] the vibration in the $565 \, \text{cm}^{-1}$ region could be due to the contribution of the siloxane rings. The adsorption peaks at 1380 and $1470 \, \text{cm}^{-1}$ are attributed to the bending vibrations of the N–H groups, indicating the presence of organic substances around the frustules [94,95]. Strong bands in the $2800–3000 \, \text{cm}^{-1}$ regions show stretching of the C–H groups [92]. Small IR vibrations are visible in the 1670, 1720, and $3660 \, \text{cm}^{-1}$ regions and they indicate the presence of the H–O–H deformation, the C = O stretching, and the O–H asymmetric stretching of the Si–OH group, according to several authors [85,90,92,94].

The X-ray powder diffraction analysis allowed us to study the crystalline structure of the sample. The results indicated the presence of amorphous silica in the sample, seen as a continuous elevation in the 2θ range from 10° to 35° [96]. Moreover, the results provided evidence for the presence of impurities in the biosilica sample: the pattern revealed the presence of calcium carbonate in the form of both vaterite and calcite [97].

Three stages could be distinguished in the TGA curve: the first one is related to the release of adsorbed water, the second one came from the decomposition of organic residue [98], and the third one indicates the decomposition of carbonaceous salts [98–100]. A more precise search revealed that the analysed sample probably had a significant amount of $CaCO_3$, as the mass loss in the characteristic temperature range (590–740 °C) was 34.8% [97]. A further decrease in the mass at higher temperatures may come from the dehydration of the silanol groups.

Knowledge about the surface charge is important for two reasons. Firstly, the value of zeta potential indicates the stability of the suspension. The data from the literature indicates that stable and non-aggregating systems are characterized by absolute zeta potential values greater than $+/-25 – +/-30$ mV [101,102]. Secondly, zeta potential determines the adsorption properties of the material. For instance, a negatively charged surface will have a higher affinity to cationic compounds. It is noteworthy to mention that the zeta potential is dependent not only on their properties but can be manipulated through changes in the pH and ionic strength of the solution. Thus, both the stability and sorption properties of the material can be changed. The sample revealed a positive charge in the acidic conditions, which is not characteristic of pure silica [103]. The respective difference could be due to the presence of a high amount of impurities in the sample, as indicated by X-ray diffraction and thermogravimetric analysis. Moreover, at a pH of 7, the examined biosilica had a zeta potential of −25.1 mV, indicating the high stability of the system. Generally, the system is stable in a pH range of 7–12. These results highlight the dissimilarity in the sorption of the different types of dye: at a pH of 7, the frustule surface with the negative charge (contributed by the $–SiO^-$, $–COO^-$, and $–NH_2^-$ groups) interacts with the anionic CR (the $–SO_3^-$ and $–NH_2^-$ groups) with electrostatic repulsion, while the cationic CV and MG have the positive charge ($=N^+$ groups) and interact with the frustules electrostatically, which resulted in a higher adsorption ability of the frustules for the cationic dyes.

The frustules of SZCZM1454 *H.* cf. *salinicola* showed a good adsorption ability. Removal of the diazo dye CR by the diatom frustules (74.9%) was comparable to activated carbon: 87.5% removal of 200 mg L^{-1} [48], as well as biosorbents; the microalgal waste showed 76.6% of removal of 50 mg L^{-1} after 120 min [57], pretreated *Scenedesmus obliquus* removed 41.15% of 20 mg L^{-1} CR [104], 87.66% removal of 20 mg L^{-1} for *Sargassum latifolium* waste [105], up to 88.7% of 100 mg L^{-1} CR removal by *Moringa* seed waste [66], 89.20% 55.04% of 100 mg L^{-1} CR for *Aspergillus fumigatus* and *Pseudomonas putida* mycelial pallets, respectively [106], and 15% and 98% removal of 50 mg L^{-1} for the unmodified and the modified diatomaceous earth, respectively [107]. At the same time, the maximum adsorption capacity of the frustules (q_{max} = 13.04 mg g^{-1}) was lower than other sorbents: 493.8 mg g^{-1} for activated carbon [48], 316.46 mg g^{-1} for mycelial pellets [106], 202.9 mg g^{-1} for the *Chlorella vulgaris* biomass [108], 20.97 mg g^{-1} for *Sargassum latifolium* waste [105], 170.7 mg g^{-1} for *Moringa* seed waste [66], 55.5 mg g^{-1} for natural perlite [109], and 23.2 mg g^{-1} and 305.8 mg g^{-1} for the unmodified and the modified diatomaceous earth, respectively [107].

The efficiency of CV removal by the frustules (94.02%) corresponded to previous studies of algal biosorbents: 75% of 50 mg L^{-1} CV at a pH of 2 by modified *Spirulina* sp. [110], around 89% of 80 mg L^{-1} CV at a pH of 10 by *Laminaria japonica* [111], 93.04% of 20 mg L^{-1} CV at a pH of 7 by red seaweed [112], 98% of 5 mg L^{-1} CV at a pH of 3 by diatom *Skeletonema costatum* [67]. For natural siliceous materials, 99.9% by zeolite [113] and close to 100% by the diatomaceous earth [64]. The maximum adsorption capacity of the frustules (q_{max} = 41.97 mg g^{-1}) was higher than the dye uptake of the *Skeletonema costatum* biomass (6.41 mg g^{-1}) [67], the leaf biomass of *Calotropis procera* (4.14 mg g^{-1}) [114], and fly ash zeo-

lite (19.6 mg g^{-1}) [115], which were almost the same as the adsorption capacity of the amino silica (40 mg g^{-1}) [116] and kaolin (47.27 mg g^{-1}) [61], and less than the capacity of modified *Spirulina* sp. (q_{max} = 101.87 mg g^{-1}) [110], red seaweed (q_{max} = 150.14 mg g^{-1}) [112], diatomaceous earth (q_{max} = 96.1 mg g^{-1}) [64], natural zeolite (q_{max} = 177.75 mg g^{-1}) and commercial activated carbon (q_{max} = 84.11 mg g^{-1}) [113].

The diatom frustules of SZCZM1454 *H.* cf. *salinicola* demonstrated the highest removal efficiency (99.81%) against the basic dye MG compared to different adsorbents: commercially available powdered activated carbon showed 96% removal of 100 mg L^{-1} MG after 15 min [117], the xerogel activated diatomaceous earth presented up to 91.73% of removal of 10 mg L^{-1} [118], while diatomite from China showed up to 93.72% removal of 20 mg L^{-1} at a pH of 7 [65], fly ash removed only 64.42% of 20 mg L^{-1} MG from the solution [119], and the modified chitosan composite demonstrated 85% removal [120]. The maximum adsorption capacity of the diatom frustules against MG was calculated as 33.19 mg g^{-1}, which is less than activated carbon (490.77 mg g^{-1} [121] and 222.2 mg g^{-1} [117]), the biomass of freshwater algae *Pithophora* sp. (117.65 mg g^{-1}) [122], and brown marine algae *Turbinaria conoides* (66.60 mg g^{-1}) [123]. It was, however, similar to zeolite (46.35 mg g^{-1}) [124], tetrahedral silica (45.05 mg g^{-1}) [125], and diatomite from China (23.64 mg g^{-1}) [65], and higher than the xerogel activated diatomaceous earth (from 4.118 to 4.202 mg g^{-1}) [118], fly ash (0.644 mg g^{-1}) [119], and modified chitosan composite (4.8 mg g^{-1}) [120]. The maximum adsorption capacities of SZCZM1454 *H.* cf. *salinicola* against CR, CV, and MG were smaller than other adsorbents (e.g., activated carbon) due to the relatively small specific surface area (S$_{BET}$) of the frustules.

To understand the possible mechanism of adsorption of CR, CV, and MG onto the SZCZM1454 *H.* cf. *salinicola* frustules, several kinetic, diffusion, and isotherm models were applied. Parameters and correlation coefficients, calculated for each type of dye, showed that CV and MG adsorption are consistent with the Pseudo-Second Order model. The model highlighted the fact that the rate of CV and MG adsorption is controlled by chemisorption, involving covalent forces sharing or exchanging electrons between the adsorbent surface and the dye molecules. The CR adsorption process predominantly follows the Pore diffusion model – modified Intra particle diffusion model, which shows that the rate-controlling step in CR adsorption onto the SZCZM1454 *H.* cf. *salinicola* frustules is mostly through the diffusion of dye molecules onto pores inside the adsorbent particles [126].

Additionally, a widely used for determination of the main resistance to mass transfer the linearity test of Boyd's model was applied. The plot for CR adsorption data passed through the origin, while the plots for CV and MG adsorption did not. Hameed et al. [127] stated that if the plot is nonlinear or linear, but does not pass through the origin, then film diffusion or chemical reaction control the adsorption rate, and if the plot is linear and passes through the origin, then the rate controlling step of mass transfer in this adsorption is through pore diffusion. We can conclude that CR adsorption was governed by pore diffusion, and for CV and MG adsorption onto the SZCZM1454 *H.* cf. *salinicola* frustules through the thin film (boundary layer), diffusion is the main resistance to mass transfer.

The adsorption Isotherms were characterized by their shape: the CV isotherm was LS-shaped, and the CR and MG were mostly L-shaped [128]. The isotherm parameters showed that for CV and MG adsorption, the Freundlich model had the best fit, thus suggesting the multilayer formation of the basic dye onto the heterogenous sites on the surface of SZCZM1454 *H.* cf. *salinicola*, and CR adsorption followed the Sips model, which combines the Freundlich and Langmuir isotherms and describes the monolayer formation onto homogenous and heterogenous sites [129]. The adsorption in the Freundlich model is considered favorable, when $1 < n < 10$, and the higher the *n*-value, the stronger the adsorption; therefore, CV (*n* = 1.18) and MG (*n* = 1.63) were favorably adsorbed onto SZCZM1454 *H.* cf. *salinicola* [130].

4. Materials and Methods

4.1. Chemicals

Malachite Green (99%, MW 364.911 Da), Crystal Violet (99%, MW 407.99 Da), and Congo Red (99%, MW 696.69 Da) were purchased from Hadron Scientific (Kielce, Poland). Thiamine hydrochloride (99%, MW 337.27 Da), biotin (>99%, MW 244.31 Da), vitamin B12 (>98%, MW 1355.37 Da), sodium hydroxide (>98%, MW 40.00), hydrochloric acid (37%, MW 36.46), and standard buffered solutions pH 2.0, 7.0, and 10.0 were supplied by Sigma-Aldrich (St. Louis, MO, USA). Hydrogen peroxide (30%, MW 34.01 Da), sodium nitrate (>99%, MW 84.99 Da), sodium dihydrogen phosphate monohydrate (>99%, MW 137.99 Da), sodium molybdate dihydrate (>99%, MW 241.95 Da), manganese (II) chloride tetrahydrate (>99%, MW 197.91 Da), and cobalt (II) chloride hexahydrate (>99%, DW 237.93 Da) were obtained from Chempur® (Piekary Śląskie, Poland). Zinc sulfate heptahydrate (>99%, MW 287.54 Da), iron (III) chloride hexahydrate (>99%, MW 270.32 Da), EDTA disodium dihydrate (>99%, MW 372.24 Da), and copper (II) sulfate pentahydrate (>99%, MW 249.68 Da) were purchased from Scharlab (Barcelona, Spain). Nonahydrate sodium metasilicate (44–47.5% total solids, MW 284.19 Da) was supplied by Acros Organics, ThermoFisher Scientific (Waltham, MA, USA). The PhosVer® 3 Phosphate Reagent Powder Pillow, Amino Acid F Reagent Powder Pillow, Citric Acid Powder Pillow, and Molybdate 3 Reagent Solution were provided by HACH-Lange (Loveland, CO, USA). Deionized water was obtained by using a Milli-Q® purification system (Millipore Co., Bedford, MA, USA).

4.2. Batch Cultivation

The SZCZM1454 *Halamphora* cf. *salinicola* strain [10] was acquired from the Szczecin Diatoms Culture Collection (SZCZ), University of Szczecin, Institute of Marine and Environmental Sciences, Poland. For growth rate determination, the monoclonal culture was maintained in a 100 mL Erlenmeyer flask containing 35 ppt Guillard's artificial seawater f/2 medium [131] (1 L of medium contained 880 μM $NaNO_3$, 36 μM NaH_2PO_4 H_2O, 106 μM Na_2SiO_3 $9H_2O$, trace metal: 0.08 μM $ZnSO_4$ $7H_2O$, 0.9 μM $MnSO_4$ H_2O, 0.03 μM Na_2MoO_4 $2H_2O$, 0.05 μM $CoCl_2$ $6H_2O$, 0.04 μM $CuCl_2$ $2H_2O$, 11.7 μM $FeCl_3$ $6H_2O$, 11.7 μM Na_2EDTA $2H_2O$, vitamin B12, biotin and thiamine) under the following conditions: 20 °C constant temperature and 100 μmol s^{-1} m^{-2} white light under a under a 12:12 day/night light cycle in a plant growth chamber (FITO1400i, Biogenet, Poland) for 24 days. The nitrate concentration in the medium was measured before and after cultivation by the UV screening method (HACH-Lange), the orthophosphate by the Ascorbic Acid method (PhosVer 3® powder pillows, HACH-Lange) and the silica content was monitored using the Heteropoly Blue method (Molybdate 3, Citric acid and Amino acid powder pillows, HACH-Lange). Cells were counted under an inverted microscope (Olympus CKX41, Olympus-Shinjuku, Tokyo, Japan) using a Malassez counting chamber (Marienfield, Germany) and the biomass was harvested by centrifugation at 3000 rpm followed by heat drying for 3 days at 50 °C. The regression curve was built, and the specific growth rate (μ) was calculated, using the following Equation (1) [132]:

$$B_t = B_0 \times e^{\mu t}, \tag{1}$$

where B_t is the biomass concentration at time (t) and B_0 is the initial biomass concentration. Moreover, the influence of nutrient enrichment (5, 10, 15, and 20 times higher concentrations of NO^{3-}, PO_4^{3-}, and SiO_3^{2-}), salinity (15, 20, and 45 ppt), temperature (15 and 30 °C), and illumination intensity (10, 50, and 150 μmol photons m^{-2} s^{-1}) on the biomass accumulation in the late exponential phase was studied. For biosilica extraction, the strain SZCZM1454 was cultured in a 70 L cylindrical, air-lifted photobioreactor under optimized conditions.

4.3. Characterization of the Frustules Surface

To obtain the frustules, the biomass was harvested in the late exponential phase and exposed to a 30% H_2O_2 solution for 3 days with a thorough cleaning with ddH_2O. The colorless frustules were heat dried at 50 °C for 3 days. A scanning electron microscope Hitachi

SU8000 equipped with an EDS detector (Hitachi, Tokyo, Japan) was used for morphological as well as elemental composition studies of the cleaned frustules. The dried sample was sputter coated with a 10 nm thick gold layer. The measurements were performed with an accelerating energy of 30.0 kV. The sonicated in ddH$_2$O control biomass and the cleaned frustules were subjected to the UV–Vis DR 6000 spectrophotometer (HACH-Lange) for optical measurements in the wavelength range of 200 to 900 nm in 10 mm cuvettes against a ddH$_2$O (blank). For absorbances higher than 2, the solution was diluted with ddH$_2$O and the dilution factors were considered in the presented graphs. The attenuated total reflection (ATR) mode on an Alpha FTIR spectrometer (Bruker Daltonics, Bremen, Germany) was used for the FTIR spectroscopic study of the cleaned frustules in the mid-infrared range (4000–400 cm^{-1}). The low-temperature nitrogen adsorption/desorption isotherms were recorded on a Quantachrome Autosorb iQ at 77.35 K. Thermogravimetric analysis (TA/TGA) of the biosilica was performed using a TA Instrument type SDT 2960 (Artisan Technology, Champaign, IL, USA) at a 0–1100 °C temperature range, 100 mL min^{-1} air flow rate, and 10 °C min^{-1} heating rate. The analysis data for TA/DTA was proceeded with the use of TA Universal Analysis software (version 4.5A, TA Instruments, New Castle, DE, USA). Zeta potential change over the pH was analysed with a Malvern Zetasizer NanoZS (Malvern Instruments, Malvern, UK) using dedicated cuvettes DTS1070 (Malvern Instruments, Malvern, UK). The analysis was made considering the Smoluchowski approximation, with the automatic selection mode of voltage and number of runs, and in the pH range of 2.0–12.0. The diatom frustules were suspended in deionized water at a concentration of 0.5 mg mL^{-1}. The solutions of 0.1M NaOH and 0.1M HCl were used for pH adjustment of the suspension. The pH of the suspension was measured using a FiveEasy Plus pH-meter (Mettler Toledo) with a combined electrode with glass membrane and Ag/AgCl reference system (Mettler Toledo). The pH-meter was calibrated using standard buffered solutions with a pH of 4.0, 7.0, and 10.0 before carrying out measurements. The X-ray diffraction analysis was made with an X'Pert Pro Analytical diffractometer (Phillips, Erlangen, Germany) with CuKα radiation source and Ni filter. The X-ray diffraction pattern analysis was obtained from the XRD Malvern Panalytical software (version 1.5a, Almelo, The Netherlands) in the 2θ range from 5 to 120° with a scan step size of 0.0167°.

4.4. Batch Adsorption Experiments

Three types of dye–Congo Red (CR), Crystal Violet (CV), and Malachite Green (MG)–were used in batch adsorption experiments. The dried frustules (20 ± 0.5 mg) were exposed to 15 mL of 20.0 mg L^{-1} CR, CV, and MG solutions (pH–7) in a Falcon tube and stirred at 3000 rpm at 20 °C for 4 h. The kinetics of adsorption were recorded spectrophotometrically (UV-Vis DR 6000, HACH-Lange) at 499 nm (CR), 586 nm (CV), and 616 nm (MG) at different time points: 5, 10, 15, 30, 45, 60, 90, 120, 180, and 240 min. The influence of different initial concentrations of dye was investigated by measuring 10 mg of the cleaned frustules in Falcon tubes containing various concentrations (5, 10, 15, 20, 50, and 100 mg L^{-1}) of CR, CV, and MG. After the mixture reached equilibrium (120 min for CR and MG and 60 min for CV), the removal was recorded spectrophotometrically, as mentioned above. The quantity of adsorbed MB by the frustules was calculated as follows (Equation (2)):

$$q_t = V \times (C_0 - C_t)/m, \tag{2}$$

where q$_t$ is the MB adsorbed on the frustules (mg g^{-1}) at a given time (t); C$_0$ and C$_t$ are the concentrations of the MB at the start and at the given time point (mg L^{-1}), respectively; V is the solution volume (L); and m is the biosilica dosage (g).

The percentage of MB removal (%) was calculated as in Equation (3):

$$\text{Removal (\%)} = 100\% \times (C_0 - C_t)/C_0, \tag{3}$$

where C$_0$ and C$_t$ are the concentrations of the MB at the start and at the given time (t), respectively (mg L^{-1}).

To understand the possible mechanisms of adsorption, the linearized forms of Pseudo-First Order, Pseudo-Second Order, Elovich kinetic models, and Langmuir, Freundlich, Temkin, and Sips isotherm models were applied (Table S1).

4.5. Data Analysis

Batch cultivation experiments were conducted in duplicate. The zeta potential measurements were performed in triplicates. Batch adsorption experiments were conducted without replication. The figures show the mean values and standard deviation. The significance of differences between groups was analysed using a one-way ANOVA analysis with Tukey HSD test. A significant difference between two groups was declared if $p < 0.05$. The batch growth experiment figures, UV–Vis, Tauc plot, FTIR spectra, batch adsorption spectra, and models were plotted using MS Excel software (version 16.73). The EDS spectra was obtained using NSS ThermoScientific software (version 1.0). The nitrogen adsorption/desorption isotherms were acquired using Quantachrome Instruments software (version 1.11). The applicability of the kinetic, diffusion, and isotherm models was validated using the Chi-square (χ^2), which is defined as (Equation (13)):

$$\chi^2 = S[(q_{cal} - q_{exp})^2/q_{exp}], \tag{4}$$

where q_{exp} and q_{cal} (mg g^{-1}) are the experimental and calculated adsorption capacity value, respectively.

5. Conclusions

The present study explored the ability of the mesoporous nanostructured siliceous frustules extracted from the diatom culture of *Halamphora* cf. *salinicola* Levkov and Díaz to perform as a novel eco-friendly adsorbent for different classes of dyes: an anionic diazo Congo Red (CR), a cationic basic Crystal Violet (CV), and Malachite Green (MG). This diatom strain is known to produce high amounts of neutral lipids, unsaturated fatty acids, fucoxanthin, and chrysolaminarin, and could be used in biodiesel, aquaculture, cosmetics, and pharmaceutics. The diatom wastes from these industries could be purified and used in wastewater treatment. This study for the first time introduced the diatom frustules as a novel efficient adsorbent of the basic and diazo dyes from wastewaters. This method resulting in no more than 75% removal of the diazo dye (CR) that decreased with increased concentrations, with the maximum adsorption capacity of 13.04 mg g^{-1}, while removal of the basic dyes (CV and MG) by diatomaceous earth was higher than 90% in every experiment, with higher adsorption capacity (41.97 and 33.19 mg g^{-1}, respectively) than several other known biosorbents.

Supplementary Materials: The following supporting information can be downloaded at: https://www.mdpi.com/article/10.3390/md21050312/s1, Figure S1: Adsorption kinetic and diffusion studies: (a) Pseudo-First Order; (b) Pseudo-Second Order; (c) Intra-particle diffusion; (d) Pore diffusion model (experimental data: orange circles–CR, violet squares–CV, green triangles–MG; calculated data: Pseudo-First Order–dashed line, Pseudo-Second Order–dash dotted line, Intra-particle diffusion–dotted line, Pore diffusion–double-dash dotted line); Figure S2: Adsorption equilibrium study: Langmuir model for (a) CR, (b) CV, (c) MG; Freundlich model for (d) CR, (e) CV, (f) MG; Temkin model for (g) CR, (h) CV, (i) MG; and Sips model for (j) CR, (k) CV, (m) MG (experimental data: orange circles–CR, violet squares–CV, green triangles–MG; calculated data: Langmuir–dashed line, Freundlich–dash dotted line, Temkin–double dash dotted line, Sips–dotted line); Figure S3. Pore size distribution of the diatom frustules of SZCZM1454 *H.* cf. *salinicola*; Table S1. Linearized forms of kinetic and isotherm models' equations and parameters [133–141].

References

1. Armbrust, E.V. The life of diatoms in the world's oceans. *Nature* **2009**, *459*, 185–192. [CrossRef] [PubMed]
2. Bowler, C.; Vardi, A.; Allen, A.E. Oceanographic and biogeochemical insights from diatom genomes. *Ann. Rev. Mar. Sci.* **2010**, *2*, 333–365. [CrossRef] [PubMed]
3. Wang, J.K.; Seibert, M. Prospects for commercial production of diatoms. *Biotechnol. Biofuels* **2017**, *10*, 16. [CrossRef] [PubMed]
4. Navarro, F.E.; Damiani, M.C.; Leonardi, P.I.; Popovich, C.A. Temperature and Salinity Effect on Tolerance and Lipid Accumulation in *Halamphora coffeaeformis*: An Approach for Outdoor Bioenergy Cultures. *Bioenerg. Res.* **2022**, *15*, 1545–1554. [CrossRef]
5. Stepanek, J.G.; Fields, F.J.; Kociolek, J.P. A comparison of lipid content metrics using six species from the genus *Halamphora* (Bacillariophyta). *Biofuels* **2016**, *7*, 521–528. [CrossRef]
6. Martin, L.A.; Popovich, C.A.; Martinez, A.M.; Damiani, M.C.; Leonardi, P.I. Oil assessment of *Halamphora coffeaeformis* diatom growing in a hybrid two-stage system for biodiesel production. *Renew. Energy* **2016**, *92*, 127–135. [CrossRef]
7. Martín, L.A.; Popovich, C.A.; Martínez, A.M.; Bilbao, P.G.S.; Damiani, M.C.; Leonardi, P.I. Hybrid two-stage culture of *Halamphora coffeaeformis* for biodiesel production: Growth phases, nutritional stages and biorefinery approach. *Renew. Energy* **2018**, *118*, 984–992. [CrossRef]
8. Scodelaro Bilbao, P.G.; Martín, L.A.; Popovich, C.A.; Almeyda, M.D.; Chamorro, V.; Leonardi, P.I. Assessment of *Halamphora coffeaeformis* growth and biochemical composition for aquaculture purposes. *J. Mar. Sci. Eng.* **2020**, *8*, 282. [CrossRef]
9. Bouzidi, N.; Zili, F.; García-Maroto, F.; Alonso, D.L.; Ouada, H.B. Impact of temperature and growth phases on lipid composition and fatty acid profile of a thermophilic Bacillariophyta strain related to the genus *Halamphora* from north-eastern Tunisia. *J. Mar. Biol. Assoc. UK* **2020**, *100*, 529–536. [CrossRef]
10. Marzec, M.; Dąbek, P.; Witkowski, A.; Monedeiro, F.; Pomastowski, P.; Buszewski, B.; Nowak, I. Lipid constituents of diatoms (*Halamphora*) as components for production of lipid nanoparticles. *Pharmaceutics* **2022**, *14*, 1171. [CrossRef]
11. Yang, R.; Wei, D.; Xie, J. Diatoms as cell factories for high-value products: Chrysolaminarin, eicosapentaenoic acid, and fucoxanthin. *Crit. Rev. Biotechnol.* **2020**, *40*, 93–1009. [CrossRef] [PubMed]
12. Popovich, C.A.; Faraoni, M.B.; Sequeira, A.; Daglio, Y.; Martín, L.A.; Martínez, A.M.; Damiani, M.C.; Matulewicz, M.C.; Leonardi, P.I. Potential of the marine diatom *Halamphora coffeaeformis* to simultaneously produce omega-3 fatty acids, chrysolaminarin and fucoxanthin in a raceway pond. *Algal Res.* **2020**, *51*, 102030. [CrossRef]
13. Bose, R.; Roychoudhury, P.; Pal, R. In-situ green synthesis of fluorescent silica–silver conjugate nanodendrites using nanoporous frustules of diatoms: An unprecedented approach. *Bioprocess Biosyst. Eng.* **2021**, *44*, 1263–1273. [CrossRef] [PubMed]
14. Roychoudhury, P.; Dąbek, P.; Gloc, M.; Golubeva, A.; Dobrucka, R.; Kurzydłowski, K.; Witkowski, A. Reducing efficiency of fucoxanthin in diatom mediated biofabrication of gold nanoparticles. *Materials* **2021**, *14*, 4094. [CrossRef] [PubMed]
15. Roychoudhury, P.; Golubeva, A.; Dąbek, P.; Gloc, M.; Dobrucka, R.; Kurzydłowski, K.; Witkowski, A. Diatom Mediated Production of Fluorescent Flower Shaped Silver-Silica Nanohybrid. *Materials* **2021**, *14*, 7284. [CrossRef]

16. Sasirekha, R.; Sheena, T.S.; Deepika, M.S.; Santhanam, P.; Townley, H.E.; Jeganathan, K.; Kumar, S.D.; Premkumar, K. Surface engineered *Amphora subtropica* frustules using chitosan as a drug delivery platform for anticancer therapy. *Mater. Sci. Eng. C* **2019**, *94*, 56–64. [CrossRef]

17. Javalkote, V.S.; Pandey, A.P.; Puranik, P.R.; Deshmukh, P.K. Magnetically responsive siliceous frustules for efficient chemotherapy. *Mater. Sci. Eng. C* **2015**, *50*, 107–116. [CrossRef]

18. Selvaraj, V.; Muthukumar, A.; Nagamony, P.; Chinnuswamy, V. Detection of typhoid fever by diatom-based optical biosensor. *Environ. Sci. Pollut. Res.* **2018**, *25*, 20385–20390. [CrossRef]

19. Squire, K.; Kong, X.; LeDuff, P.; Rorrer, G.L.; Wang, A.X. Photonic crystal enhanced fluorescence immunoassay on diatom biosilica. *J. Biophotonics* **2018**, *11*, e201800009. [CrossRef]

20. Kong, X.; Squire, K.; Li, E.; LeDuff, P.; Rorrer, G.L.; Tang, S.; Chen, B.; McKay, C.P.; Navarro-Gonzalez, R.; Wang, A.X. Chemical and biological sensing using diatom photonic crystal biosilica with in-situ growth plasmonic nanoparticles. *IEEE Trans. Nanobiosci.* **2016**, *15*, 828–834. [CrossRef]

21. Kamińska, A.; Sprynskyy, M.; Winkler, K.; Szymborski, T. Ultrasensitive SERS immunoassay based on diatom biosilica for detection of interleukins in blood plasma. *Anal. Bioanal. Chem.* **2017**, *409*, 6337–6347. [CrossRef] [PubMed]

22. Marella, T.K.; Saxena, A.; Tiwari, A. Diatom mediated heavy metal remediation: A review. *Bioresour. Technol.* **2020**, *305*, 123068. [CrossRef]

23. Roychoudhury, P.; Bose, R.; Dąbek, P.; Witkowski, A. Photonic Nano-/Microstructured Diatom Based Biosilica in Metal Modification and Removal—A Review. *Materials* **2022**, *15*, 6597. [CrossRef]

24. Mu, W.; Jia, K.; Liu, Y.; Pan, X.; Fan, Y. Response of the freshwater diatom *Halamphora veneta* (Kützing) Levkov to copper and mercury and its potential for bioassessment of heavy metal toxicity in aquatic habitats. *Environ. Sci. Pollut. Res.* **2017**, *24*, 26375–26386. [CrossRef]

25. O'Neill, C.; Hawkes, F.R.; Hawkes, D.L.; Lourenço, N.D.; Pinheiro, H.M.; Delée, W. Colour in textile effluents–sources, measurement, discharge consents and simulation: A review. *J. Chem. Technol. Biotechnol.* **1999**, *74*, 1009–1018. [CrossRef]

26. Sarkar, A.K.; Pal, A.; Ghorai, S.; Mandre, N.R.; Pal, S. Efficient removal of malachite green dye using biodegradable graft copolymer derived from amylopectin and poly(acrylic acid). *Carbohydr. Polym.* **2014**, *111*, 108–115. [CrossRef]

27. Husain, Q. Potential applications of the oxidoreductive enzymes in the decolorization and detoxification of textile and other synthetic dyes from polluted water: A review. *Crit. Rev. Biotechnol.* **2006**, *26*, 201–221. [CrossRef]

28. Zeng, L.X.; Chen, Y.F.; Zhang, Q.Y.; Kang, Y.; Luo, J.W. Adsorption of Congo red by cross-linked chitosan resins. *Desalination Water Treat.* **2014**, *52*, 7733–7742. [CrossRef]

29. Lachheb, H.; Puzenat, E.; Houas, A.; Ksibi, M.; Elaloui, E.; Guillard, C.; Herrmann, J.M. Photocatalytic degradation of various types of dyes (Alizarin S, Crocein Orange G, Methyl Red, Congo Red, Methylene Blue) in water by UV-irradiated titania. *Appl. Catal. B Environ.* **2002**, *39*, 75–90. [CrossRef]

30. Ameen, S.; Akhtar, M.S.; Nazim, M.; Shin, H.S. Rapid photocatalytic degradation of crystal violet dye over ZnO flower nanomaterials. *Mater. Lett.* **2013**, *96*, 228–232. [CrossRef]

31. Yang, J.; Chen, C.; Ji, H.; Ma, W.; Zhao, J. Mechanism of TiO_2-assisted photocatalytic degradation of dyes under visible irradiation: Photoelectrocatalytic study by TiO_2-film electrodes. *J. Phys. Chem. B* **2005**, *109*, 21900–21907. [CrossRef] [PubMed]

32. Gopinath, K.P.; Muthukumar, K.; Velan, M. Sonochemical degradation of Congo red: Optimization through response surface methodology. *Chem. Eng. J.* **2010**, *157*, 427–433. [CrossRef]

33. Guzman-Duque, F.; Pétrier, C.; Pulgarin, C.; Peñuela, G.; Torres-Palma, R.A. Effects of sonochemical parameters and inorganic ions during the sonochemical degradation of crystal violet in water. *Ultrason. Sonochem.* **2011**, *18*, 440–446. [CrossRef] [PubMed]

34. Berberidou, C.; Poulios, I.; Xekoukoulotakis, N.P.; Mantzavinos, D. Sonolytic, photocatalytic and sonophotocatalytic degradation of malachite green in aqueous solutions. *Appl. Catal. B Environ.* **2007**, *74*, 63–72. [CrossRef]

35. Gharbani, P.; Tabatabaii, S.M.; Mehrizad, A. Removal of Congo red from textile wastewater by ozonation. *Int. J. Environ. Sci. Technol.* **2008**, *5*, 495–500. [CrossRef]

36. Wu, J.; Gao, H.; Yao, S.; Chen, L.; Gao, Y.; Zhang, H. Degradation of crystal violet by catalytic ozonation using Fe/activated carbon catalyst. *Sep. Purif. Technol.* **2015**, *147*, 179–185. [CrossRef]

37. Zhou, X.J.; Guo, W.Q.; Yang, S.S.; Zheng, H.S.; Ren, N.Q. Ultrasonic-assisted ozone oxidation process of triphenylmethane dye degradation: Evidence for the promotion effects of ultrasonic on malachite green decolorization and degradation mechanism. *Bioresour. Technol.* **2013**, *128*, 827–830. [CrossRef]

38. Venkatesh, S.; Pandey, N.D.; Quaff, A.R. Decolorization of synthetic dye solution containing Congo red by advanced oxidation process (AOP). *Int. J. Adv. Res. Civ. Struct. Environ. Infrastruct. Eng. Dev.* **2014**, *2*, 49–55.

39. Jana, S.; Purkait, M.K.; Mohanty, K. Removal of crystal violet by advanced oxidation and microfiltration. *Appl. Clay Sci.* **2010**, *50*, 337–341. [CrossRef]

40. Modirshahla, N.; Behnajady, M.A. Photooxidative degradation of malachite green (MG) by UV/H_2O_2: Influence of operational parameters and kinetic modeling. *Dyes Pigm.* **2006**, *70*, 54–59. [CrossRef]

41. Lahkimi, A.; Oturan, M.A.; Oturan, N.; Chaouch, M. Removal of textile dyes from water by the electro-Fenton process. *Environ. Chem. Lett.* **2006**, *5*, 35–39. [CrossRef]

42. Fan, H.J.; Huang, S.T.; Chung, W.H.; Jan, J.L.; Lin, W.Y.; Chen, C.C. Degradation pathways of crystal violet by Fenton and Fenton-like systems: Condition optimization and intermediate separation and identification. *J. Hazard. Mater.* **2009**, *171*, 1032–1044. [CrossRef] [PubMed]

43. Chen, F.; Ma, W.; He, J.; Zhao, J. Fenton degradation of malachite green catalyzed by aromatic additives. *J. Phys. Chem. A* **2002**, *106*, 9485–9490. [CrossRef]

44. Neoh, C.H.; Lam, C.Y.; Lim, C.K.; Yahya, A.; Bay, H.H.; Ibrahim, Z.; Noor, Z.Z. Biodecolorization of recalcitrant dye as the sole source of nutrition using *Curvularia clavata* NZ2 and decolorization ability of its crude enzymes. *Environ. Sci. Pollut. Res. Int.* **2015**, *22*, 11669–11678. [CrossRef] [PubMed]

45. Bumpus, J.A.; Brock, B.J. 1988. Biodegradation of crystal violet by the white rot fungus *Phanerochaete chrysosporium*. *Appl. Environ. Microbiol.* **1988**, *54*, 1143–1150. [CrossRef]

46. An, S.Y.; Min, S.K.; Cha, I.H.; Choi, Y.L.; Cho, Y.S.; Kim, C.H.; Lee, Y.C. Decolorization of triphenylmethane and azo dyes by *Citrobacter* sp. *Biotechnol. Lett.* **2002**, *24*, 1037–1040. [CrossRef]

47. Raval, N.P.; Shah, P.U.; Shah, N.K. Malachite green "a cationic dye" and its removal from aqueous solution by adsorption. *Appl. Water Sci.* **2017**, *7*, 3407–3445. [CrossRef]

48. Kannan, N.; Meenakshisundaram, M. Adsorption of Congo Red on various activated carbons. A comparative study. *Water Air Soil Pollut.* **2002**, *138*, 289–305. [CrossRef]

49. Abbas, M.; Harrache, Z.; Trari, M. Removal of gentian violet in aqueous solution by activated carbon equilibrium, kinetics, and thermodynamic study. *Adsorp. Sci. Technol.* **2019**, *37*, 566–589. [CrossRef]

50. Qu, W.; Yuan, T.; Yin, G.; Xu, S.; Zhang, Q.; Su, H. Effect of properties of activated carbon on malachite green adsorption. *Fuel* **2019**, *249*, 45–53. [CrossRef]

51. Liu, J.; Wang, N.; Zhang, H.; Baeyens, J. Adsorption of Congo red dye on FexCo$_{3-x}$O$_4$ nanoparticles. *J. Environ. Manag.* **2019**, *238*, 473–483. [CrossRef] [PubMed]

52. Samrot, A.V.; Ali, H.H.; Selvarani, J.; Faradjeva, E.; Raji, P.; Prakash, P. Adsorption efficiency of chemically synthesized Superparamagnetic Iron Oxide Nanoparticles (SPIONs) on crystal violet dye. *Curr. Res. Green Sustain. Chem.* **2021**, *4*, 100066. [CrossRef]

53. Dehbi, A.; Dehmani, Y.; Omari, H.; Lammini, A.; Elazhari, K.; Abdallaoui, A. Hematite iron oxide nanoparticles (α-Fe$_2$O$_3$): Synthesis and modelling adsorption of malachite green. *J. Environ. Chem. Eng.* **2020**, *8*, 103394. [CrossRef]

54. Kamil, A.M.; Mohammed, H.T.; Alkaim, A.F.; Hussein, F.H. Adsorption of Congo red on multiwall carbon nanotubes: Effect of operational parameters. *J. Chem. Pharm. Sci.* **2016**, *9*, 1128–1133.

55. Sabna, V.; Thampi, S.G.; Chandrakaran, S. Adsorption of crystal violet onto functionalised multi-walled carbon nanotubes: Equilibrium and kinetic studies. *Ecotoxicol. Environ. Saf.* **2016**, *134*, 390–397. [CrossRef]

56. Kiani, G.; Dostali, M.; Rostami, A.; Khataee, A.R. Adsorption studies on the removal of Malachite Green from aqueous solutions onto halloysite nanotubes. *Appl. Clay Sci.* **2011**, *54*, 34–39. [CrossRef]

57. Nautiyal, P.; Subramanian, K.A.; Dastidar, M.G. Adsorptive removal of dye using biochar derived from residual algae after in-situ transesterification: Alternate use of waste of biodiesel industry. *J. Environ. Manag.* **2016**, *182*, 187–197. [CrossRef]

58. Mittal, A.; Mittal, J.; Malviya, A.; Kaur, D.; Gupta, V.K. Adsorption of hazardous dye crystal violet from wastewater by waste materials. *J. Colloid Interface Sci.* **2010**, *343*, 463–473. [CrossRef]

59. Ahmad, R.; Kumar, R. Adsorption studies of hazardous malachite green onto treated ginger waste. *J. Environ. Manag.* **2010**, *91*, 1032–1038. [CrossRef]

60. Vimonses, V.; Lei, S.; Jin, B.; Chow, C.W.; Saint, C. Adsorption of congo red by three Australian kaolins. *Appl. Clay Sci.* **2009**, *43*, 465–472. [CrossRef]

61. Nandi, B.K.; Goswami, A.; Das, A.K.; Mondal, B.; Purkait, M.K. Kinetic and equilibrium studies on the adsorption of crystal violet dye using kaolin as an adsorbent. *Sep. Sci. Technol.* **2008**, *43*, 1382–1403. [CrossRef]

62. Caponi, N.; Collazzo, G.C.; Jahn, S.L.; Dotto, G.L.; Mazutti, M.A.; Foletto, E.L. Use of Brazilian kaolin as a potential low-cost adsorbent for the removal of malachite green from colored effluents. *Mater. Res.* **2017**, *20*, 14–22. [CrossRef]

63. Nodehi, R.; Shayesteh, H.; Kelishami, A.R. Enhanced adsorption of congo red using cationic surfactant functionalized zeolite particles. *Microchem. J.* **2020**, *153*, 104281. [CrossRef]

64. Bautista, M.M.C.; Arrieta, B.M.C.; Colpas, J.E.J.; Aldana, L.C.M.; Ríos, J.S.V.; Ortega, G.C.C. Evaluation of diatomaceous earth in the removal of crystal violet dye in solution. *J. Appl. Res. Technol.* **2022**, *20*, 387–398. [CrossRef]

65. Tian, L.; Zhang, J.; Shi, H.; Li, N.; Ping, Q. Adsorption of malachite green by diatomite: Equilibrium isotherms and kinetic studies. *J. Dispers. Sci. Technol.* **2016**, *37*, 1059–1066. [CrossRef]

66. Khamis Soliman, N.; Moustafa, A.F.; Aboud, A.A.; Halim, K.S.A. Effective utilization of *Moringa* seeds waste as a new green environmental adsorbent for removal of industrial toxic dyes. *J. Mater. Res. Technol.* **2019**, *8*, 1798–1808. [CrossRef]

67. Ashour, M.; Alprol, A.E.; Khedawy, M.; Abualnaja, K.M.; Mansour, A.T. Equilibrium and Kinetic Modeling of Crystal Violet Dye Adsorption by a Marine Diatom, *Skeletonema costatum*. *Materials* **2022**, *15*, 6375. [CrossRef]

68. Giri, B.S.; Sonwani, R.K.; Varjani, S.; Chaurasia, D.; Varadavenkatesan, T.; Chaturvedi, P.; Yadav, S.; Katiyar, V.; Singh, R.S.; Pandey, A. Highly efficient bio-adsorption of Malachite green using Chinese Fan-Palm Biochar (*Livistona chinensis*). *Chemosphere* **2022**, *287*, 132282. [CrossRef]

69. Van Eynde, E.; Lenaerts, B.; Tytgat, T.; Verbruggen, S.W.; Hauchecorne, B.; Blust, R.; Lenaerts, S. Effect of pretreatment and temperature on the properties of *Pinnularia* biosilica frustules. *RSC Adv.* **2014**, *4*, 56200–56206. [CrossRef]

70. Gholami, P.; Khataee, A.; Bhatnagar, A. Environmentally superior cleaning of diatom frustules using sono-Fenton process: Facile fabrication of nanoporous silica with homogeneous morphology and controlled size. *Ultrason. Sonochem.* **2020**, *64*, 105044. [CrossRef]

71. Chu, W.L.; Phang, S.M.; Goh, S.H. Environmental effects on growth and biochemical composition of *Nitzschia inconspicua* Grunow. *J. Appl. Phycol.* **1996**, *8*, 389–396. [CrossRef]

72. Jiang, Y.; Laverty, K.S.; Brown, J.; Brown, L.; Chagoya, J.; Burow, M.; Quigg, A. Effect of silicate limitation on growth, cell composition, and lipid production of three native diatoms to Southwest Texas desert. *J. Appl. Phycol.* **2015**, *27*, 1433–1442. [CrossRef]

73. Daglio, Y.; Maidana, N.I.; Matulewicz, M.C.; Rodríguez, M.C. Changes in motility and induction of enzymatic activity by nitrogen and phosphate deficiency in benthic *Halamphora luciae* (Bacillariophyceae) from Argentina. *Phycologia* **2016**, *55*, 493–505. [CrossRef]

74. Jauffrais, T.; Agogué, H.; Gemin, M.P.; Beaugeard, L.; Martin-Jézéquel, V. Effect of bacteria on growth and biochemical composition of two benthic diatoms *Halamphora coffeaeformis* and *Entomoneis paludosa*. *J. Exp. Mar. Biol. Ecol.* **2017**, *495*, 65–74. [CrossRef]

75. Dahmen-Ben Moussa, I.; Boukhriss, S.; Athmouni, K.; Ayadi, H. Secondary metabolites production combined with lead bioremediation by *Halamphora* sp. marine diatom microalgae and their physiological response. *Int. J. Aquac. Fish. Sci.* **2022**, *8*, 25–36. [CrossRef]

76. Avşar, Ö.; Avşar, U.; Arslan, Ş.; Kurtuluş, B.; Niedermann, S.; Güleç, N. Subaqueous hot springs in Köyceğiz Lake, Dalyan Channel and Fethiye-Göcek Bay (SW Turkey): Locations, chemistry and origins. *J. Volcanol. Geotherm. Res.* **2017**, *345*, 81–97. [CrossRef]

77. Thommes, M.; Kaneko, K.; Neimark, A.V.; Olivier, J.P.; Rodriguez-Reinoso, F.; Rouquerol, J.; Sing, K.S. Physisorption of gases, with special reference to the evaluation of surface area and pore size distribution (IUPAC Technical Report). *Pure Appl. Chem.* **2015**, *87*, 1051–1069. [CrossRef]

78. Shiraishi, S. Electric double layer capacitors. In *Carbon Alloys*; Yasuda, E.I., Inagaki, M., Kaneko, K., Endo, M., Tanabe, Y., Eds.; Elsevier Science: Amsterdam, The Netherlands, 2003; pp. 447–457. [CrossRef]

79. Sprynskyy, M.; Szczyglewska, P.; Wojtczak, I.; Nowak, I.; Witkowski, A.; Buszewski, B.; Feliczak-Guzik, A. Diatom biosilica doped with palladium (II) chloride nanoparticles as new efficient photocatalysts for methyl orange degradation. *Int. J. Mol. Sci.* **2021**, *22*, 6734. [CrossRef]

80. Vrieling, E.G.; Sun, Q.; Tian, M.; Kooyman, P.J.; Gieskes, W.W.C.; van Santen, R.A.; Sommerdijk, N.A.J.K. Salinity-dependent diatom biosilicification implies an important role of external ionic strength. *Proc. Natl. Acad. Sci. USA* **2007**, *104*, 10441–10446. [CrossRef]

81. Luo, Y.; Li, S.; Shen, K.; Song, Y.; Zhang, J.; Su, W.; Yang, X. Study on the Hemostasis Characteristics of Biomaterial Frustules Obtained from Diatom *Navicula australoshetlandica* sp. *Materials* **2021**, *14*, 3752. [CrossRef]

82. Dalagan, E.G.; Enriquez, E.P. Interaction of diatom silica with graphene. *Philipp. Sci. Lett.* **2013**, *6*, 119–127.

83. Verma, J.; Bhattacharya, A. Analysis on synthesis of silica nanoparticles and its effect on growth of *T. Harzianum* & *Rhizoctonia* species. *Biomed. J. Sci. Technol. Res.* **2018**, *10*, 7890–7897. [CrossRef]

84. Prasetyanto, E.A.; Sujandi, S.; Lee, S.C.; Park, S.E. Highly dispersed CuO nanoparticles on SBA-16 type mesoporous silica with cyclam SBA-16 as a precursor. *Bull. Korean Chem. Soc.* **2007**, *28*, 2359–2362. [CrossRef]

85. Roychoudhury, P.; Golubeva, A.; Dąbek, P.; Pryshchepa, O.; Sagandykova, G.; Pomastowski, P.; Gloc, M.; Dobrucka, R.; Kurzydłowski, K.; Buszewski, B.; et al. Study on Biogenic Spindle-Shaped Iron-Oxide Nanoparticles by *Pseudostaurosira trainorii* in Field of Laser Desorption/Ionization Applications. *Int. J. Mol. Sci.* **2022**, *23*, 11713. [CrossRef] [PubMed]

86. Jeffrey, S.W.; Humphrey, G.F. New spectrophotometric equations for determining chlorophylls a, b, c1 and c2 in higher plants, algae and natural phytoplankton. *Biochem. Physiol. Pflanz.* **1975**, *167*, 191–194. [CrossRef]

87. Trabelsi, L.; M'sakni, N.H.; Ben Ouada, H.; Bacha, H.; Roudesli, S. Partial characterization of extracellular polysaccharides produced by cyanobacterium *Arthrospira platensis*. *Biotechnol. Bioprocess Eng.* **2009**, *14*, 27–31. [CrossRef]

88. Jones, J.T.; Segnit, E.R. The nature of opal I. *Nomenclature and constituent phases. J. Geol. Soc. Aust.* **1971**, *18*, 57–68. [CrossRef]

89. Tesson, B.; Hildebrand, M. Extensive and intimate association of the cytoskeleton with forming silica in diatoms: Control over patterning on the meso-and micro-scale. *PLoS ONE* **2010**, *5*, e14300. [CrossRef]

90. Zhang, X.; Wu, Y.; He, S.; Yang, D. Structural characterization of sol–gel composites using TEOS/MEMO as precursors. *Surf. Coat. Techol.* **2007**, *201*, 6051–6058. [CrossRef]

91. Kiraz, N.; Kesmez, Ö.; Burunkaya, E.; Budama, L.; Acar, B.; Asiltürk, M.; Camurlu, H.E.; Arpaç, E. Antibacterial glass films prepared on metal surfaces by sol–gel method. *J. Sol-Gel. Sci. Tehcnol.* **2010**, *56*, 227–235. [CrossRef]

92. Camargo, E.; Jaime, P.C.J.; Lin, C.F.; Lin, M.S.; Yu, T.Y.; Wu, M.C.; Lai, S.Y.; Wang, M.Y. Chemical and optical characterization of *Psammodictyon panduriforme* (Gregory) Mann comb. nov. (Bacillariophyta) frustules. *Opt. Mater. Express* **2016**, *6*, 1436–1443. [CrossRef]

93. Karmakar, B.; De, G.; Ganguli, D. Dense silica microspheres from organic and inorganic acid hydrolysis of TEOS. *J. NonCryst. Solids* **2000**, *272*, 119–126. [CrossRef]

94. Li, K.M.; Jiang, J.G.; Tian, S.C.; Chen, X.J.; Yan, F. Influence of silica types on synthesis and performance of amine—Silica hybrid materials used for CO_2 capture. *J. Phys. Chem. C* **2014**, *118*, 2454–2462. [CrossRef]

95. Otzen, D. The role of proteins in biosilicification. *Scientifica* **2012**, *2012*, 867562. [CrossRef]

96. Nowak, A.P.; Sprynskyy, M.; Wojtczak, I.; Trzciński, K.; Wysocka, J.; Szkoda, M.; Buszewski, B.; Lisowska-Oleksiak, A. Diatoms Biomass as a Joint Source of Biosilica and Carbon for Lithium-Ion Battery Anodes. *Materials* **2020**, *13*, 1673. [CrossRef]

97. Wan, X.; Liu, D.; Ye, Y.; Luo, J. Preparation of Highly Dispersed $CaCO_3$ Nanoparticles in a Novel Membrane Dispersion Microreactor by a Chemical Coprecipitation Process. *Ind. Eng. Chem. Res.* **2022**, *61*, 7842–7851. [CrossRef]

98. Chen, W.-H.; Chu, Y.-S.; Liu, J.-L.; Chang, J.-S. Thermal Degradation of Carbohydrates, Proteins and Lipids in Microalgae Analyzed by Evolutionary Computation. *Energy Convers. Manag.* **2018**, *160*, 209–219. [CrossRef]

99. Choi, S.-B.; Kim, N.-W.; Lee, D.-K.; Yu, H. Growth Mechanism of Cubic MgO Granule via Common Ion Effect. *J. Nanosci. Nanotechnol.* **2013**, *13*, 7577–7580. [CrossRef]

100. Dong, B.; Xu, Y.; Lin, S.; Dai, X. Characterizing and Exploring the Formation Mechanism of Salt Deposition by Reusing Advanced-Softened, Silica-Rich, Oilfield-Produced Water (ASOW) in Superheated Steam Pipeline. *Sci. Rep.* **2015**, *5*, 17274. [CrossRef]

101. Pryshchepa, O.; Pomastowski, P.; Buszewski, B. Silver Nanoparticles: Synthesis, Investigation Techniques, and Properties. *Adv. Colloid. Interface Sci.* **2020**, *284*, 102246. [CrossRef]

102. Gumustas, M.; Sengel-Turk, C.T.; Gumustas, A.; Ozkan, S.A.; Uslu, B. Effect of Polymer-Based Nanoparticles on the Assay of Antimicrobial Drug Delivery Systems. In *Multifunctional Systems for Combined Delivery, Biosensing and Diagnostics*; Elsevier: Amsterdam, The Netherlands, 2017; pp. 67–108.

103. Xu, P.; Wang, H.; Tong, R.; Du, Q.; Zhong, W. Preparation and Morphology of SiO_2/PMMA Nanohybrids by Microemulsion Polymerization. *Colloid. Polym. Sci.* **2006**, *284*, 755–762. [CrossRef]

104. Abou-El-Souod, G.; Hamouda, R.A.; El-Sheekh, M. Influence of heavy metal as co-contamination on biodegradation of dyes by free and immobilized Scenedesmus obliquus. *Desalin. Water Treat.* **2020**, *182*, 351–358. [CrossRef]

105. Fawzy, M.A.; Gomaa, M. Low-cost biosorption of methylene blue and Congo red from single and binary systems using *Sargassum latifolium* biorefinery waste/wastepaper xerogel: An optimization and modeling study. *J. Appl. Phycol.* **2020**, *33*, 675–691. [CrossRef]

106. Wu, K.; Pan, X.; Zhang, J.; Zhang, X.; Salah Zene, A.; Tian, Y. Biosorption of Congo red from aqueous solutions based on self-immobilized mycelial pellets: Kinetics, isotherms, and thermodynamic studies. *ACS Omega* **2020**, *5*, 24601–24612. [CrossRef] [PubMed]

107. Sriram, G.; Uthappa, U.T.; Losic, D.; Kigga, M.; Jung, H.Y.; Kurkuri, M.D. Mg–Al-layered double hydroxide (LDH) modified diatoms for highly efficient removal of Congo red from aqueous solution. *Appl. Sci.* **2020**, *10*, 2285. [CrossRef]

108. Hernández-Zamora, M.; Cristiani-Urbina, E.; Martínez-Jerónimo, F.; Perales-Vela, H.V.; Ponce-Noyola, T.; Montes-Horcasitas, M.C.; Cañizares-Villanueva, O. Bioremoval of the azo dye Congo Red by the microalga *Chlorella vulgaris*. *Environ. Sci. Pollut. Res.* **2015**, *22*, 10811–10823. [CrossRef]

109. Vijayakumar, G.; Dharmendirakumar, M.; Renganathan, S.; Sivanesan, S.; Baskar, G.; Elango, K.P. Removal of Congo red from aqueous solutions by perlite. *CLEAN Soil Air Water* **2009**, *37*, 355–364. [CrossRef]

110. Guler, U.A.; Ersan, M.; Tuncel, E.; Dügenci, F. Mono and simultaneous removal of crystal violet and safranin dyes from aqueous solutions by HDTMA-modified *Spirulina* sp. *Process Saf. Environ. Prot.* **2016**, *99*, 194–206. [CrossRef]

111. Wang, X.S.; Liu, X.; Wen, L.; Zhou, Y.; Jiang, Y.; Li, Z. Comparison of basic dye crystal violet removal from aqueous solution by low-cost biosorbents. *Sep. Sci. Technol.* **2008**, *43*, 3712–3731. [CrossRef]

112. Essekri, A.; Aarab, N.; Hsini, A.; Ajmal, Z.; Laabd, M.; El Ouardi, M.; Ait Addi, A.; Lakhmiri, R.; Albourine, A. Enhanced adsorptive removal of crystal violet dye from aqueous media using citric acid modified red-seaweed: Experimental study combined with RSM process optimization. *J. Dispers. Sci. Technol.* **2022**, *43*, 1359–1372. [CrossRef]

113. Sarabadan, M.; Bashiri, H.; Mousavi, S.M. Removal of crystal violet dye by an efficient and low cost adsorbent: Modeling, kinetic, equilibrium and thermodynamic studies. *Korean J. Chem. Eng.* **2019**, *36*, 1575–1586. [CrossRef]

114. Ali, H.; Muhammad, S.K. Biosorption of crystal violet from water on leaf biomass of *Calotropis procera*. *J. Environ. Sci. Technol.* **2008**, *1*, 143–150. [CrossRef]

115. Bertolini, T.C.; Izidoro, J.C.; Magdalena, C.P.; Fungaro, D.A. Adsorption of crystal violet dye from aqueous solution onto zeolites from coal fly and bottom ashes. *Orbital Electron. J. Chem.* **2013**, *5*, 179–191.

116. Yang, H.; Zhou, D.; Chang, Z.; Zhang, L. Adsorption of crystal violet onto amino silica: Optimization, equilibrium, and kinetic studies. *Desalination Water Treat.* **2014**, *52*, 6113–6121. [CrossRef]

117. Malik, R.; Ramteke, D.S.; Wate, S.R. Adsorption of malachite green on groundnut shell waste based powdered activated carbon. *Waste Manag.* **2007**, *27*, 1129–1138. [CrossRef]

118. Sriram, G.; Uthappa, U.T.; Kigga, M.; Jung, H.Y.; Altalhi, T.; Brahmkhatri, V.; Kurkuri, M.D. Xerogel activated diatoms as an effective hybrid adsorbent for the efficient removal of malachite green. *New J. Chem.* **2019**, *43*, 3810–3820. [CrossRef]

119. Khan, T.A.; Ali, I.; Singh, V.V.; Sharma, S. Utilization of fly ash as low-cost adsorbent for the removal of methylene blue, malachite green and rhodamine B dyes from textile wastewater. *J. Environ. Prot. Sci.* **2009**, *3*, 11–22.

120. Arumugam, T.K.; Krishnamoorthy, P.; Rajagopalan, N.R.; Nanthini, S.; Vasudevan, D. Removal of malachite green from aqueous solutions using a modified chitosan composite. *Int. J. Biol. Macromol.* **2019**, *128*, 655–664. [CrossRef]

121. Kumar, K.V.; Sivanesan, S. Pseudo second order kinetics and pseudo isotherms for malachite green onto activated carbon: Comparison of linear and non-linear regression methods. *J. Hazard. Mater.* **2006**, *136*, 721–726. [CrossRef]

122. Kumar, K.V.; Sivanesan, S.; Ramamurthi, V. Adsorption of malachite green onto *Pithophora* sp., a fresh water algae: Equilibrium and kinetic modelling. *Process Biochem.* **2005**, *40*, 2865–2872. [CrossRef]

123. Kannan, R.R.; Rajasimman, M.; Rajamohan, N.; Sivaprakash, B. Brown marine algae *Turbinaria conoides* as biosorbent for Malachite green removal: Equilibrium and kinetic modeling. *Front. Environ. Sci. Eng. China* **2010**, *4*, 116–122. [CrossRef]

124. Wang, S.; Ariyanto, E. Competitive adsorption of malachite green and Pb ions on natural zeolite. *J. Colloid Interface Sci.* **2007**, *314*, 25–31. [CrossRef] [PubMed]

125. Kannan, C.; Sundaram, T.; Palvannan, T. Environmentally stable adsorbent of tetrahedral silica and non-tetrahedral alumina for removal and recovery of malachite green dye from aqueous solution. *J. Hazard. Mater.* **2008**, *157*, 137–145. [CrossRef]

126. Manzoor, K.; Batool, M.; Naz, F.; Nazar, M.F.; Hameed, B.H.; Zafar, M.N. A comprehensive review on application of plant-based bioadsorbents for Congo red removal. *Biomass Convers. Biorefin.* **2022**. [CrossRef]

127. Hameed, B.H.; El-Khaiary, M.I. Malachite green adsorption by rattan sawdust: Isotherm, kinetic and mechanism modeling. *J. Hazard. Mater.* **2008**, *159*, 574–579. [CrossRef] [PubMed]

128. Giles, C.H.; Smith, D.; Huitson, A. A general treatment and classification of the solute adsorption isotherm. I. Theoretical. *J. Colloid Interface Sci.* **1974**, *47*, 755–765. [CrossRef]

129. Kalam, S.; Abu-Khamsin, S.A.; Kamal, M.S.; Patil, S. Surfactant adsorption isotherms: A review. *ACS Omega* **2021**, *6*, 32342–32348. [CrossRef]

130. Lu, Z.; Maroto-Valer, M.M.; Schobert, H.H. Catalytic effects of inorganic compounds on the development of surface areas of fly ash carbon during steam activation. *Fuel Process. Tehcnol.* **2010**, *89*, 3436–3441. [CrossRef]

131. Guillard, R.R. Culture of phytoplankton for feeding marine invertebrates. In *Culture of Marine Invertebrate Animals*; Smith, W.L., Chanley, M.H., Eds.; Springer: Boston, MA, USA, 1975; pp. 29–60. [CrossRef]

132. Kirchman, D.L. Calculating microbial growth rates from data on production and standing stocks. *Mar. Ecol. Prog. Ser.* **2002**, *233*, 303–306. [CrossRef]

133. Lagergren, S. Zur theorie der sogenannten adsorption geloster stoffe. *Kungliga Svenska Vetenskapsakademiens. Handlingar* **1898**, *24*, 1–39.

134. Blanchard, G.; Maunaye, M.; Martin, G. Removal of heavy metals from waters by means of natural zeolites. *Water Res.* **1984**, *18*, 1501–1507. [CrossRef]

135. Boyd, G.E.; Adamson, A.W.; Myers Jr, L.S. The exchange adsorption of ions from aqueous solutions by organic zeolites. II. Kinetics. *J. Am. Chem. Soc.* **1947**, *69*, 2836–2848. [CrossRef]

136. Weber Jr, W.J.; Morris, J.C. Kinetics of adsorption on carbon from solution. *J. Sanit. Eng. Div.* **1963**, *89*, 31–59. [CrossRef]

137. Bangham, A.D.; Standish, M.M.; Watkins, J.C. Diffusion of univalent ions across the lamellae of swollen phospholipids. *J. Mol. Biol.* **1965**, *13*, 238–252. [CrossRef]

138. Langmuir, I. The adsorption of gases on plane surfaces of glass, mica and platinum. *J. Am. Chem. Soc.* **1918**, *40*, 1361–1403. [CrossRef]

139. Freundlich, H.M.F. Over the adsorption in solution. *J. Phys. Chem.* **1906**, *57*, 385–471.

140. Temkin, M.J.; Pyzhev, V. Recent modifications to Langmuir isotherms. *Acta Physochim URSS* **1940**, *12*, 217–225.

141. Sips, R. On the structure of a catalyst surface. *J. Phys. Chem.* **1948**, *16*, 490–495. [CrossRef]

SUPPLEMENTARY MATERIALS

Article

Removal of the Basic and Diazo Dyes from Aqueous Solution by the Frustules of *Halamphora* cf. *salinicola* (Bacillariophyta)

Aleksandra Golubeva[1*], Piya Roychoudhury[1], Przemysław Dąbek[1], Oleksandra Pryshchepa[2], Paweł Pomastowski[2], Jagoda Pałczyńska[3], Piotr Piszczek[3], Michał Gloc[4], Renata Dobrucka[4,5], Agnieszka Feliczak-Guzik[6], Izabela Nowak[6], Bogusław Buszewski[7,8] and Andrzej Witkowski[1*]

[1] Institute of Marine and Environmental Sciences, University of Szczecin, Mickiewicza 16a, 70-383 Szczecin, Poland; alexandra.golubeva@phd.usz.edu.pl (A.G); piyaroychoudhury2@gmail.com (P.R.); przemyslaw.dabek@usz.edu.pl (P.D.); andrzej.witkowski@usz.edu.pl (A.W.).

[2] Centre for Modern Interdisciplinary Technologies, Nicolaus Copernicus University, Wileńska 4, 87-100, Toruń, Poland; pryshchepa.alexie@gmail.com (O.P.); pomastowski.pawel@gmail.com (P.P.).

[3] Department of Inorganic and Coordination Chemistry, Faculty of Chemistry, Nicolaus Copernicus University in Toruń, Gagarina 7, 87-100 Toruń, Poland; 296600@stud.umk.pl (J.P.); piszczek@umk.pl (P.P).

[4] Faculty of Materials Science and Engineering, Warsaw University of Technology, Wołoska 141, 02-507 Warsaw, Poland; michalgloc@wp.pl (M.G.); renata.dobrucka@pw.edu.pl (R.D.).
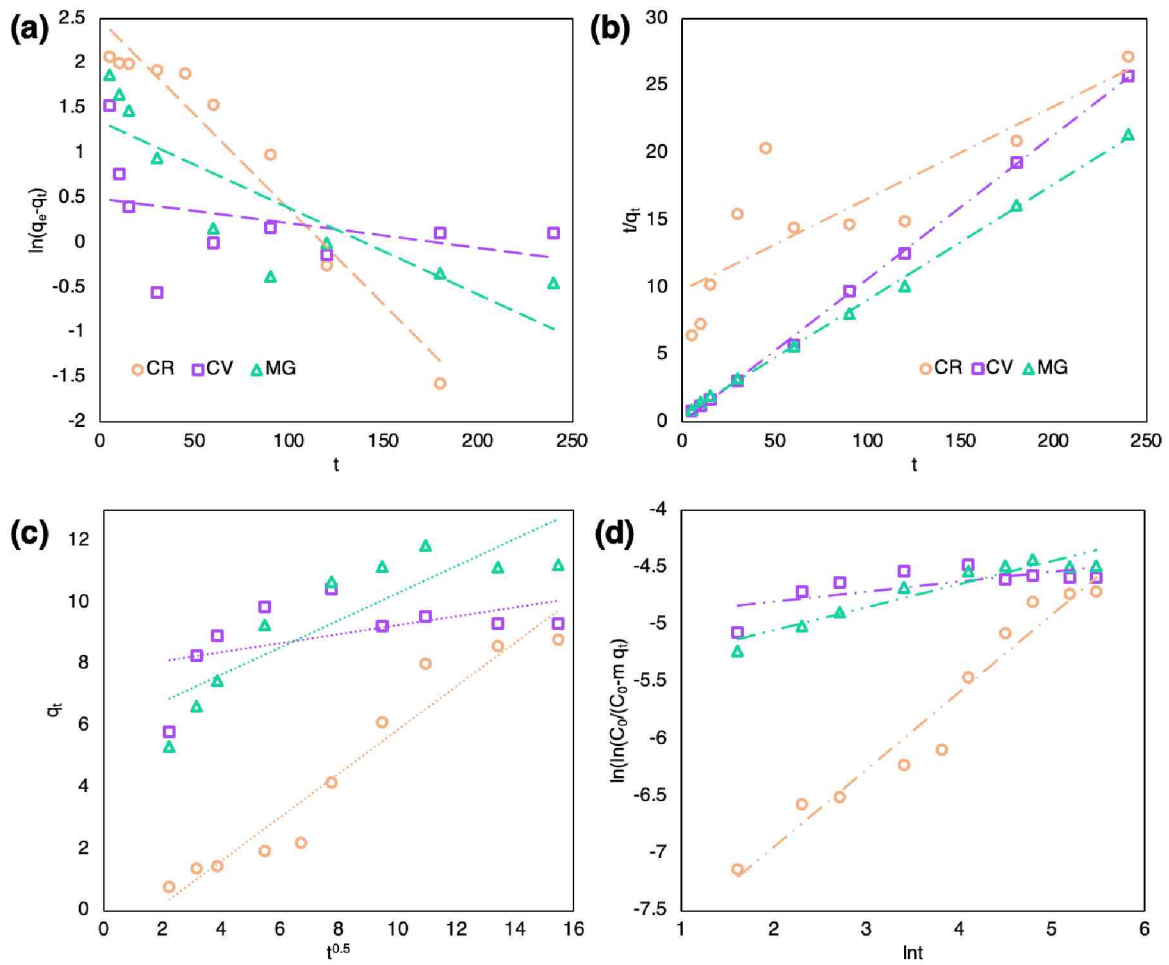
[5] Department of Industrial Products and Packaging Quality, Institute of Quality Science, Poznań University of Economics and Business, al. Niepodległości 10, 61-875 Poznan, Poland; renata.dobrucka@ue.poznan.pl (R.D.).

[6] Department of Applied Chemistry, Faculty of Chemistry, Adam Mickiewicz University, Uniwersytetu Poznańskiego 8, 61-614, Poznań, Poland; agnieszka.feliczak-guzik@amu.edu.pl (A.F-G.); nowakiza@amu.edu.pl (I.N.).
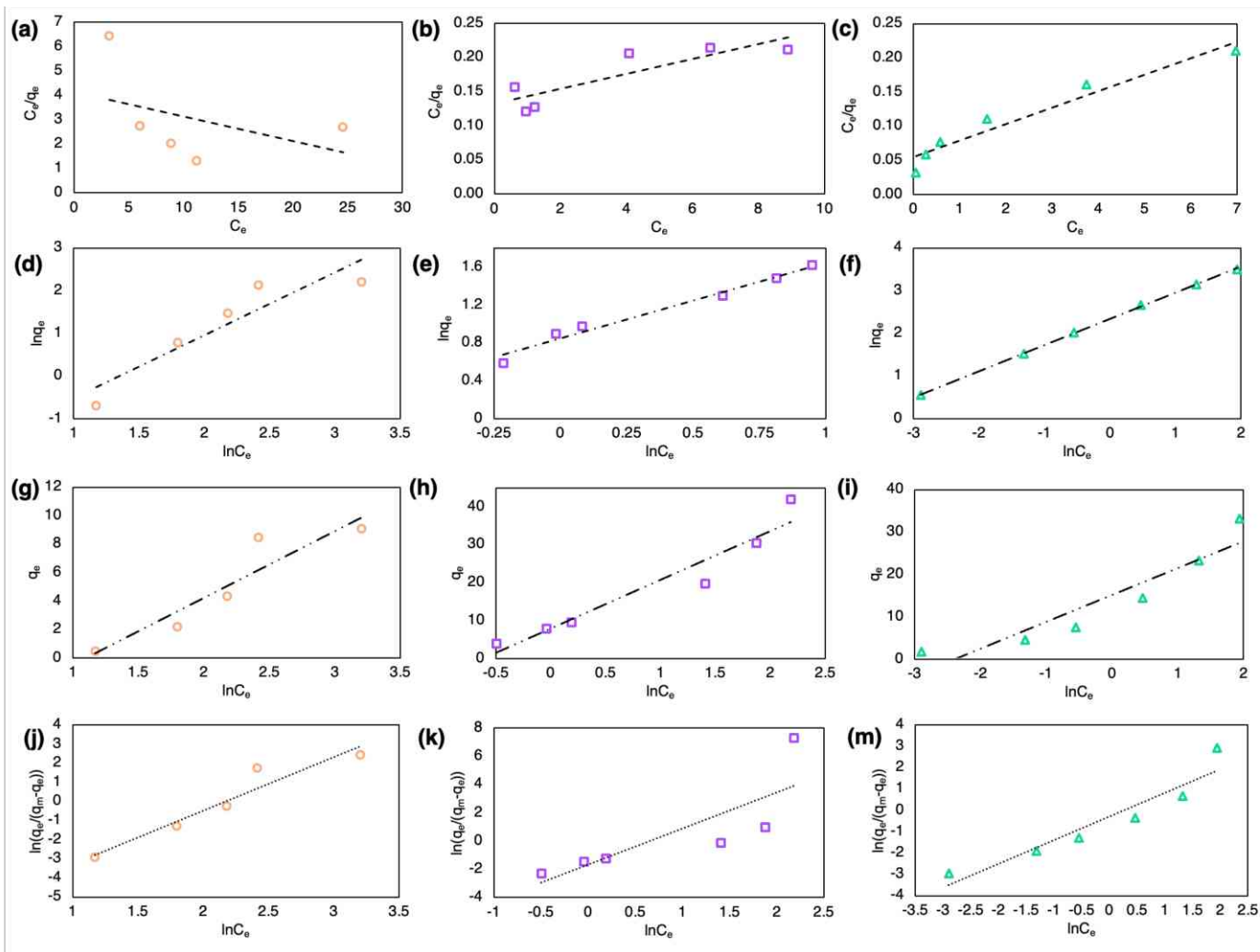
[7] Department of Environmental Chemistry and Bioanalysis, Faculty of Chemistry, Nicolaus Copernicus University, Gagarina 7, 87-100 Toruń, Poland; bbusz@umk.pl (B.B.).

[8] Prof. Jan Czochralski Kuyavian-Pomeranian Research & Development Centre, Krasińskiego 4, 87-100 Toruń, Poland; bbusz@umk.pl (B.B.).
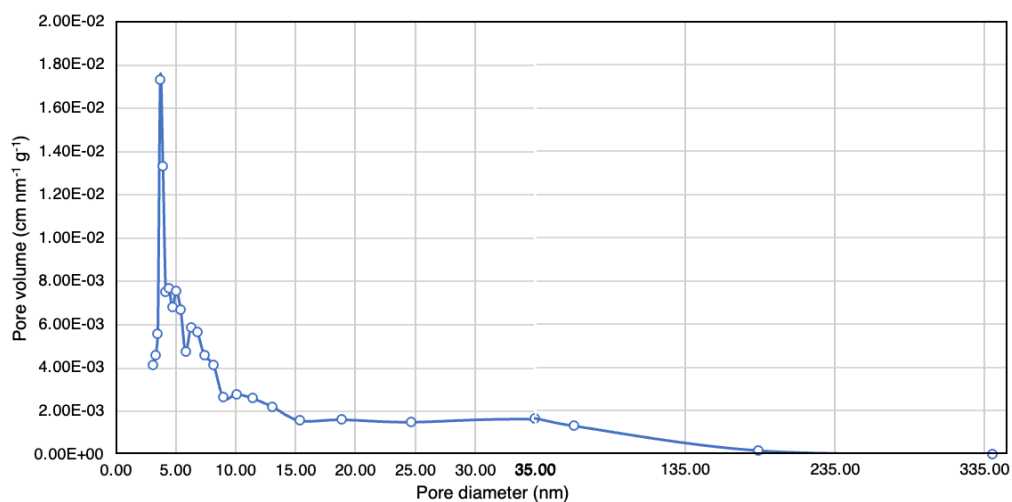
* Correspondence: alexandra.golubeva@phd.usz.edu.pl, Tel.: +48-534-030-336; andrzej.witkowski@usz.edu.pl

Figure S1. Adsorption kinetic and diffusion studies: **(a)** Pseudo-First Order; **(b)** Pseudo-Second Order; **(c)** Intra-particle diffusion; **(d)** Pore diffusion model (experimental data: orange circles – CR, violet squares – CV, green triangles – MG; calculated data: Pseudo-First Order – dashed line, Pseudo-Second Order – dash dotted line, Intra-particle diffusion – dotted line, Pore diffusion – double-dash dotted line).

Figure S2. Adsorption equilibrium study: Langmuir model for **(a)** CR, **(b)** CV, **(c)** MG; Freundlich model for **(d)** CR, **(e)** CV, **(f)** MG; Temkin model for **(g)** CR, **(h)** CV, **(i)** MG; and Sips model for **(j)** CR, **(k)** CV, **(m)** MG (experimental data: orange circles – CR, violet squares – CV, green triangles – MG; calculated data: Langmuir – dashed line, Freundlich – dash dotted line, Temkin – double dash dotted line, Sips – dotted line)

Figure S3. Pore size distribution of the diatom frustules of SZCZM1454 *H*. cf. *salinicola*

Table S1. Linearized forms of the kinetic and isotherm models' equations and parameters

Models	Equation		Description of parameters	Ref.
Kinetic study				
Pseudo-first order	$\ln(q_1 - q_t) = \ln q_1 - k_1 t$	(1)	q_t (mg g^{-1}) – amount adsorbed at given time (t, min) q_1 (mg g^{-1}) – adsorbent capacity at equilibrium k_1 (min^{-1}) – Pseudo-first order constant rate	[133]
Pseudo-second order	$\dfrac{t}{q_t} = \dfrac{1}{k_2 q_2^2} + \dfrac{1}{q_2}$	(2)	q_2 (mg g^{-1}) – adsorbent capacity at equilibrium k_2 (g (mg min)$^{-1}$) – Pseudo-second order constant rate α (mg (g min)$^{-1}$) – initial adsorption rate β (mg g^{-1}) – desorption constant	[134]
Diffusion study				
Boyd's	$B_t = -0.4977 - \ln(1 - \dfrac{q_t}{q_e})$	(3)	q_e (mg g^{-1}) – amount adsorbed at equilibrium B_t – mathematical function of F F – the fraction of metal ion adsorbed at any time (t)	[135]
Intra particle diffusion	$q_t = k_{wm} t^{0.5} + B$	(4)	q_t (mg g^{-1}) – amount adsorbed at given time (t, min) K_{wm} (mg (g min$^{0.5}$)$^{-1}$) – Intra-particle diffusion rate constant	[136]
Pore diffusion	$\log \log \left(\dfrac{C_0}{C_0 - mq_t}\right) = \log \left(\dfrac{mK_\beta}{2.303V}\right) + \Delta\beta \log t$	(5)	B (mg g^{-1}) – intercept C_0 (mg L^{-1}) – initial concentration of MB m (g) – mass of adsorbent g $\Delta\beta$ and K_β - Bangham constants V (mL) – volume of solution	[137]
Equilibrium study (isotherms)				
Langmuir	$\dfrac{C_e}{q_e} = \dfrac{1}{K_L Q_{max}} + \dfrac{C_e}{Q_{max}}$	(6)	q_e (mg g^{-1}) – adsorption capacity at equilibrium C_e (mg L^{-1}) – concentration of MB dye at equilibrium	[138]
Freundlich	$\ln q_e = \ln K_F + \dfrac{1}{n} \ln C_e$	(7)	q_{max} (mg g^{-1}) – maximum monolayer adsorption capacity of Langmuir	[139]
Temkin	$q_e = \dfrac{RT}{b} \ln C_e + \dfrac{RT}{b} \ln K_m$	(8)	K_L (L mg^{-1}) – Langmuir constant K_F [(mg g^{-1}) (mg L^{-1})$^{-n}$] – Freundlich constant	[140]
Sips	$\ln \left(\dfrac{q_e}{q_m - q_e}\right) = \dfrac{1}{n} \ln C_e + \ln K_S^{\frac{1}{n}}$	(9)	n – dimensionless Freundlich intensity parameter R (J [mol K]$^{-1}$) – universal gas constant T (K) – temperature b (J mol^{-1}) – Temkin constant related to sorption heat Km (L g^{-1}) – Temkin isotherm constant q_m (mg g^{-1}) – the Sips maximum adsorption capacity K_S [(mg L^{-1})$^{-1/n}$] – the Sips equilibrium constant n – the exponent of Sips where $0<1/n\leq1$	[141]

Aleksandra Golubeva

Institute of Marine and Environmental Sciences

University of Szczecin

Mickiewicza 16a, 70-383 Szczecin, Poland

Declaration

I hereby declare that my contribution in the preparation of article: " Removal of the Basic and Diazo Dyes from Aqueous Solution by the Frustules of *Halamphora* cf. *salinicola* (Bacillariophyta)" published in Marine Drugs, 21: 312, of which I am co-author with., Roychoudhury P., Dąbek P., Pryshchepa O., Pomastowski P., Pałczyńska J., Piszczek P., Gloc M., Dobrucka R., Feliczak-Guzik A., Nowak I., Buszewski B., and Witkowski A. equals to 70% (percent). For the purpose of the study, I conceptualized the study, performed the experiments, interpreted the data, performed statistical analysis and mathematical modeling, prepared figures and tables, drafted original manuscript, revised it after co-authors suggestions, led the revision process after the peer review, and submitted final version.

Aleksandra Golubeva

Instytut Nauk o Morzu i Środowisku: ul. Adama Mickiewicza 16, 70-383 Szczecin
Sekretariat: tel. 914442461, e-mail sekretariat.nms@usz.edu.pl
Dyrektor Instytutu: tel. 91 4442462, e-mail: dyrektor.nms@usz.edu.pl

Dr Piya Roychoudhury

Institute of Marine and Environmental Sciences

University of Szczecin

Mickiewicza 16a, 70-383 Szczecin, Poland

Declaration

I hereby declare that my contribution in the preparation of article: "Removal of the Basic and Diazo Dyes from Aqueous Solution by the Frustules of *Halamphora* cf. *salinicola* (Bacillariophyta)" published in Marine Drugs, 21: 312, of which I am co-author with Golubeva A., Dąbek P., Pryshchepa O., Pomastowski P., Pałczyńska J., Piszczek P., Gloc M., Dobrucka R., Feliczak-Guzik A., Nowak I., Buszewski B., and Witkowski, A. equals to 5% (percent). For the purpose of the study, I took part in conceptualization, SEM, EDS, UV-vis and FTIR investigation, and reviewed the original draft.

Piya Roychoudhury

Instytut Nauk o Morzu i Środowisku: ul. Adama Mickiewicza 16, 70-383 Szczecin
Sekretariat: tel. 914442461, e-mail sekretariat.nms@usz.edu.pl
Dyrektor Instytutu: tel. 91 4442462, e-mail: dyrektor.nms@usz.edu.pl

Dr Przemysław Dąbek

Institute of Marine and Environmental Sciences

University of Szczecin

Mickiewicza 16a, 70-383 Szczecin, Poland

Declaration

I hereby declare that my contribution in the preparation of article: " Removal of the Basic and Diazo Dyes from Aqueous Solution by the Frustules of *Halamphora* cf. *salinicola* (Bacillariophyta)" published in Marine Drugs, 21: 312, of which I am co-author with Golubeva A., Roychoudhury P., Pryshchepa O., Pomastowski P., Pałczyńska J., Piszczek P., Gloc M., Dobrucka R., Feliczak-Guzik A., Nowak I., Buszewski B., and Witkowski, A. equals to 2% (percent). For the purpose of the study, I supervised the work of PhD student Golubeva A., and took part in methodology development and revision of the original draft.

Przemysław Dąbek

Instytut Nauk o Morzu i Środowisku: ul. Adama Mickiewicza 16, 70-383 Szczecin
Sekretariat: tel. 914442461, e-mail sekretariat.nms@usz.edu.pl
Dyrektor Instytutu: tel. 91 4442462, e-mail: dyrektor.nms@usz.edu.pl

UNIWERSYTET
MIKOŁAJA KOPERNIKA
W TORUNIU
Interdyscyplinarne Centrum
Nowoczesnych Technologii

Dr. Paweł Pomastowski, DSc., Prof. NCU

Centre for Modern Interdisciplinary Technologies

Nicolaus Copernicus University in Toruń

Wileńska 4, 87-100, Toruń, Poland

Declaration

I hereby declare that my contribution in the preparation of article: "Removal of the Basic and Diazo Dyes from Aqueous Solution by the Frustules of *Halamphora* cf. *salinicola* (Bacillariophyta)" published in Marine Drugs, 21: 3112, of which I am co-author with Golubeva A., Roychoudhury P., Dąbek P., Pryshchepa O., Pałczyńska J., Piszczek P., Gloc M., Dobrucka R., Feliczak-Guzik A., Nowak I., Buszewski B., and Witkowski A. equals to 3% (percent). For the purpose of the study, I took part in conceptualization of the study, reviewed the original draft, and helped with revision in peer-review process.

Prof. Dr hab. Andrzej Witkowski

Institute of Marine and Environmental Sciences

University of Szczecin

Mickiewicza 16a, 70-383 Szczecin, Poland

Declaration

I hereby declare that my contribution in the preparation of article: " Removal of the Basic and Diazo Dyes from Aqueous Solution by the Frustules of *Halamphora* cf. *salinicola* (Bacillariophyta)" published in Marine Drugs, 21: 312, of which I am co-author with Golubeva A., Roychoudhury P., Dąbek P., Pryshchepa O., Pomastowski P., Pałczyńska J., Piszczek P., Gloc M., Dobrucka R., Feliczak-Guzik A., Nowak I., and Buszewski B. equals to 1% (percent). For the purpose of the study, I supervised the work of PhD student Golubeva A., and revised of the original draft.

Andrzej Witkowski

Instytut Nauk o Morzu i Środowisku: ul. Adama Mickiewicza 16, 70-383 Szczecin
Sekretariat: tel. 914442461, e-mail sekretariat.nms@usz.edu.pl
Dyrektor Instytutu: tel. 91 4442462, e-mail: dyrektor.nms@usz.edu.pl

ANNEX III

Roychoudhury, P., **Golubeva, A.,** Dąbek, P., Pryshchepa, O., Sagandykova, G., Pomastowski, P., Gloc, M., Dobrucka, R., Kurzydłowski, K., Buszewski, B. & Witkowski, A. (2022) Study on Biogenic Spindle-Shaped Iron-Oxide Nanoparticles by *Pseudostaurosira trainorii* in Field of Laser Desorption/Ionization Applications. *International Journal of Molecular Sciences*, *23*, 11713.

Article

Study on Biogenic Spindle-Shaped Iron-Oxide Nanoparticles by *Pseudostaurosira trainorii* in Field of Laser Desorption/Ionization Applications

Piya Roychoudhury [1,*], Aleksandra Golubeva [1], Przemysław Dąbek [1], Oleksandra Pryshchepa [2], Gulyaim Sagandykova [2], Paweł Pomastowski [2], Michał Gloc [3], Renata Dobrucka [3,4], Krzysztof Kurzydłowski [5], Bogusław Buszewski [2,6] and Andrzej Witkowski [1]

[1] Institute of Marine and Environmental Sciences, University of Szczecin, Mickiewicza 16a, 70-383 Szczecin, Poland
[2] Centre for Modern Interdisciplinary Technologies, Nicolaus Copernicus University, Wileńska 4, 87-100 Toruń, Poland
[3] Faculty of Materials Science and Engineering, Warsaw University of Technology, Wołoska 141, 02-507 Warsaw, Poland
[4] Department of Industrial Products and Packaging Quality, Institute of Quality Science, Poznań University of Economics and Business, al. Niepodległości 10, 61-875 Poznań, Poland
[5] Faculty of Mechanical Engineering, Białystok University of Technology, Wiejska 45c, 15-351 Białystok, Poland
[6] Department of Environmental Chemistry and Bioanalysis, Faculty of Chemistry, Nicolaus Copernicus University, Gagarina 7, 87-100 Toruń, Poland
* Correspondence: piya.roychoudhury@usz.edu.pl

Abstract: Nanostructures-assisted laser desorption/ionization mass spectrometry (NALDI-MS) is gaining attention for the analysis of a wide range of molecules. In this present investigation, *Pseudostaurosira trainorii* mediated biosynthesized iron-oxide nanoparticles (IONPs) have been utilized as nanostructures assisting ionization and desorption for laser desorption/ionization mass spectrometry (LDI-MS). The chain forming diatom, *P. trainorii* showed efficiency in the production of IONPs against 0.01 M Fe^{+3} (pH 2) aqueous solution at the intracellular and extracellular level. The whole biomass and external media turned dark orange in color after 3 days of reaction with Fe^{3+} solution. Scanning electron microscopic (SEM) images illustrated that the surface of Fe^{3+} exposed frustules of *P. trainorii* were entirely covered by synthesized nanostructures contrasting with the natural surface ornamentation of control cells. The IONPs loaded frustules also exhibited catalytic properties by decolorizing yellow colored nitrophenol after 3 h of reaction. Transmission electron microscopic (TEM) images confirmed that the produced particles are spindle-shaped with ~50–70 nm length and ~10–30 nm width. The biogenic IONPs were utilized as an inorganic matrix in LDI-MS and showed high sensitivity towards small molecules as glucose, alanine and triacylglycerols at nano- and picomolar level per spot, respectively. The presented biocompatible technique offers new perspectives in nanobiotechnology for the production of spindle-shaped IONPs that can be applied in future for the preparation of NALDI plates.

Keywords: iron-oxide nanoparticles; biogenesis; diatom; LDI-MS; nano-spindle

1. Introduction

Iron-oxide nanoparticles (IONPs) are an exceptional and prominent category of metal nanoparticles because of their intrinsic magnetic properties. These magnetic nanomaterials have drawn the attention of biomedical researchers, especially for their utility in hyperthermia-based therapy of cancer due to their heat dissipation ability under an alternating magnetic field [1]. IONPs are also promising candidates for drug delivery [2], catalysis [3], magnetic inks for jet printing [4], killing microorganisms [5], magnetic separation [6], biosensing [7], gene therapy [8], environmental remediation [9] and as contrast

agents for magnetic resonance imaging [10] and magnetic fluid hyperthermia [11]. The most used methodologies to produce IONPs are microemulsion, thermal decomposition, co-precipitation, sol–gel [12] and colloidal processing [13]. However, these methods require the usage of hazardous chemicals, such as sodium borohydrate [14], and do not follow the eco-friendly route in IONPs fabrication. Though IONPs are considered completely safe for biological systems, the involvement of such toxic chemicals in synthetic production limits their utilization in medical applications. For this reason, biogenesis has become most popular for the formation of biocompatible IONPs. Some higher plants [15,16], fungi [17,18], bacteria [19,20] have already been exploited as bioreagents for biogenic production of IONPs. Only few reports on algae-based synthesis of IONPs are available. Algae including *Ulva flexuosa* [21], *Padina pavonica* and *Sargassum acinarium* [22], *Gracilaria edulis* [23], *Kappaphycus alvarezii* [24], *Turbinaria decurrens* [25] showed efficiency in production of IONPs against ferric chloride solution. However, no reports are available regarding diatom mediated production of IONPs. Diatom inspired approaches become most successful in the construction of silica conjugated metal nanoparticles. Doping of metal particles on a layer of silica is sometimes essential to make the particles more stable, harder, and more effective for catalysis [26]. Certain metal nanoparticles, namely gold, silver, platinum, titanium, germanium, palladium, have already been modified by using the natural siliceous shells of *Amphora copulata* [27], *Halamphora subturgida* [28], *Coscinodiscus wailesii* [29], *Thalassiosira weissflogii* [30], *Pinnularia* sp. [31], *P. trainorii* [32], respectively. In this study, we have reported the bio-protocol for construction of IONPs decorated frustules of *P. trainorii* for the first time.

p-Nitrophenol is considered as one of the most highly toxic compounds for the environment as it consists of nitro group in its aromatic ring structure. p-Nitrophenol is commonly used in pharmaceuticals, fungicides, insecticides, and dye industries. This pollutant from contaminated industrial wastes is continuously entering the ecosystem and induces significant health risks. Presently, scientists are trying to degrade p-nitrophenol by exploiting the catalytic activity of various nanoparticles. It has been reported that iron nanoparticles synthesized by *Jatropha* [33] and *Artocarpus heterophyllus* [34] leaf extracts showed potential catalytic activity to degrade nitrophenol. It was also reported that iron oxides are capable of degrading nitrophenol in the presence of oxalate [35]. Fe^{3+}/iron oxide/SiO_2 xerogel also showed catalytic effect in nitrophenol reduction by photo-fenton reaction [36]. Therefore, it can be said that biogenic IONPs doped frustules of *P. trainorii* will be an effective photocatalytic agent for nitrophenol degradation.

Nanoparticles with a wide center portion and having both tapering ends in the size ranges of 1–100 nm in any dimension are known as nanospindle, a prominent category of various nanoforms. Among the various shapes, rod/spindle-shaped particles are gaining attention because they are more effective in photothermal therapy. Increased accumulation of spindle-shaped nanoparticles at the tumor site than spherical particles was also reported [37]. Chemically synthesized rod-shaped IONPs showed more potential effect in magnetic hyperthermia than polyhedral shape [37]. Few authors reported bioreagents mediated production of rod/spindle-shaped IONPs. Brayner et al. 2009 [38] reported that rod-shaped akaganeite (β-FeOOH) nanoparticles production at the intracellular level is possible by cyanobacteria, *Anabaena* sp. and *Calothrix* sp. and green alga, *Klebsormidium* sp. at room temperature. Spindle-shaped zero valent nanoiron was synthesized by *Arthrospira platensis* [39] and *Leptolyngbya valderiana* [40]. No report is available regarding diatom assisted biogenic production of spindle-shaped IONPs.

Matrix-assisted laser desorption/ionization (MALDI) has become an important tool for the determination of molecular mass of macromolecules such as proteins. In contrast, MALDI has limitations for applications below m/z 500 due to suppression effects and chemical background interfering with low molecular weight analytes [41]. In addition, various nanomaterials were applied as inorganic matrix for analysis of low molecular weight compounds in LDI-MS. Gold, silver, zinc oxide, platinum nanoparticles have been used as matrix and showed significant sensitivity for determination of molar mass of carbohydrate [42], triglycerides [43], polyethylene glycol [44], saccharides [45], respectively. IONPs have been used in MALDI instead of matrix for analysis of glycan and peptides [46]. Citric acid capped IONPs have been recognized as an effective matrix for polymers [47]. Dihydrobenzoic acid modified IONPs has been used as matrix for the determination of diverse structures of small molecules [48]. Therefore, it was hypothesized that IONPs synthesized in the proposed, cost-effective way, may serve as nanomaterials assisting with ionization and desorption in LDI-MS analysis of low molecular weight analytes.

In the present investigation, spindle-shaped IONPs have been synthesized using diatom-strain, *P. trainorii* (BA170) E.A. Morales (2001) [49] procured from the Culture Collection of Baltic Algae, Institute of Oceanography, University of Gdańsk, Poland with further detailed characterization using analytical techniques followed by an evaluation of LDI-MS efficiency of IONPs as a nanomaterial for the preparation of NALDI plates.

2. Results

2.1. Diatom Mediated Biofabrication of IONPs

The reduction of Fe^{3+} ions and subsequent production of biogenic IONPs at the intracellular and extracellular level was initially detected by observing color changes in biomass and experimental media. The whole biomass of *P. trainorii* exhibited a time-dependent color change during 3 days of the incubation period with 0.01 M (pH 2) Fe^{3+} solution. The yellowish-green cells (Figure 1b) of *P. trainorii* started to turn orangish in color after 24 h of reaction. However, all cells of *P. trainorii* turned dark orange in color after 3 days of reaction (Figure 1c). Not only that, but the external media also turned dark orange in color (Figure 1h,i). After 3 days of reaction, no further color change in cells and in experimental media was observed. It was noted that during the development of orange color, *P. trainorii* lost all its chlorophyll and carotenoids contents (Figure 1c), which was also confirmed by fluorescent microscopy (Figure 1d–f) and UV-Vis spectroscopy (Figure 1a). Under the fluorescent microscope at 450–490 nm excitation the control cells of *P. trainorii* showed red fluorescence of chlorophyll (Figure 1d). However, after 24 h of Fe^{3+} exposure maximum cells of *P. trainorii* showed green fluorescence property (Figure 1e) as well as after 3 days of reaction all cells only emitted green fluorescence (Figure 1f). The metal stress related morphological changes, e.g., the high rate of cell division (Figure 1e) and loss of cellular integrity (Figure 1f) were also documented in Fe^{3+} treated *P. trainorii* which signified iron toxicity.
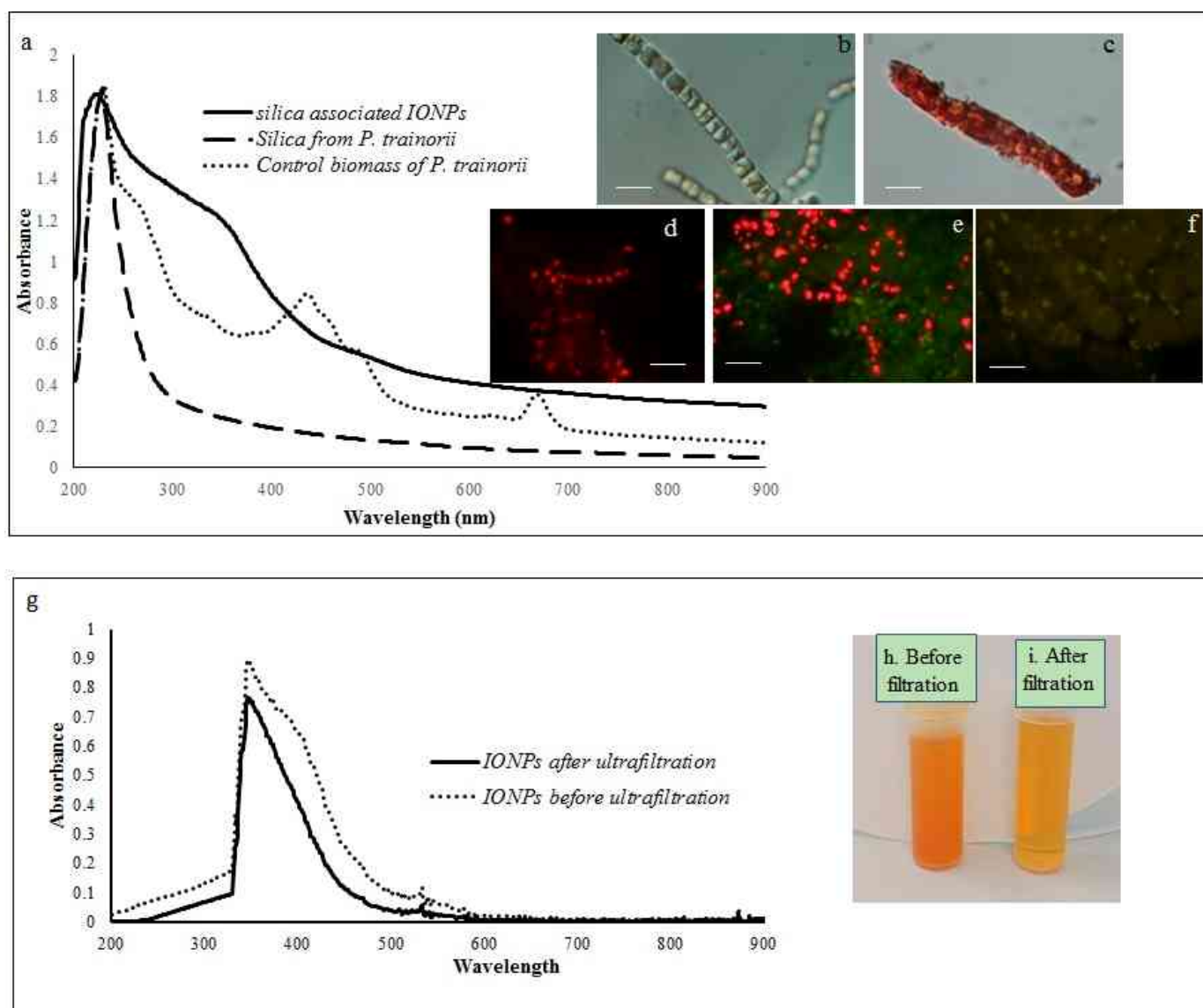
Figure 1. Showing UV-Vis spectroscopy of control biomass, cleaned frustules and IONP-loaded frustules (**a**). LM images of *P. trainorii* before (**b**) and after (**c**) treatment with Fe^{3+} solution [scale bar 1 μm]. Fluorescent images control (**d**) and Fe^{3+} exposed *P. trainorii* taken at 24 h (**e**), 72 h (**f**) of reaction [scale bar 1 μm]. UV-Vis spectroscopy of extracellular IONPs before and after ultrafiltration (**g**). Extracellular IONPs suspension before (**h**) and after (**i**) ultrafiltration.

2.2. SEM Analysis of Fe^{3+} Treated P. trainorii with EDAX and Elemental Mapping

SEM images illustrated the surface decoration of siliceous frustules of *P. trainorii* before (Figure 2a) and after treatment with Fe^{3+} solution (Figure 2b–d). SEM micrographs revealed the biosynthesis of nanostructures and their deposition on the surface of Fe^{3+} treated *P. trainorii* (Figure 2b–d). Surfaces of Fe^{3+} exposed frustules were entirely covered by synthesized nanostructures contrasting natural surface ornamentation of control cells. Elemental mapping (Figure 3b–g) as well as EDAX (Figure 3a) study of nanoparticles loaded cells confirmed the presence of silicon, oxygen, and iron all over the frustules. A strong signal of gold (Au) was also observed as Au was used as coating material for SEM study. Elemental mapping of a single frustule loaded with IONPs illustrated the distributional pattern of the elements, namely silicon, oxygen, and iron (Figure 3b–g).
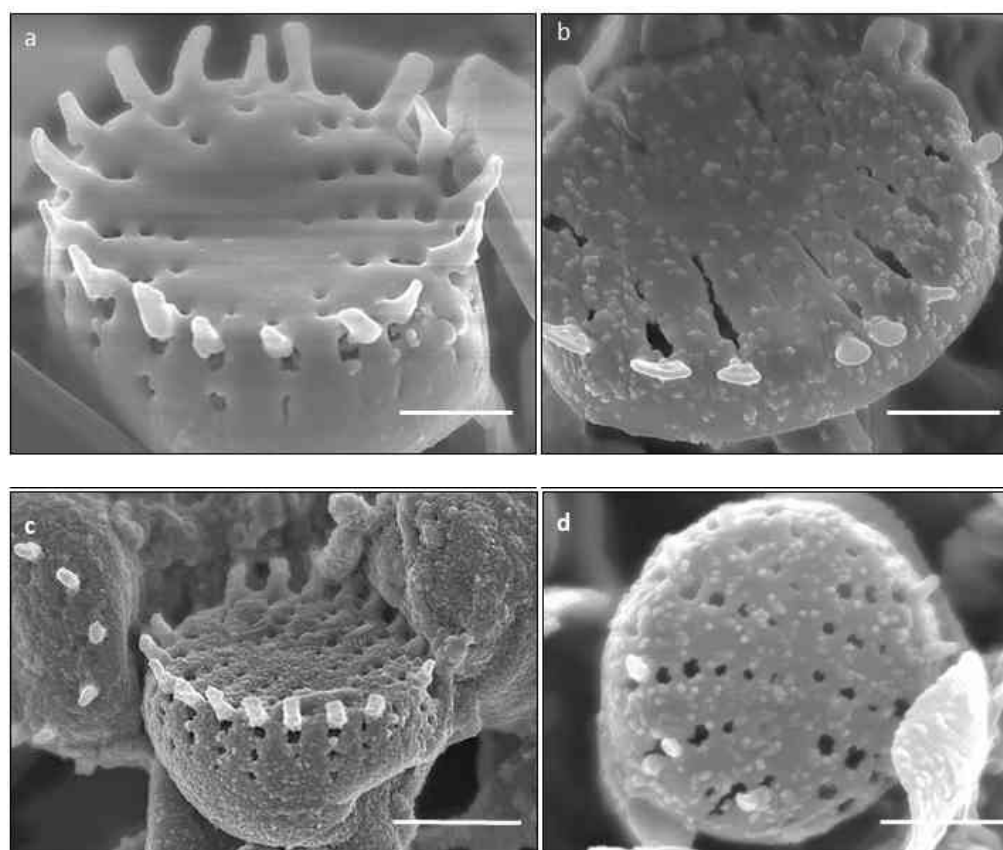
Figure 2. SEM images showing surface morphology of control (**a**) and IONPs loaded (**b–d**) frustules *P. trainorii* [scale bar 1 μm].
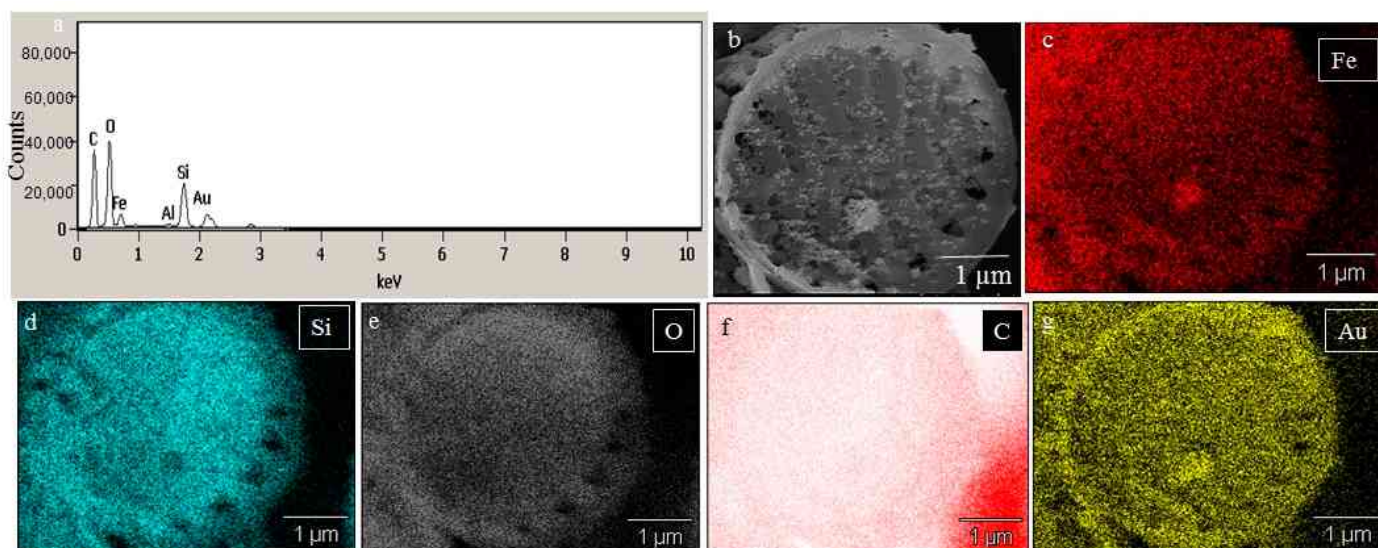

Figure 3. EDAX spectra of IONPs loaded frustules (**a**). Elemental mapping of IONPs loaded single frustules confirmed presence of iron, silicon and oxygen all over the frustules (**b–g**).

2.3. UV-Vis and Fourier Transform Infrared Spectroscopy

A comparative spectral analysis among water extracts of control biomass, cleaned frustules and IONPs loaded frustules of *P. trainorii* have been performed. In UV-Vis spectroscopy, water extracts of the control biomass of *P. trainorii* showed three distinct peaks at 270, 450, and 663 nm (Figure 1a). These three consecutive peaks at 270, 450, 663 nm

revealed the presence of silica, carotenoids and chlorophyll, respectively, in untreated cells. The H_2O_2 washed frustules' extract of *P. trainorii* showed maximum absorbance at 270 nm and confirmed the presence of only silica particles as pigment content was below the detectable limit (Figure 1a). The Fe^{3+} exposed orange colored biomass' extract of *P. trainorii* showed two characteristic peaks at ~270 and ~350 nm, respectively (Figure 1a). The extracellular brown suspension also showed distinct peak at ~350 nm before and after ultrafiltration (Figure 1g).

FTIR spectra revealed the chemical nature of control and IONPs loaded frustules of *P. trainorii* as well as extracellular IONPs as shown in Figure 4. During the measurement of control silica and silica doped IONPs, peaks appeared at 3664, 2979, 2924, 2855, 1741, 1633, 1531, 1380, 1144, 1058, 954, 434 cm^{-1}. These peaks revealed the presence of O–H, C–H, C=O, N–H, Si–O–Si and Si–O functional groups on the surface of frustules as well as frustules loaded with synthesized IONPs. However, a distinct peak at 556 cm^{-1} has been observed only in IR spectra of silica loaded IONPs and externally produced IONPs which has been identified as characteristic peak of Fe-O.
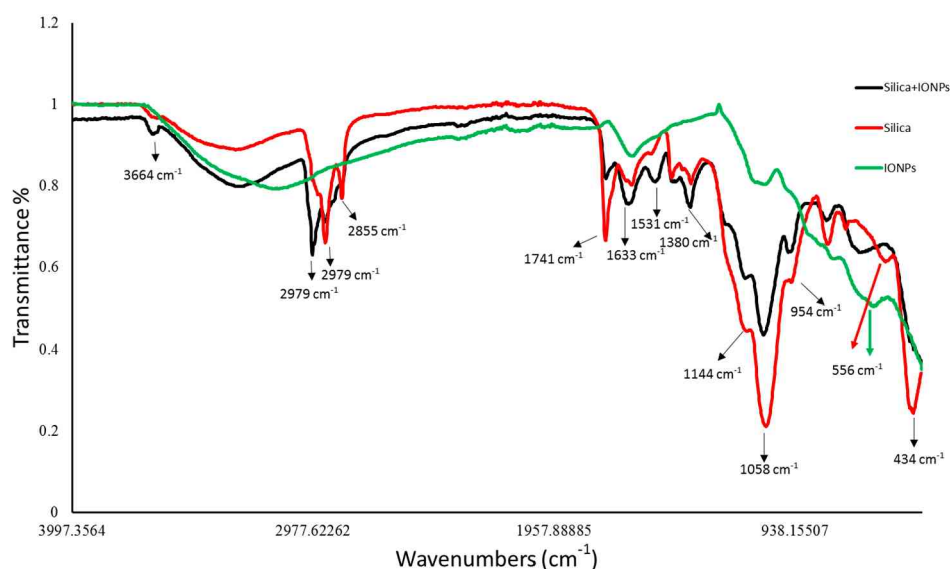

Figure 4. FTIR peaks revealed the functional groups present surrounding the surfaces of control silica, silica loaded particles and extracellular IONPs.

2.4. ICP-MS, Zeta Potential and X-ray Diffraction

The ICP-MS study confirmed that the concentration of ultrafiltered extracellular IONPs suspension was 152 mgL^{-1}. Zeta potential values of IONPs were measured as +24.6 mV (Figure 5). It stated that produced nanoparticles had positively charged surface. The XRD spectra did not show any specific peak for externally synthesized IONPs (Figure 6) and revealed that synthesized IONPs were amorphous in nature.
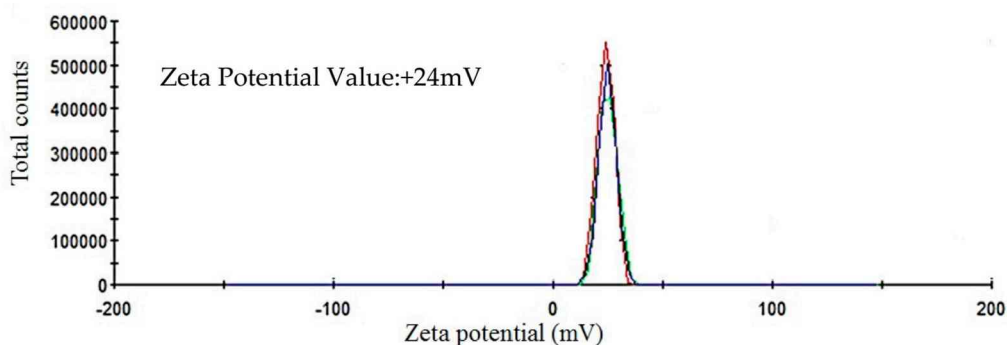

Figure 5. Showing zeta potential value of extracellular IONPs.
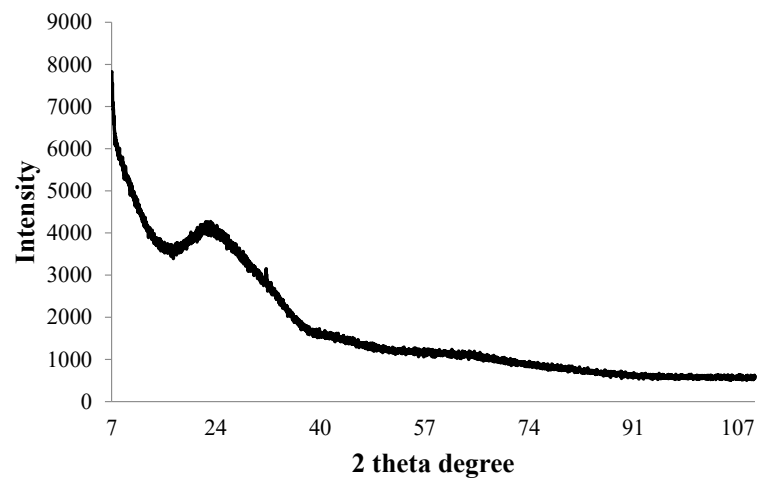
Figure 6. X-ray diffraction pattern of synthesized IONPs by *P. trainorii*.

2.5. TEM and EDAX

The TEM observations represent a clear picture regarding the shape and size of IONPs produced by the experimental taxa (Figures 7 and 8). The TEM study confirmed that all synthesized particles (extracted and extracellular) are spindle-shaped with almost the same size. The average length of the nano-spindle was in the range of 50–70 nm with the width of 10–30 nm range.
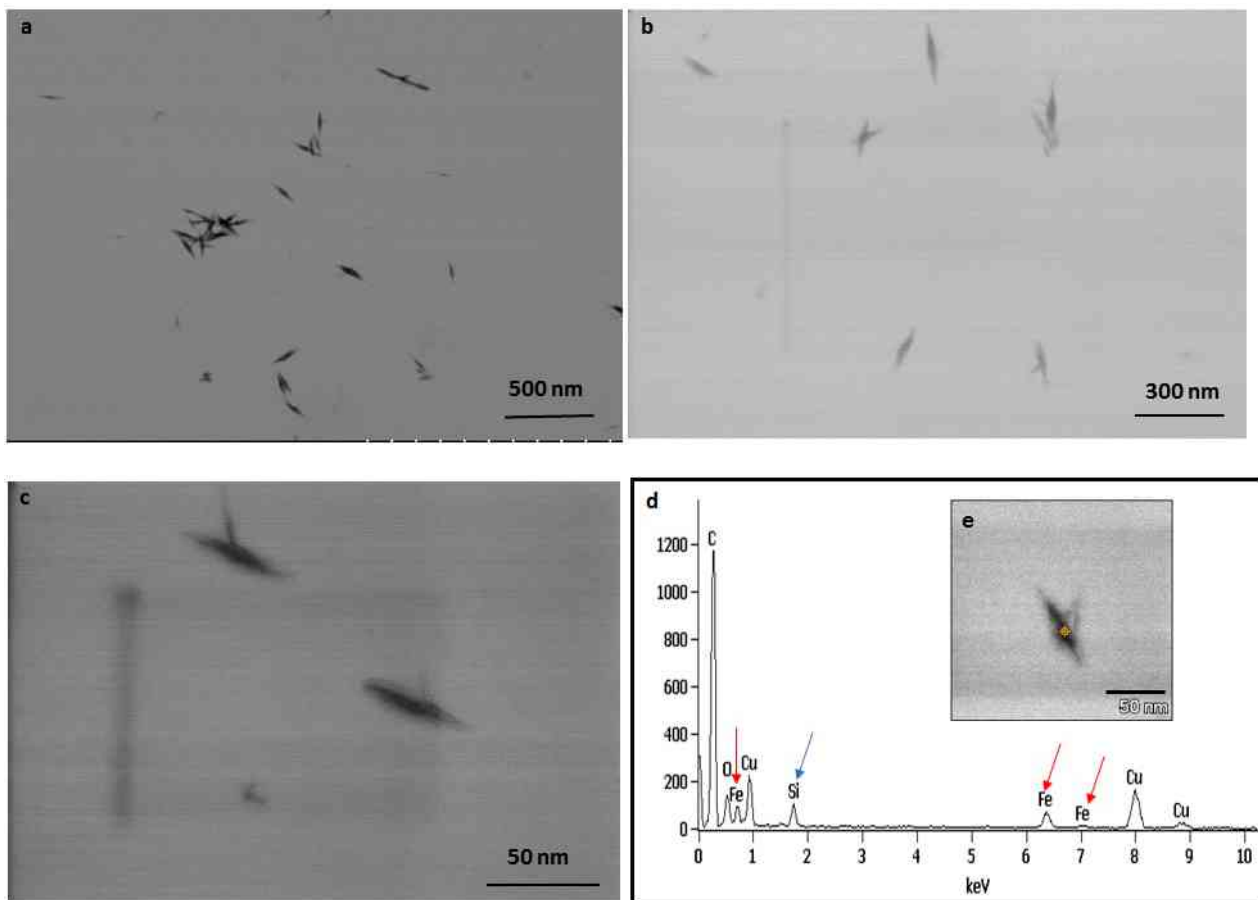
Figure 7. TEM images of extracted IONPs from particle loaded frustules captured in various magnification (**a**–**c**). EDAX study of single particle confirming presence of iron, silica and oxygen (**d**). TEM image of single spindle shaped IONP (**e**).
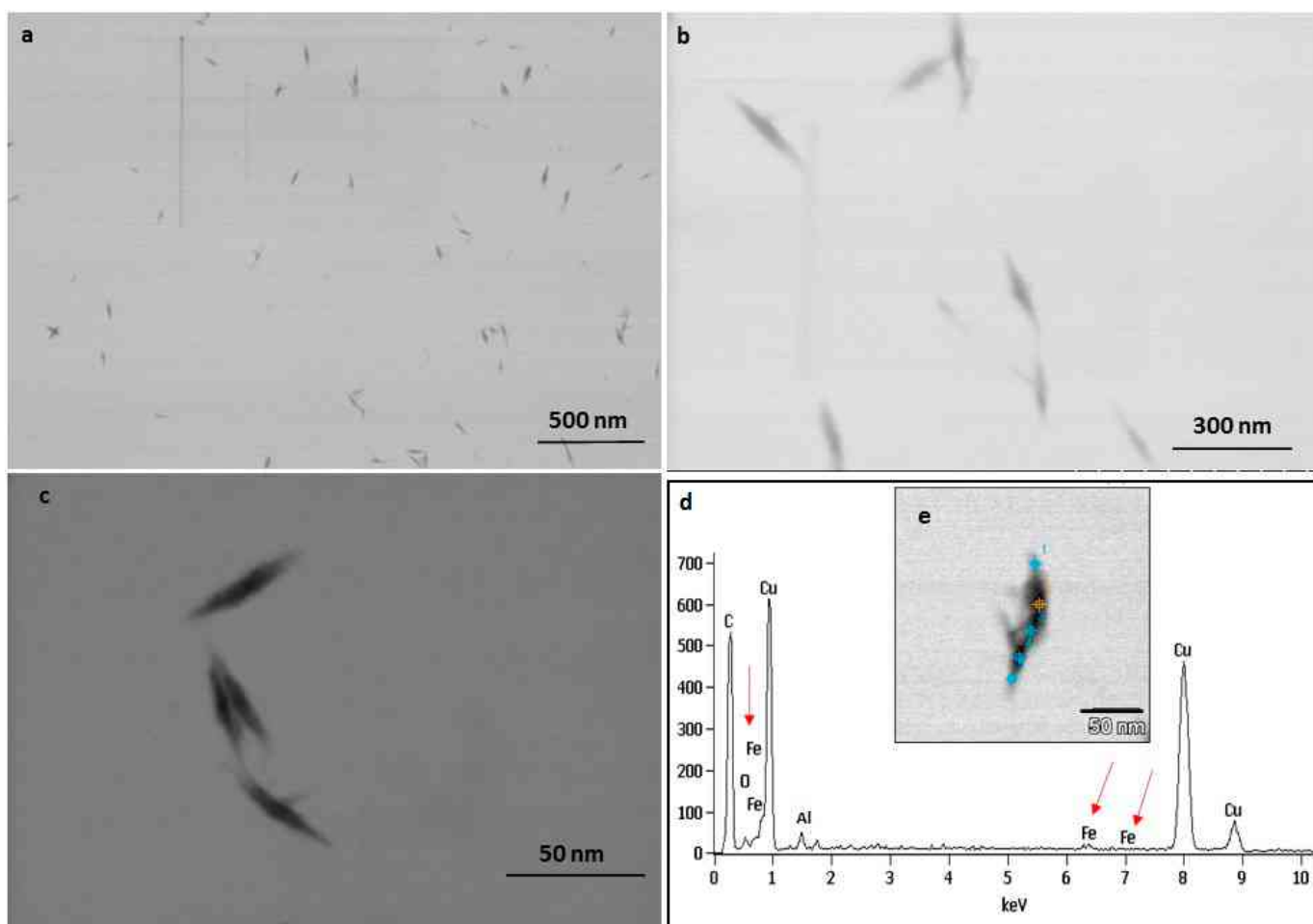
Figure 8. TEM images of extracellular IONPs captured in various magnification (**a–c**). EDAX study of single particle confirming presence of iron, oxygen (**d**). TEM image of single extracellular IONP (**e**).

The EDX spectra of extracted and extracellular IONPs are shown in Figures 7d and 8d, respectively. The EDX spectra of extracted nanostructures from NP loaded frustules showed three distinct peaks, which corresponds to the signals of silica, oxygen, and iron, respectively. The same signals were observed from seven different spots of a single particle. However, EDX spectra of extracellular IONPs showed only two strong signals of iron and oxygen.

2.6. 4-Nitrophenol Degradation by IONPs Decorated Frustules

The IONPS decorated frustules of *P. trainorii* showed positive responses in degradation of 4-nitrophenol under light. The degradation of 4-Nitrophenol after exposure to IONPs loaded frustules was preliminarily confirmed by the color change of nitrophenol. During the reaction, gradually, the yellow color of nitrophenol faded away with time. After 3 h of reaction, the solution became completely colorless. Spectroscopic data showed a sharp decrease in absorbance with an increase in reaction time, which revealed the degradation of 4-nitrophenol (Figure 9). After 180 min of reaction, 94% ± SE 0.157 of 4-nitrophenol degradation was confirmed by spectroscopic analysis (Figure 9). The control set of 4-nitrophenol without IONPs loaded frustules did not show any significant change (Figure 9).
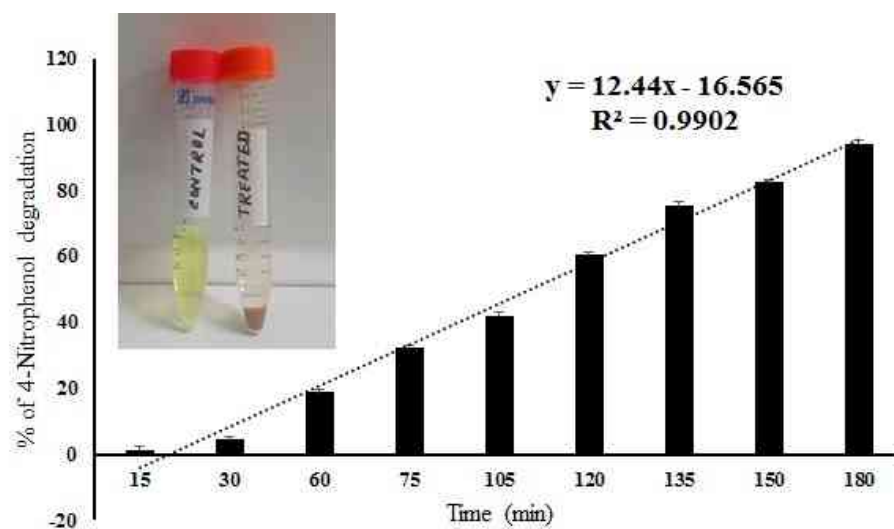
Figure 9. Percentage of 4-nitrophenol degradation by IONPs doped frustules of *P. trainorii* and experimental solution of 4-nitrophenol before and after treatment with IONPs loaded frustules of *P. trainorii*.

2.7. LDI-Mass Spectrometry

The LDI-MS spectra of biogenic IONPs utilized as nanomaterial assisting ionization and desorption is presented in Figure 10. IONPs utilized for LDI-MS analysis showed sensitivity towards low molecular weight analytes such as glucose, alanine and triacylglycerols (Figure 11).
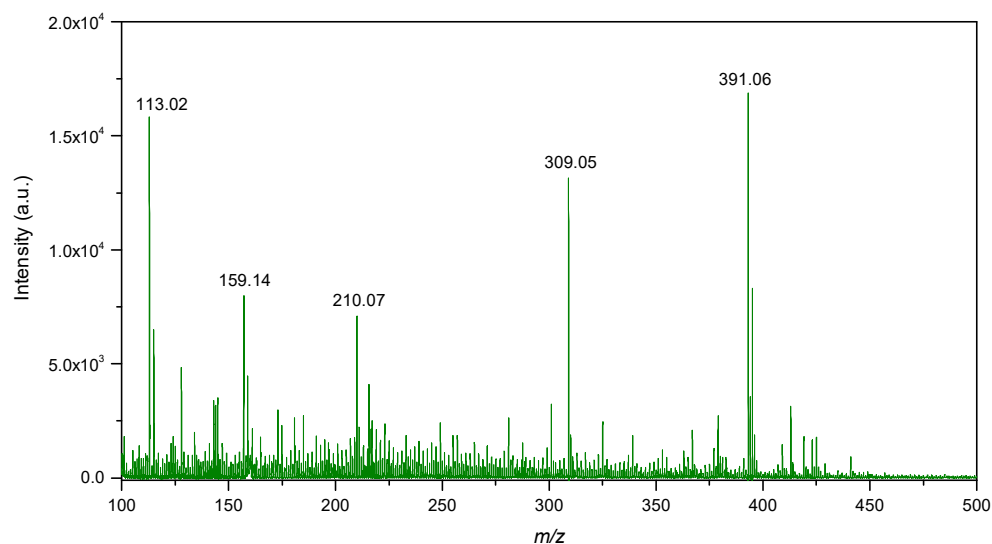
Figure 10. LDI-MS spectra of IONPs in the low mass region.
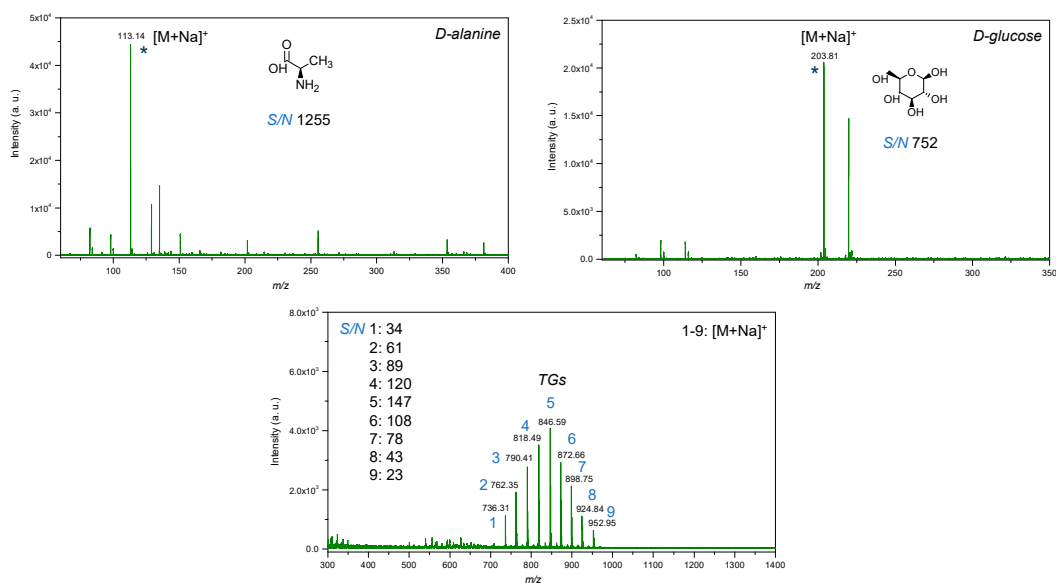
Figure 11. LDI-MS spectra of low molecular weight compounds (glucose, alanine, mixture of triacylglycerols) with utilization of IONPs as an inorganic matrix, where: 1—14:0-13:0-14:0 TG (25 μg/mL); 2—14:0-15:1-14:0 TG (50 μg/mL); 3—14:0-17:1-14:0 TG (75 μg/mL); 4—16:0-15:1-16:0 TG (100 μg/mL); 5—16:0-17:1-16:0 TG (125 μg/mL); 6—16:0-19:2-16:0 TG (100 μg/mL); 7—18:1-17:1-18:1 TG (75 μg/mL); 8—18:1-19:2-18:1 TG (50 μg/mL); 9—18:1-21:2-18:1 TG (25 μg/mL); * is molecular ion.

3. Discussion

It is well known that pure iron or IONP has a distinct color that varies from yellow to dark brown and further to complete black depending upon the size, shape and concentration of the particles [39]. It is reported by many authors that faint yellowish FeCl₃ solution turned dark orange in color during interaction with some reducing agents due to the production of pure iron [39]/IONPs [50]. Likewise, in this study, the occurrence of orange color in the green biomass of *P. trainorii* as well as in the medium initially confirmed the development of iron associated nanostructures at intracellular and extracellular level. However, the color change could not reveal the production of IONPs which was later confirmed by EDAX, XRD and LDI-Mass spectrometry. A preliminary color change was observed after 12 h of exposure; therefore, it can be said that production of IONPs by *P. trainorii* have started after 12 h of reaction and the reduction procedure has been completed after 3 days as no further color change was observed. Extracellular nanoparticle production is more acceptable since the extraction steps, e.g., ultrasonication and vortexing, are not required. On the other hand, cell-associated nanoparticles are needed to extract using some additional nano-capping agents, such as sodium citrate [51], and cetyltrimethyl ammonium bromide (CTAB) [52] to control their stability and to keep away from aggregation. During such extraction, some cellular fragments can be associated with the nanoparticles, whereas extracellular production is comparatively pure. Therefore, it can be inferred that extracellular fabrication of IONPs by *P. trainorii* is a timesaving, biocompatible and cost-effective technique.

Diatoms are natural, attractive bioreagents for continuous production of amorphous nanosilica within silica deposition vesicle [53]. These silica nanoparticles are responsible for the generation of a mesoporous, siliceous outer covering, known as frustules. Frustules are promising resources for nanobiotechnology because of their easy availability, biocompatibility, porous structure and high surface area. The frustule's morphology is species-specific and the initial key for species identification. Not only in taxonomic identification, diatomaceous biosilica has also been exploited as a catalyst [54], in optical devices and biosensors [55] and as a drug delivery vehicle [56] because of its unique optoelectrical property. The pure form of these amorphous nanostructures can easily be fabricated in

laboratory conditions by culturing diatoms. In this study, *P. trainorii* has been cultured in laboratory conditions without any contamination and further used as reducing agents for production of iron doped siliceous frustules. Chemically synthesized iron doped silica nanoparticles have already been reported as catalyst [57] and potential agents for magnetic resonance imaging [58]. Moreover, frustules are widely used in material engineering for fabrication of three-dimensional metal doped nanosilica because silica provides extra stability to metal nanoparticles as well as intrinsic luminescent property. However, physical and chemical process to fabricate silica conjugated metal particles involve high temperature/pressure and hazardous chemicals, respectively. In this study, the development of silica doped IONPs production was possible at room temperature without involving any toxic chemicals, which was confirmed by SEM study. Additionally, the IONP doped frustules also showed 4-nitrophenol degradation efficiency. The decolorization of 4-nitrophenol possibly happened due to its reduction into aminophenol as mentioned by Tang et al. (2015) [57] while utilizing zero-valent iron particles immobilized on mesoporous silica in reductive degradation of aqueous p-nitrophenol.

In UV-Vis spectroscopy of extracted IONPs from NP loaded frustules, the appearance of two peaks at ~270 and ~350 nm confirmed the presence of both silica and IONPs in the suspension; it is well known that pure silica shows a distinct peak in spectroscopy at 230–290 nm [51]. Extracellular IONPs showed only single peak at 350 nm, confirming no contamination of nanosilica. Chemically synthesized IONPs by the co-precipitation method also showed maximum absorbance at 340 nm in UV-Vis spectroscopy [59]. Biogenically synthesized iron particles by *Ageratum conyzoides* [60] and *Terminalia chebula* [61] leaf showed surface plasmon resonance at 390 nm and 327 nm, respectively. The composite IONPs ($Fe_3O_4 / \alpha\text{-}Fe_2O_3$) fabricated by pulp of *Syzygium cumini* exhibited maximum absorbance at 350 nm [62]. Therefore, it can be concluded intra- and extracellular production of IONPs by *P. trainorii*. FTIR measurement was performed for identification of the potential surface molecular constituents responsible for reduction of Fe^{3+}. In IR spectrum of extracellular IONPs and IONPs doped frustules, the appeared peak at 556 cm^{-1} confirmed the presence of Fe-O group as the same was observed by Yew et al. 2016 [24] while synthesizing IONPs using seaweeds *Kappaphycus alvarezii*. The characteristic IR peaks for silica were observed in both control and particles loaded frustules at 434, 954, 1058, 1144 cm^{-1} corresponds to bending vibration and asymmetrical stretching of Si-O-Si [63]. The peaks at 1380, 1531, 1633 cm^{-1} have been observed for strong bending vibrations of N–H functional groups [64]. The peak at 1741 cm^{-1} indicated C=O stretching [64–66]. The signals at 2855, 2924, 2979 cm^{-1} were referred as C–H stretching [64,67]. The signal at 3664 cm^{-1} was for O–H stretching [64]. Therefore, it can be said that the identified functional groups, N–H, C=O, C–H provided efficient stabilization of fabricated IONPs.

The stability of IONPs was also confirmed by high positive (+24.6 mV) zeta potential value. High positive or negative surface charge (±20 mV) reveals particles stability as the particles with high zeta potential value repel each other, prevent aggregation and precipitation. The recorded XRD spectra for IONPs is very similar with the XRD data obtained by other authors while producing amorphous IONPs chemically [68] or biogenically [40]. So, it can be said that synthesized particles are amorphous in nature.

The TEM study revealed the advantage of using *P. trainorii* as a reducing agent in the production of IONPs. This bioreagent produced only spindle-shaped IONPs against the 10 mM $FeCl_3$ (pH 2). It is difficult in biogenesis to produce similar shapes, because all the reducing agents, e.g., pigments, proteins, polysaccharides, etc., work together against metal stress. Therefore, it is common to synthesize particles with variable shapes and sizes. However, in this method, it was possible to synthesize only spindle-shaped particles without any trace of other shapes. EDAX study of extracellular particles confirmed the production of IONPs as two strong signals from Fe and O have been detected. On the other hand, sonicated out particles from frustules (loaded with particles) showed an additional signal of silica in EDAX. Therefore, it can be said that extracellular particles have been characterized by higher purity and lack of silica contamination.

LDI-MS spectra showed intense signals in the low mass region at m/z 113.02, 159.14, 210.07, 309.05 and 391.06 (Figure 10). The signal at m/z 113.02 probably corresponds to FeO as adduct with 1 molecule of water and sodium $[M+H_2O+Na]^+$. The signal at m/z 391.06 probably corresponds to Fe_4O_5 as adduct with 1 molecule of water and 3 atoms of sodium $[M+H_2O+3Na]^+$. On the other hand, isotopic distribution of the signals was not observed to be similar as for iron oxide compounds. Therefore, mentioned signals could also correspond to organic compounds originating from the synthesis of IONPs.

LDI-MS spectra of standards of low molecular weight compounds with utilization of IONPs as matrix showed intense signals in low mass region. All standards such as glucose, amino acid and triacylglycerols were detected as adducts with sodium $[M+Na]^+$ (Figure 11). It was expected since trace amounts of sodium may be present in water used for the synthesis and in addition, as compared to silver and gold nanostructures, iron oxides do not tend to form adducts with analytes. Notably, the LDI-MS spectra of glucose demonstrated less rich chemical background in low mass region as compared to alanine, that probably can be explained by differences in distribution of standard compounds on the surface of IONPs. Since IONPs were deposited by pipetting onto the plate, which was followed by drying on air, the coffee ring effect [69] could affect the distribution of analytes on the surface of IONPs and should be further studied for their further applications in LDI-MS. The deposition method of the nanomaterial onto NALDI plate affects its distribution and therefore, LDI spectra, further studies are necessary for evaluation of applicability of IONPs for preparation of NALDI plates with utilization of presented approach. For example, techniques such as magnetron sputtering and vapor deposition allow for a higher degree of control rather than wet and dry chemical methods. Pre-mixing prior to deposition provided insignificant difference in intensity for alanine, and in contrast, intensity for glucose was observed to be three times higher as compared to dried droplet method. This probably can be caused by differences in chemical structure of compounds and thus, interactions between analytes and IONPs.

In addition, it is important to note that chemical background of IONPs did not interfere with molecular ions of low molecular weight compounds that were detected at nanomolar level (per spot).

Triacylglycerols were detected at picomolar detection level (per spot), which shows high sensitivity of LDI-MS technique with utilization of IONPs as inorganic matrix. As compared to the previous work with utilization of silver nanostructures [70], it was not necessary to adjust parameters of global attenuator and laser parameter set as well as the value of detector gain to obtain intense molecular ions for triacylglycerols. Furthermore, TG 9 at m/z 952.95 was not detected in case of utilization of silver nanostructures as matrix. Such a difference can probably be explained by differences in catalytic properties since silver is possessed as highly active catalyst as compared to iron, which may lead to enhanced fragmentation of lipids and absence of the molecular ion, thus complicating identification. Furthermore, pre-mixing of IONPs and TGs prior to deposition onto the LDI plate provided less intense molecular ions as compared to dried droplet technique.

Values of signal-to-noise ratio were high for all standard compounds, which shows that the limit of detection of the technique with utilization of IONPs as nanostructures assisting ionization and desorption processes is potentially significantly lower than utilized concentrations (Figure 11).

Diatoms are excellent bioreagents for biosynthesis of various nanoparticles because of their high growth rate and high metal uptake capacity. These microscopic, silica nanofactories have already been exploited for biogenic production of various nanoparticles, namely gold [71], silver [51]. Since the production of nanoparticles is common in the metal stress response of diatoms against particular reducing environment. Here, *P. trainorii* showed pigment loss against Fe^{3+} stress as well as spindle-shaped IONPs production. The gradual disappearance of red fluorescence in Fe^{3+} treated *P. trainorii* confirmed loss of chlorophyll. The loss of chlorophyll and carotenoids in Fe^{3+} treated *P. trainorii* was also recorded by observing no peak at 663 and 450 nm in UV-Vis spectroscopy, respectively. The appearance

of only green fluorescence after 3 days of reaction confirmed cell death as silica shows intrinsic green luminescent property under blue light region. A fragment of IONPs associated frustules would be beneficial for optical imaging guided cancer therapy.

4. Materials and Methods

4.1. Chemicals

Thiamine hydrochloride (99%, MW 337.27), biotin (>99%, MW 244.31), vitamin B12 (>98%, MW 1355.37), and α-Cyano-4-hydroxycinnamic acid (>99%, MW 189.17), 4-Nitrophenol (>99%, MW 139.11) were supplied by Sigma-Aldrich (St. Louis, MO, USA). Hydrogen peroxide (30%, MW 34.01), sodium nitrate (>99%, MW 84.99), sodium dihydrogen phosphate monohydrate (>99%, MW 137.99), sodium molybdate dihydrate (>99%, MW 241.95), manganese (II) chloride tetrahydrate (>99%, MW 197.91), and cobalt (II) chloride hexahydrate (>99%, DW 237.93) were obtained from Chempur® (Piekary Śląskie, Poland). Zinc sulfate heptahydrate (>99%, MW 287.54), iron (III) chloride hexahydrate (>99%, MW 270.32), EDTA disodium dihydrate (>99%, MW 372.24), and copper (II) sulfate pentahydrate (>99%, MW 249.68) were purchased from Scharlab (Barcelona, Spain). Sodium metasilicate nonahydrate (44–47.5% total solids, MW 284.19) were supplied by Acros Organics, ThermoFisher Scientific (Waltham, MA, USA). Deionized water was obtained by using a Milli-Q® purification system (Millipore Co., Bedford, MA, USA). Standards of D-glucose (>99%), D-alanine (>99%) and cesium triiodide (>99%) were purchased from Sigma-Aldrich (Steinheim, Germany). Standard mixture of triacylglycerols (TG internal standard, Ultimate SPLASH™) was purchased from Avanti Polar Lipids (Alabaster, AL, USA).

4.2. Diatom Mediated Biosynthesis of IONPs

4.2.1. Cultivation of Diatom

The pure culture of the selected diatom strain, *P. trainorii* BA170 (collected from Gulf of Gdańsk, Baltic Sea, Poland) was procured from Diatom Culture Collection, University of Szczecin, Poland. The culture was maintained using standard 7 ppt Guillard's artificial seawater f/2 medium [72] (1 L of medium contains 880 μM $NaNO_3$, 36 μM NaH_2PO_4 H_2O, 106 μM Na_2SiO_3 $9H_2O$, trace metal: 0.08 μM $ZnSO_4$ $7H_2O$, 0.9 μM $MnSO_4$ H_2O, 0.03 μM Na_2MoO_4 $2H_2O$, 0.05 μM $CoCl_2$ $6H_2O$, 0.04 μM $CuCl_2$ $2H_2O$, 11.7 μM $FeCl_3$ $6H_2O$, 11.7 μM Na_2EDTA $2H_2O$, vitamin B12, biotin and thiamine) at 20 °C under a 12:12 day:night cycle, illuminated with 100 μmol photons m^{-2} s^{-1} of white light. The strain was cultivated for 14 days to obtain healthy growing biomass from exponential growth phase.

4.2.2. Biofabrication of Spindle-Shaped IONPs

The whole biomass of diatom strain *P. trainorii* was used as reducing agent for the production of biogenic spindle-shaped IONPs. The healthy cells of *P. trainorii* were centrifuged at 6000 rpm for 10 min, after that washed with double distilled water (ddH_2O) for three times to remove excess salts from medium and recollected followed by an additional step of centrifugation at 6000 rpm for 10 min. The thoroughly washed biomass (300 mg FW) was exposed to 400 mL, 0.01 M Fe^{3+} solution with pH 2. The whole experiment was maintained in dark at room temperature for 3 days.

4.2.3. Purification of Diatom Based Biosynthesized IONPs

After 3 days of reaction, the resultant golden yellow colored biomass was collected by centrifugation at 8000 rpm for 20 min. The harvested biomass was rinsed 3–4 times using ddH_2O and stored at 4 °C for further characterizations. The orange colored external nanosuspension was also collected separately. The produced IONPs at extracellular level were purified by ultrafiltration using Amicon® Ultra Ultracel-30 regenerated cellulose membrane centrifugal filters with NMWL 30 kDa. The ultrafiltration was performed by centrifugation of 15 mL of external nanosuspension at 10,000 rpm for 15 min followed by a thorough wash (3 times) of accumulated particles using deionized water. After washing, the particles were dispersed within water by sonication in ultrasonic water bath for 20 min

followed by a 2 min of vortexing at 2000 rpm using Vortex-Genie® 2 (Scientific Industries, Inc., New York, NY, USA) The consecutive steps of sonication and vortexing were repeated three times. After that, the pH of water dispersed nanoparticles was measured by FiveEasy Plus pH meter (Mettler Toledo, Columbus, OH, USA). The cleaned, well dispersed IONPs were stored at 4 °C for further experiments.

4.3. Microscopic Analysis of Fe^{3+} Treated P. trainorii with EDAX and Elemental Mapping

Associated morphological differences in *P. trainorii* before and after 3 days of reaction with Fe^{3+} solution were documented by producing light microscopic images with ZEISS Axioscope A1 (Jena, Germany) at $400\times$ magnification. The changes of fluorescent properties in NPs loaded cells were observed by an Axioscope A1 Zeiss fluorescence micro-scope (excitation: 450–490 nm and emission: 515 nm). To record surface topography of control and Fe^{3+} treated *P. trainorii*, the SEM images were captured using a Hitachi SU8020 (Hitachi, Tokyo, Japan). For SEM study, the 40 μL of samples were dried overnight on Nuclepore™ 5.0 μm Track-Etch Membrane (Whatman™, Cytiva, Freiburg im Breisgau, Germany) at room temperature. The properly dried samples were mounted on M4 cylinder SEM sample aluminum stub (Hitachi, Tokyo, Japan) using conductive carbon adhesive black tape and coated with a 10 nm thick gold layer. Deposition of IONPs on the surface of frustules was confirmed by EDAX and elemental mapping. The measurement was performed with an accelerating energy 30.0 kV using NSS Thermo Scientific.

4.4. Characterizations of Frustule Associated and External Biogenic IONPs

4.4.1. UV-Vis Spectroscopy and Fourier Transform Infrared Spectroscopy

Control biomass, cleaned frustules (boiled with 30% H_2O_2 for 24 h and washed thrice with ddH_2O) and IONPs loaded frustules of *P. trainorii* were sonicated with water using Hielscher UP100H ultrasonic processor (Teltow, Germany) for 20 min at 60% amplitude. After sonication, the experimental suspensions were centrifuged at 3000 rpm for 5 min and the supernatants were subjected to UV–Vis spectrophotometer DR 6000 (HACH–Lange) for optical measurements in the wavelength range of 200–900 nm. The UV-Vis spectra of orange-colored external counterpart was recorded before and after ultrafiltration in the 200–900 nm wavelength range by Nano Drop 2000c UV–Vis spectrophotometer (Thermo Fisher Scientific, Waltham, MA, USA).

FTIR measurements of control and IONPs loaded frustules of *P. trainorii* as well as extracellular IONPs (purified form) were carried out using ATR-FTIR (Bruker, Billerica, MA, USA). For FTIR measurement all samples were dried overnight at 50 °C and properly dried samples were subjected for IR measurements with wavenumber range of 4000–400 cm^{-1}.

4.4.2. Inductively Coupled Plasma Mass Spectrometry, Zeta Potential and X-ray Diffraction

After purification, the final concentration of external nanosuspension was quantified by inductively coupled plasma mass (ICP-MS) spectrometry (Agilent, Santa Clara, CA, USA). The zeta potential value of the synthesized spindle-shaped IONPs was measured by Malvern Zetasizer NanoZS (Malvern, UK) using Zeta cuvette DTS1070 (Malvern, UK). The analysis was carried out in the automatic selection mode of voltage and number of runs. Zeta potential measurements were performed in triplicate. The X-ray diffraction (XRD) spectra were recorded with an X'Pert Pro Analytical X-ray diffractometer (Philips, Würzburg, Germany) with Cu-Kα radiation (λ = 0.1541 nm, 40 kV, 30 mA); 1mL of dried sample on glass slide was scanned in the 2θ range between 5° and 100° with step sizes of 0.0167.

4.4.3. TEM and EDAX

The frustule associated particles, extracted by sonication (20 min at 60% amplitude) following centrifugation at 3000 rpm for 5 min and ultrafiltered extracellular IONPs were dried on a carbon-coated copper grid (Sigma-Aldrich, St. Louis, MO, USA), and the size-shape analysis was carried out by a Hitachi STEM S5500 (Hitachi, Tokyo, Japan). The EDAX

study was performed using the same grids and the same microscope (Hitachi STEM S5500 attached with EDAX) to understand the elemental composition and purity of the particles.

4.5. Photocatalytic Degradation of 4-Nitrophenol by IONPs Decorated Frustules

The degradation of 4-nitrophenol by IONPs loaded frustules were investigated by spectroscopy. To determine 4-nitrophenol degradation kinetics, 5 mg of IONPs doped frustules were suspended into 10 mL of 20 ppm 4-nitrophenol (pH 7.0) aqueous solution and the resultant suspension was stirred for 3 h under light at room temperature. The decolorization of 4-nitrophenol was measured by spectrophotometer at 400 nm at different reaction time points, namely 15, 30, 60, 75, 105, 120, 135, 150, 180 min. Before every measurement, the reaction mixture was centrifuged at 4000 rpm for 3 min to avoid the interference of IONPs loaded frustules. The experiment was performed in triplicates. A control set of 4-nitrophenol without IONPs loaded frustules was also maintained in the same reaction conditions.

The amount of nitrophenol degradation was calculated by this equation

$$\% \text{ of 4-nitrophenol degradation} = 100 \times (C0 - C)/C0$$

where C0 is the initial and C is the concentration of nitrophenol after specific time of reaction [Concentration of 4-nitrophenol have been determined by calibration curve].

4.6. LDI-MS Analysis

Laser desorption ionization (LDI) analysis was performed using ultraFlextreme MALDI-TOF-MS apparatus (Bruker Daltonics, Bremen, Germany) equipped with a modified neodymium- doped yttrium aluminium garnet (Nd:YAG) laser operating at 355 nm and frequency 2 kHz. The plate (stainless steel, H17) was cut to pieces 2.5×7.5 cm, pre-cleaned using acetone, methanol and acetonitrile (10 min in ultrasonic bath) and inserted to MTP Slide-Adapter II (Bruker Daltonics, Bremen, Germany).

The LDI-MS spectra for characterization of IONPs were recorded in a reflectron positive mode in the range of m/z 60 to 3500 with the acceleration voltage of 5.5 kV, laser power 50%, global attenuator offset 30%. All spectra from a single spot were acquired by 5 laser shots with 500 laser frequency with 1.956 kV of reflector voltage. HCCA was used for external mass calibration. Blank area of metal plate was used as a negative control. All data were processed using using Flex Control (version 3.4, build 135) and Flex Analysis (version 3.4, build 50) software (Bruker Daltonics, Bremen, Germany). For characterization of IONPs, 1 μL of ultrafiltered extracellular IONPs was spotted to the plate.

The LDI-MS spectra for evaluation of LDI-MS efficiency of IONPs as nanomaterial assisting ionization/desorption were recorded in a reflectron positive mode in the range of m/z 60 to 1400, laser power 80%, global attenuator offset 30%, reflector voltage values as 26.63 and 13.59 kV, reflector voltage 1.940 kV with detector gain $2.51\times$. LDI-MS efficiency of IONPs was evaluated using standard solutions of glucose, alanine at concentration 1 mg/mL and mixture of triacylglycerols (50–125 μg/mL). Standard solutions of analytes were spotted using two approaches: (i) dried droplet, (ii) equal volumes (2.5 μL) of IONPs and analytes were pre-mixed and 1 μL of the mixture was spotted. External mass calibration was carried out using CsI_3 solution and the procedure was as follows: equal volumes (2.5 μL) of 10 mg/mL of CsI_3 in methanol and 20 mg/mL of DHB in methanol were premixed and 0.5 μL of the mixture was spotted. All spectra were collected using 2000 shots (500 shots $\times$ 4). Quadratic calibration model was used for external mass calibration.

5. Conclusions

In this study, a rapid, simple, eco-friendly technique has been proposed to synthesize IONPs in a cost-effective way. The selected strain, *P. trainorii* has been characterized as an efficient bioreagent for production of intra and extracellular IONPs within 3 days of reaction with 10 mM Fe^{3+} solution at room temperature. Luminescent property of the frustules/IONPs loaded frustules of *P. trainorii* can be exploited for various medical appli-

cations. IONPs loaded frustules showed efficiency in 94% of 4-nitrophenol degradation within 180 min of reaction. This catalytic activity of IONPs doped frustules can be used for nitrophenol removal from polluted water in future. The fabricated particles are all spindle-shaped and monodisperse in nature with well-marked hydrosphere surrounding the surface. The resultant structures can be utilized in various fields such as hyperthermia cancer therapy, bio-sensing SERS detection and electronic device designing, as well as in catalysis. The synthesized IONPs showed high positive zeta potential value and conferred high stability without any additional stabilizing agent. Bio-fabricated IONPs utilized as nanomaterial assisting ionization and desorption in LDI-MS showed intense signals for low molecular weight analytes at nano- and picomolar level (per spot). Therefore, the obtained results showed potential for the application of IONPs for the preparation of NALDI plates.

References

1. Estelrich, J.; Busquets, M.A. Iron oxide nanoparticles in photothermal therapy. *Molecules* **2018**, *23*, 1567. [CrossRef] [PubMed]
2. Vangijzegem, T.; Stanicki, D.; Laurent, S. Magnetic iron oxide nanoparticles for drug delivery: Applications and characteristics. Expert. *Opin. Drug Deliv.* **2019**, *16*, 69–78. [CrossRef]
3. Theofanidis, S.A.; Galvita, V.V.; Konstantopoulos, C.; Poelman, H.; Marin, G.B. Fe-Based Nano-Materials in Catalysis. *Materials.* **2018**, *11*, 831. [CrossRef]
4. Vaseem, M.; Ghaffar, F.A.; Farooqui, M.F.; Shamim, A. Iron Oxide Nanoparticle-Based Magnetic Ink Development for Fully Printed Tunable Radio-Frequency Devices. *Adv. Mater. Technol.* **2018**, *3*, 1700242. [CrossRef]
5. Arakha, M.; Pal, S.; Samantarrai, D.; Panigrahi, T.K.; Mallick, B.C.; Pramanik, K.; Mallick, B.; Jha, S. Antimicrobial activity of iron oxide nanoparticle upon modulation of nanoparticle-bacteria interface. *Sci. Rep.* **2015**, *5*, 14813. [CrossRef] [PubMed]
6. Kläser, K.; Graeser, M.; Steinhagen, D.; Luedtke-Buzug, K. Construction of a device for magnetic separation of superparamagnetic iron oxide nanoparticles. *Curr. Dir. Biomed. Eng.* **2015**, *1*, 306–309. [CrossRef]
7. Rahman, S.S.U.; Qureshi, M.T.; Sultana, K.; Rehman, W.; Khan, M.Y.; Asif, M.H.; Farooq, M.; Sultana, N. Single step growth of iron oxide nanoparticles and their use as glucose biosensor. *Results Phys.* **2017**, *7*, 4451–4456. [CrossRef]
8. Wei, W.; Xu, C.; Wu, H. Magnetic iron oxide nanoparticles mediated gene therapy for breast cancer–an in vitro study. *J. Huazhong Univ. Sci. Technol. Med. Sci.* **2006**, *26*, 728–730. [CrossRef]
9. Yan, W.; Lien, H.L.; Koel, B.E.; Zhang, W.X. Iron nanoparticles for environmental clean-up: Recent developments and future outlook. *Environ. Sci. Process. Impacts* **2013**, *15*, 63–77. [CrossRef]
10. Wabler, M.; Zhu, W.; Hedayati, M.; Attaluri, A.; Zhou, H.; Mihalic, J.; Geyh, A.; DeWeese, T.L.; Ivkov, R.; Artemov, D. Magnetic resonance imaging contrast of iron oxide nanoparticles developed for hyperthermia is dominated by iron content. *Int. J. Hyperth.* **2014**, *30*, 192–200. [CrossRef]
11. Hufschmid, R.; Teeman, E.; Mehdi, B.L.; Krishnan, K.M.; Browning, N.D. Observing the colloidal stability of iron oxide nanoparticles in situ. *Nanoscale* **2019**, *11*, 13098–13107. [CrossRef] [PubMed]
12. Yusoff, A.H.M.; Salimi, M.N.; Jamlos, M.F. A review: Synthetic strategy control of magnetite nanoparticles production. *Adv. Nano Res.* **2018**, *6*, 1–19.
13. Shasha, C.; Krishnan, K.M. Nonequilibrium dynamics of magnetic nanoparticles with applications in biomedicine. *Adv. Mater.* **2021**, *33*, 1904131. [CrossRef] [PubMed]

14. Farahmandjou, M.; Soflaee, F. Synthesis of Iron Oxide Nanoparticles using Borohydride Reduction. *Int. J. Bio Inorg. Hybrid Nanomater.* **2014**, *3*, 203–206.

15. Pravallika, P.L.; Mohan, G.K.; Rao, K.V.; Shanker, K. Biosynthesis, characterization and acute oral toxicity studies of synthesized iron oxide nanoparticles using ethanolic extract of *Centella asiatica* plant. *Mater. Lett.* **2019**, *236*, 256–259. [CrossRef]

16. Beheshtkhoo, N.; Kouhbanani, M.A.J.; Savardashtaki, A.; Amani, A.M.; Taghizadeh, S. Green synthesis of iron oxide nanoparticles by aqueous leaf extract of Daphne mezereum as a novel dye removing material. *Appl. Phys. A* **2018**, *124*, 1–7. [CrossRef]

17. Abdeen, M.; Sabry, S.; Ghozlan, H.; El-Gendy, A.A.; Carpenter, E.E. Microbial-physical Synthesis of Fe and Fe₃O₄ Magnetic Nanoparticles Using Aspergillus niger YESM1 and Supercritical Condition of Ethanol. *J. Nanomater.* **2016**, *2016*, 1–7. [CrossRef]

18. Chatterjee, S.; Mahanty, S.; Das, P.; Chaudhuri, P.; Das, S. Biofabrication of Iron Oxide Nanoparticles Using Manglicolous Fungus Aspergillus niger BSC-1 and Removal of Cr (VI) from Aqueous Solution. *Chem. Eng. J.* **2020**, *385*, 123790. [CrossRef]

19. Sundaram, P.A.; Augustine, R.; Kannan, M. Extracellular Biosynthesis of Iron Oxide Nanoparticles by Bacillus Subtilis Strains Isolated from Rhizosphere Soil. *Biotechnol. Bioprocess Eng.* **2012**, *17*, 835–840. [CrossRef]

20. Jubran, A.S.; Al-Zamely, O.M.; Al-Ammar, M.H. A Study of Iron Oxide Nanoparticles Synthesis by Using Bacteria. *Int. J. Pharm. Qual. Assur.* **2020**, *11*, 01–08. [CrossRef]

21. Mashjoor, S.; Yousefzadi, M.; Zolgharnain, H.; Kamrani, E.; Alishahi, M. Organic and inorganic nano-Fe₃O₄: Alga Ulva flexuosa-based synthesis, antimicrobial effects and acute toxicity to briny water rotifer *Brachionus rotundiformis*. *Environ. Pollut.* **2018**, *237*, 50–64. [CrossRef] [PubMed]

22. El-Kassas, H.Y.; Aly-Eldeen, M.A.; Gharib, S.M. Green synthesis of iron oxide (Fe₃O₄) nanoparticles using two selected brown seaweeds: Characterization and application for lead bioremediation. *Acta Oceanol. Sin.* **2016**, *35*, 89–98. [CrossRef]

23. Subhashini, G.; Ruban, P.; Daniel, T. Biosynthesis and characterization of magnetic (Fe₃O₄) iron oxide nanoparticles from a red seaweed gracilaria edulis and its antimicrobial activity. *Int. J. Adv.* **2018**, *3*, 184–189.

24. Yew, Y.P.; Shameli, K.; Miyake, M.; Kuwano, N.; Bt Ahmad Khairudin, N.B.; Bt Mohamad, S.E.; Lee, K.X. Green synthesis of magnetite (Fe₃O₄) nanoparticles using seaweed (*Kappaphycus alvarezii*) extract. *Nanoscale Res. Lett.* **2016**, *11*, 1–7. [CrossRef]

25. Khaleelullah, M.M.S.I.; Murugan, M.; Radha, K.V.; Thiyagarajan, D.; Shimura, Y.; Hayakawa, Y. Synthesis of super-paramagnetic iron oxide nanoparticles assisted by brown seaweed *Turbinaria decurrens* for removal of reactive navy-blue dye. *Mater. Res. Express* **2017**, *4*, 105038. [CrossRef]

26. Brzozowska, W.; Sprynskyy, M.; Wojtczak, I.; Dąbek, P.; Witkowski, A.; Buszewski, B. "Outsourcing" diatoms in fabrication of metal-doped 3D biosilica. *Materials* **2020**, *13*, 2576. [CrossRef]

27. Roychoudhury, P.; Nandi, C.; Pal, R. Diatom-based biosynthesis of gold-silica nanocomposite and their DNA binding affinity. *J. Appl. Phycol.* **2016**, *28*, 2857–2863. [CrossRef]

28. Bose, R.; Roychoudhury, P.; Pal, R. In-situ green synthesis of fluorescent silica–silver conjugate nanodendrites using nanoporous frustules of diatoms: An unprecedented approach. *Bioprocess Biosyst. Eng.* **2021**, *44*, 1263–1273. [CrossRef]

29. Jantschke, A.; Herrmann, A.K.; Lesnyak, V.; Eychmüller, A.; Brunner, E. Decoration of diatom biosilica with noble metal and semiconductor nanoparticles (<10 nm): Assembly, characterization, and applications. *Asian J. Chem.* **2021**, *7*, 85–90. [CrossRef]

30. Lang, Y.; Monte, F.D.; Rodriguez, B.J.; Dockery, P.; Finn, D.P.; Pandit, A. Integration of TiO2 into the diatom *Thalassiosira weissflogii* during frustule synthesis. *Sci. Rep.* **2013**, *3*, 3205. [CrossRef]

31. Jeffryes, C.; Gutu, T.; Jiao, J.; Rorrer, G.L. Two-stage photobioreactor process for the metabolic insertion of nanostructured germanium into the silica microstructure of the diatom *Pinnularia* sp. *Mater. Sci. Eng.* **2008**, *28*, 107–118. [CrossRef]

32. Sprynskyy, M.; Szczyglewska, P.; Wojtczak, I.; Nowak, I.; Witkowski, A.; Buszewski, B.; Feliczak-Guzik, A. Diatom biosilica doped with palladium (II) chloride nanoparticles as new efficient photocatalysts for methyl orange degradation. *Int. J. Mol. Sci.* **2021**, *22*, 6734. [CrossRef] [PubMed]

33. Rawat, S.; Singh, J.; Koduru, J.R. Effect of ultrasonic waves on degradation of phenol and para-nitrophenol by iron nanoparticles synthesized from Jatropha leaf extract. *Environ. Technol. Innov.* **2021**, *24*, 101857. [CrossRef]

34. Raiza, A.J.; Pandian, K.; Gopinath, S.C.B. Biosynthesis of zerovalent iron nanoparticles for catalytic reduction of 4-Nitrophenol and decoloration of textile dyes. *Biotechnol. Appl. Biochem.* **2022**, in press. [CrossRef] [PubMed]

35. Li, F.; Zhu, K.; Liu, B.; Wang, N.; Liu, H.; Chen, R. Comprehensive Effect of P-Nitrophenol Degradation in the Iron Oxide/Oxalate Suspension. *Water. Air Soil Pollut.* **2018**, *229*, 91. [CrossRef]

36. Mahy, J.G.; Tasseroul, L.; Herlitschke, M.; Hermann, R.P.; Lambert, S.D. Fe³⁺/iron oxide/SiO2 xerogel catalysts for p-nitrophenol degradation by photo-Fenton effects: Influence of thermal treatment on catalysts texture. *Mater. Today Proc.* **2016**, *3*, 464–469. [CrossRef]

37. Mona, L.P.; Songca, S.P.; Ajibade, P.A. Synthesis and encapsulation of iron oxide nanorods for application in magnetic hyperthermia and photothermal therapy. *Nanotechnol. Rev.* **2022**, *11*, 176–190. [CrossRef]

38. Brayner, R.; Yéprémian, C.; Djediat, C.; Coradin, T.; Herbst, F.; Livage, J.; Fernand, F.; Couté, A. Photosynthetic microorganism-mediated synthesis of akaganeite (β-FeOOH) nanorods. *Langmuir* **2009**, *25*, 10062–10067. [CrossRef]

39. Banerjee, S.; Bhattacharya, A.; Roychoudhury, P.; Dasgupta, A.K.; Dutta, M.; Pal, R. Arthrospira platensis (Cyanobacteria)–a potential biofactory for fluoromagnetic nanoiron production. *Phycologia* **2021**, *60*, 62–72. [CrossRef]

40. Banerjee, S.; Banerjee, I.; Dutta, M.; Pal, R. Fabrication of iron nanoparticles using *Leptolyngbya* valderiana and investigation of its Cr (VI) removal potential in the free and biomass associated forms. *Algal Res.* **2021**, *58*, 102373. [CrossRef]

41. Pomastowski, P.; Buszewski, B. Complementarity of matrix-and nanostructure-assisted laser desorption/ionization approaches. *Nanomater* **2019**, *9*, 260. [CrossRef] [PubMed]
42. Su, C.L.; Tseng, W.L. Gold nanoparticles as assisted matrix for determining neutral small carbohydrates through laser desorption/ionization time-of-flight mass spectrometry. *Anal. Chem.* **2007**, *79*, 1626–1633. [CrossRef]
43. Gamez, R.C.; Castellani, E.T.; Russell, D.H. Sol-Gel-derived silver-nanoparticle-embedded thin film for mass spectrometry-based biosensing. *Langmuir* **2013**, *29*, 6502–6507. [CrossRef] [PubMed]
44. Watanabe, T.; Kawasaki, H.; Yonezawa, T.; Arakawa, R. Surface-assisted laser desorption/ionization mass spectrometry (SALDI-MS) of low molecular weight organic compounds and synthetic polymers using zinc oxide (ZnO) nanoparticles. *J. Mass Spectrom.* **2008**, *43*, 1063–1071. [CrossRef] [PubMed]
45. Kawasaki, H.; Ozawa, T.; Hisatomi, H.; Arakawa, R. Platinum vapor deposition surface-assisted laser desorption/ionization for imaging mass spectrometry of small molecules. *Rapid Commun. Mass Spectrom.* **2012**, *26*, 1849–1858. [CrossRef]
46. Antone, A.J.; Liang, Q.; Sherwood, J.A.; Weiss, J.C.; Wilson, J.M.; Deb, S.; Cassady, C.J.; Bao, Y. Surface Effects of Iron Oxide Nanoparticles on the MALDI In-Source Decay Analysis of Glycans and Peptides. *ACS Appl. Nano Mater.* **2019**, *2*, 3999–4008. [CrossRef]
47. Liang, Q.; Sherwood, J.; Macher, T.; Wilson, J.M.; Bao, Y.; Cassady, C.J. Citric acid capped iron oxide nanoparticles as an effective MALDI matrix for polymers. *J. Am. Soc. Mass Spectrom.* **2016**, *28*, 409–418. [CrossRef]
48. Tseng, M.C.; Obena, R.; Lu, Y.W.; Lin, P.C.; Lin, P.Y.; Yen, Y.S.; Lin, J.T.; Huang, L.D.; Lu, K.L.; Lai, L.L.; et al. Dihydrobenzoic acid modified nanoparticle as a MALDI-TOF MS matrix for soft ionization and structure determination of small molecules with diverse structures. *J. Am. Soc. Mass Spectrom.* **2010**, *21*, 1930–1939. [CrossRef]
49. Morales, E.A. Morphological studies in selected fragilarioid diatoms (Bacillariophyceae) from Connecticut waters (U.S.A.). *Proc. Acad. Nat. Sci. Phila.* **2001**, *151*, 105–120. [CrossRef]
50. Devi, H.S.; Boda, M.A.; Shah, M.A.; Parveen, S.; Wani, A.H. Green synthesis of iron oxide nanoparticles using Platanus orientalis leaf extract for antifungal activity. *Green Process. Synth.* **2019**, *8*, 38–45. [CrossRef]
51. Roychoudhury, P.; Golubeva, A.; Dąbek, P.; Gloc, M.; Dobrucka, R.; Kurzydłowski, K.; Witkowski, A. Diatom Mediated Production of Fluorescent Flower Shaped Silver-Silica Nanohybrid. *Materials* **2021**, *14*, 7284. [CrossRef] [PubMed]
52. Gan, L.; Lu, Z.; Cao, D.; Chen, Z. Effects of cetyltrimethylammonium bromide on the morphology of green synthesized Fe_3O_4 nanoparticles used to remove phosphate. *Mater. Sci. Eng. C* **2018**, *82*, 41–45. [CrossRef] [PubMed]
53. Martin-Jézéquel, V.; Hildebrand, M.; Brzezinski, M.A. Silicon metabolism in diatoms: Implications for growth. *J. Phycol.* **2000**, *36*, 821–840. [CrossRef]
54. Chen, Y.C.; Lin, D.Y.; Chen, B.H. Metasilicate-based catalyst prepared from natural diatomaceous earth for biodiesel production. *Renew. Energy* **2019**, *138*, 1042–1050. [CrossRef]
55. De Tommasi, E.; De Luca, A.C. Diatom biosilica in plasmonics: Applications in sensing, diagnostics and therapeutics. *Biomed. Opt. Express* **2022**, *13*, 3080–3101. [CrossRef]
56. Ruggiero, I.; Terracciano, M.; Martucci, N.M.; De Stefano, L.; Migliaccio, N.; Tatè, R.; Rendina, I.; Arcari, P.; Lamberti, A.; Rea, I. Diatomite silica nanoparticles for drug delivery. *Nanoscale Res. Lett.* **2014**, *9*, 329. [CrossRef]
57. Tang, L.; Tang, J.; Zeng, G.; Yang, G.; Xie, X.; Zhou, Y.; Pang, Y.; Fang, Y.; Wang, J.; Xiong, W. Rapid reductive degradation of aqueous p-nitrophenol using nanoscale zero-valent iron particles immobilized on mesoporous silica with enhanced antioxidation effect. *Appl. Surf. Sci.* **2015**, *333*, 220–228. [CrossRef]
58. Iqbal, M.Z.; Ma, X.; Chen, T.; Ren, W.; Xiang, L.; Wu, A. Silica-coated super-paramagnetic iron oxide nanoparticles (SPIONPs): A new type contrast agent of T 1 magnetic resonance imaging (MRI). *J. Mater. Chem. B* **2015**, *3*, 5172–5181. [CrossRef]
59. Hashem, F.; Nasr, M.; Ahmed, Y. Preparation and evaluation of iron oxide nanoparticles for treatment of iron deficiency anemia. *Int. J. Pharm. Pharm. Sci.* **2018**, *10*, 142–146. [CrossRef]
60. Madivoli, E.S.; Kareru, P.G.; Maina, E.G.; Nyabola, A.O.; Wanakai, S.I.; Nyang'au, J.O. Biosynthesis of iron nanoparticles using Ageratum conyzoides extracts, their antimicrobial and photocatalytic activity. *SN Appl. Sci.* **2019**, *1*, 500. [CrossRef]
61. Saif, S.; Tahir, A.; Asim, T.; Chen, Y.; Adil, S.F. Polymeric nanocomposites of iron–oxide nanoparticles (IONPs) synthesized using Terminalia chebula leaf extract for enhanced adsorption of arsenic (V) from water. *Colloids Interfaces* **2019**, *3*, 17. [CrossRef]
62. Srivastava, N.; Srivastava, M.; Alhazmi, A.; Mohammad, A.; Khan, S.; Pal, D.B.; Haque, S.; Singh, R.; Mishra, P.K.; Gupta, V.K. Sustainable green approach to synthesize Fe_3O_4/α-Fe_2O_3 nanocomposite using waste pulp of Syzygium cumini and its application in functional stability of microbial cellulases. *Sci. Rep.* **2021**, *11*, 24371. [CrossRef] [PubMed]
63. Anbalagan, G.; Prabakaran, A.R.; Gunasekaran, S. Spectroscopic characterization of Indian standard sand. *J. Appl. Spectrosc.* **2010**, *77*, 86–94. [CrossRef]
64. Rupiasih, N.N.; Suharta, W.G.; Sumadiyasa, M.; Islami, M.N. The Current-Voltage Properties of Ch/AgNP Composite Membranes: A Study on the Effect of AgNP Content. *Mater. Sci. Eng.* **2019**, *515*, 012064. [CrossRef]
65. Kamnev, A.A.; Dyatlova, Y.A.; Kenzhegulov, O.A.; Vladimirova, A.A.; Mamchenkova, P.V.; Tugarova, A.V. Fourier transform infrared (FTIR) spectroscopic analyses of microbiological samples and biogenic selenium nanoparticles of microbial origin: Sample preparation effects. *Molecules* **2021**, *26*, 1146. [CrossRef]
66. El-Sherbiny, I.M.; Salih, E.; Reicha, F.M. Green synthesis of densely dispersed and stable silver nanoparticles using myrrh extract and evaluation of their antibacterial activity. *J. Nanostruct. Chem.* **2013**, *3*, 8. [CrossRef]

67. Prabaharan, D.M.D.M.; Sadaiyandi, K.; Mahendran, M.; Sagadevan, S. Structural, optical, morphological and dielectric properties of cerium oxide nanoparticles. *Mater. Res.* **2016**, *19*, 478–482. [CrossRef]

68. Yadav, V.K.; Ali, D.; Khan, S.H.; Gnanamoorthy, G.; Choudhary, N.; Yadav, K.K.; Thai, V.N.; Hussain, S.A.; Manhrdas, S. Synthesis and characterization of amorphous iron oxide nanoparticles by the sonochemical method and their application for the remediation of heavy metals from wastewater. *Nanomaterials* **2020**, *10*, 1551. [CrossRef]

69. Hu, J.B.; Chen, Y.C.; Urban, P.L. Coffee-ring effects in laser desorption/ionization mass spectrometry. *Anal. Chim. Acta* **2013**, *766*, 77–82. [CrossRef]

70. Sagandykova, G.; Piszczek, P.; Radtke, A.; Mametov, R.; Pryshchepa, O.; Gabryś, D.; Kolankowski, M.; Pomastowski, P. Silver Nanostructured Substrates in LDI-MS of Low Molecular Weight Compounds. *Materials* **2022**, *15*, 4660. [CrossRef]

71. Roychoudhury, P.; Dąbek, P.; Gloc, M.; Golubeva, A.; Dobrucka, R.; Kurzydłowski, K.; Witkowski, A. Reducing Efficiency of Fucoxanthin in Diatom Mediated Biofabrication of Gold Nanoparticles. *Materials* **2021**, *14*, 4094. [CrossRef] [PubMed]

72. Guillard, R.R.; Ryther, J.H. Studies of marine planktonic diatoms.1. Cyclotella nana hustedt, and detonula confervacea (cleve) gran. *Can. J. Microbiol.* **1962**, *8*, 229–239. [CrossRef] [PubMed]

Aleksandra Golubeva

Institute of Marine and Environmental Sciences

University of Szczecin

Mickiewicza 16a, 70-383 Szczecin, Poland

Declaration

I hereby declare that my contribution in the preparation of article: " Study on Biogenic Spindle-Shaped Iron-Oxide Nanoparticles by *Pseudostaurosira trainorii* in Field of Laser Desorption/Ionization Applications" published in International Journal of Molecular Sciences, 23: 11713, of which I am co-author with Roychoudhury P., Dąbek P., Pryshchepa O., Sagandykova, G., Pomastowski P., Gloc M., Dobrucka R., Kurzydłowski, K., Buszewski B., and Witkowski A. equals to 20% (percent). For the purpose of this study, I cultivated *P. trainorii* strain and provided live biomass and clean frustules for the studies, took part in investigation of the morphology, elemental and functional analysis of the IONPs decorated frustules and control frustules and preliminary LDI–MS investigation of IONPs, performed the zeta potential measurements of IONPs, helped to obtain, analyze, and illustrate the data.

Aleksandra Golubeva

Instytut Nauk o Morzu i Środowisku: ul. Adama Mickiewicza 16, 70-383 Szczecin
Sekretariat: tel. 914442461, e-mail sekretariat.nms@usz.edu.pl
Dyrektor Instytutu: tel. 91 4442462, e-mail: dyrektor.nms@usz.edu.pl

Dr Piya Roychoudhury

Institute of Marine and Environmental Sciences

University of Szczecin

Mickiewicza 16a, 70-383 Szczecin, Poland

Declaration

I hereby declare that my contribution in the preparation of article: " Study on Biogenic Spindle-Shaped Iron-Oxide Nanoparticles by *Pseudostaurosira trainorii* in Field of Laser Desorption/Ionization Applications" published in International Journal of Molecular Sciences, 23: 11713, of which I am co-author with Golubeva A., Dąbek P., Pryshchepa O., Sagandykova, G., Pomastowski P., Gloc M., Dobrucka R., Kurzydłowski, K., Buszewski B. and Witkowski A. equals to 25% (percent). For the purpose of the study, I developed the concept and design of the study, performed biosynthesis of IONPs, TEM, EDS, UV-vis, fluorescence microscopy, catalytic activity study, took part in FTIR, MALDI, XRD analyses, prepared the original draft and revised it during peer-review process.

Piya Roychoudhury

Instytut Nauk o Morzu i Środowisku: ul. Adama Mickiewicza 16, 70-383 Szczecin
Sekretariat: tel. 914442461, e-mail sekretariat.nms@usz.edu.pl
Dyrektor Instytutu: tel. 91 4442462, e-mail: dyrektor.nms@usz.edu.pl

Dr Przemysław Dąbek

Institute of Marine and Environmental Sciences

University of Szczecin

Mickiewicza 16a, 70-383 Szczecin, Poland

Declaration

I hereby declare that my contribution in the preparation of article: "Study on Biogenic Spindle-Shaped Iron-Oxide Nanoparticles by *Pseudostaurosira trainorii* in Field of Laser Desorption/Ionization Applications" published in International Journal of Molecular Sciences, 23: 11713, of which I am co-author with Roychoudhury P., Golubeva A., Pryshchepa O., Sagandykova, G., Pomastowski P., Gloc M., Dobrucka R., Kurzydłowski, K., Buszewski B. and Witkowski A. equals to 10% (percent). For the purpose of the study, I supervised the work of PhD student Golubeva A., and took part in methodology development and revision of the original draft.

Przemysław Dąbek

Instytut Nauk o Morzu i Środowisku: ul. Adama Mickiewicza 16, 70-383 Szczecin
Sekretariat: tel. 914442461, e-mail sekretariat.nms@usz.edu.pl
Dyrektor Instytutu: tel. 91 4442462, e-mail: dyrektor.nms@usz.edu.pl

UNIWERSYTET
MIKOŁAJA KOPERNIKA
W TORUNIU
Interdyscyplinarne Centrum
Nowoczesnych Technologii

Dr. Paweł Pomastowski, DSc., Prof. NCU

Centre for Modern Interdisciplinary Technologies

Nicolaus Copernicus University in Toruń

Wileńska 4, 87-100, Toruń, Poland

Declaration

I hereby declare that my contribution in the preparation of article: " Study on Biogenic Spindle-Shaped Iron-Oxide Nanoparticles by Pseudostaurosira trainorii in Field of Laser Desorption/Ionization Applications. International Journal of Molecular Sciences " published in International Journal of Molecular Sciences, 23: 11713, of which I am co-author with Roychoudhury P., Golubeva A., Dąbek P., Pryshchepa O., Sagandykova, G., Gloc M., Dobrucka R., Kurzydłowski, K., Buszewski B. and Witkowski A. equals to 5% (percent). For the purpose of the study, I took part in conceptualization of the study, reviewed the original draft, and helped with revision in peer-review process.

Prof. Dr hab. Andrzej Witkowski

Institute of Marine and Environmental Sciences

University of Szczecin

Mickiewicza 16a, 70-383 Szczecin, Poland

Declaration

I hereby declare that my contribution in the preparation of article: " Study on Biogenic Spindle-Shaped Iron-Oxide Nanoparticles by *Pseudostaurosira trainorii* in Field of Laser Desorption/Ionization Applications" published in International Journal of Molecular Sciences, 23: 11713, of which I am co-author with Roychoudhury P., Golubeva A., Dąbek P., Pryshchepa O., Sagandykova, G., Pomastowski P., Gloc M., Dobrucka R., Kurzydłowski, K., and Buszewski B. equals to 10% (percent). I supervised the investigation and work of PhD student Golubeva A., and revised the original draft.

Andrzej Witkowski

Instytut Nauk o Morzu i Środowisku: ul. Adama Mickiewicza 16, 70-383 Szczecin
Sekretariat: tel. 914442461, e-mail sekretariat.nms@usz.edu.pl
Dyrektor Instytutu: tel. 91 4442462, e-mail: dyrektor.nms@usz.edu.pl